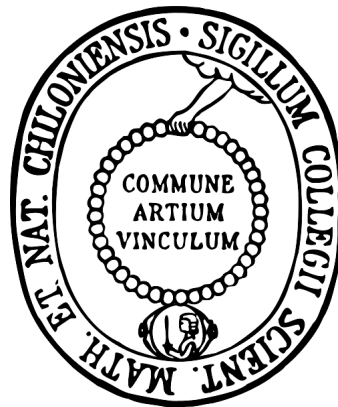


Geochronology and Geochemistry of the Tristan-Gough Hotspot Track

Dissertation

zur Erlangung des Doktorgrades
der Mathematisch-Naturwissenschaftlichen Fakultät
der Christian-Albrechts-Universität zu Kiel



vorgelegt von

Joana Kristin Rohde

Kiel, 2013

Erster Gutachter: Prof. Dr. Kaj Hoernle

Zweiter Gutachter: Dr. habil. Jörg Geldmacher

Tag der mündlichen Prüfung: 25.06.2013

Zum Druck genehmigt:

.....
Der Dekan

Hiermit erkläre ich, dass ich die vorliegende Doktorarbeit selbständig und ohne Zuhilfenahme unerlaubter Hilfsmittel erstellt habe. Sie stellt, abgesehen von der Beratung durch meinen Betreuer, nach Inhalt und Form meine eigene Arbeit dar. Diese Arbeit wurde nie an einer anderen Hochschule im Rahmen eines Prüfungsverfahrens vorgelegt, veröffentlicht oder zur Veröffentlichung vorgelegt. Im Rahmen meiner Diplomarbeit wurden Voruntersuchungen zum Thema der vorliegenden Arbeit gemacht. Einige Daten und Basisinterpretationsansätze sind zum Teil in die vorliegende Arbeit mit eingeflossen, wurden aber unter Zuhilfenahme eines neuen, umfangreichen Datensatzes umfassend neu und selbständig interpretiert und in einen komplexen Zusammenhang gestellt. Ferner versichere ich, dass die Arbeit unter Einhaltung der Regeln guter wissenschaftlicher Praxis der Deutschen Forschungsgemeinschaft entstanden ist.

Kiel, den.....

Joana Kristin Rohde

Preface

The following dissertation is composed of three independent chapters that are either published in an international journal, accepted for publication or are in preparation for submission to international journals. Chapter I is published in *Tectonophysics*, Chapter II is published in *Geology* and Chapter III is in preparation for submission to *Earth and Planetary Science Letters*.

This dissertation was written within the framework of the projects Ho 1833/17-1 and 17-2 funded through the Priority Program 1375 (SAMPLE = South Atlantic Margin Processes and Links with onshore Evolution) of the German Research Foundation (DFG). The research objectives of this program are the investigation of processes related to the rifting of the South Atlantic continental margins ranging e.g. from lithospheric, mantle and magmatic as well as sedimentary aspects and the associated topographic, tectonic and climatic effects.

Abstract

Age progressive chains of volcanoes are commonly believed to reflect movement of lithosphere over buoyant mantle plumes or hotspots. The V-shaped northeast-southwest striking Tristan-Gough hotspot track in the South Atlantic, thought to represent a classic example of a hotspot track (e.g., Wilson, 1963; O'Connor and Duncan, 1990; O'Connor and Le Roex, 1992), consists of the aseismic Walvis Ridge in the northeast and the associated Guyot Province to the southwest. The latter consists of various dispersed volcanic edifices in the form of isolated seamounts and small volcanic ridges shaping the spatially separated Tristan and Gough subtracks. The bathymetric anomalies associated with the seamount chains become less continuous and diverge towards the Tristan da Cunha and Gough island groups. The Tristan-Gough hotspot track connects these islands, representing the volcanically active center of the Tristan-Gough plume, with the Etendeka continental flood basalts (CFBs) in Namibia. A similar spatial link is proposed for the Paraná CFBs in Brazil and the Rio Grande Rise, a massive northwest-southeast trending volcanic structure in the South Atlantic on the South American Plate. The latter is considered to have formed contemporaneously with the Walvis Ridge.

The major goals of this study were to investigate the age distribution of volcanism along the Tristan-Gough volcanic track and the Rio Grande Rise with a detailed high-quality $^{40}\text{Ar}/^{39}\text{Ar}$ age data set on mineral separates, to evaluate geochemical variations along and across the Tristan-Gough hotspot track in order to test for a possible geochemical zonation and to understand the long-term evolution the Tristan-Gough plume. Furthermore, the origin and geochemical characteristics of the mantle sources contributing to the Tristan-Gough hotspot system should be determined, especially to provide constraints about the origins of the EM-I mantle endmember and the large-scale geochemical DUPAL anomaly in the South Atlantic mantle. Therefore, all available igneous basement samples from the Walvis Ridge, the Rio Grande Rise and the Guyot Province (Tristan and Gough subtracks), dredged during various international cruises and cored at five DSDP sites, were investigated.

Since previous attempts of volcanic age determination on altered rock groundmass from samples of the Tristan-Gough volcanic track mainly produced statistically invalid

results, detailed laser step-heating $^{40}\text{Ar}/^{39}\text{Ar}$ analyses were carried out on mineral separates from the Tristan-Gough volcanic track and the Rio Grande Rise. The new results clearly illustrate that valid $^{40}\text{Ar}/^{39}\text{Ar}$ ages can be obtained even for up to 114 Ma old submarine samples if mineral separates are analyzed and the effects of alteration on the K-Ar isotope system are critically evaluated. Although the age results in most cases differ significantly from the published ones for the same samples and for samples from the same locations, the inferred ages clearly confirm the suggested age progression from the Etendeka CFBs to Tristan da Cunha and Gough, which is consistent with a mantle plume origin for this volcanism (O'Connor and Duncan, 1990; O'Connor and Le Roex, 1992) rather than solely a tectonic origin.

In addition to the geochronological investigations, intensive major and incompatible trace element and Sr-Nd-Hf-Pb DS (double spike) isotope measurements were carried out. These data reveal a long-term bilateral zonation with two distinct mantle source components within the Guyot Province. The Gough component is isotopically enriched with elevated $^{207}\text{Pb}/^{204}\text{Pb}$ and $^{208}\text{Pb}/^{204}\text{Pb}$ at a given $^{206}\text{Pb}/^{204}\text{Pb}$, but low $^{143}\text{Nd}/^{144}\text{Nd}$ and $^{176}\text{Hf}/^{177}\text{Hf}$ and generally higher $^{87}\text{Sr}/^{86}\text{Sr}$ compared to the Tristan component. Both components can be traced from the islands of Tristan and Gough 70 Ma through the Guyot Province to the DSDP transect at southwestern end of the Walvis Ridge. In contrast to the Guyot Province, the >70 Ma parts of the Tristan-Gough hotspot track (Walvis Ridge and Rio Grande Rise), do not exhibit a geochemical zonation. Instead, these portions of the track are dominated by the enriched mantle (EM-) or DUPAL-type isotopic signature of the Gough domain, which is also found in the Paraná and Etendeka CFBs. In addition to the Gough domain, the Etendeka flood basalts are also influenced by the Tristan-type component. Consequently, both components were present in the plume source during the plume head stage. The fact that the Tristan source was not present in the early plume tail stage indicates that it was either not sampled during that time or that its presence was masked by extensive melting while the plume was located beneath the Mid-Atlantic Ridge.

Samples from the Rio Grande Rise, the oldest, northeastern part of the Walvis Ridge as well as some samples from the Paraná and Etendeka CFBs are isotopically as enriched as samples from DSDP Site 525A, which is considered to be the type locality for

the EM-I mantle endmember in the South Atlantic (Zindler and Hart, 1986). The existence of this component during the initial plume head and the early plume tail stage indicates that this component is not only of local extent, but that it is a major component in the Tristan-Gough plume.

The Gough isotopic domain can be derived through deep recycling of an EM-I-type component (e.g., SCLM peridotite) and a FOZO/HIMU-type component (subducted oceanic crust as eclogite) \pm an EM-II-type component (marine sediments). Entrainment of ambient depleted lower mantle into the northwest side of the plume, possibly followed by mixing with the enriched Gough component can explain the formation of the Tristan compositional domain, which appears at ~ 70 Ma. A possible mechanism to explain the range of the Gough domain is deep recycling of EM-type continental lithosphere, oceanic crust (FOZO) and EM-type sediments that possibly subducted into the lower mantle from where it rises back to the surface at the boundary of the large-scale, lower-mantle, low-seismic-velocity anomaly (LLSVP) beneath Southern Africa via the Tristan-Gough mantle plume. This suggests that both continental and oceanic lithosphere are present in the African LLSVP (see also Rohde et al., 2013).

Many asymmetrically zoned hotspot tracks in the Pacific Ocean (e.g., Galápagos, Hawaii, Samoa, the Society Islands or the Marquesas) are located more or less at the border of the LLSVP beneath the southern Pacific. Their zonation has been ascribed to asymmetric zonation of these plumes, rising from the deep mantle in the form of vertical stripes or filaments (Hoernle et al., 2000; Kerr and Mériaux, 2004; Abouchami et al., 2005; Farnetani and Hofmann, 2009; Lohmann et al., 2009; Huang et al., 2011; Weis et al., 2011; Chauvel et al., 2012). It has been proposed that the enriched domain of these zoned hotspots represent the Pacific LLSVP material (Huang et al., 2011; Weis et al., 2011; Chauvel et al., 2012; Payne et al., 2013). The Tristan-Gough plume is the first zoned plume to be recognized that is located above the margin of the African LLSVP. Furthermore, the coexistence of the geochemical distinct trends within the Tristan-Gough hotspot track can be traced for 70 Ma, which is four times longer than documented for Pacific zoned hotspot tracks. The isotope data and the location of the active plume center above the African LLSVP indicate that the enriched southern Gough-type source, present during the entire evolution of the Tristan-Gough hotspot track, represents the African LLSVP composition.

At around 50-60 Ma, the Tristan-Gough hotspot track shows changes in major and

trace elements composition, coinciding with a morphological change from the older voluminous Walvis Ridge to the younger more diffuse Guyot Province. The latter comprises alkalic and silica-undersaturated rocks that are characterized by a stronger enrichment in highly to moderately incompatible trace elements, whereas the samples from the Walvis Ridge are generally less alkalic with mostly tholeiitic compositions. A compositional difference between the Walvis Ridge and the Guyot Province can also be seen in the isotopic composition of the rocks. These geochemical differences can be explained by the change from the formation beneath the MAR to the formation in an intraplate setting. Higher degrees of melting at shallower depths beneath the MAR led to the greater volume and the major and trace element as well as isotopic compositions of the Walvis Ridge, while the rocks of the less voluminous Guyot Province were formed at lower degrees of melting at deeper average depths in an intraplate setting (“lid effect”, Niu et al., 2003). But although the lithospheric thickness (lid effect) influences the major and trace elements and the isotopic composition explaining the temporal changes at the transition from the Walvis Ridge to the Guyot Province, it cannot explain the existence of the zonation within the Guyot Province.

From the spatial age progression, the morphology of the track and the geochemical characteristics a geodynamic model of plume evolution can be derived. According to this model, plume volcanism started at ~132 Ma with the formation of Etendeka-Paraná CFBs (Renne et al., 1996), which do not show a geochemical zonation, but which are influenced by both Gough- and Tristan-type components. Afterwards, the plume head turned into a stable ridge-centered plume conduit, which formed the Gough source-dominated Walvis Ridge and Rio Grande Rise. This plume conduit seemed to become weaker and bifurcated at <60-70 Ma, shortly after the first evidence of plume zonation, suggesting a connection between geochemical zonation of the plume and a potential bifurcation of the plume conduit. Finally the plume might have been disaggregated in its waning stages (~35-45 Ma) into single blobs, which explains the diffuse character of the Guyot Province.

Comparing the Tristan-Gough hotspot track with the zoned Hawaiian hotspot track unravels that there are fundamental differences in their compositional evolution over their life spans although they are both located above the borders of the African and the Pacific LLSVPs.

References

- Abouchami, W., Hofmann, A.W., Galer, S.J.G., Frey, F.A., Eisele, J., and Feigenson, M., 2005, Lead isotopes reveal bilateral asymmetry and vertical continuity in the Hawaiian mantle plume: *Nature*, v. 434, p. 851-856, doi:10.1038/nature03402.
- Chauvel, C., Maury, R.C., Blais, S., Lewin, E., Guillou, H., Guille, G., Rossi, P., and Gutscher, M.-A., 2012, The size of plume heterogeneities constrained by Marquesas isotopic stripes: *Geochemistry, Geophysics, Geosystems*, v. 13, Q07005, doi:10.1029/2012GC004123.
- Farnetani, C.G., and Hofmann, A.W., 2009, Dynamics and internal structure of a lower mantle plume conduit: *Earth and Planetary Science Letters*, v. 282, p. 314-322, doi:10.1016/j.epsl.2009.03.035.
- Hoernle, K., Werner, R., Phipps Morgan, J., Garbe-Schönberg, D., Bryce, J., and Mrazek, J., 2000, Existence of complex spatial zonation in the Galápagos plume for at least 14 m.y: *Geology*, v. 28, p. 435-438, doi: 10.1130/0091-7613.
- Huang, S., Hall, P.S., and Jackson, M.G., 2011, Geochemical zoning of volcanic chains associated with Pacific hotspots: *Nature Geoscience*, v. 4, p. 874-878, doi:10.1038/ngeo1263.
- Kerr, R.C., and Mériaux, C., 2004, Structure and dynamics of sheared mantle plumes: *Geochemistry, Geophysics, Geosystems*, v. 5, Q12009, doi: 10.1029/2004GC000749.
- Lohmann, F.C., Hort, M., and Phipps Morgan, J., 2009, Flood basalts and ocean island basalts: A deep source or shallow entrainment?: *Earth and Planetary Science Letters*, v. 284, p. 553-563, doi:10.1016/j.epsl.2009.05.025.
- Niu, Y., and O'Hara, M.J., 2003, Origin of ocean island basalts: A new perspective from petrology, geochemistry, and mineral physics considerations: *Journal of Geophysical Research*, v. 108, 2209, doi:10.1029/2002JB002048.
- O'Connor, J.M., and Duncan, R.A., 1990, Evolution of the Walvis Ridge-Rio Grande Rise hot spot system: implications for African and South American plate motions over plumes: *Journal of Geophysical Research*, v. 95, p. 17,475-17,502, doi: 10.1029/JB095iB11p17475.
- O'Connor, J.M., and Le Roex, A.P., 1992, South Atlantic hot spot-plume systems: 1. Distribution of volcanism in time and space: *Earth and Planetary Science Letters*, v. 113, p. 343-364, doi:10.1016/0012-821X(92)90138-L.

- Payne, J.A., Jackson, M.G., and Hall, P.S., 2013, Parallel volcano trends and geochemical asymmetry of the Society Islands hotspot track: *Geology*, v. 41, p. 19-22, doi:10.1130/G33273.1.
- Renne, P.R., Glen, J.M., Milner, S.C., and Duncan, A.R., 1996, Age of Etendeka flood volcanism and associated intrusions in southwestern Africa: *Geology*, v. 24, p. 659-662, doi:10.1130/0091-7613.
- Rohde, J., Hoernle, K., Hauff, F., Werner, R., O'Connor, J., Class, C., Garbe-Schönberg, D., and Jokat, W., 2013, 70 Ma chemical zonation of the Tristan-Gough hotspot track: *Geology*, v. 41, p. 335-338, doi:10.1130/G33790.1.
- Weis, D., Garcia, M.O., Rhodes, J.M., Jellinek, M., and Scoates, J.S., 2011, Role of the deep mantle in generating the compositional asymmetry of the Hawaiian mantle plume: *Nature Geoscience*, v. 4, p. 831-838, doi:10.1038/ngeo1328.
- Wilson, J.T., 1963, A possible origin of the Hawaiian Islands: *Canadian Journal of Physics*, v. 41, p. 863-870, doi: 10.1139/p63-094.
- Zindler, A., and Hart, S., 1986, Chemical Geodynamics: *Annual Review of Earth and Planetary Sciences*, v. 14, p. 493-571.

Kurzfassung

Es wird vermutet, dass altersprogressive Vulkanketten die Bewegung der Lithosphäre über auftreibende Plumes oder Hotspots widerspiegeln. Die V-förmige, von Nordost nach Südwest verlaufende Tristan-Gough Hotspot-Spur im Südatlantik ist vermutlich ein klassisches Beispiel einer Hotspot-Spur (z.B. Wilson, 1963; O'Connor und Duncan, 1990; O'Connor und Le Roex, 1992). Sie besteht aus dem aseismischen Walvis-Rücken im Nordosten und der daran anschließenden Guyot-Provinz im Südwesten. Letztere besteht aus diversen zerstreuten vulkanischen Strukturen in Form von isolierten Tiefseebergen und kleinen vulkanischen Rücken, die die räumlich getrennten Tristan- und Gough-Ketten ausbilden. Die bathymetrischen Anomalien, die mit diesen Tiefseebergketten zusammen hängen, werden unregelmäßiger und laufen in Richtung Inselgruppen von Tristan da Cunha und Gough auseinander. Die Tristan-Gough Hotspot-Spur verbindet diese Inseln, die das vulkanisch aktive Zentrum des Tristan-Gough Plumes darstellen, mit den kontinentalen Etendeka Flutbasalten in Namibia. Ein ähnlicher räumlicher Zusammenhang besteht wahrscheinlich zwischen den kontinentalen Paraná Flutbasalten in Brasilien und dem Rio Grande Rise, einer massiven vulkanischen Struktur im Südatlantik auf der südamerikanischen Platte, die von Nordwest nach Südost verläuft. Von der letzteren wird vermutet, dass sie zeitgleich mit dem Walvis-Rücken entstanden ist.

Die Hauptziele dieser Studie waren, mithilfe eines detaillierten hochqualitativen $^{40}\text{Ar}/^{39}\text{Ar}$ -Altersdatensatzes an Mineralseparaten die Altersverteilung des Vulkanismus entlang der vulkanischen Tristan-Gough Spur und dem Rio Grande Rise zu untersuchen, geochemische Variationen entlang und innerhalb der Tristan-Gough Hotspot-Spur zu beurteilen, um eine mögliche geochemische Zonierung aufzudecken und die langfristige Entwicklung des Tristan-Gough Plumes zu verstehen. Darüber hinaus sollten die Herkunft und die geochemischen Eigenschaften der Mantelquellen bestimmt werden, die zum Tristan-Gough Hotspotsystem beigetragen haben, vor allem im Hinblick darauf, Hinweise über das EM-I Mantelendglied und die großräumige geochemische DUPAL-Anomalie im Mantel unter dem Südatlantik zu liefern. Deshalb wurden alle verfügbaren vulkanischen Gesteine vom Walvis-Rücken, dem Rio Grande Rise und der Guyot-Provinz (Tristan- und Gough-

Kette) untersucht, die während diverser internationaler Schiffsexpeditionen (Dredge-Proben) und fünf DSDP-Bohrkampagnen genommen wurden.

Da bisherige Versuche, anhand von alterierter Grundmasse vulkanische Alter entlang der vulkanischen Tristan-Gough Spur zu bestimmen, größtenteils statistisch ungültige Ergebnisse erzielt haben, wurden detaillierte $^{40}\text{Ar}/^{39}\text{Ar}$ -Analysen mittels Laser-Stufenheizungsverfahren an Mineralseparaten von der vulkanischen Tristan-Gough Spur und dem Rio Grande Rise durchgeführt. Die neuen Ergebnisse zeigen eindeutig, dass gültige $^{40}\text{Ar}/^{39}\text{Ar}$ -Alter auch an bis zu 114 Millionen Jahre alten submarinen Proben bestimmt werden können, wenn man Mineralseparate untersucht und Alterationseffekte auf das K-Ar-System kritisch abschätzt. Obwohl die Alter in den meisten Fällen signifikant von den veröffentlichten Altern der gleichen Proben und Proben von gleichen Lokationen abweichen, bestätigen die ermittelten Alter eindeutig die angenommene Altersprogression von den kontinentalen Etendeka Flutbasalten zu den Inseln Tristan da Cunha und Gough. Dies stimmt eher mit einer Herkunft für diesen Vulkanismus durch einen Mantelplume überein (O'Connor und Duncan, 1990; O'Connor und Le Roex, 1992) als durch ausschließlich tektonische Prozesse.

Zusätzlich zu den geochronologischen Untersuchungen wurden intensive Hauptelement- und inkompatible Spurenelement- sowie Sr-Nd-Hf-Pb DS (Double Spike) Isotopenmessungen durchgeführt. Diese Daten decken eine langfristige bilaterale Zonierung mit zwei verschiedenen Mantelquellkomponenten innerhalb der Guyot-Provinz auf. Die Gough-Komponente ist mit erhöhtem $^{207}\text{Pb}/^{204}\text{Pb}$ und $^{208}\text{Pb}/^{204}\text{Pb}$ bei einem bestimmten $^{206}\text{Pb}/^{204}\text{Pb}$, aber geringem $^{143}\text{Nd}/^{144}\text{Nd}$ und $^{176}\text{Hf}/^{177}\text{Hf}$ und generell höherem $^{87}\text{Sr}/^{86}\text{Sr}$ im Vergleich zur Tristan-Komponente isotopisch angereichert. Beide Komponenten können von den Inseln etwa 70 Millionen Jahre entlang der Guyot-Provinz bis zum DSDP-Bohrprofil am südwestlichen Ende des Walvis-Rückens zurückverfolgt werden. Im Gegensatz zur Guyot-Provinz zeigt der Teil der Tristan-Gough Hotspot-Spur, der älter als 70 Millionen Jahre alt ist (Walvis-Rücken und Rio Grande Rise), keine Zonierung. Stattdessen zeigen diese Bereiche eine Beeinflussung durch die angereicherte (EM-) oder DUPAL-typische Isotopensignatur der Gough-Domäne, die man auch in den kontinentalen Paraná und Etendeka Flutbasalten findet. Zusätzlich zur Gough-Domäne zeigen die Etendeka Flutbasalte auch einen Einfluss durch die Tristan-Komponente.

Deshalb waren beide Komponenten während der Plumekopf-Phase in der Plumequelle vorhanden. Die Tatsache, dass die Tristan-Komponente in der frühen Plumestamm-Phase nicht vorhanden war, deutet an, dass sie in dieser Phase entweder nicht angezapft wurde oder dass ihre Anwesenheit durch intensives Schmelzen überdeckt wurde während der Plume unterhalb des Mittelatlantischen Rückens lag.

Proben vom Rio Grande Rise, vom älteren, nordöstlichen Teil des Walvis-Rückens und auch einige Proben von den Paraná und Etendeka Flutbasalten sind isotopisch so angereichert wie die Proben von der DSDP Lokation 525A, die die Typlokalität für das EM-I Mantelendglied im Südatlantik darstellt (Zindler und Hart, 1986). Die Existenz dieser Komponentewährend der initialen Plumekopf- und der frühen Plumestamm-Phase deutet an, dass diese Komponente nicht nur von lokalem Ausmaß ist, sondern dass sie eine Hauptkomponente im Tristan-Gough Plume ist.

Die isotopische Gough-Domäne kann aus tiefem Recycling von einer EM-I-ähnlichen Komponente (z.B. SCLM-Peridotit) und einer FOZO/HIMU-ähnlichen Komponente (subduzierte ozeanische Kruste als Eklogit) \pm einer EM-II-ähnlichen Komponente (marine Sedimente) abgeleitet werden. Die Aufnahme von umgebendem verarmtem Material aus dem unteren Mantel in die nordwestliche Seite des Plumes und die unter Umständen anschließend stattfindende Mischung mit der angereicherten Gough-Komponente kann die Bildung der Tristan-Komponente erklären, die bei ~70 Millionen Jahren auftritt. Ein möglicher Mechanismus, den Umfang der Gough-Komponente zu erklären, ist tiefes Recycling EM-ähnlicher kontinentaler Kruste, ozeanischer Kruste (FOZO) und EM-ähnlicher Sedimente, die möglicherweise in den unteren Mantel subduziert wurden, von wo aus sie am Rand der großräumigen seismischen Anomalie im unteren Mantel unter dem südlichen Afrika (LLSVP; geringe seismische Schergeschwindigkeiten) in Form des Tristan-Gough Plumes wieder zur Oberfläche aufsteigen. Das deutet an, dass sowohl kontinentale als auch ozeanische Lithosphäre in der afrikanischen LLSVP vorhanden sind (siehe auch Rohde et al., 2013).

Viele asymmetrisch zonierte Hotspot-Spuren im Pazifik (z.B. Galápagos, Hawaii, Samoa, die Society-Inseln oder die Marquesas-Inseln) liegen mehr oder weniger über dem Rand der LLSVP unter dem südlichen Pazifik. Deren Zonierung hat man der asymmetrischen Zonierung der Plumes zugeschrieben, die in Form von Streifen oder Fasern aus dem unteren Mantel aufsteigen (Hoernle et al., 2000; Kerr und Mériaux, 2004;

Abouchami et al., 2005; Farnetani und Hofmann, 2009; Lohmann et al., 2009; Huang et al., 2011; Weis et al., 2011; Chauvel et al., 2012). Es wird angenommen, dass die angereicherte Domäne dieser Plumes das Material aus der pazifischen LLSVP repräsentiert (Huang et al., 2011; Weis et al., 2011; Chauvel et al., 2012; Payne et al., 2013). Der Tristan-Gough Plume ist der erste zonierte Plume, der über dem Rand der afrikanischen LLSVP liegt. Des Weiteren kann die Koexistenz der geochemisch unterschiedlichen Trends innerhalb der Tristan-Gough Hotspot-Spur 70 Millionen Jahre zurückverfolgt werden. Das ist viermal länger als für alle bisher entdeckten zonierten pazifischen Plumes. Die Isotopendaten und die Lage des aktiven Plume-Zentrums über der afrikanischen LLSVP deuten an, dass die angereicherte südliche Gough-Quelle, die während der gesamten Entwicklung der Tristan-Gough Hotspot-Spur gegenwärtig war, die Zusammensetzung der afrikanischen LLSVP widerspiegelt.

Bei etwa 50-60 Millionen Jahren zeigt die Tristan-Gough Hotspot-Spur Veränderungen in den Haupt- und Spurenelementzusammensetzungen. Dies stimmt mit einer Veränderung in der Morphologie vom älteren, voluminöseren Walvis-Rücken zur jüngeren, zerstreuteren Guyot-Provinz überein. Letztere umfasst alkalische und Silica-untersättigte Gesteine, die durch eine stärkere Anreicherung von stark bis moderat inkompatiblen Spurenelementen charakterisiert sind. Dahingegen sind die Proben vom Walvis-Rücken generell weniger alkalisch und haben meist tholeiitische Zusammensetzungen. Einen Unterschied in der Zusammensetzung zwischen dem Walvis-Rücken und der Guyot Provinz kann man auch in der isotopischen Zusammensetzung der Gesteine beobachten. Diese geochemischen Unterschiede können durch einen Wechsel von der Bildung unterhalb des MAR zur Bildung in einem Intraplatten-Milieu erklärt werden. Höhere Aufschmelzgrade bei geringeren Tiefen unterhalb des MAR führten zu dem größeren Volumen des Walvis-Rückens sowie dessen Haupt- und Spurenelement- sowie Isotopenzusammensetzungen. Im Gegensatz dazu wurden die Gesteine der weniger voluminösen Guyot-Provinz bei geringeren Aufschmelzgraden und höheren Durchschnittstiefen in einem Intraplatten-Milieu gebildet ("Lid Effect", Niu et al., 2003). Aber obwohl die Lithosphärendicke (Lid Effect) die Haupt- und Spurenelemente sowie die isotopische Zusammensetzung beeinflusst, was wiederum die zeitlichen Veränderungen am Übergang vom Walvis-Rücken zur Guyot-Provinz erklärt, kann sie dennoch nicht die Existenz der Zonierung innerhalb der Guyot Province erklären.

Mithilfe der räumlichen Altersprogression, der Morphologie der Spur und den geochemischen Eigenschaften kann man ein Entwicklungsmodell für den Plume ableiten. Nach diesem Modell begann der Plume-Vulkanismus vor etwa 132 Millionen Jahren mit der Bildung der kontinentalen Etendeka und Paraná Flutbasalte (Renne et al., 1996), die keine geochemische Zonierung zeigen, aber sowohl von der Gough- als auch von der Tristan-Komponente beeinflusst sind. Anschließend wandelte sich der Plumekopf in einen stabilen Plumestamm unter dem Mittelatlantischen Rücken um, der den von der Gough-Quelle dominierten Walvis-Rücken und die Guyot-Provinz geformt hat. Dieser Plumestamm wurde scheinbar schwächer und gabelte sich bei etwa 60-70 Millionen Jahren, kurz nachdem zum ersten Mal Anzeichen für eine Zonierung auftraten. Dies deutet an, dass es eine Verbindung zwischen der geochemischen Zonierung des Plumes und einer möglichen Aufspaltung des Plumestamms gibt. Schließlich ist der Plume in seiner schwächer werdenden Phase (~35-45 Millionen Jahre) unter Umständen in einzelne „Tropfen“ zerfallen. Das würde das diffuse Erscheinungsbild der Guyot-Provinz erklären.

Ein Vergleich zwischen der Tristan-Gough Hotspot-Spur und der zonierten hawaiianischen Hotspot-Spur deckt auf, dass es fundamentale Unterschiede in der Entwicklung der Zusammensetzungen im Laufe ihrer Lebensdauer gibt, obwohl beide Plumes über den Rändern der afrikanischen und pazifischen LLSVP liegen.

References

- Abouchami, W., Hofmann, A.W., Galer, S.J.G., Frey, F.A., Eisele, J., und Feigenson, M., 2005, Lead isotopes reveal bilateral asymmetry and vertical continuity in the Hawaiian mantle plume: *Nature*, v. 434, p. 851-856, doi:10.1038/nature03402.
- Chauvel, C., Maury, R.C., Blais, S., Lewin, E., Guillou, H., Guille, G., Rossi, P., und Gutscher, M.-A., 2012, The size of plume heterogeneities constrained by Marquesas isotopic stripes: *Geochemistry, Geophysics, Geosystems*, v. 13, Q07005, doi:10.1029/2012GC004123.
- Farnetani, C.G., und Hofmann, A.W., 2009, Dynamics and internal structure of a lower mantle plume conduit: *Earth and Planetary Science Letters*, v. 282, p. 314-322, doi:10.1016/j.epsl.2009.03.035.

- Hoernle, K., Werner, R., Phipps Morgan, J., Garbe-Schönberg, D., Bryce, J., und Mrazek, J., 2000, Existence of complex spatial zonation in the Galápagos plume for at least 14 m.y: *Geology*, v. 28, p. 435-438, doi: 10.1130/0091-7613.
- Huang, S., Hall, P.S., und Jackson, M.G., 2011, Geochemical zoning of volcanic chains associated with Pacific hotspots: *Nature Geoscience*, v. 4, p. 874-878, doi:10.1038/ngeo1263.
- Kerr, R.C., und Mériaux, C., 2004, Structure and dynamics of sheared mantle plumes: *Geochemistry, Geophysics, Geosystems*, v. 5, Q12009, doi: 10.1029/2004GC000749.
- Lohmann, F.C., Hort, M., und Phipps Morgan, J., 2009, Flood basalts and ocean island basalts: A deep source or shallow entrainment?: *Earth and Planetary Science Letters*, v. 284, p. 553-563, doi:10.1016/j.epsl.2009.05.025.
- Niu, Y., und O'Hara, M.J., 2003, Origin of ocean island basalts: A new perspective from petrology, geochemistry, and mineral physics considerations: *Journal of Geophysical Research*, v. 108, 2209, doi:10.1029/2002JB002048.
- O'Connor, J.M., und Duncan, R.A., 1990, Evolution of the Walvis Ridge-Rio Grande Rise hot spot system: implications for African and South American plate motions over plumes: *Journal of Geophysical Research*, v. 95, p. 17,475-17,502, doi: 10.1029/JB095iB11p17475.
- O'Connor, J.M., und Le Roex, A.P., 1992, South Atlantic hot spot-plume systems: 1. Distribution of volcanism in time and space: *Earth and Planetary Science Letters*, v. 113, p. 343-364, doi:10.1016/0012-821X(92)90138-L.
- Payne, J.A., Jackson, M.G., und Hall, P.S., 2013, Parallel volcano trends and geochemical asymmetry of the Society Islands hotspot track: *Geology*, v. 41, p. 19-22, doi:10.1130/G33273.1.
- Renne, P.R., Glen, J.M., Milner, S.C., und Duncan, A.R., 1996, Age of Etendeka flood volcanism and associated intrusions in southwestern Africa: *Geology*, v. 24, p. 659-662, doi:10.1130/0091-7613.
- Rohde, J., Hoernle, K., Hauff, F., Werner, R., O'Connor, J., Class, C., Garbe-Schönberg, D., und Jokat, W., 2013, 70 Ma chemical zonation of the Tristan-Gough hotspot track: *Geology*, v. 41, p. 335-338, doi:10.1130/G33790.1.
- Weis, D., Garcia, M.O., Rhodes, J.M., Jellinek, M., und Scoates, J.S., 2011, Role of the deep mantle in generating the compositional asymmetry of the Hawaiian mantle plume: *Nature Geoscience*, v. 4, p. 831-838, doi:10.1038/ngeo1328.

Wilson, J.T., 1963, A possible origin of the Hawaiian Islands: Canadian Journal of Physics, v. 41, p. 863-870, doi: 10.1139/p63-094.

Zindler, A., und Hart, S., 1986, Chemical Geodynamics: Annual Review of Earth and Planetary Sciences, v. 14, p. 493-571.

Danksagung

Die vorliegende Arbeit entstand im Rahmen der durch die Deutsche Forschungsgemeinschaft (DFG) geförderten Projekte HO 1833/17-1 und 17-2 innerhalb des Schwerpunktprogramms 1375 (SAMPLE = South Atlantic Margin Processes and Links with onshore Evolution). Für die Ausarbeitung und das Stellen der Projektanträge möchte ich mich ganz herzlich bei Prof. Dr. Kaj Hoernle, Dr. Folkmar Hauff und Dr. Reinhard Werner bedanken.

Mein ganz besonderer Dank gilt meinem Betreuer Prof. Dr. Kaj Hoernle für die Vergabe dieser Arbeit, seine Diskussionsbereitschaft sowie seine Ideen und Denkanstöße, die mich immer wieder voran gebracht und meine Arbeit in die richtige Richtung gelenkt haben. Die kritische Durchsicht meiner Manuskripte sowie seine Unterstützung bei der Interpretation meiner analytischen Daten waren mir immer eine sehr große Hilfe.

Des Weiteren bedanke ich mich ganz herzlich bei Dr. Jörg Geldmacher für die Übernahme des zweiten Gutachtens.

Ganz besonders bedanken möchte ich mich bei Dr. Folkmar Hauff für die Einarbeitung in die „Kunst“ der Isotopenanalyse, für seine Unterstützung bei der Auswertung und Interpretation meiner Daten sowie für seine Gesprächsbereitschaft bei Fragen aller Art. Ich danke ihm außerdem für die kritische Durchsicht meiner Manuskripte und Konferenzbeiträge, die Durchführung einiger Isotopenanalysen, aber besonders dafür, dass er mich seit mehr als zehn Jahren auf meinem geologischen Weg begleitet und unterstützt hat.

Bei Dr. Paul van den Bogaard möchte ich mich für die Durchführung der $^{40}\text{Ar}/^{39}\text{Ar}$ -Datierungen sowie für die Auswertung und die Hilfe bei der Interpretation der Altersdaten bedanken.

Darüber hinaus bedanke ich mich herzlich bei Dr. John O'Connor und Roel van Elsas für die Einarbeitung und Hilfestellung bei der Separation der Mikrofeldspäte, die Aufbereitung meiner Proben für die Datierung, für die Organisation und Durchführung der Altersdatierungen sowie für zwei sehr schöne Aufenthalte in Amsterdam.

Bei Prof. Dr. Susan E. Humphris, Prof. Dr. Roger Hekinian, Prof. Dr. Wilfried Jokat, Prof. Dr. Karsten Haase, Prof. Dr. Anton Le Roex und Dr. John O'Connor möchte

ich mich ganz herzlich bedanken für die Bereitstellung der Proben, ohne die dieses Projekt und diese Arbeit nicht möglich gewesen wären.

Ein besonderer Dank gilt auch Prof. Dr. Stefan Jung und Dagmar Rau für die RFA-Analytik, Dr. Jan Fietzke für die Hf-Isotopenanalytik und Dipl.-Ing. Jan Sticklus für die Unterstützung bei den $^{40}\text{Ar}/^{39}\text{Ar}$ -Analysen. Des Weiteren bedanke ich mich ganz besonders bei Silke Hauff für die Einarbeitung und die tatkräftige Unterstützung im Labor, für die Aufbereitung und Isotopenanalysen einiger meiner Proben, aber auch für die vielen Tassen Kaffee und die netten „Messwochenenden“, die wir zusammen verbracht haben. Mein Dank gebührt auch Dr. Dieter Garbe-Schönberg, Dipl.-Ing. Ulrike Westernströer und Petra Fiedler für die Unterstützung bei der Vorbereitung der Proben zur ICP-MS-Analytik, für die Spurenelementanalysen und -auswertung und auch für die vielen netten Gespräche und Kaffeepausen. Lasse Heuer und Tianyu Chen gilt mein Dank für die Einarbeitung am Nu Plasma MC-ICPMS.

Paulina, Steffi, Uwe und Sarah danke ich für die Unterstützung bei der Aufbereitung meiner Proben.

Bei Julia Mahlke, Antje Herbrich, Antje Dürkefälden, David Gilbert und Guillaume Jacques möchte ich mich ganz besonders für die gegenseitige Unterstützung, für die Verteilung von „Motivations-Schokolade“ sowie für die lebhaften fachlichen aber auch persönlichen Diskussionen aller Art bedanken. Dabei danke ich vor allem Antje Herbrich für die Vorbereitung einiger Proben zur ICP-MS-Analytik und Julia für die jahrelange Freundschaft, die unzähligen Tassen hawaiianischen Kaffees und dafür, dass sie nicht nur als Büronachbarin immer für mich da war. Bei ihr, David, Anna und Rauno möchte ich mich außerdem für die vielen netten Ablenkungen von der Arbeit bedanken.

Ein ganz besonderer Dank geht an meine Familie, und besonders an meine Mutter, für die jahrelange Unterstützung und den Glauben an mich und das, was ich mache.

Mein größter Dank geht jedoch an meinen Mann Philipp für seine unendliche Unterstützung und Kraft, die er mir in all der Zeit gegeben hat, aber auch für die vielen kleinen Dinge, die mir besonders zum Ende der Arbeit immer wieder viel Freude gemacht haben.

Introduction

Volcanism along mid-ocean ridges and subduction zones can be explained by the model of plate tectonics. As a result of oceanic and continental plates drifting apart or subducting beneath each other, the magmatic activity at these settings can be attributed to adiabatic decompression melting and melting predominantly induced by fluids added to the mantle wedge above the subducting plate by dehydration processes. In contrast to that, the origin of continental or oceanic intraplate volcanism (e.g., Hawaii, Galápagos or Tristan da Cunha) is still controversial.

In 1963, Wilson postulated that the age progressive intraplate volcanic chains are induced by the movement of the lithosphere across stationary unusually hot mantle material, the so-called hotspots. Based on this idea, Morgan (1971; 1972) concluded that these hotspots are upwelling mantle plumes rising from the deep mantle in the form of more or less vertical diapiric structures. Referring to this plume theory, Richards et al. (1989) developed the plume head-plume tail model. It ascribes areas of massive volcanism or Large Igneous Provinces (LIPs, e.g., the Deccan Traps in India, the Siberian Traps in Russia or the Etendeka-Paraná continental flood basalt (CFB) provinces in Namibia and Brazil; see Fig. 1), which are spatially connected with hotspot chains, to large mantle plume heads at the initiation of a hotspot. According to his model starting plume heads develop when the rising mantle material impinges the base of the lithosphere and spreads out laterally. The initial large volume plume head volcanism is then followed by time progressive hotspot chains and fed by the plume conduit or tail. But the mantle plume hypothesis is recently challenged by the „The Great Plume Debate”. Alternative models for the generation of intraplate volcanism have been introduced opposing the classic plume theory and ascribing the volcanic activity e.g. to lithospheric processes (e.g., Smith and Lewis, 1999; Anderson, 2000; 2005; Foulger, 2002; Hoernle et al., 2006).

The Tristan-Gough volcanic system is the research area of the study presented here. Due to the connection of a LIP (Paraná-Etendeka CFB province) with the volcanically active island groups of Tristan da Cunha and Gough by a bathymetric anomaly and the assignment by Courtillot et al. (2003) that the Tristan-Gough system belongs to one of the few primary hotspots with a supposedly deep mantle origin, this area is an ideal setting to

examine different models for intraplate volcanism and to test deep versus shallow mantle origins.

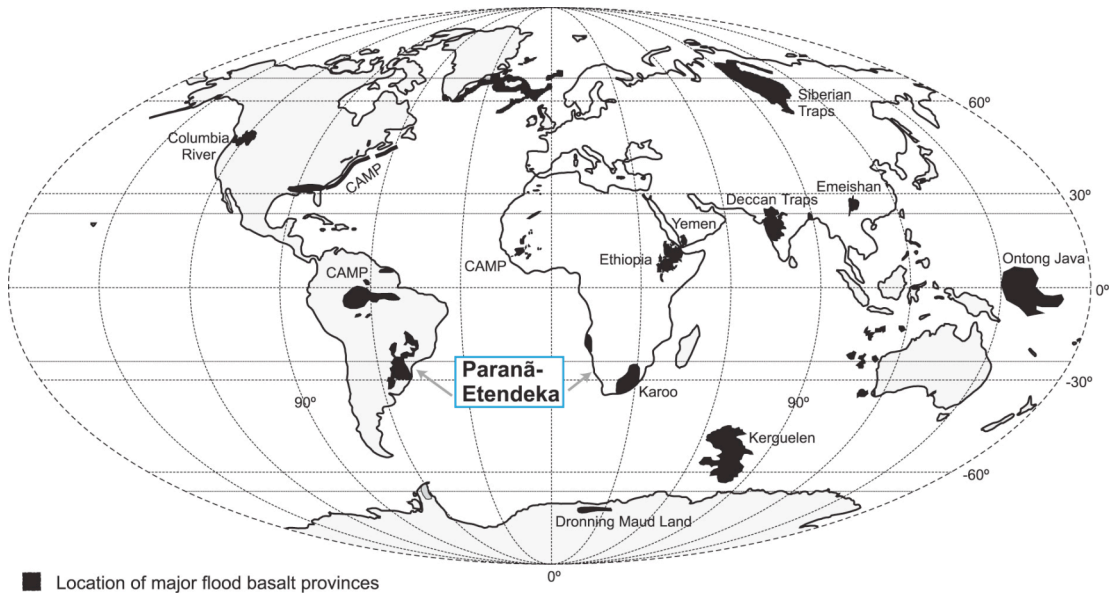


Fig. 1: Locations of major flood basalt provinces (modified after Jerram and Widdowson, 2005).

The dissertation at hand comprises a detailed $^{40}\text{Ar}/^{39}\text{Ar}$ geochronological and geochemical study (major and trace elements and Sr-Nd-Hf-Pb double spike (DS) data) of volcanic rocks from the Tristan-Gough magmatic system. This includes samples from the Tristan-Gough volcanic track and the Rio Grande Rise, the two most prominent bathymetric features in the South Atlantic (Fig. 2). The analyses were carried out on available samples collected during several international cruises and DSDP Legs. Samples from the northeastern part of the Tristan-Gough track (Walvis Ridge) and the Gough subtrack within the Guyot Province (Fig. 2) are of special interest, because these areas are only sparsely investigated (Walvis Ridge) or are not investigated at all (Gough subtrack). One aim of the study is to produce a high quality laser step-heating $^{40}\text{Ar}/^{39}\text{Ar}$ age data set to test for the suggested age progression for the Tristan-Gough volcanic track (O'Connor and Duncan, 1990; O'Connor and Le Roex, 1992) since this area is lacking sufficiently reliable age data. Another objective is to generate a comprehensive geochemical data set in

order to evaluate geochemical variations along and across the Tristan-Gough volcanic track and the Rio Grande Rise, to decipher the mantle sources contributing to the volcanic system through time and to provide constraints on the origin and evolution of the Tristan-Gough plume.

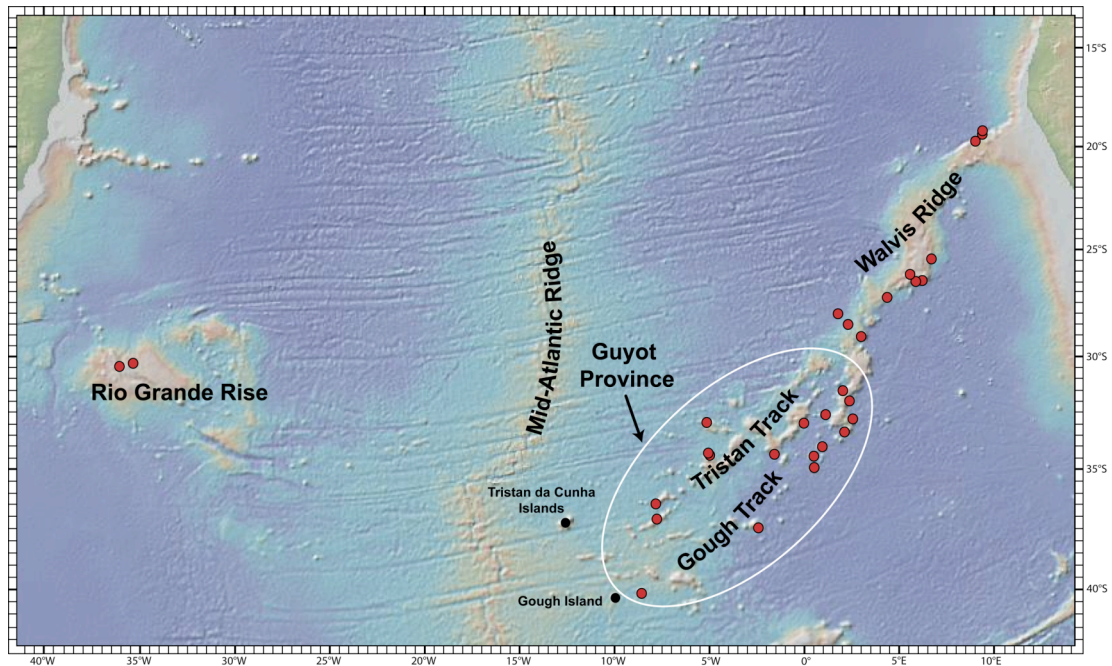


Fig. 2: Bathymetric overview map of the Tristan-Gough volcanic track and the Rio Grande Rise displaying the sample locations considered in this study (red circles).

This dissertation is composed of three independent chapters contributing to the above-mentioned objectives. The first chapter is a geochronological study presenting new high quality laser step-heating $^{40}\text{Ar}/^{39}\text{Ar}$ ages of mineral separates from samples from the Tristan-Gough volcanic track (comprising the Walvis Ridge and the Guyot Province) and the Rio Grande Rise (Fig. 2). This is a very important contribution to understand the temporal evolution of the Tristan-Gough volcanic system since almost all previously published $^{40}\text{Ar}/^{39}\text{Ar}$ ages of altered rock groundmass (O'Connor and Duncan, 1990; O'Connor and Le Roex, 1992) did not meet the criteria for statistically valid ages and alteration tests (Baksi, 1999; 2007a; 2007b). In order to determine the volcanic age distribution within this volcanic system and to test if statistically valid ages confirm the suggested age progression indicating the formation through an upwelling mantle plume

(O'Connor and Duncan, 1990; O'Connor and Le Roex, 1992), 24 samples (primarily feldspar crystals, but also biotite crystals and whole rock chips) were analyzed from throughout the Tristan-Gough volcanic track and the Rio Grande Rise.

The second chapter focuses on the geochemical variations along and across the V-shaped Guyot Province, the southwestern part of the Tristan-Gough hotspot track (Fig. 2), from Tristan da Cunha and Gough islands to the DSDP transect across the southwestern end of the Walvis Ridge, where two spatially separated seamount chains have been formed (Tristan and Gough subtracks). Since asymmetrically zoned hotspot tracks have been detected in the Pacific Ocean (e.g., Galápagos, Hawaii, Samoa and the Marquesas), it is of special interest if such a geochemical zonation can also be found in the Atlantic. In order to test for a zonation, 16 samples from the Guyot Province and the Walvis Ridge have been analyzed for trace elements and Sr-Nd-Hf-Pb DS isotopic ratios. It is striking that the volcanically active end of the Tristan-Gough hotspot track is located above the margin the African large low-shear-velocity province (LLSVP), which also applies to the zoned plumes above a LLSVP in the Pacific Ocean. In this chapter, a potential connection between the African LLSVP and a zoned plume is discussed. Furthermore, the mantle endmembers contributing to the geochemical composition of the Tristan-Gough hotspot systems are investigated. Since isotopic ratios do not fractionate during processes of partial melting or fractional crystallization, they can be used as tracers for the different existing endmembers in the Earth's mantle (e.g. EM-I and EM-II = enriched mantle 1 and 2, DMM = depleted MORB mantle or HIMU = high μ ($^{238}\text{U}/^{204}\text{Pb}$); Zindler and Hart, 1986). DSDP Site 525A at the southwestern end of the Walvis Ridge is the type locality for the EM-I endmember in the mantle beneath the South Atlantic. On the basis of the geochemical data it is further tried to decipher the origin of this enriched mantle endmember.

The third chapter is a detailed geochemical study and mainly deals with the >70 Ma old part of the Tristan-Gough hotspot track (i.e. 70-132 Ma), namely the Walvis Ridge, the Rio Grande Rise and the Etendeka-Paraná CFBs. Sixty-two dredge and drill core samples, mainly from the Walvis Ridge and the Rio Grande Rise, have been analyzed for major and trace elements and 41 of them for Sr-Nd-Hf-Pb (DS) radiogenic isotope ratios in order to determine the long-term geochemical evolution of the Tristan-Gough plume and to investigate the contributions of the mantle sources during the early plume evolution as well as their geochemical characteristics and origin. Another aim is to further specify the

enriched Gough-type source detected in the Guyot Province (Gough subtrack) and to derive possible mechanisms that led to geochemical variations of the Tristan-Gough hotspot track and the Rio Grande Rise. By comparing the long-term evolution of the Tristan-Gough hotspot with that of the zoned Hawaiian hotspot, it is attempted to provide insights into the cause and longevity of zonation in mantle plumes.

References

- Anderson, D.L., 2000, The thermal state of the upper mantle: No role for mantle plumes: *Geophysical Research Letters*, v. 27, p. 3623-3626.
- Anderson, D.L., 2005, Scoring hotspots: the plume and plate paradigms, *in* Foulger, G.R., Natland, J.H., Presnall, D.C., and Anderson, D.L., eds., *Plates, Plumes, and Paradigms: Geological Society of America Special Paper 388*, p. 31-54.
- Baksi, A.K., 1999, Reevaluation of plate motion models based on hotspot tracks in the Atlantic and Indian Oceans: *Journal of Geology*, v. 107, p. 13-26.
- Baksi, A.K., 2007a. A quantitative tool for detecting alteration in undisturbed rocks and minerals - I: water, chemical weathering, and atmospheric argon, *in* Foulger, G.R., and Jurdy, D.M., eds., *Plates, Plumes and Planetary Processes: Geological Society of America Special Paper 430*, p. 285-303.
- Baksi, A.K., 2007b. A quantitative tool for detecting alteration in undisturbed rocks and minerals - II: application to argon ages related to hotspots *in* Foulger, G.R., and Jurdy, D.M., eds., *Plates, Plumes and Planetary Processes: Geological Society of America Special Paper 430*, p. 305-333.
- Courtillot, V., Davaille, A., Besse, J., and Stock, J., 2003, Three distinct types of hotspots in the Earth's mantle: *Earth and Planetary Science Letters*, v. 205, p. 295-308.
- Foulger, G.R., 2002, Plumes, or plate tectonic processes?: *Astronomy & Geophysics*, v. 43, p. 6.19-6.23.
- Hoernle, K., White, J.D.L., van den Bogaard, P., Hauff, F., Coombs, D.S., Werner, R., Timm, C., Garbe-Schönberg, D., Reay, A., and Cooper, A.F., 2006, Cenozoic intraplate volcanism on New Zealand: Upwelling induced by lithospheric removal: *Earth and Planetary Science Letters*, v. 248, p. 350-367.
- Jerram, D.A., and Widdowson, M., 2005, The anatomy of Continental Flood Basalt Provinces: geological constraints on the processes and products of flood volcanism: *Lithos*, v. 79, p. 385-405.
- Morgan, W.J., 1971, Convection plumes in the lower mantle: *Nature*, v. 230, p. 42-43.

- Morgan, W.J., 1972, Plate motions and deep mantle convection: Geological Society of America Memoirs, v. 132, p. 7-22.
- O'Connor, J.M., and Duncan, R.A., 1990, Evolution of the Walvis Ridge-Rio Grande Rise hot spot system: implications for African and South American plate motions over plumes: Journal of Geophysical Research, v. 95, p. 17,475-17,502.
- O'Connor, J.M., and Le Roex, A.P., 1992, South Atlantic hot spot-plume systems: 1. Distribution of volcanism in time and space: Earth and Planetary Science Letters, v. 113, p. 343-364.
- Richards, M.A., Duncan, R.A., and Courtillot, V.E., 1989, Flood basalts and hot-spot tracks: Plume heads and tails: Science, v. 246, p. 103-107.
- Smith, A.D., and Lewis C., 1999, The planet beyond the plume hypothesis: Earth Science Reviews, v. 48, p. 135-182.
- Wilson, J.T., 1963, A possible origin of the Hawaiian Islands: Canadian Journal of Physics, v. 41, p. 863-870.
- Zindler, A., and Hart, S., 1986, Chemical Geodynamics: Annual Review of Earth and Planetary Sciences, v. 14, p. 493-571.

Contents

Preface	I
Abstract	II
Kurzfassung	VIII
Danksagung	XV
Introduction	XVII

CHAPTER I

Evidence for an age progression along the Tristan-Gough volcanic track from new $^{40}\text{Ar}/^{39}\text{Ar}$ ages on phenocryst phases

Abstract	4
1. Introduction	5
2. Sampling locations and sample description	7
3. Analytical methods	10
3.1. Sample selection and preparation	10
3.2. $^{40}\text{Ar}/^{39}\text{Ar}$ measurements	10
4. Results	11
4.1. Walvis Ridge	13
4.2. Rio Grande Rise.....	17
4.3. Guyot Province	18
5. Discussion	21
5.1. Evolution of the Tristan-Gough volcanic track	21
5.2. Geodynamic model	23
6. Conclusions	25
Acknowledgments	26

CHAPTER II

70 Ma chemical zonation of the Tristan-Gough hotspot track

Abstract	27
1. Introduction	28
2. Results	30
3. Discussion and Conclusions	32
Acknowledgments	36

CHAPTER III

The geochemical evolution of the older Tristan-Gough hotspot track: Walvis Ridge and Rio Grande Rise

Abstract	37
1. Introduction	38
2. Geological background and sampling locations	40
3. Sample preparation and analytical procedures	41
4. Results	44
4.1. Major elements	44
4.2. Trace elements.....	45
4.3. Sr-Nd-Pb-Hf isotopes.....	48
5. Discussion	53
5.1. Compositional variations along the Tristan-Gough hotspot track.....	53
5.1.1. Variations in geochemistry associated with the change from a ridge-centered to an intraplate hotspot.....	53
5.1.2. Are both Tristan and Gough components present in the plume head stage (Paraná and Etendeka flood basalts)?.....	57
5.2. Origin of the Gough and Tristan components	59
5.3. Evolution of the Tristan-Gough volcanic system	62
5.4. Comparison of Tristan-Gough long-term history with that of Hawaii	66

6. Conclusion	68
Acknowledgments	69
References	70
Appendices	84
Appendix I (CHAPTER I)	84
Appendix II (CHAPTER II)	92
Appendix II a.....	92
Appendix II b.....	93
Appendix II c.....	106
Appendix II d.....	107
Appendix II e.....	109
Appendix III (CHAPTER III)	110
Appendix III a.....	110
Appendix III b.....	118
Appendix III c.....	142
Appendix III d.....	144
Appendix III e.....	153
Appendix IV	154
CURRICULUM VITAE	155

CHAPTER I

Evidence for an age progression along the Tristan-Gough volcanic track from new $^{40}\text{Ar}/^{39}\text{Ar}$ ages on phenocryst phases

Joana Kristin Rohde, Paul van den Bogaard, Kaj Hoernle, Folkmar Hauff, Reinhard Werner

GEOMAR, Helmholtz Centre for Ocean Research Kiel, Dynamics of the Ocean Floor, Magmatic and Hydrothermal Systems, Wischhofstraße 1-3, 24148 Kiel, Germany

Published in Tectonophysics

Keywords: Tristan mantle plume, Hotspot, South Atlantic, Walvis Ridge, Age progression, $^{40}\text{Ar}/^{39}\text{Ar}$ geochronology

Abstract

Age progressive hotspot chains are commonly believed to form by decompression melting as the lithosphere moves over a mantle plume. The Tristan-Gough volcanic track in the South Atlantic, composed of the Walvis aseismic ridge and the associated Guyot Province, extends from the Etendeka continental flood basalts (CFBs) in Namibia to the volcanically active islands of Tristan da Cunha and Gough. Here we present new laser step-heating $^{40}\text{Ar}/^{39}\text{Ar}$ ages of mineral separates from samples from the Tristan-Gough volcanic track and the Rio Grande Rise. The $^{40}\text{Ar}/^{39}\text{Ar}$ ages have primarily been determined on feldspar crystals, but also on biotite crystals (one sample) and whole rock chips (one sample). Our data indicate a younging age progression from the Etendeka CFBs to Tristan da Cunha and Gough. The ages range from 114 Ma at the northeastern end to 58-72 Ma for DSDP Sites 525A and 528 at the southwestern end of the Walvis Ridge, to 27-49 Ma for the Guyot Province and to 80-87 Ma for the Rio Grande Rise, which is believed to represent the counterpart of the Walvis Ridge on the South American Plate. We also found anomalously young (late-stage) volcanism on the Walvis Ridge (~55 Ma) and the Rio Grande Rise (~46 Ma), which, like late-stage volcanism on other hotspot tracks, represents more silica-undersaturated compositions than the main “shield stage” tholeiitic volcanism. Combining our new ages with published ages for the Etendeka CFBs yields a

general volcanic migration rate of ~ 30 mm/a for the Tristan-Gough track assuming a constant velocity of the African Plate. Our new geochronological constraints for an age progression provide further support for a mantle plume origin of the Tristan-Gough track. Finally our new age data imply a faster volcanic migration rate for this hotspot track than previously published rates, which needs to be factored into plate tectonic reconstruction models.

1. Introduction

The northeast-southwest trending Tristan-Gough volcanic track is one of the most distinct morphologic features in the South Atlantic, connecting the Etendeka continental flood basalts (CFBs) with the Tristan da Cunha and Gough island groups (Fig. 1.1). As defined here, this volcanic track comprises the aseismic Walvis Ridge in the northeast, an up to 250 km wide continuous bathymetric high (up to 3000 m above the surrounding seafloor), and the associated Guyot Province in the southwest, consisting of various volcanic features including isolated volcanoes, seamount chains and smaller ridges. At its southwestern end, the Walvis Ridge bifurcates, forming two spatially separated subtracks within the Guyot Province (Tristan and Gough Track). These subtracks diverge and become less continuous as they approach Tristan da Cunha and Gough Islands that lie ~ 450 - 570 km from the Mid-Atlantic Ridge and ~ 400 km apart from each other. The massive volcanic structures of the northwest-southeast trending aseismic Rio Grande Rise are roughly in spatial connection to the Paraná CFBs in Brazil (Fig. 1.1), the South American counterpart of the Etendeka province in southern Africa. Seafloor morphology indicates that the Rio Grande Rise formed adjacent to the Walvis Ridge and was then separated from it through mid-ocean ridge spreading. It is composed of two different morphological units, the Western Rio Grande Rise, which is a large elliptical plateau, and the north-south trending Eastern Rio Grande Rise that runs parallel to the present day Mid-Atlantic Ridge axis (Fig. 1.1). It is assumed that a westward migration of the Mid-Atlantic spreading axis during the Late Cretaceous (ca 70 Ma ago) caused the isolated position of the Rio Grande Rise. After ridge migration, the volcanic setting changed from on-axis to intraplate volcanism on the African Plate (O'Connor and Duncan, 1990).

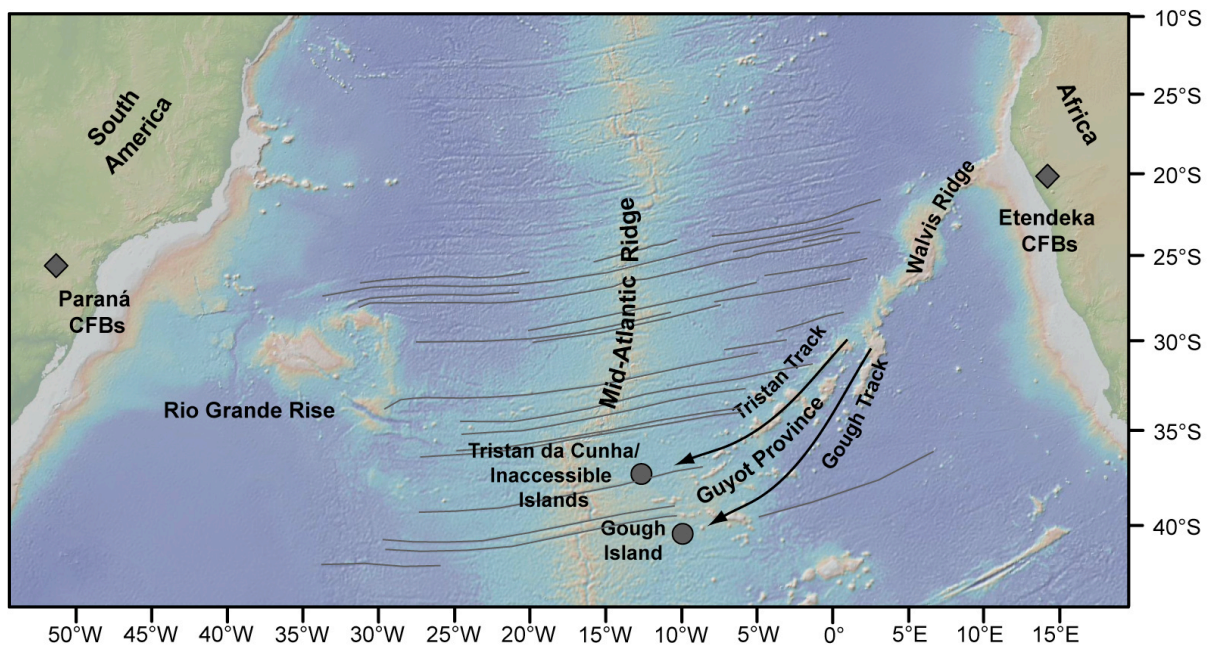


Fig. 1.1: Bathymetric overview map of the Tristan-Gough volcanic track (Walvis Ridge and Guyot Province, including Tristan da Cunha and Gough island groups) and the Rio Grande Rise. Gray lines: linear features visible on the seafloor that are interpreted to be the traces of fracture zones. Source of the map: GeoMapApp (<http://www.geomapapp.org>).

Because the Tristan-Gough volcanic track is one of the few hotspot tracks that exhibits a clear spatial link between CFB provinces (Etendeka and Paraná) and an active hotspot system (Tristan-Gough) and because this system belongs to the group of 7 primary hotspots after Courtillot et al. (2003), a detailed geochronological data set is of crucial importance for global plate reconstructions and for understanding the formation and evolution of such volcanic trails.

Previous attempts to determine the age of volcanism in the Tristan-Gough volcanic track by $^{40}\text{Ar}/^{39}\text{Ar}$ analyses of altered rock groundmass (O'Connor and Duncan, 1990; O'Connor and Le Roex, 1992) produced invalid results (Baksi, 1999, 2007a). Only one analysis (RSA Seamount, 19 Ma; O'Connor and Le Roex, 1992) withstands tests of statistical validity and alteration (Baksi, 2007b). The inferred ages indicate that volcanism in the southwestern Walvis Ridge (DSDP Sites 525A and 528) is ~50 Ma younger than the Etendeka CFBs (~135-132 Ma, Renne, 2011; Renne et al., 1996) and that seamount ages further decrease towards Tristan and Gough Islands, respectively, but due to the deficits in sample choice (altered groundmass) and statistical evaluation of $^{40}\text{Ar}/^{39}\text{Ar}$ analytical results, the age distribution of volcanism in the Tristan-Gough volcanic track is not well

constrained.

Here we report new $^{40}\text{Ar}/^{39}\text{Ar}$ laser step-heating analyses of 17 dredge samples from 12 sites and 7 DSDP core samples from three sites along the Tristan-Gough volcanic track and the Rio Grande Rise. The goal of our study is to investigate the age distribution of volcanism along the Walvis Ridge, the Tristan-Gough subtracks, and the Rio Grande Rise, and to evaluate if statistically valid ages are consistent with a possible age progression and hotspot hypothesis.

2. Sampling locations and sample description

Samples analyzed in this study were collected during the U.S. American cruises AII-93 in 1975 (R/V Atlantis II) and RC11 in 1967 (R/V Robert D. Conrad), during DSDP Legs 72 (Site 516F; R/V Glomar Challenger) and 74 (Sites 525A and 528; R/V Glomar Challenger) in 1980, during the French cruise CH19 (R/V Jean Charcot) in 1971, during a Russian cruise with the R/V Akademik Kurchatov in 1975 and during the German R/V Polarstern ANTXXIII-5 (PS69) expedition in 2006 (Table 1.1 and Fig. 1.2). Our sample collection comprises dredge samples from three sites along the Walvis Ridge, including two sites at its northeastern-most end close to the Namibian shelf (CH19, DR3 and 4) and one site at the southern flank halfway to the Guyot Province (AII-93-19-4). We dated four samples from two DSDP Leg 74 Sites 525A (525A-57-2, 91-103, 525 A-57-5, 141-148) and 528 (528-42-5, 31-46, 528-43-2, 80-98) along a northwest-southeast trending transect across the southwestern end of the Walvis Ridge. We also analyzed 10 samples from eight dredge sites within the Guyot Province. Five samples come from four sites along the northern Tristan Track (AII-93-3-1B, AII-93-3-25, AII-93-5-3, AII-93-6-1 and AK-1695-6) and five samples from four sites along the southern Gough Track (PS69/420-1-DR21-1, PS69/423-1-DR25-4, PS69/440-1-DR32-2, PS69/440-1-DR32-5b, AII-93-10-11). Sampling locations from the Rio Grande Rise include one dredge site close to the canyon that intersects the Western Rio Grande Rise (RC11-2RD P5) and three samples from DSDP Leg 72 Site 516F (516F-126-3, 56-73, 516F-127-3, 59-76, 516F-128-2, 63-84) located on the main platform of the Western Rio Grande Rise.

According to the TAS-diagram (silica versus total alkali diagram for chemical classification and nomenclature of volcanic rocks, Fig. 1.3), the majority of the samples

have alkalic compositions (plotting above the alkalic-tholeiitic division line of Macdonald and Katsura, 1964), ranging from alkali basalts to trachybasalts, basaltic trachyandesites and trachytes roughly following a trachytic fractionation trend, and from tephrites to phonotephrites. A few samples are tholeiitic basalts and basaltic andesites. Generally, the samples from the Guyot Province are more alkalic compared to those from the Walvis Ridge.

Table 1.1: Samples used for $^{40}\text{Ar}/^{39}\text{Ar}$ laser step-heating analyses.

Sample	Latitude (°)	Longitude (°)	Depth (mbsl)	Description
WALVIS RIDGE				
CH19 DR3-2	-19.37	9.33	3840	Tephrite
CH19 DR3-22	-19.37	9.33	3840	Alkali Basalt
CH19 DR4-1	-19.85	9.02	2738	Basaltic Andesite
CH19 DR4-2	-19.85	9.02	2738	Basaltic Trachyandesite
CH19 DR4-3	-19.85	9.02	2738	Basaltic Trachyandesite
AII-93-19-4	-26.48	6.25	2450-2400	Trachyte
DSDP Leg 74-525A-57-2, 91-103	-29.07	2.99	3074	Alkali Basalt
DSDP Leg 74-525A-57-5, 141-148	-29.07	2.99	3088	Alkali Basalt
DSDP Leg 74-528-42-5, 31-46	-28.53	2.32	4318	Tholeiitic Basalt
DSDP Leg 74-528-43-2, 80-98	-28.53	2.32	4323	Tholeiitic Basalt
GUYOT PROVINCE				
<i>Tristan Track</i>				
AII-93-5-3	-34.29	-5.03	3100-3000	Alkali Basalt
AII-93-6-1	-34.35	-4.98	2460-2360	Tephrite
AK-1695-6	-36.42	-7.73	1450-1050	Trachyte
AII-93-3-1B	-37.10	-7.78	2600-2000	Alkali Basalt
AII-93-3-25	-37.10	-7.78	2600-2000	Alkali Basalt
<i>Gough Track</i>				
PS69/420-1-DR21-1	-32.79	2.55	2515-1920	Trachyte
PS69/423-1-DR25-4	-34.93	0.55	2075-1900	Trachyte
AII-93-10-11	-34.34	-1.57	2300-2000	Alkali Basalt
PS69/440-1-DR32-2	-37.48	-2.43	1895-1390	Trachybasalt
PS69/440-1-DR32-5b	-37.48	-2.43	1895-1390	Trachybasalt
RIO GRANDE RISE				
DSDP Leg 72-516F-126-3, 56-73	-30.28	-35.29	2579	Alkali Basalt
DSDP Leg 72-516F-127-3, 59-76	-30.28	-35.29	2584	Tholeiitic Basalt
DSDP Leg 72-516F-128-2, 63-84	-30.28	-35.29	2592	Tholeiitic Basalt
RC11-2RD P5	-30.42	-35.97	1245-655	Phonotephrite

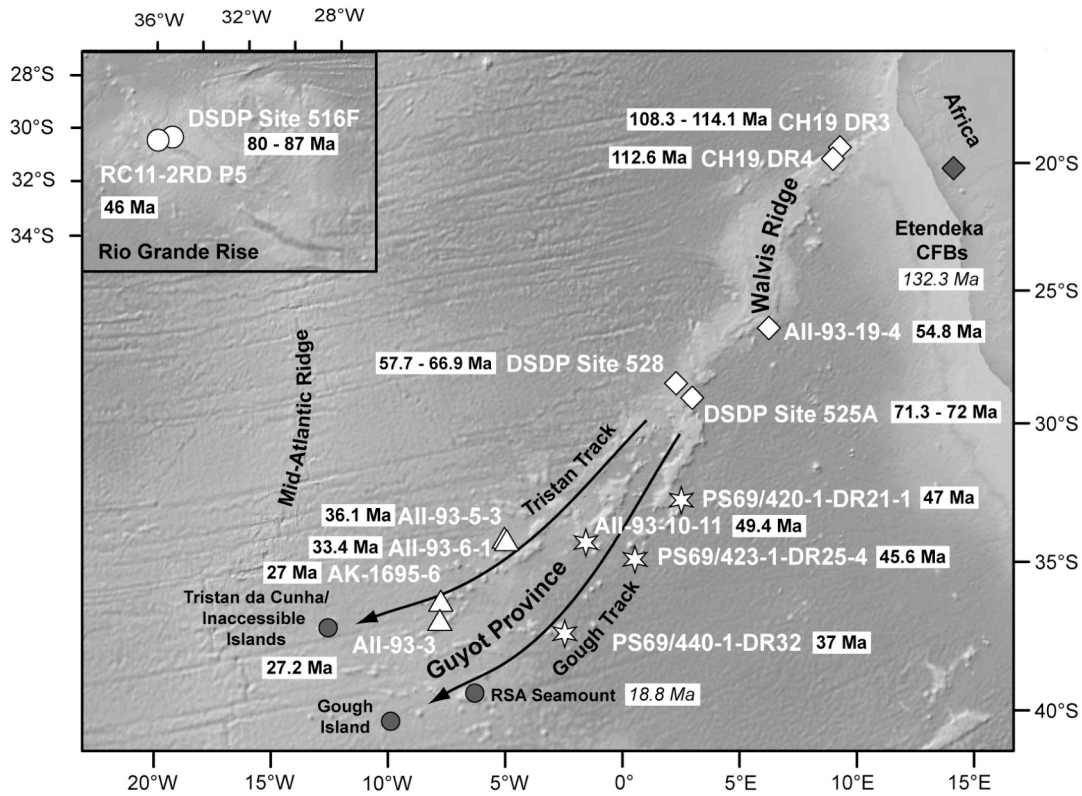


Fig. 1.2: Bathymetric overview map of the Tristan-Gough volcanic track and the Rio Grande Rise (inset map) displaying the sampling locations along with the new $^{40}\text{Ar}/^{39}\text{Ar}$ ages (bold) and published $^{40}\text{Ar}/^{39}\text{Ar}$ ages (italics) for the Etendeka CFBs (Renne et al., 1996) and RSA Seamount (O'Connor and Le Roex, 1992). Source of the maps: GeoMapApp (<http://www.geomapp.org>).

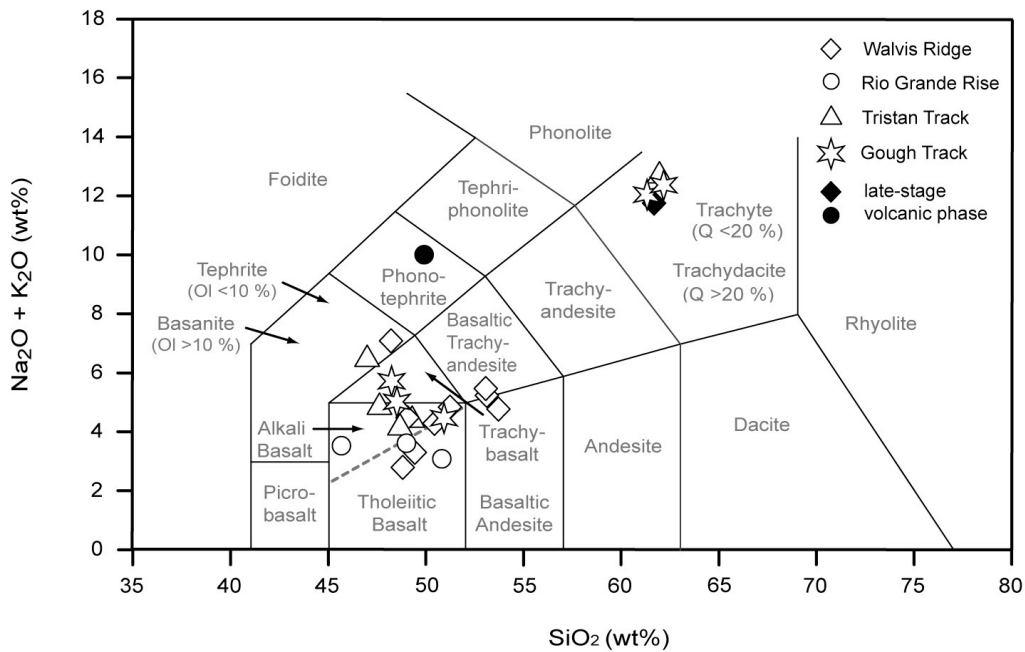


Fig. 1.3: Chemical classification and nomenclature of volcanic rocks from the Tristan-Gough volcanic track and the Rio Grande Rise based on the silica versus total alkali diagram (TAS-diagram) of Le Maitre et al. (1989). Values are normalized to 100 % on a volatile-free basis. Qtz = Quartz, Ol = Olivine. Subdivision line between alkali basalts and tholeiitic basalts (gray dashed line) after Macdonald and Katsura (1964).

3. Analytical methods

3.1. Sample selection and preparation

After inspection of the thin sections under a polarizing microscope in order to screen for sufficient amounts of fresh phenocryst phases, glass or matrix material dateable with the laser step-heating technique, 15 samples from the Walvis Ridge, 10 from the Guyot Province and 5 samples from the Rio Grande Rise were selected. Only the least altered inner parts of these samples were used after removal of any surface weathering and manganese crusts. Subsequent to jawcrushing and sieving, the rock chips were repeatedly cleaned in an ultrasonic bath with de-ionized water for about 20-30 min to remove dust and soluble residues by decantation. Thereafter, the freshest minerals, whole rock and glass chips (0.25-0.5 mm and 0.5-1 mm, depending on availability and freshness) were hand-picked under a binocular microscope. The selected feldspar separates were etched in 5 % hydrofluoric acid for 8-15 min (depending on crystal size) and then rinsed repeatedly in de-ionized water. Subsequently, they were washed in an ultrasonic bath with de-ionized water for 8 min and dried at 50 °C for at least 12 h. The whole rock and glass chips were treated like the feldspar crystals omitting the leaching step and the glass chips were washed in the ultrasonic bath only at low intensity and for 1-2 min. The biotite crystals were only rinsed with de-ionized water. After drying the mineral separates, whole rock chips and glass chips were loaded in aluminum trays and irradiation cans that were wrapped in cadmium foil and irradiated for seven days with fast neutrons at the 5 MW reactor of the Helmholtz-Zentrum Geesthacht (HZG).

3.2. $^{40}\text{Ar}/^{39}\text{Ar}$ measurements

The $^{40}\text{Ar}/^{39}\text{Ar}$ laser step-heating analyses were carried out at the GEOMAR Geochronology Laboratory using a 20 W SpectraPhysics Argon-Ion laser and an MAP 216 series noble gas mass spectrometer. Laser step-heating analyses were mainly carried out on feldspar crystals (plagioclase and K-feldspar), but also on biotite crystals and matrix chips. Taylor Creek Rhyolite Sanidine (TCR-2, 27.87 ± 0.04 Ma; Lanphere and Dalrymple, 2000) was used to monitor the neutron flux. The measured Ar isotope ratios were corrected for

mass discrimination, background and blank values, for interfering neutron reactions on Ca and K, and for J-value gradients. After correction, the step-heating data were interpreted as age spectra (apparent age and 2 sigma error versus cumulative ^{39}Ar).

We consider valid plateaus to have >3 consecutive steps with >50 % of the ^{39}Ar released and ages that overlap within 2 sigma errors. The calculated plateau ages represent the inverse-variance weighted mean of the plateau step ages and errors. Values of MSWD (mean square weighted deviates) and probability of fit were calculated to test the statistical validity of the plateau age averages at 2 sigma/95 % confidence levels (Baksi, 1999). Additionally, we calculated alteration indices as defined in Baksi (2007a). Alteration indices (A.I.s) were calculated from the measured $^{36}\text{Ar}/^{37}\text{Ar}$ ratios (for plagioclase or matrix; ^{36}Ar representing the proxy for atmospheric contamination and ^{37}Ar representing the proxy for mass in case of Ca-rich phases) or $^{36}\text{Ar}/^{39}\text{Ar}$ ratios (for K-feldspar, biotite; ^{39}Ar representing the proxy for mass in case of K-rich phases), corrected for $^{36}\text{Ar}_{\text{Ca}}$ and normalized to $J = 0.01$ (Baksi, 2007a).

4. Results

Overall, 30 samples were analyzed within this study, of which 24 (22 feldspar samples, one matrix and one biotite sample) yielded statistically valid plateau ages. The other 6 samples gave scattered age spectra, too low Ar yields ($^{39}\text{Ar} < 50\%$) or statistically invalid plateaus, or excessively high alteration indices and are not considered further. The results are listed in Table 1.2, selected age spectra are presented in Figs. 1.4-1.6, and full analytical data are contained in Appendix I. All errors within this paper are reported as 2 sigma.

Table 1.2: $^{40}\text{Ar}/^{39}\text{Ar}$ step-heating results. Spectra from boldface analyses are shown in Figs. 4-6.

Sample	Analysis / Lab No.	Irradiation can	Plateau age (Ma)	\pm	2σ	MSWD	Probability	% ^{39}Ar	Steps
WALVIS RIDGE									
CH19 DR3-2	JD8fss	34	113.8	\pm 0.6		1.15	0.33	75.2	8 to 15
	JD8fs2	34	114.5	\pm 0.5		0.43	0.88	72.8	6 to 13
	wtd mean		114.1	\pm 0.4		3.00	0.08		
CH19 DR3-22	JD9fss	34	108.9	\pm 1.5		1.50	0.20	51.6	8 to 12
	JD9fs2	34	108.0	\pm 1.0		1.90	0.02	65.2	5 to 19
	wtd mean		108.3	\pm 0.8		1.07	0.30		
CH19 DR4-1	JD10fss	34	112.8	\pm 0.9		0.51	0.85	69.3	6 to 14
CH19 DR4-2	JD11fss	34	112.4	\pm 1.1		1.16	0.31	54.9	6 to 18
CH19 DR4-3	JD12fss	34	112.6	\pm 0.8		0.59	0.80	52.4	6 to 15
CH19 DR4	wtd mean		112.6	\pm 0.5		0.18	0.84		
All-93-19-4	All93fss	33	54.9	\pm 0.1		2.20	0.02	95.4	6 to 16
	Isochron plateau		54.8	\pm 0.1		1.40	0.15	100.0	2 to 16
DSDP Leg 74- 525A-57-2, 91-103	JD5fss	34	71.0	\pm 1.4		1.01	0.43	55.7	6 to 15
	JD5fs2	34	71.4	\pm 0.9		1.60	0.14	59.6	3 to 10
	wtd mean		71.3	\pm 0.8		0.23	0.63		
DSDP Leg 74- 525A-57-5, 141-148	JD6fss	34	72.0	\pm 1.2		0.39	0.89	66.2	3 to 9
DSDP Leg 74- 528-42-5, 31-46	971fss	33	57.7	\pm 4.7		0.97	0.46	93.9	5 to 14
DSDP Leg 74- 528-43-2, 80-98	972fss	33	66.9	\pm 3.9		0.80	0.59	87.1	4 to 11
GUYOT PROVINCE									
<i>Tristan Track</i>									
All-93-5-3	5-3fss	33	36.1	\pm 1.0		0.86	0.55	73.5	7 to 15
All-93-6-1	6-1fss	33	33.4	\pm 1.0		1.40	0.22	89.1	5 to 11
AK-1695-6	16956fss	33	27.0	\pm 0.1		0.84	0.52	70.9	11 to 16
All-93-3-1B	3-1Bfss	33	27.7	\pm 1.4		0.47	0.83	80.0	6 to 12
All-93-3-25	3-25fss	33	26.7	\pm 1.5		0.69	0.72	84.4	7 to 16
All-93-3	wtd mean		27.2	\pm 1.0		0.95	0.33		
<i>Gough Track</i>									
PS69/420-1-DR21-1	21-1mxs	33	47.0	\pm 0.2		0.97	0.46	78.4	9 to 17
PS69/423-1-DR25-4	25-4fss	33	45.6	\pm 0.1		1.50	0.12	97.6.7	8 to 19
All-93-10-11	10-11fss	33	49.4	\pm 0.7		0.59	0.88	95.6	6 to 20
PS69/440-1-DR32-2	32-2fss	33	37.1	\pm 0.2		1.40	0.18	93.5	6 to 14
PS69/440-1-DR32-5b	32-5Bfss	33	36.9	\pm 0.2		1.60	0.10	92.1	6 to 17
PS69/440-1-DR32	wtd mean		37.0	\pm 0.2		2.50	0.12		
RIO GRANDE RISE									
DSDP Leg 72- 516F-126-3, 56-73	979fss	33	80.0	\pm 2.0		1.20	0.28	66.2	7 to 14
DSDP Leg 72- 516F-127-3, 59-76	JD3fss	34	84.8	\pm 3.5		0.95	0.51	81.6	3 to 19
	JD3fs2	34	86.9	\pm 3.3		0.75	0.75	89.3	2 to 19
	wtd mean		85.9	\pm 2.4		0.76	0.38		
DSDP Leg 72- 516F-128-2, 63-84	981fss	33	84.7	\pm 2.0		0.98	0.46	72.6	5 to 15
RC11-2RD P5	JD2bt2	34	46.0	\pm 0.1		1.30	0.23	69.3	8 to 17

4.1. Walvis Ridge

All samples, however rigorous the preparation, cleaning, and leaching procedures, exhibit argon isotope signatures of partial alteration and uptake of atmospheric ^{36}Ar (and ^{40}Ar) for some heating steps. Therefore, forceful monitoring of the Alteration Index permits an assessment of the impact of alteration on the age-relevant argon isotope ratios of individual steps independent of plateau criteria, adding confidence in the accuracy of the determined plateau ages. Most plagioclase plateau steps show A.I. values ranging from fresh, unaltered plagioclase ($\text{A.I.} \leq 6 \cdot 10^{-5}$; Baksi, 2007a) to slightly altered plagioclase (A.I. up to $6 \cdot 10^{-4}$).

The age and A.I. spectra of analysis JD8fs (Sample CH19 DR3-2) serves as an example (Fig. 1.4a). This analysis yielded a mid- to high-temperature plateau that comprises ca 75 % of the total ^{39}Ar released, and consists of 8 consecutive heating steps whose ages are identical within the small 2 sigma errors. Alteration indices are low throughout the plateau steps ($3 \cdot 10^{-5}$ to $2 \cdot 10^{-4}$), indicating degassing from largely unaltered sites with undisturbed argon isotope compositions. Low-temperature heating steps, in contrast, yielded much higher alteration indices (A.I.s up to $4 \cdot 10^{-2}$) and apparent ages significantly lower than the plateau mean of 113.8 ± 0.6 Ma, indicating that plagioclase alteration goes along with a significant loss of radiogenic ^{40}Ar from affected “open-system” mineral sites, at least in this case.

A second step-heating analysis (JD8fs2) on a different plagioclase split from the same sample yielded essentially the same results, and the same plateau age within 2 sigma errors (114.5 ± 0.5 Ma). Both results may therefore be combined into a single weighted mean age of 114.1 ± 0.4 Ma for plagioclase from Walvis Ridge sample CH19-DR3-2.

Plagioclase step-heating analysis JD9fs (Sample CH19 DR3-22) yielded a small 5-step mid-temperature plateau with 52 % ^{39}Ar and a weighted mean plateau age of 108.9 ± 1.5 Ma (Fig. 1.4b). Plateau step alteration indices are low ($6 \cdot 10^{-5}$ to $2 \cdot 10^{-4}$), albeit systematically at or above the cut-off value for unaltered plagioclase ($6 \cdot 10^{-5}$; Baksi, 2007a).

Similar results were obtained by a second step-heating analysis (JD9fs2), which yielded a low-probability 65 %-plateau (0.02) at 108.0 ± 1.0 Ma. The weighted mean age of both is 108.3 ± 0.8 Ma, but this should be considered as a minimum age estimate

because the small-volume, partly low-probability plateaus show slightly elevated alteration indices.

Plagioclase step-heating analyses of three samples from dredge CH19-DR-4 (JD10fss, JD11fss, and JD12fss) yielded identical plateau ages (Table 1.2), and a statistically valid weighted mean age of 112.6 ± 0.5 Ma. Plateau step alteration indices are low ($1 \cdot 10^{-4}$ to $3 \cdot 10^{-4}$) (JD10fss, Fig. 1.4c), but A.I.s rise steeply in the low temperature heating steps (up to $1 \cdot 10^{-1}$) and highest-temperature steps (up to $2 \cdot 10^{-2}$).

Step-heating analysis AII93fss (Fig. 1.4d) is on K-feldspar from sample AII-93-19-4 and yielded a large (95.4 %) low-probability plateau (0.02) at 54.9 ± 0.1 Ma (and an assumed initial $^{40}\text{Ar}/^{36}\text{Ar}$ ratio of 295.5). Alteration indices (here based on $^{36}\text{Ar}/^{39}\text{Ar}$ because for K-rich phases ^{39}Ar is the proxy for mass) are reasonably low throughout most of the spectrum ($2 \cdot 10^{-5}$ to $6 \cdot 10^{-4}$) indicating little or no alteration effects on the K-feldspar's Ar isotope composition. Isotope correlation diagrams, however, show that virtually all heating steps are isochronous at an initial $^{40}\text{Ar}/^{36}\text{Ar}$ ratio of 310.6 ± 6.2 and a plateau age of 54.8 ± 0.1 Ma, which we consider the best estimate for the age of the AII93fss K-feldspars.

Plagioclase step-heating analyses JD5fss and JD5fs2 (Fig. 1.4e) (Sample DSDP Leg 74-525A-57-2) yielded somewhat scattered plateaus and alteration indices ($2 \cdot 10^{-5}$ to $2 \cdot 10^{-3}$), but plateau ages are identical within error with a weighted mean age of 71.3 ± 0.8 Ma. The age is confirmed by a second sample from the same hole (DSDP Leg 74-525A-57-5), whose plagioclase step-heating analysis (JD6fss, Fig. 1.4f) yielded a better plateau and lower plateau step alteration indices ($2 \cdot 10^{-5}$ to $3 \cdot 10^{-4}$). The plateau age is determined as 72.0 ± 1.2 Ma.

It is worth noting that both plagioclase ages from Leg 74 525A fit ocean crust ages estimated for this site based on paleomagnetism (~ 70 Ma; Thompson and Humphris, 1984), but are 7-8 Ma younger than estimates based on $^{40}\text{Ar}/^{39}\text{Ar}$ analyses of altered rock matrix (~ 79 Ma; O'Connor and Duncan, 1990).

Plagioclases from neighboring sites DSDP Leg 74-528-42-5 (analysis 971fss) and DSDP Leg 74-528-43-2 (analysis 972fss) differ in age and composition. The Ca/K ratios of ~ 400 and ^{39}Ar yields of $\sim 3 \cdot 10^{-16}$ Mol/g (compared to Ca/K ~ 60 and ^{39}Ar yields of $\sim 1.5 \cdot 10^{-15}$ Mol/g from JD5 and JD6 feldspars) indicate significantly lower K contents,

which explains the smaller argon isotope yields and larger errors of individual heating step ages and plateau ages (Fig. 1.4g and h).

Plateau step alteration indices range from $2 \cdot 10^{-5}$ to $2 \cdot 10^{-4}$ for both 971fss and 972fss, indicating analysis from nearly unaltered sites. Plateau ages are 58 ± 5 Ma (971fss) and 67 ± 4 Ma (972fss). Again, our age for DSDP Leg 74-528-43-2 closely fits Site 528 basement age estimates from paleomagnetic anomalies (~ 68 Ma; Thompson and Humphris, 1984), but is ~ 10 Ma younger than previous results of $^{40}\text{Ar}/^{39}\text{Ar}$ analyses of altered rock matrix samples from the same DSDP site (~ 78 Ma; O'Connor and Duncan, 1990).

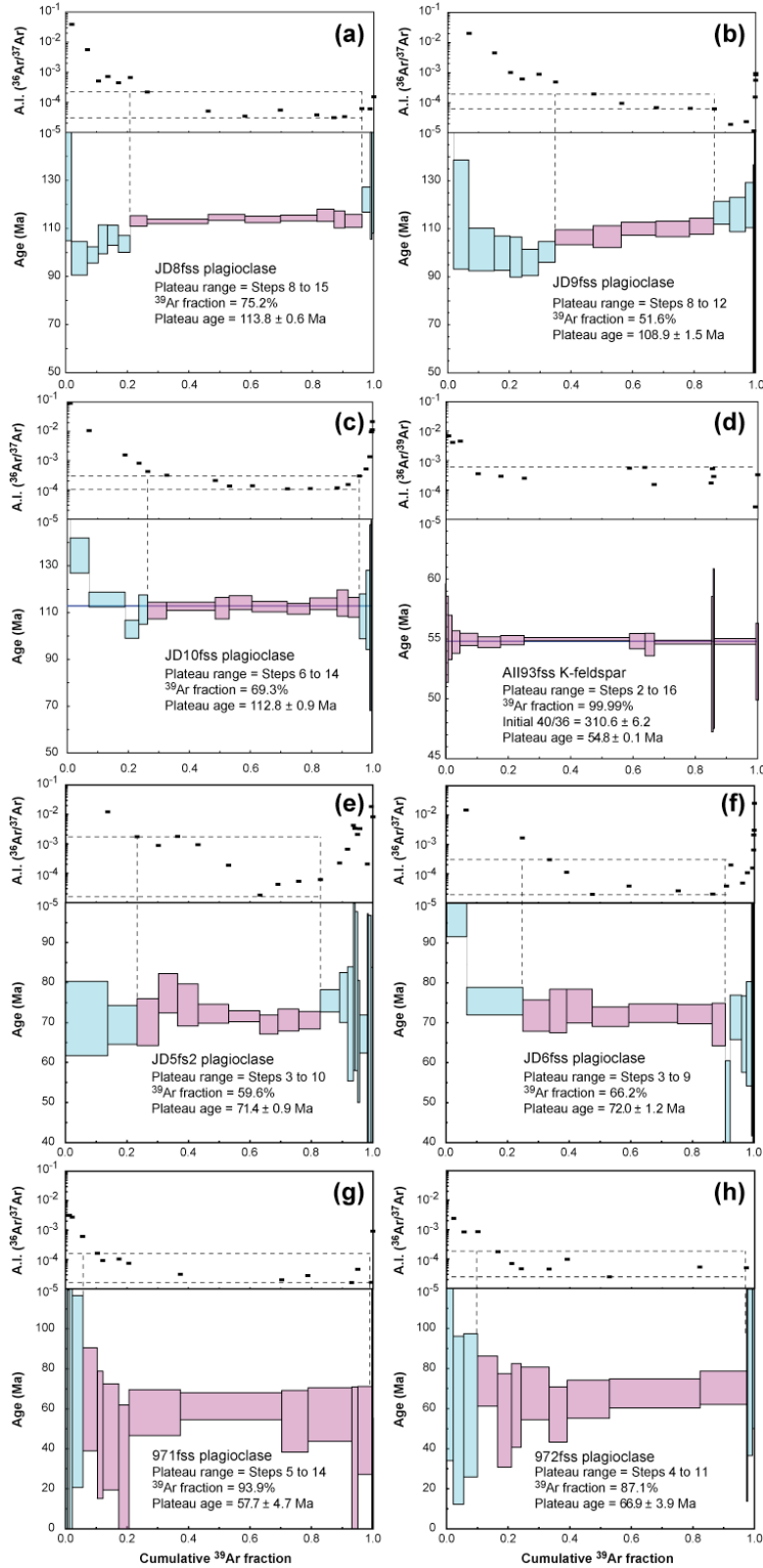


Fig. 1.4: $^{40}\text{Ar}/^{39}\text{Ar}$ step-heating age spectra and alteration indices from the Walvis Ridge. Heating temperatures and cumulative ^{39}Ar volumes increase from left to right. Plateau steps are magenta, rejected steps are cyan. Error bars are ± 2 sigma. Dashed lines mark ranges of alteration indices corresponding to plateaus.

4.2. Rio Grande Rise

Plagioclase step-heating analyses on DSDP Leg 72 516 rocks (analyses 979fss, JD3fss, -fs2, and 981fss) yielded plateau ages of 80 ± 2 Ma, 85 ± 4 Ma, 87 ± 3 Ma, and 85 ± 2 Ma, respectively (Fig. 1.5a, b and c). The plagioclase separates are nearly as K-poor as those from Leg 74 Site 528 described above, and slightly more altered (plateau step alteration indices from 1×10^{-4} to 1×10^{-3}). Given these uncertainties, we choose not to combine these data into a single average age, even though the plateau age results partly overlap within error. We conclude an age range of 80 to 87 Ma for the Rio Grande Rise basement basalts.

Two biotite step-heating analyses on material dredged from a small seamount on the Rio Grande Plateau (Sample RC11-2RD P5) yielded plateau ages of 46.2 ± 0.1 Ma (JD2bts) and 46.0 ± 0.1 Ma (JD2bt2, Fig. 1.5d). Plateau step alteration indices are low (2×10^{-5} to 2×10^{-4}). The plateau ages are similar, but not indistinguishable within error. We, however, prefer the 46.0 ± 0.1 Ma age from sample JD2bt2 from this site, because of the larger plateau ($^{39}\text{Ar} = 69\%$).

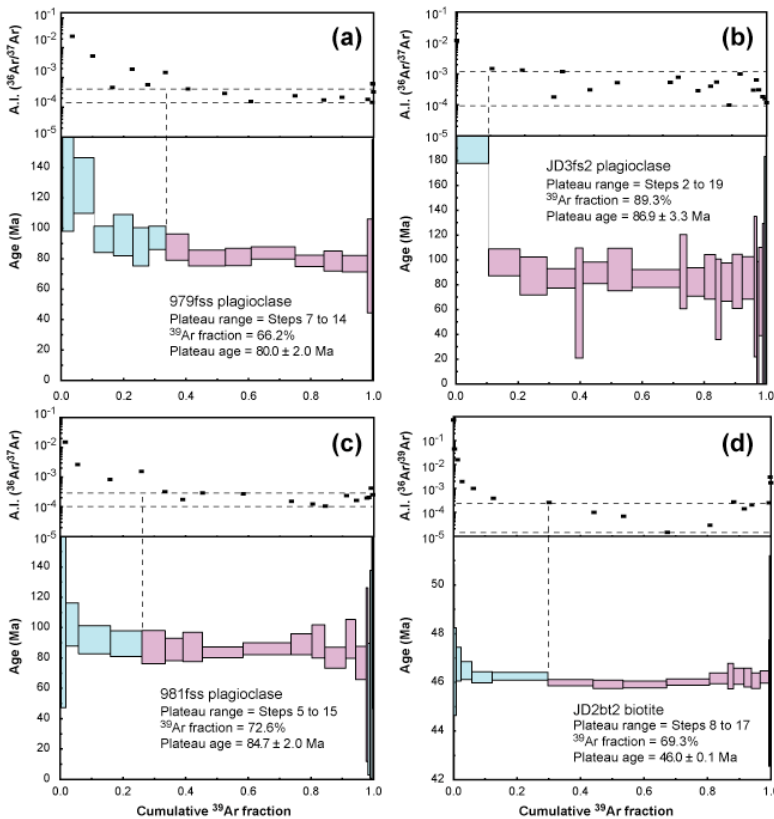


Fig. 1.5: $^{40}\text{Ar}/^{39}\text{Ar}$ step-heating age spectra and alteration indices from the Rio Grande Rise. Heating temperatures and cumulative ^{39}Ar volumes increase from left to right. Plateau steps are magenta, rejected steps are cyan. Error bars are ± 2 sigma. Dashed lines mark ranges of alteration indices corresponding to plateaus.

4.3. Guyot Province

Four samples were analyzed from the western Tristan branch of the Guyot Province (Fig. 1.2). Plagioclase step-heating of sample AII-93-5-3 yielded an 8-step-, 74 %-plateau at 36.1 ± 1.0 Ma. Plateau step alteration indices are low (1×10^{-4} to 5×10^{-4}), but indicate slight alteration (analysis 5-3fss; Fig. 1.6a).

Step-heating of plagioclase from sample AII-93-6-1 yielded a 7-step-, 89 %-plateau at 33.4 ± 1.0 Ma (6-1fss; Fig. 1.6b). Plateau step alteration indices (1×10^{-5} to 1×10^{-4}) indicate degassing from fresh, unaltered sites, 6 out of 7 plateau steps yielding alteration indices below the cut-off value for fresh plagioclase ($< 6 \times 10^{-5}$; Baksi, 2007a).

K-feldspars from rock sample AK-1695-6 (16956fss; Fig. 1.6c) yielded a 6-step, 71 %-plateau at 27.0 ± 0.1 Ma. Low alteration indices ($^{36}\text{Ar}/^{39}\text{Ar}$) indicate degassing from barely altered sites (3×10^{-5} to 3×10^{-4}).

Plagioclase step-heating of samples AII-93-3-1B and -25 yielded similar plateau ages of 27.7 ± 1.4 Ma (3-18fss) and 26.7 ± 1.5 Ma (3-25fss; Fig. 1.6d). Alteration is low in the plateau step range (2×10^{-5} to 3×10^{-4}). We assume that both samples are from the same rock unit, and calculate a single weighted mean plateau age of 27.2 ± 1.0 Ma for AII-93-3.

Four samples from the eastern Gough branch of the Guyot Province gave intermediate age results. Chips of feldspar-rich groundmass (appearing fresh in thin section) from sample PS69/420-1-DR21-1 yielded a step-heating age spectrum with a 9-step-, 78 %-plateau at 47.0 ± 0.2 Ma (21-1mxs; Fig. 1.6e). Alteration indices based on corrected $^{36}\text{Ar}/^{37}\text{Ar}$ ratios (which are directly comparable to results from plagioclase analyses), are comparable to fresh to barely altered plagioclase (4×10^{-5} to 3×10^{-4}). Together with the relatively uniform Ca/K ratios of ~ 6.5 , this is interpreted to reflect analyses from unaltered groundmass feldspar.

K-feldspars from rock sample PS69/423-1-DR25-4 yielded a large (98 % ^{39}Ar) plateau, comprising 12 consecutive steps (10 with significant volume), at 45.6 ± 0.1 Ma (25-4fss; Fig. 1.6f). Alteration indices indicate degassing of \pm fresh material over the plateau range (3×10^{-5} to 5×10^{-4}).

Plagioclase step-heating of sample A-93-10-11 yielded a large (96 % ^{39}Ar), flat, 15-step plateau (12 with significant volume) at 49.4 ± 0.7 Ma (10-11fss; Fig. 1.6g).

Alteration indices are low (1×10^{-5} to 3×10^{-4}). We note that the statistically valid plagioclase plateau age is 3 Ma older than the invalid “plateau age” determined by altered matrix step-heating on the same sample (O'Connor and Duncan, 1990; Table 1.3).

Plagioclases from samples PS69/440-1 DR-32-2 and DR-32-5b also yielded plateau steps with low alteration (A.I. = 1×10^{-5} to 3×10^{-4}) and plateau ages identical within error (32-2fss: 37.1 ± 0.2 Ma, 32-5fss: 36.9 ± 0.2 Ma; Fig. 1.6h). We assume that both samples are from the same rock unit, and calculate a single weighted mean plateau age of 37.0 ± 0.2 Ma for PS69/440-1-DR-32.

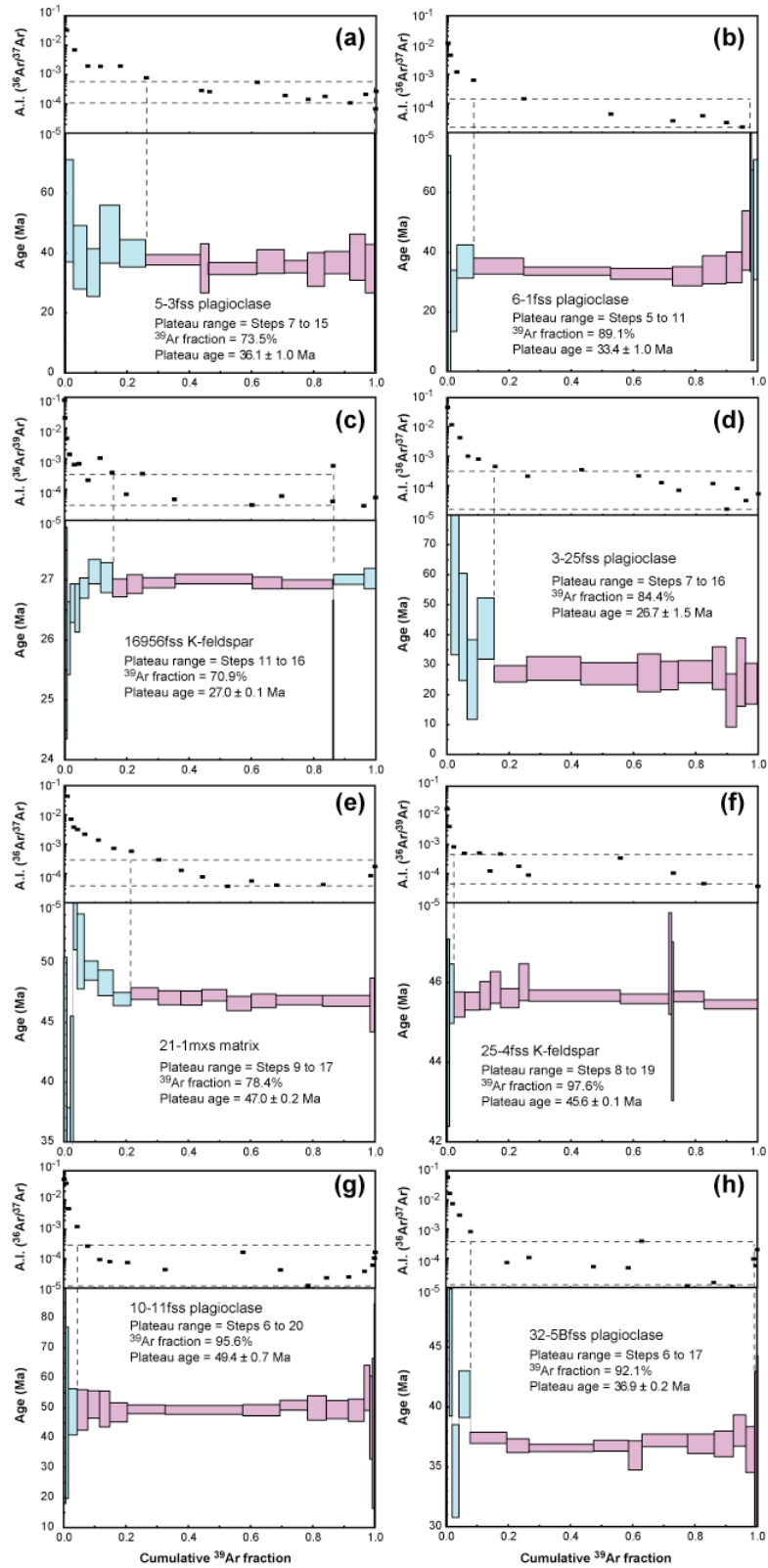


Fig. 1.6: $^{40}\text{Ar}/^{39}\text{Ar}$ step-heating age spectra and alteration indices from the Guyot Province. Heating temperatures and cumulative ^{39}Ar volumes increase from left to right. Plateau steps are magenta, rejected steps are cyan. Error bars are ± 2 sigma. Dashed lines mark ranges of alteration indices corresponding to plateaus.

Table 1.3: Comparison of $^{40}\text{Ar}/^{39}\text{Ar}$ age data from O'Connor and Duncan (1990) and from this study.

	O'Connor and Duncan, 1990		This study		
Sample	"Plateau" age (Ma)	$\pm 2\sigma$	Plateau age (Ma)	$\pm 2\sigma$	Δ (Ma)
All-93-3-1	29.2	± 0.4	27.7	± 1.4	-1.5
All-93-3-25	31.0	± 0.4	26.7	± 1.5	-4.3
All-93-5-3	38.7	± 0.4	36.1	± 1.0	-2.6
All-93-10-11	46.2	± 0.6	49.4	± 0.7	+3.2
DSDP 74-525A-57-5 [#]	79.4	± 0.8	72.0	± 1.2	-7.4

[#] Paleomagnetic anomaly 32; ~70 Ma (Thompson and Humphris, 1984)

5. Discussion

5.1. Evolution of the Tristan-Gough volcanic track

The new $^{40}\text{Ar}/^{39}\text{Ar}$ data set indicates a general age progression along the Tristan-Gough volcanic track becoming successively younger from the Etendeka CFBs (~135-132 Ma, Renne, 2011; Renne et al., 1996) to the islands of Tristan da Cunha and Gough. Our ages differ significantly from the published ones when the same rock samples and rock samples from the same units were analyzed (Table 1.3).

Along the Walvis Ridge, ages range from 114.1 ± 0.4 Ma at the northeastern end to 72 ± 1 Ma at DSDP Site 525A near the southwestern end (Fig. 1.2). The DSDP Site 528 lavas are significantly younger with ages of 58 ± 5 and 67 ± 4 Ma, but they have tholeiitic compositions, compared to alkali basalt compositions at Site 525A, which may explain the larger analytical errors due to the lower K content of tholeiitic basalts. If one moves the Rio Grande Rise along fracture zones to a position adjacent to the Walvis Ridge, our ages of 80 ± 2 Ma to 87 ± 3 Ma (DSDP Site 516F) fit the age progression for that position (see Figs. 1.2 and 1.7). Within the Guyot Province, ages range from 49 to 46 Ma near the northeastern end, to 27 Ma at the southwestern end of the Tristan seamount chain. Intermediate samples from the central portion of the Guyot Province yielded ages of 37 to 33 Ma.

Taken together, the time-distance relationship for the Guyot Province and the Walvis Ridge, defines a systematic age progression (see Fig. 1.7). One RSA Seamount trachyte from O'Connor and Le Roex (1992; 19 Ma) fits the age progression. Subordinate occurrences of younger seamounts within the Walvis Ridge (AII-93-19-4, 55 Ma) and the Rio Grande Rise (RC11-2RD P5, 46 Ma) may be related to late-stage volcanism similar to the “post-erosional” or “rejuvenated” volcanism in other hotspot systems, such as the Hawaiian, Galápagos, Canary and Madeira systems (e.g. Clague and Dalrymple, 1987; Geldmacher et al., 2005; Hoernle and Schmincke, 1993a, b; O'Connor et al., 2007; Werner et al., 2003). This is also implied by the generally more alkalic compositions of these younger samples (see Fig. 1.3). Samples from the main volcanic phases (“shield stages”) of the Walvis Ridge and Rio Grande Rise generally have a more tholeiitic composition (with the exception of one sample with altered groundmass) compared to samples from the Guyot Province and from the late-stage more silica-undersaturated volcanic phase on the Walvis Ridge and Rio Grande Rise (see Fig. 1.3).

In summary, our $^{40}\text{Ar}/^{39}\text{Ar}$ data set demonstrates that the Etendeka and Paraná CFBs, the Walvis Ridge/Rio Grande Rise, Guyot Province and the Tristan-Gough island groups are not only spatially connected, but show an overall age progression, consistent with the formation of the Tristan-Gough volcanic track through movement of the lithosphere over a relatively stationary mantle plume as also suggested by O'Connor and Duncan (1990). Previous $^{40}\text{Ar}/^{39}\text{Ar}$ dating results from the Walvis Ridge and Guyot Province were interpreted to reflect a volcanic migration rate of 22 mm/a (O'Connor et al., 1999). Considering our new $^{40}\text{Ar}/^{39}\text{Ar}$ ages, together with published ages for the Etendeka CFBs (Renne et al., 1996), a considerably faster migration rate of ~30 mm/a is inferred for the Tristan-Gough hotspot track, assuming a constant velocity of the African Plate (Fig. 1.7, black solid regression line). For the Walvis Ridge alone, we determine a rate of 28 mm/a (Fig. 1.7, gray dashed regression line).

Additional and more detailed sampling of the Tristan-Gough hotspot track, especially along the Walvis Ridge, is necessary to fill the existing age gaps and more accurately determine the volcanic migration rate. In particular, modern bathymetric surveys could better identify multiple volcanic phases and guide sampling targets to better constrain the duration of volcanism along a given part of the Walvis Ridge and the seamounts of the Tristan and Gough subtracks.

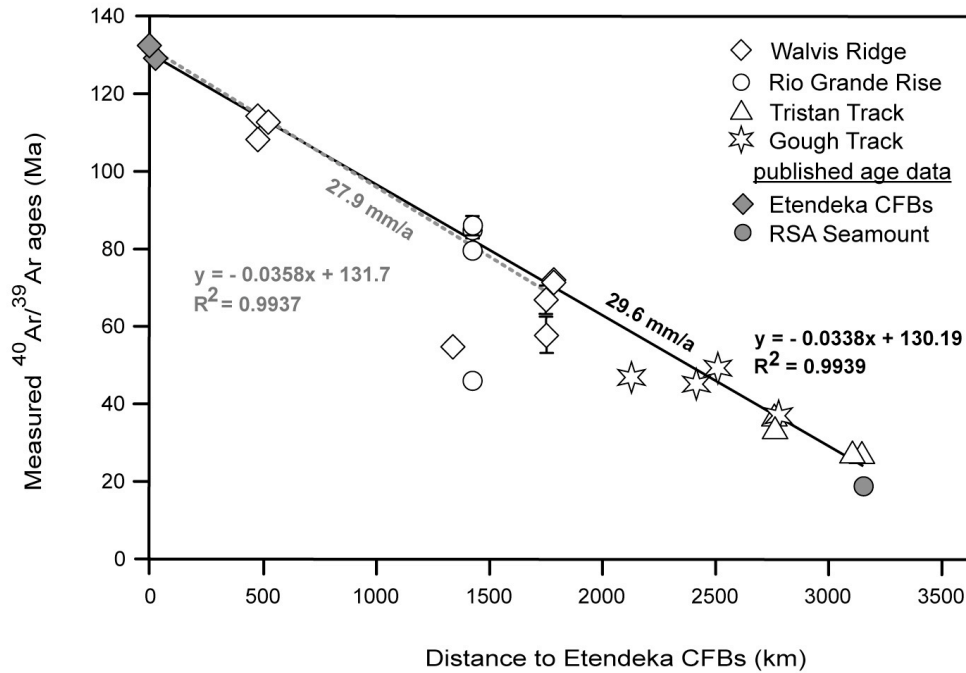


Fig. 1.7: Distance to the Etendeka CFBs versus measured $^{40}\text{Ar}/^{39}\text{Ar}$ ages for the Tristan-Gough hotspot track and Rio Grande Rise including published ages for the Etendeka CFBs from Renne et al. (1996) and for RSA Seamount from O'Connor and Le Roex (1992). The sampling locations of the Rio Grande Rise are rotated back next to the Walvis Ridge along the apparent fracture zones. Error bars are shown whenever errors (2 sigma) are larger than the symbols. The distance to the Etendeka CFBs is calculated by orthogonally projecting the sampling locations onto a hypothetical line connecting the Etendeka CFBs and the midpoint between Tristan da Cunha and Gough. Black solid line = regression line for the Tristan-Gough hotspot track. Gray dashed line = regression line for the Walvis Ridge. Only the oldest ages of each site as well as the maximum age of the Etendeka CFBs are included in the calculation of the regression lines. Not included are all trachyte and phonotephrite samples and the samples from the Rio Grande Rise, because their initial sites of formation can only be estimated.

5.2. Geodynamic model

Both hotspot and tectonic models have been proposed to explain the origin of the Tristan-Gough hotspot track. Francheteau and Le Pichon (1972) proposed a model of episodic fracturing of the oceanic crust to explain the evolution of the Walvis Ridge-Rio Grande Rise system stating that both features are composed of east-west and north-south sections formed by transform faults and probably by crustal modifications due to changing poles of rotation during the early opening stages of the South Atlantic, respectively. Fairhead and Wilson (2005) published a similar model, suggesting that changes in relative plate motion are responsible for the periodic stress release of the African Plate, which led to faulting and fracturing of the oceanic lithosphere and subsequently to volcanic eruptions. It is, however, not clear why a northeast-southwest oriented volcanic track would be formed with decreasing age progression to the southwest by tectonic processes

alone and therefore explore a mantle plume origin below.

According to the classic hotspot model, volcanic chains, such as the Tristan-Gough hotspot track, are thought to have formed where the lithosphere moved over a relatively stationary melting anomaly in the underlying mantle (e.g. DePaolo and Manga, 2003; Morgan, 1971, 1972; Wilson, 1963). The Tristan-Gough hotspot track is one of the few volcanic tracks on Earth, which is directly linked to flood basalt provinces on the conjugate continental margins (Etendeka-Paraná) and with active volcanic islands (Tristan-Gough) at the seaward end. In accordance with the plume head-plume tail model (Richards et al., 1989), the widespread massive flood basalt eruptions of the Etendeka-Paraná province represent the initial stage of volcanic activity of the starting plume (Fig. 1.8a). Subsequent to the formation of the Etendeka-Paraná CFBs the Walvis Ridge and the Rio Grande Rise formed as a single large plateau-like structure from the plume tail located near the South Atlantic mid-ocean ridge spreading axis (Fig. 1.8b). At around 75 Ma, there appear to have been multiple ridge jumps, mainly in eastward direction, resulting in the 80-87 Ma Rio Grande Rise becoming an isolated plateau-like structure on the South American Plate, while volcanism continued in an intraplate setting on the extension of the Walvis Ridge. During the transition from the Walvis Ridge to the Guyot Province westward ridge jumps dominated. In contrast to the spatially continuous structures of the Walvis Ridge and Rio Grande Rise, the diffuse character of the volcanic edifices within the Guyot Province with its isolated seamounts and smaller seamount chains and ridges as well as the V-shaped alignment of the Tristan and Gough subtracks indicate that it cannot have formed through a single classical plume tail with a diameter of ~100-300 km. The discontinuous bathymetric character of the Guyot Province implies a decrease of the hotspot activity and a weakening plume conduit that might have split into two or more separate plume arms and eventually into clusters of discrete blobs (Fig. 1.8c). Finally, although a mantle plume beneath Tristan and Gough Islands has not been tomographically imaged (Anderson, 2005), the lack of a seismic tomographic evidence might simply reflect the insufficient resolution of the tomographic models in the South Atlantic (e.g. Ritsema et al., 1999, 2011).

In conclusion, we favor a hotspot (mantle plume) origin for the Tristan-Gough hotspot track and the associated CFBs. Lithospheric structures, such as faults and/or fractures, however, no doubt also had an influence on the detailed spatial distribution of volcanism.

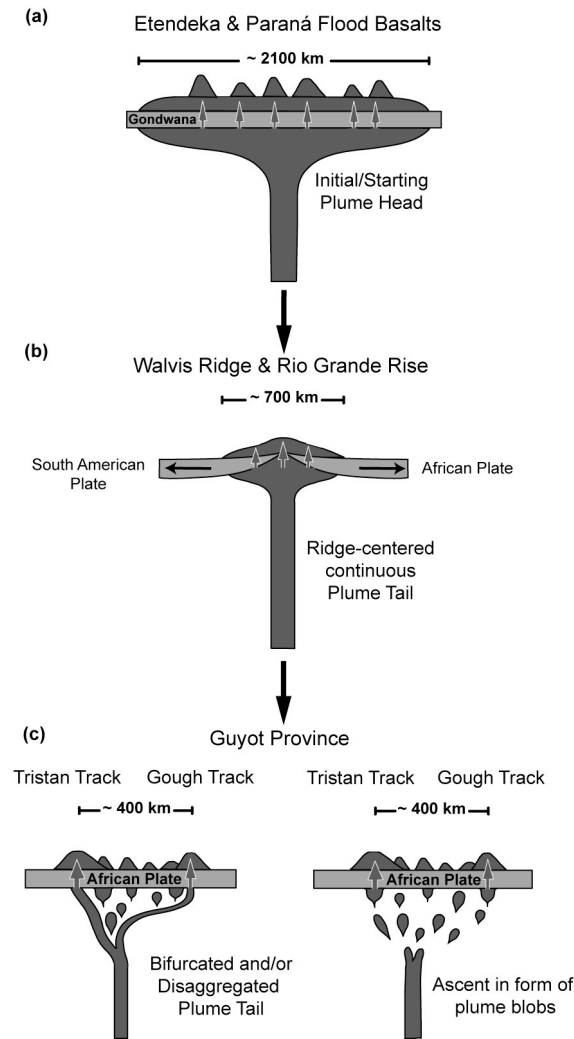


Fig. 1.8: Large-scale model for the formation of the a) Etendeka/Paraná CFB provinces from a plume head located beneath Gondwana, b) formation of the Rio Grande Rise and Walvis Ridge through a ridge-centered hotspot conduit (tail), and c) formation of the Guyot Province from a bifurcated to disaggregated plume tail, reflecting the waning (dying) stage of the hotspot.

6. Conclusions

Our new $^{40}\text{Ar}/^{39}\text{Ar}$ age data clearly show age progressive volcanism along the Tristan-Gough volcanic track, which is consistent with a mantle plume origin for these large-scale volcanic structures on the African and South American margins and on the seafloor. In summary, the age progression and the decreasing amount of volcanism along the Tristan-Gough volcanic track are consistent with it having formed over a mantle plume, which started at ~135-132 Ma with the formation of Etendeka and Paraná CFBs, then switched to a large and stable ridge-centered plume conduit to form the Walvis Ridge and Rio Grande Rise and finally became unstable and bifurcating at <60-70 Ma and then

breaking-up into blobs between ~35-45 Ma to form the fan-shaped Guyot Province, located solely on the African Plate.

We have shown that it is possible to produce valid $^{40}\text{Ar}/^{39}\text{Ar}$ ages for samples from the Tristan-Gough hotspot track, even for marine samples up to 114 Ma old by analyzing mineral separates and critically evaluating the effects of alteration on the Ar isotope system. Our age results in most cases differ significantly from the published ones for the same samples and for samples from the same locations (Table 1.3). The scattered age progression within the Guyot Province does not exclude a plume origin, but is consistent with a weakening (dying) plume breaking apart in its waning stages. Our age results also indicate that late-stage or rejuvenated volcanism can occur up to ~40 Ma after formation of the main volcanic structures, even \pm simultaneously at the Walvis Ridge and Rio Grande Rise when they were more than 1000 km apart.

The age progression along the Tristan-Gough hotspot track, together with the link between a volcanic chain and flood basalt volcanism, support a mantle plume rather than solely tectonic origin for this volcanism. Further detailed sampling, however, is of crucial importance to fill the age gaps, especially along the Walvis Ridge, to improve constraints on the volcanic migration rates and to better understand the temporal evolution of magmatism in the Guyot Province.

Since the time-distance relationship of volcanism along the Tristan-Gough hotspot track is a cornerstone in not only tracing African Plate motion (Duncan, 1981; Morgan, 1981; Müller et al., 1993; O'Connor and Duncan, 1990; O'Connor and Le Roex, 1992), but also global plate motions (e.g. Norton, 2000), current plate motion models need to be revised in the light of our new $^{40}\text{Ar}/^{39}\text{Ar}$ ages.

Acknowledgments

This study was funded by the Deutsche Forschungsgemeinschaft (DFG) under grants Ho 1833/17-1 and HO 1833/17-2 to KH and FH as part of the DFG Priority Program SPP 1375 “South Atlantic Margin Processes and Links with onshore Evolution”. Special thanks go to J. Sticklus for the analytical support, to R. Hekinian, K. Haase, S. E. Humphris, W. Jokat and J. O'Connor who provided samples for this study and to R. Trumbull and an anonymous reviewer for constructive reviews of this manuscript.

CHAPTER II

70 Ma chemical zonation of the Tristan-Gough hotspot track

Joana Rohde¹, Kaj Hoernle¹, Folkmar Hauff¹, Reinhard Werner¹, John O'Connor^{2,3,4},
Cornelia Class⁵, Dieter Garbe-Schönberg⁶, and Wilfried Jokat²

¹ GEOMAR Helmholtz Centre for Ocean Research Kiel, Wischhofstrasse 1-3, 24148 Kiel, Germany

² Alfred Wegener Institute for Polar and Marine Research, Columbusstrasse, 27568 Bremerhaven, Germany

³ Faculty of Earth and Life Sciences, VU University Amsterdam, De Boelelaan 1085, 1081 HV Amsterdam, The Netherlands

⁴ GeoZentrum Nordbayern, University of Erlangen-Nürnberg, Schlossgarten 5, 91054 Erlangen, Germany

⁵ Lamont-Doherty Earth Observatory, Columbia University, 61 Route 9W, Palisades, New York 10964-8000, USA

⁶ Institute of Geosciences, Christian-Albrechts-University of Kiel, Ludewig-Meyn-Strasse 10, 24118 Kiel, Germany

Published in Geology

Abstract

Asymmetrically zoned hotspot tracks in the Pacific Ocean are interpreted to have formed from zoned plumes originating from the large-scale, lower-mantle, low-seismic-velocity anomaly (superplume?) beneath the southern Pacific, providing direct information about lower mantle compositional heterogeneity. New trace element and Sr-Nd-Hf-Pb isotope data from the classic Tristan-Gough hotspot track in the South Atlantic also display a bilateral, asymmetric zonation with two distinct mantle source components, making it the first zoned plume to be recognized overlying the African superplume. The plume zonation can be traced for 70 m.y., four times longer than recognized for Pacific zoned hotspot tracks. These findings confirm that the proposed zonation of Pacific hotspots is not simply a geochemical oddity, but could be a major feature of plumes derived from lower-mantle superplumes. We propose that the enriched southern Gough subtrack source with elevated $^{207}\text{Pb}/^{204}\text{Pb}$ and $^{208}\text{Pb}/^{204}\text{Pb}$ at a given $^{206}\text{Pb}/^{204}\text{Pb}$, but low $^{143}\text{Nd}/^{144}\text{Nd}$ and $^{176}\text{Hf}/^{177}\text{Hf}$ (DUPAL-like composition), may reflect the African superplume composition, whereas the

more depleted northern Tristan subtrack source could represent a mixture of the superplume with the surrounding depleted mantle. Our results strengthen arguments that the enriched signature (DUPAL anomaly) in the South Atlantic could be derived from the lower mantle.

1. Introduction

Spatial geochemical zonation has been documented at the Galápagos, Hawaiian, Samoan, and Marquesan hotspot tracks in the Pacific Ocean, and is interpreted to reflect asymmetric, bi- or trilateral (vertically striped) chemical zonation of the plumes feeding these hotspots (Hoernle et al., 2000; Werner et al., 2003; Abouchami et al., 2005; Weis et al., 2011; Huang et al., 2011; Chauvel et al., 2012). The zonation has been related to chemical differences in the plume source (see previous references and Kerr and Mériaux, 2004; Farnetani and Hofmann, 2009; Lohmann et al., 2009), possibly related to plume generation at the margins of the large-scale, lower-mantle, low-seismic-velocity anomaly (superplume) beneath the southern Pacific Ocean (Huang et al., 2011; Weis et al., 2011; Chauvel et al., 2012). These large-scale upwellings are thought to develop at the core-mantle boundary and rise up to depths as shallow as 1000 km (e.g., Suetsugu et al., 2009; Ritsema et al., 2011). If this model is correct, then zoned plumes are also expected to be associated with the African superplume, but have not been recognized thus far.

The Tristan-Gough hotspot track extends from the Etendeka flood basalt province in southern Africa southwestward to the volcanically active Tristan da Cunha and Gough island groups (Fig. 2.1). The track comprises the aseismic Walvis Ridge, formed at the Mid-Atlantic Ridge together with the Rio Grande Rise, and the Guyot Province to the southwest, comprising volcanic ridges and seamounts, including guyots (flat-topped, former ocean-island volcanoes). Ar/Ar ages increase systematically from <1 Ma at Tristan da Cunha and Gough Islands to 135 Ma at Etendeka (Fig. 2.1), supporting a mantle-plume origin for this hotspot track (see Rohde et al., 2013b). The active end of this hotspot track is located above the southwest margin of the African superplume; therefore this hotspot track could provide insights into the compositions on both sides of the boundary.

Many of the volcanic rocks of the Tristan-Gough hotspot track have enriched mantle (EM)-type isotopic compositions, falling within the large-scale mantle geochemical

anomaly in the Southern Hemisphere termed the DUPAL anomaly (cf. Hart, 1984). Deep Sea Drilling Project (DSDP) Site 525 on the Walvis Ridge is considered to be the Atlantic type locality for the enriched mantle 1 (EM-I) endmember. The origin of the EM- or DUPAL-type signature in the Southern Hemisphere is controversial. It has commonly been attributed to the shallow recycling of continental lithosphere (e.g., Hawkesworth et al., 1986; Hanan et al., 2004; Hoernle et al., 2011), but deep origins for this anomaly have also been proposed (Castillo, 1988; Class and Le Roex, 2011). An important question is to what extent the DUPAL geochemical anomaly in volcanic rocks from the South Atlantic and Indian Oceans is derived from the African superplume (Castillo, 1988).

Here we evaluate the geochemical variations along and across the Tristan-Gough hotspot track from Tristan da Cunha and Gough Islands through the Guyot Province to the Walvis Ridge, in order to determine if the hotspot track shows geochemical zonation and to better constrain the origin of the EM-I mantle end member and the large-scale DUPAL anomaly. A total of 16 samples from the Guyot Province and Walvis Ridge have been analyzed for trace elements and Sr, Nd, Hf, and Pb double-spike (DS) isotopic ratios (see Appendices II a-e).

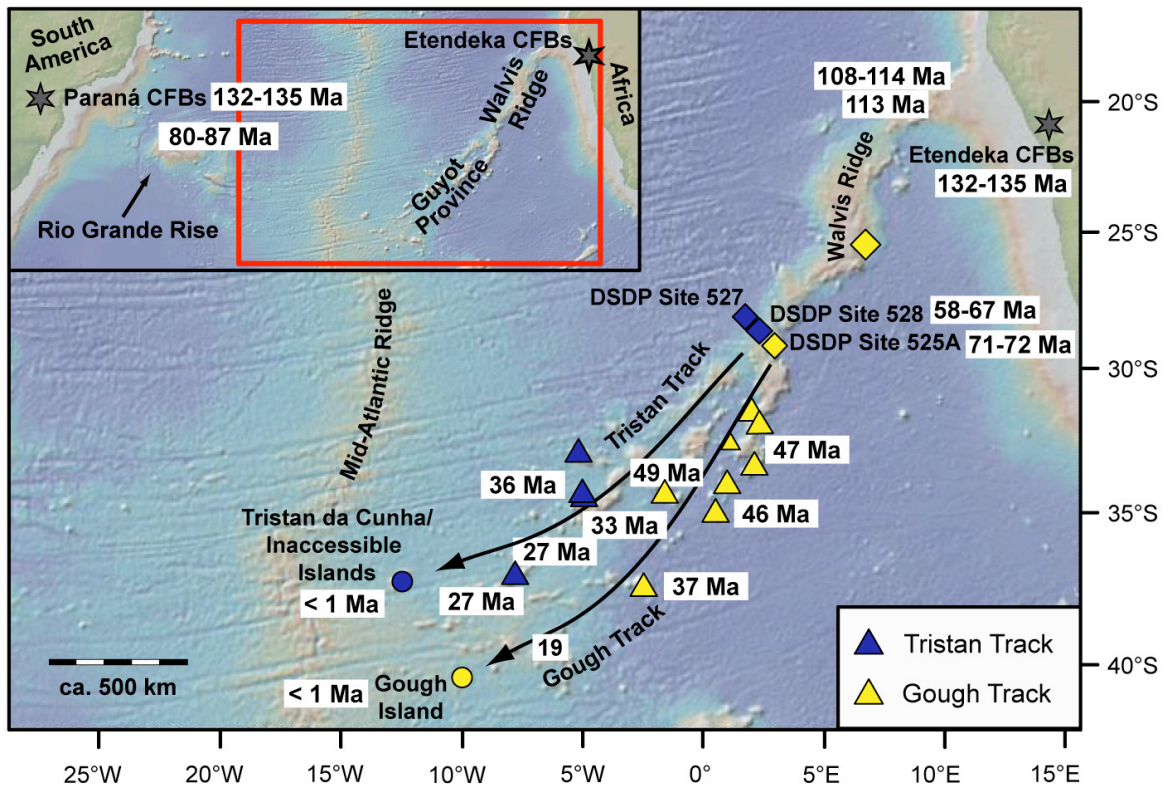


Fig. 2.1: Bathymetric overview map of Tristan-Gough hotspot track (South Atlantic), showing Tristan and Gough subtracks. Symbol shapes denote sample locations from islands (circles), Guyot Province (triangles), and Walvis Ridge (diamonds), while symbol colors denote Gough (yellow) and Tristan (blue) geochemical domains considered in this study. $^{40}\text{Ar}/^{39}\text{Ar}$ ages are from Rohde et al. (2013b, and references therein). Inset map shows locations of Paraná and Etendeka continental flood basalts (CFBs, gray stars), which were connected before the breakup of Gondwana, and Rio Grande Rise, which formed with the Walvis Ridge above the Mid-Atlantic Ridge during initial stages of the Tristan-Gough plume. Red box in inset designates area of main map figure. Source of base maps is <http://www.geomapapp.org>. DSDP - Deep Sea Drilling Project.

2. Results

The hotspot track has been divided into (1) the Gough subtrack, consisting of Gough Island and the southeastern part of the Guyot Province and Walvis Ridge (including DSDP Site 525A), and (2) the Tristan subtrack, comprising Tristan da Cunha-Inaccessible Islands and the northwestern part of the Guyot Province and Walvis Ridge (DSDP Sites 527 and 528). Although both subtracks have ocean-island-basalt-type incompatible-element patterns, which largely overlap (Appendix II c), their isotopic compositions are distinct (Fig. 2.2; Appendix II d). The Gough subtrack generally displays more enriched isotopic compositions, having higher $^{207}\text{Pb}/^{204}\text{Pb}$ and $^{208}\text{Pb}/^{204}\text{Pb}$ for a given $^{206}\text{Pb}/^{204}\text{Pb}$,

lower $^{143}\text{Nd}/^{144}\text{Nd}$ and $^{176}\text{Hf}/^{177}\text{Hf}$, and generally higher $^{87}\text{Sr}/^{86}\text{Sr}$ ratios than the Tristan subtrack (Fig. 2.2; Appendices II b and d). Pb isotope ratios crudely decrease with age for both subtracks over the past 70 m.y.

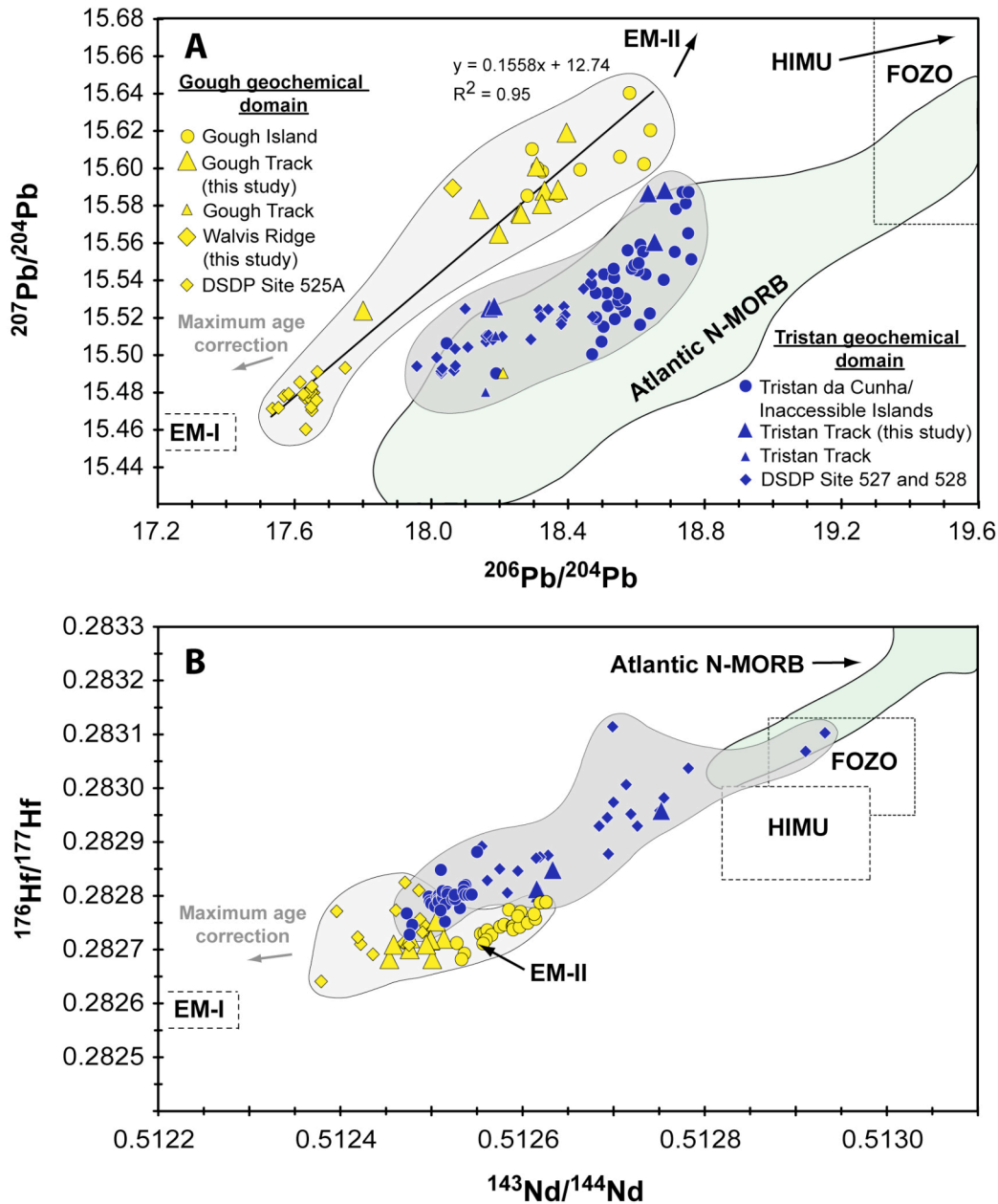


Fig. 2.2: Pb, Nd, and Hf isotope variation diagrams. $^{206}\text{Pb}/^{204}\text{Pb}$ versus $^{207}\text{Pb}/^{204}\text{Pb}$ (A) and $^{143}\text{Nd}/^{144}\text{Nd}$ versus $^{176}\text{Hf}/^{177}\text{Hf}$ (B) plots for the Tristan and Gough subtracks (South Atlantic), including published data from GEOROC (<http://georoc.mpch-mainz.gwdg.de/georoc/>), demonstrate that the domains of Tristan and Gough are geochemically distinct. Additional data sources: FOZO (focal zone) and HIMU (high μ , where μ is $^{238}\text{U}/^{204}\text{Pb}$) mantle components (after Stracke et al., 2005), enriched mantle EM-I and EM-II (after Stracke et al., 2003), and Atlantic normal mid-oceanic ridge basalt (N-MORB) (from PetDB, <http://www.petdb.org/>). Equation for best-fit correlation and correlation coefficient (R^2) for the Gough subtrack and average reduction in isotopic ratios resulting from age correction for our Tristan and Gough data (gray arrow) are also shown. DSDP - Deep Sea Drilling Project.

3. Discussion and Conclusions

Although there is good evidence that shallow recycling of continental lithosphere contributes to the origin of the enriched mantle (DUPAL) signature (e.g., Hanan et al., 2004; Hoernle et al., 2011), this is unlikely to be the source of the EM material in the South Atlantic hotspots. Geodynamic constraints show that only African lithosphere was likely to be located beneath the South Atlantic, but it does not have the appropriate composition to explain the composition of the Gough subtrack and other extreme DUPAL signatures in the South Atlantic (Class and Le Roex, 2011). It is also not clear how interaction of a plume with shallow continental material could generate a spatially zoned hotspot track extending ~1700 km that cuts across fracture zones in the seafloor and projected boundaries of major crustal units on the South African continent. In addition, the chemical zonation of the Tristan-Gough track is independent of age and thickness of the overlying lithosphere, which varied through time with volcanism being on-axis during formation of the Walvis Ridge and progressively further off-axis (intraplate) thereafter (Gibson et al., 2005). Therefore we interpret the chemical heterogeneity in the Tristan-Gough hotspot track to reflect a chemically heterogeneous plume.

The Galápagos, Hawaiian, Samoan, and Marquesan hotspots also show asymmetrical spatial geochemical zonation (Fig. 2.3; Appendix II d (B)) that cannot be attributed to shallow processes (Hoernle et al., 2000; Abouchami et al., 2005; Huang et al., 2011; Weis et al., 2011; Chauvel et al., 2012). The spatial zonation in isotopic composition of these four Pacific hotspot tracks has been attributed to asymmetric spatial zonation of these plumes, in the form of vertical stripes (sheets) or filaments (see previous references and Kerr and Mériaux, 2004; Farnetani and Hofmann, 2009; Lohmann et al., 2009). Thus far, chemical zonation has been traced for 5 m.y. at Hawaii (Weis et al., 2011), 15-20 m.y. at the Galápagos Islands (Hoernle et al., 2000; Werner et al., 2003), ~1.2 m.y. at Samoa, and ~5.5 m.y. at the Marquesas Islands (Clouard and Bonneville, 2005; Huang et al., 2011). Although the Hawaiian-Emperor chain can be traced back for ~80 m.y., only the Kea component has been found in the Emperor Seamounts (>47 Ma portion of the Hawaiian hotspot track) (Weis et al., 2011). The zonation of the Tristan-Gough hotspot track, however, demonstrates that bilateral geochemical zonation can survive in plumes for at least 70 m.y.

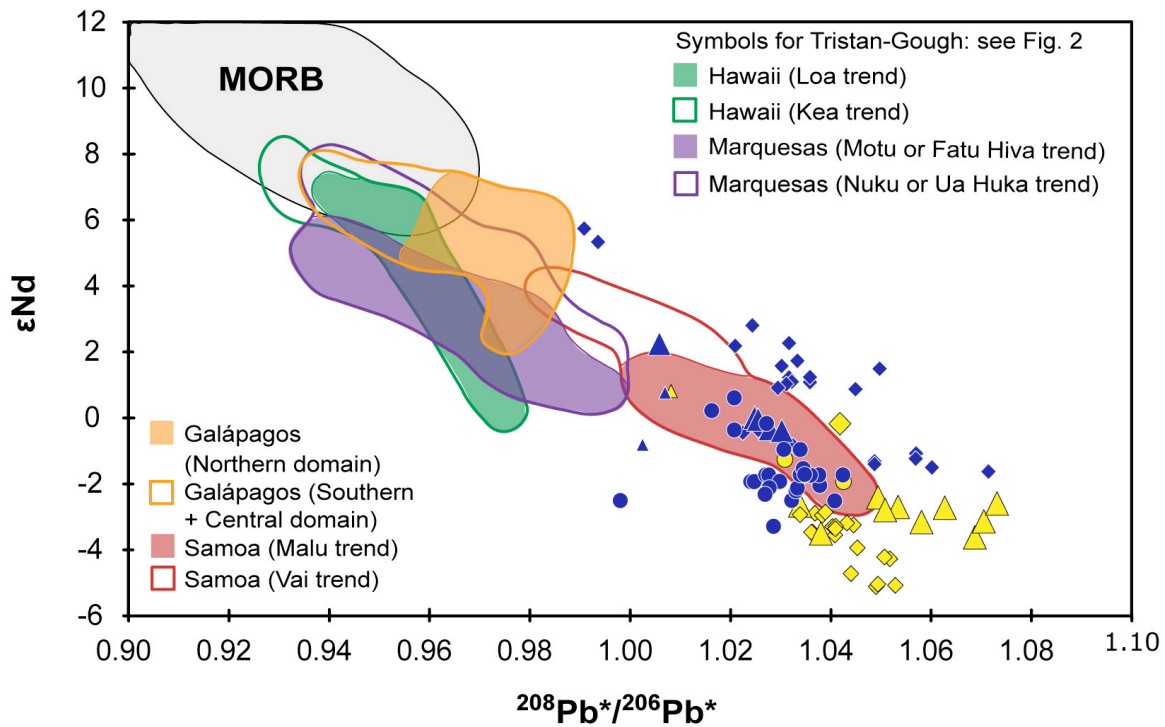


Fig. 2.3: $^{208}\text{Pb}^*/^{206}\text{Pb}^*$ [time-integrated $^{232}\text{Th}/^{238}\text{U}$ since Earth formation = $(^{208}\text{Pb}/^{204}\text{Pb} - 29.475)/(^{206}\text{Pb}/^{204}\text{Pb} - 9.307)$; Galer and O’Nions, 1985] versus ϵNd $\{[(^{143}\text{Nd}/^{144}\text{Nd})/0.512638 - 1] \times 1000$ for Nd isotopic measurements normalized to $^{146}\text{Nd}/^{144}\text{Nd} = 0.7219\}$ plot for the Tristan and Gough subtracks and certain Pacific hotspots, including published data from GEOROC (<http://georoc.mpch-mainz.gwdg.de/georoc/>). Comparison of Tristan-Gough hotspot track (South Atlantic) with zoned Pacific hotspots shows that zonation can be explained by mixing of an enriched component with depleted (mid-oceanic ridge basalt [MORB] source)-type mantle with the possible exception of Marquesas Islands. See Appendix DR4B (see footnote 1) for same diagram with individual data points. MORB data from PetDB (<http://www.petdb.org/>).

Numerical simulations and laboratory experiments show that compositional variations within the lowermost mantle can survive during the ascent of plume material and thus the lateral geochemical zonation of plumes can reflect the heterogeneities within the source region (Kerr and Mériaux, 2004; Farnetani and Hofmann, 2009; Lohmann et al., 2009). Recently it has been proposed that Pacific zoned plumes may be sampling the margins of the Pacific superplume (Huang et al., 2011; Weis et al., 2011) and the enriched composition (lower ϵNd but higher $^{208}\text{Pb}/^{204}\text{Pb}$ at a given $^{206}\text{Pb}/^{204}\text{Pb}$ and $^{208}\text{Pb}^*/^{206}\text{Pb}^*$, measuring radiogenic ingrowth of ^{208}Pb and ^{206}Pb and thus time-integrated Th/U during the Earth’s history; Fig. 2.3; Appendix II d (B)) of the southwestern Hawaiian and Marquesan and the southern Samoan hotspot track zones may reflect the composition of the superplume (Fig. 2.4A). The Tristan-Gough plume is the first example of a zoned plume located above the margin of the African superplume. As for the Pacific hotspots, its zonation might be a result of tapping the superplume margin.

The isotopic data can be explained through mixing of the Gough source with Atlantic mid-oceanic ridge basalt (MORB) \pm the focal zone (FOZO) mantle component (lower mantle and/or recycled oceanic crust; cf. Stracke et al., 2005) to form the Tristan group (Fig. 2.4B). Therefore, the enriched Gough source with elevated $^{207}\text{Pb}/^{204}\text{Pb}$ and $^{208}\text{Pb}/^{204}\text{Pb}$ at a given $^{206}\text{Pb}/^{204}\text{Pb}$ and $^{208}\text{Pb}^*/^{206}\text{Pb}^*$, but low $^{143}\text{Nd}/^{144}\text{Nd}$ and $^{176}\text{Hf}/^{177}\text{Hf}$, might represent the African superplume composition (Fig. 2.2; Appendices II b and d). On the uraniumogenic Pb isotope diagram (Fig. 2.2A), the linear array for the Gough group samples could reflect a mean age of enrichment for the Gough source of 2.4 Ga or, alternatively, mixing between different enriched mantle components. In either case, the Gough group composition could reflect deep recycling of continental lithosphere (lower crust and/or metasomatized mantle). For example, the lithospheric mantle beneath the Rio Apa-Luis Alves craton of southern Brazil and Paraguay, which underwent subduction-related metasomatism in the early Proterozoic, could serve as the Gough component with unradiogenic Pb and Nd but radiogenic Sr isotopic composition (Gibson et al., 2005), suggesting that the African superplume contains delaminated continental lithosphere.

The data for all zoned hotspot tracks considered together form a broad inverse correlation on the $^{208}\text{Pb}^*/^{206}\text{Pb}^*$ versus ϵNd plot, with MORB plotting at the depleted end and the Gough subtrack at the enriched end (Fig. 2.3). For each of the zoned hotspots except possibly the Marquesas Islands, mixing between the enriched subtrack and MORB (\pm FOZO) can explain the composition of the depleted subtrack from the same hotspot track. This observation is consistent with the enriched subtrack from each zoned hotspot ultimately being derived from enriched Pacific and African superplumes in the lower mantle, and the more depleted subtrack being derived through mixing of the ambient mantle with the enriched superplume material.

There are, however, some problems with the straightforward interpretation that zoned hotspot tracks are derived from the margins of superplumes. Although the orientation of the zonation at Hawaii and the Marquesas Islands is similar to the orientation of the underlying margin of the seismic low-velocity anomaly, this is not the case for the other zoned plumes (Fig. 2.4A). It is, however, questionable if the orientation of the zonation in the hotspot track will accurately reflect the geochemical boundary in the lower mantle, e.g., the plume conduit may twist during ascent. In addition, the resolution of the seismic tomography may not be high enough to resolve the orientation of the velocity-

anomaly boundary in detail, unless the catchment area of the plume is sufficiently large, as for Hawaii and the Marquesas Islands (~1900 km and ~1600 km, respectively). The catchment areas are much smaller for Samoa (960 km), the Galápagos Islands (760 km), and Tristan-Gough (540 km) (Kerr and Mériaux, 2004). Another problem is that some of the plumes (e.g., Samoan and Marquesan) appear to be coming from the top of the low-velocity anomalies rather than the margins, which could reflect tilting of plumes such that their base is actually located at the margin of the anomalies. Significant tilting, however, is not consistent with numerical models (Steinberger and O'Connell, 1997) and seismic tomographic results (e.g., Montelli et al., 2006). Alternatively, some of these plumes may be derived from the upper rather than marginal boundaries of the superplumes and the orientation of the zoning in the plume could reflect the local orientation of the superplume boundary (Fig. 2.4B) or heterogeneity in the superplume, as recently proposed for the Marquesas Islands (Chauvel et al., 2012). A final question is why the Tristan-Gough track becomes discontinuous and much wider (400-700 km) at its southwestern end in comparison to other zoned hotspot tracks (~100-200 km, and up to 400 km wide for the Galápagos Islands affected by plume-ridge interaction). These observations could reflect bifurcation of a waning plume at ca. 60-70 Ma (southwest end of the Walvis Ridge), succeeded by disaggregation of the plume into blobs after ca 40 Ma (Rohde et al., 2013b).

In conclusion, the association of zoned plumes with large, lower-mantle, seismic-low-velocity anomalies supports the hypothesis that these anomalies are not simply thermal but are also chemical in nature, and that plumes may preferentially form at thermochemical boundaries within the mantle. Finally, the morphology of hotspot tracks, e.g., dual trends of volcanoes, appears to be a good tool for predicting geochemical zonation of the plume and thus for the location of thermochemical boundaries in the mantle.

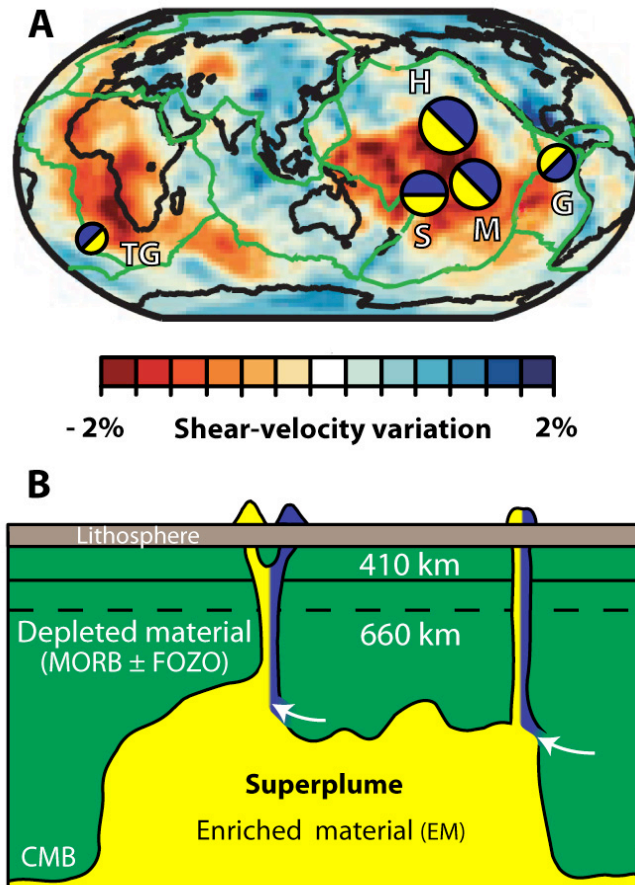


Fig. 2.4: Lower-mantle seismic tomographic image and schematic model showing the origin of geochemically zoned plumes from superplume boundaries. A: Shear-velocity map at 2800 km depth (e.g., for the S40RTS model, after Ritsema et al., 2011) shows two large low-velocity anomalies beneath the southern and central Pacific and southern Africa, possibly representing superplumes and/or domes that rise to depths as shallow as 1000 km (e.g., Suetsugu et al., 2009). Circles designate vertical projection of zoned hotspots to 2800 km (yellow - enriched zones; blue - depleted zones). Size of circles reflects diameter of catchment areas from Kerr and Mériaux (2004). G - Galápagos Islands; H - Hawaii; M - Marquesas Islands; S - Samoa; TG - Tristan da Cunha and Gough Islands. B: Schematic model for the generation of geochemically zoned mantle plumes at the boundaries of superplumes. Note that variable topography in the top region of the superplume can lead to deviations in orientation of the zones. Enriched and depleted zones may diverge in the mantle transition. MORB - mid-oceanic ridge basalt; FOZO - focal zone; CMB - core-mantle boundary.

Acknowledgments

We thank S. Humphris for providing samples; D. Rau, U. Westernströer, J. Fietzke, and S. Hauff for analytical support; the German Science Foundation Priority Program SAMPLE (grant Ho 1833/17-1, 2) for funding this project; and the U.S. National Science Foundation (grant OCE07-38437) for support for C. Class. C. Chauvel and A. Hofmann are thanked for constructive reviews.

CHAPTER III

The geochemical evolution of the older Tristan-Gough hotspot track: Walvis Ridge and Rio Grande Rise

Joana Rohde¹, Kaj Hoernle¹, Folkmar Hauff¹

¹ GEOMAR Helmholtz Centre for Ocean Research Kiel, Wischhofstrasse 1-3, 24148 Kiel, Germany

In preparation for submission to Earth and Planetary Science Letters

Abstract

The volcanic Tristan-Gough Islands, Guyot Province, Walvis Ridge, the Rio Grande Rise and the Etendeka-Paraná continental flood basalts (CFBs) in and on the margins of the South Atlantic comprise the classic inventory of a mantle plume derived hotspot track (e.g., Wilson, 1963; O'Connor and Duncan, 1990; O'Connor and Le Roex, 1992). Still, over the past 70 Ma, the Tristan-Gough hotspot track shows a bilateral geochemical zonation into Tristan and Gough isotopic domains (Rohde et al., 2013a). Here we present new major and incompatible trace element and Sr-Nd-Hf-Pb DS (double spike) isotope data for 62 samples from the Rio Grande Rise, the Walvis Ridge and the Guyot Province to evaluate if the geochemical zonation can be traced further back in the history of the hotspot system. Our results reveal that the >70 Ma parts of the hotspot track do not show geochemical zonation, but that the Walvis Ridge and the Rio Grande Rise are dominated by the enriched mantle (EM-) or DUPAL-type isotopic signature of the Gough domain. The Paraná flood basalts show signs of a Walvis Ridge/Rio Grande Rise-type of Gough component, while the Etendeka flood basalts appear to be influenced by both Gough- and Tristan-type components. The Tristan-Gough volcanic track shows changes in major and trace elements and also in isotopic composition at ~50-60 Ma, which coincides with changes in morphology from the voluminous Walvis Ridge to the more diffuse Guyot Province. This change appears ~10-20 Ma after the beginning of plume zoning.

Interestingly, the plume track bifurcates shortly after geochemical zonation is observed in the hotspot track suggesting a connection between geochemical zonation of the plume and the formation of dual volcanic chains. Comparison of the Tristan-Gough and Hawaiian systems shows that there are fundamental differences in the compositional evolution of hotspot systems over their lifespans.

1. Introduction

Spatial geochemical zonation is increasingly recognized in hotspot tracks. In the Pacific Ocean, zonation has been documented along the Galápagos (Hoernle et al., 2000; Geldmacher et al., 2003; Werner et al., 2003; Harpp et al., 2005), the Hawaiian (Abouchami et al., 2005; Weis et al., 2011), the Samoan and Marquesan (Huang et al., 2011; Chauvel et al., 2012) and the Society (Payne et al., 2013) hotspot tracks, which are located at the border of the large lower mantle shear wave velocity province (LLSVP) beneath the southern Pacific. The longevity of these zonations is variable for the different Pacific hotspots. It can be traced 15-20 Ma along the Galápagos hotspot track (Hoernle et al., 2000; Werner et al., 2003), ~4 Ma along the Society hotspot track (Payne et al., 2013; Clouard and Bonneville, 2005), ~5.5 Ma along the Marquesas and ~1.2 Ma along the Samoan Islands (Clouard and Bonneville, 2005; Huang et al., 2011). The coexistence of the geochemically distinct Loa and Kea trends of the Hawaiian mantle plume (Abouchami et al., 2005) has been traced for 5 Ma along the island chain (Weis et al., 2011), but has not yet been recognized in the Hawaiian or Emperor seamounts. Thus far, only the Kea component has been detected in the >47 Ma Emperor seamounts (Weis et al., 2011) and ophiolitic basalts in Kamchatka believed to represent accreted parts of older (~100 Ma) Emperor Seamounts (Portnyagin et al., 2008).

Recently published incompatible trace element and Sr-Nd-Hf-Pb DS (double spike) isotope data of samples from the Tristan-Gough hotspot track, whose presently active volcanic center is located at the margin of the African LLVSP, reveal that bilateral chemical zonation can be traced from the active island groups of Tristan da Cunha and Gough through the Guyot Province to the SW end of the Walvis Ridge (Fig. 3.1). This indicates that the plume has been zoned for at least 70 Ma (Rohde et al., 2013a). But available data is insufficient to establish chemical zonation along the Walvis Ridge beyond

70 Ma. In order to constrain further the evolution of the Tristan-Gogh hotspot track and the longevity and initiation of zonation in mantle plumes, we present new major and trace element and Sr-Nd-Hf-Pb DS isotope data from the older portions of the Tristan-Gough hotspot track, i.e. Walvis Ridge and Rio Grande Rise, and additional data from the Guyot Province. Moreover, we also want to further explore the origin of the Tristan and the Gough components and evaluate if deep or shallow lithospheric recycling drives mantle source characteristics of this hotspot system. Finally we will also assess published data from the Paraná and Etendeka flood basalts to perceive Tristan and Gough components at plume initiation.

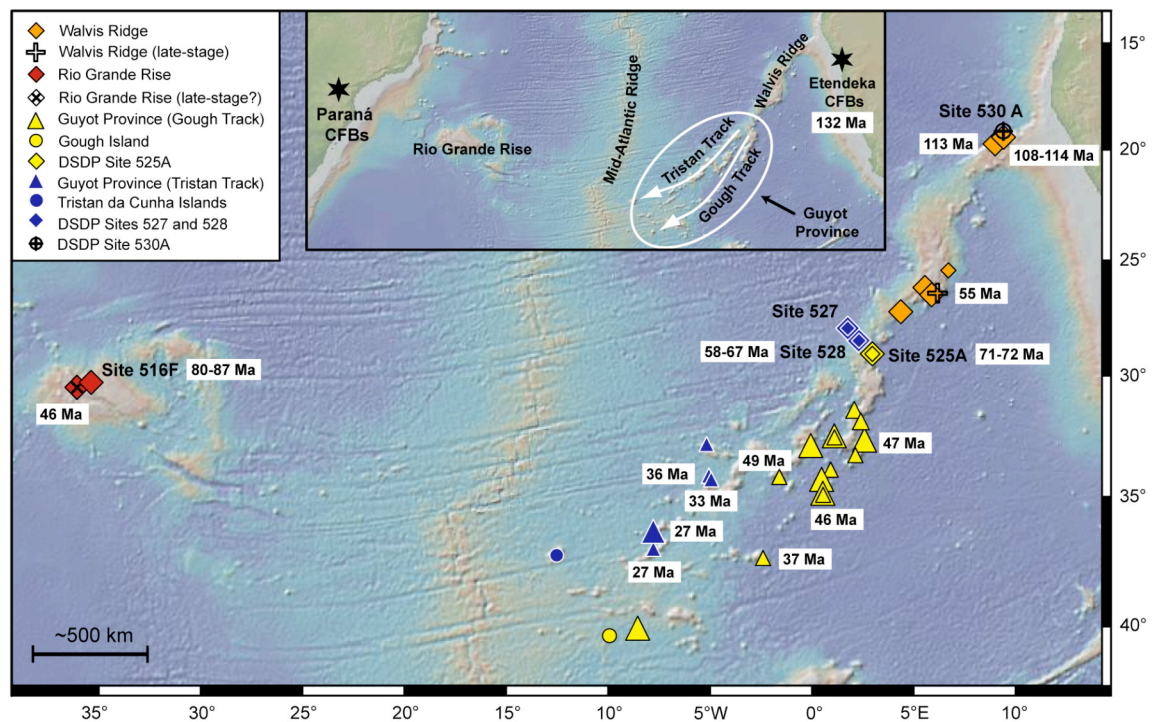


Fig. 3.1: Overview bathymetric map of the South Atlantic, showing the Tristan-Gough hotspot track (Walvis Ridge and Guyot Province) on the African Plate and the Rio Grande Rise on the South American Plate. Sample locations of this study (represented by enlarged symbols) and of published studies (represented by small symbols) are shown, as are age data from Rohde et al. (2013b). Age for the Etendeka CFBs are from Renne et al. (1996). Inset map shows the general morphological division of the studied areas and the locations of the Paraná and Etendeka CFBs (black stars). Source of the maps: <http://www.geomapp.org>.

2. Geological background and sampling locations

The northeast-southwest trending Tristan-Gough volcanic track, located on the African Plate in the South Atlantic (Fig. 3.1), is thought to represent a classic example of a hotspot track formed by movement of lithosphere over an upwelling mantle plume (Rohde et al. 2013b and references therein). Based on the morphology, the hotspot track can be subdivided into the Walvis Ridge, an aseismic volcanic ridge in the northeast, and the V-shaped Guyot Province to the southwest, characterized by dispersed volcanic edifices (e.g., isolated seamounts and small volcanic ridges). The Guyot Province can be further subdivided into two distinct volcanic subtracks based on morphology and geochemistry. These subtracks become less continuous and diverge with increasing proximity to the island groups of Tristan da Cunha (Tristan subtrack) and Gough (Gough subtrack), located ~450 and ~570 km from the Mid-Atlantic Ridge (MAR) respectively (Fig. 3.1).

The key characteristic relating this magmatism to a hotspot (mantle plume) is the progression to systematically older ages of volcanism from the active Tristan-Gough island groups to the Etendeka continental flood basalt (CFB) province in southern Africa. The Paraná CFB province in eastern South America was connected with the Etendeka CFBs, when they formed at ~132 Ma (Renne et al., 1996). The Rio Grande Rise offshore of South America formed contemporaneously with the Walvis Ridge at the MAR between ~114 Ma ($^{40}\text{Ar}/^{39}\text{Ar}$ age from northeastern end of the Walvis Ridge) to 72-58 Ma ($^{40}\text{Ar}/^{39}\text{Ar}$ ages for DSDP Sites 528 and 525A located near the southwestern end of the Walvis Ridge), whereas the few $^{40}\text{Ar}/^{39}\text{Ar}$ ages from the Rio Grande Rise range from 80-87 Ma (Rohde et al., 2013b). Ages from the Guyot Province fall between 49 and 27 Ma (Rohde et al., 2013b), while the Tristan da Cunha and Gough island groups are both still active (Fig. 3.1).

As shown by Rohde et al. (2013a) samples from the two geographically separated Tristan and Gough subtracks (Fig. 3.1), along with samples from the DSDP transect form two distinct arrays on the uraniumogenic Pb isotope diagram (Tristan and Gough isotopic domains), interpreted to reflect a bilateral geochemical zonation of the Tristan-Gough plume for at least the last 70 Ma. The Gough domain (comprising Gough Island, the Gough subtrack and the Walvis Ridge, including DSDP Site 525A on the SW end of the Walvis Ridge) has more enriched compositions than the Tristan domain (including Tristan da Cunha island group, the Tristan subtrack and DSDP Sites 527 and 528 on the SW end

of the Walvis Ridge), which exhibits lower $^{207}\text{Pb}/^{204}\text{Pb}$ and $^{208}\text{Pb}/^{204}\text{Pb}$ for a given $^{206}\text{Pb}/^{204}\text{Pb}$, but higher $^{143}\text{Nd}/^{144}\text{Nd}$ and $^{176}\text{Hf}/^{177}\text{Hf}$ ratios and generally lower $^{87}\text{Sr}/^{86}\text{Sr}$ ratios (Rohde et al., 2013a).

Sixty-two dredge and drill core samples from previously sampled basement locations were obtained for this study (Fig. 3.1). These samples were obtained from several repositories and were originally recovered during the U.S. American cruises RC11 and RC16 (R/V Robert D. Conrad) in 1967 and 1972, the CIRCE cruise (R/V Argo) in 1968, cruise VM 29 (R/V Vema) in 1972, cruise AII-93 (R/V Atlantis II) in 1975, during the French cruise (WALDA-002) CH19 (R/V Jean Charcot) in 1971, during a Russian cruise with the R/V Akademik Kurchatov in 1975, during cruise 51 of the South African ship R/V S. A. Agulhas, during DSDP Legs 72 (Site 516F), 74 (Sites 525A, 527 and 528) and 75 (Site 530A) with the R/V Glomar Challenger in 1980 and during a German expedition with the R/V Polarstern (ANTXXIII-5 (PS69)) in 2006. Forty samples are from sites located along and near the Walvis Ridge, including dredge samples from the northern flank at its northeastern-most end close to the Namibian coast and from the southern flank of the southwestern part, from DSDP Sites 525A, 527 and 528, which form a transect across the southwestern end of the Walvis Ridge, and from DSDP Site 530A located in the Angola Basin about 20 km north of the most northeastern part of the Walvis Ridge. Twelve samples were obtained from the Rio Grande Rise. These include two dredge sites at the border of a northwest-southeast trending canyon that cuts the Western Rio Grande Rise and from DSDP Site 516F on the main platform of the Rio Grande Rise. We also analyzed ten additional primarily evolved dredge samples from the Gough subtrack and one from the Tristan subtrack within the Guyot Province.

3. Sample preparation and analytical procedures

Sixty-two dredge and drill core samples were analyzed for major and trace elements and 41 of them for Sr-Nd-Hf-Pb DS isotope ratios in the framework of this study (Appendix III and IV).

For the geochemical analyses only the least altered inner parts of the selected rock samples were used to prepare rock chips and powders. After initial jaw-crushing the rock chips were sieved (fractions: <0.25 mm, 0.25-0.5 mm, 0.5-1 mm, 1-2 mm, 2-4 mm and >4

mm) and thereafter repeatedly cleaned in an ultrasonic bath with deionized water for about 20-30 minutes until a clear solution was obtained. The freshest chips were then hand-picked under a binocular microscope. About 5-10 g of 1-4 mm sized whole rock chips were taken to prepare bulk rock powders (in an agate mortar and agate ball-mill) for major and trace element and Hf isotope analyses. In addition, 500 mg of whole rock chips (0.5-1 mm fraction) were picked under a binocular microscope for Sr-Nd-Pb-Hf isotope analyses. Sample data are shown in Appendix IIIa and IIIb.

Major elements were determined by X-Ray Fluorescence Analysis (XRF) at GEOMAR Helmholtz Centre for Ocean Research Kiel (using a Philips X'Unique PW 1480 X-ray fluorescence spectrometer), at the Institute of Mineralogy and Petrography at the University of Hamburg (using a Magix Pro PW 2540 XRF) and by ICP-ES in the Acme Analytical Laboratories Ltd. in Vancouver. Eleven international rock standards were measured along with the samples (JA-2, JA-3, JB-2, JB-3, JG-2, JG-3, JGB-1, JR-1, AGV-2, BIR-1, BHVO-2 and BCR-2). Information about data quality is presented in Appendix IIIc.

Trace element analyses were carried out on an AGILENT 7500cs inductively coupled plasma mass spectrometer at the Institute of Geosciences at the Christian-Albrechts-University of Kiel after the methods of Garbe-Schönberg (1993) and in the Acme Analytical Laboratories Ltd. in Vancouver by inductively coupled plasma mass spectrometry (ICP-MS) subsequent to a lithium metaborate/tetraborate fusion and nitric acid as well as an Aqua Regia digestion. BIR-1, BHVO-2, BCR-2 and AGV-2 were analyzed as geochemical reference materials. Information about data quality is given in Appendix III d.

Isotope analyses were carried out at GEOMAR Helmholtz Centre for Ocean Research Kiel applying static multi-collector (MC) thermal ionization mass spectrometry (TIMS) for Sr-Nd-Pb isotope ratios and static MC-inductively coupled plasma mass spectrometry (ICP-MS) for Hf isotope ratios. For Sr-Nd-Pb analyses, ca 100-250 mg whole rock chips were leached in warm 2N HCl at 70 °C for 1 hour and subsequently triple rinsed in ELGA water to minimize the effects of alteration and sample handling. Ion chromatography followed established standard procedures (Hoernle and Tilton, 1991; Hoernle et al., 2008). Sr, Nd and Pb isotope analyses were performed on a Finnigan MAT

262 RPQ²⁺ (Sr and Pb) and on a Thermo Fisher TRITON TIMS (Sr and Nd). Nd and Sr ratios were normalized to $^{146}\text{Nd}/^{144}\text{Nd} = 0.7219$ and $^{86}\text{Sr}/^{88}\text{Sr} = 0.1194$ within each scan. During the sample analyses measurements of reference material NBS987 were $^{87}\text{Sr}/^{86}\text{Sr} = 0.710250 \pm 0.000013$ (n = 42; 2 σ external reproducibility) on the MAT262 RPQ²⁺ and $^{87}\text{Sr}/^{86}\text{Sr} = 0.710250 \pm 0.000013$ (n = 5; 2 σ external reproducibility) on the TRITON, where a small subset of samples was determined. La Jolla gave $^{143}\text{Nd}/^{144}\text{Nd} = 0.511850 \pm 0.000007$ (n = 25; 2 σ external reproducibility) and our in-house SPEX Nd monitor 0.511715 ± 0.000005 (n = 13; 2 σ external reproducibility). The Pb double-spike (DS) technique after Hoernle et al. (2011) was used to mass bias correct Pb isotopic ratios. The following double-spike corrected ratios for NBS981 were obtained along with the analysis of the samples: $^{206}\text{Pb}/^{204}\text{Pb} = 16.9416 \pm 0.0024$, $^{207}\text{Pb}/^{204}\text{Pb} = 15.4992 \pm 0.0024$ and $^{208}\text{Pb}/^{204}\text{Pb} = 36.7246 \pm 0.0061$ (n = 18; 2 σ external reproducibility). The Pb chemistry blanks were 10-40 pg and thus negligible. Hf isotope analyses followed the two-column procedure of Blichert-Toft et al. (1997) and were carried out on a VG Axiom MC-ICPMS and on a Nu plasma MC-ICPMS that operated in static MC mode. Our in-house SPEX Hf ICP standard solution (Lot #9) was normalized to JMC 475 ($^{176}\text{Hf}/^{177}\text{Hf} = 0.282163$; Blichert-Toft et al. 1997) and gave an average standard bracketing normalized ratio of $^{176}\text{Hf}/^{177}\text{Hf} = 0.282173 \pm 0.000008$ (n = 132; 2 σ external reproducibility; VG Axiom MC-ICPMS) and 0.282170 ± 0.000004 (n = 48; 2 σ external reproducibility; Nu plasma MC-ICPMS). Replicate analyses for Sr-Nd-Pb isotopes by means of a second sample digest were carried out on ten samples using the 2 N HCl leaching procedure of whole rock chips described above. While the reproducibility of $^{143}\text{Nd}/^{144}\text{Nd}$ lies within the external 2 σ errors of the standards, offsets outside the external 2 σ array of the standards are observed for radiogenic Sr and Pb isotope ratios in some samples (Appendix IIIe). In detail, five out of nine Sr replicates reproduce within the external standard errors, three samples (DSDP Leg 74 528 42 1W 29-45, DSDP Leg 75 530A 108 3W 78-84 and AII-93-3-25) reproduce slightly outside and the largest offset is observed for PS69/424-1-DR 26-1. The somewhat limited reproducibility for Sr on leached whole rock chips is ascribed to variable degrees of seawater alteration even in visually homogeneous sample chips and the inability of the leaching reagent to fully penetrate the sample and thus remove all Sr introduced through

secondary processes. Pb isotope ratios are reproduced within the external 2σ errors for NBS981 for eight out of ten samples in $^{207}\text{Pb}/^{204}\text{Pb}$ and seven out of ten samples in $^{208}\text{Pb}/^{204}\text{Pb}$, while $^{206}\text{Pb}/^{204}\text{Pb}$ is reproduced for only five samples under these specifications. Interaction with seawater during low temperature alteration and seafloor weathering can lead to a heterogeneous enrichment of uranium that causes variable degrees of ^{206}Pb ingrowth over time. In this respect it is worth noting that $^{207}\text{Pb}/^{204}\text{Pb}$ is less affected by secondary U enrichment as ^{235}U is 137.88 times less abundant than ^{238}U . The three samples, for which $^{208}\text{Pb}/^{204}\text{Pb}$ is reproduced outside the external 2σ array of NBS981, seem to have undergone a more complex alteration history that includes Pb removal at high temperatures in addition to U enrichment at low temperatures. Hf replicate analysis on sample DSDP Leg 74 525 A 57 5W 141-148 agreed within the external 2σ errors of the standard. Furthermore, USGS reference material BHVO-2 gave $^{176}\text{Hf}/^{177}\text{Hf} = 0.283107$, which compares well with the mean of compiled values at GEOREM ($^{176}\text{Hf}/^{177}\text{Hf} = 0.283109 \pm 0.000012$).

4. Results

4.1. Major elements

The analyzed samples show a large range in major element composition (Appendix IIIa and IV; Fig. 3.2). The majority of samples from the Tristan-Gough hotspot track and the Rio Grande Rise are alkali basalts and tholeiites. Some samples range from trachybasalts, basaltic trachyandesites to trachytes with a few having basanitic, tephritic and tephriphonolitic compositions. The major element compositions (normalized to 100% on a volatile-free basis) of the samples with LOI (loss on ignition) $< 3.5\%$ have MgO between 1.9-11.0 wt.%, except for a few samples with MgO < 1 wt%, and SiO₂ from 45-62 wt.%.

Considering only the hotspot track on the African Plate and mafic samples with MgO > 4.5 wt. %, it becomes obvious that a change in silica saturation and alkalinity coincides with a change in morphology. All samples from the more diffuse, younger part

of the hotspot track (<60 Ma, Guyot Province) are alkalic and silica undersaturated (Fig. 3.2). In contrast, samples from the older, more voluminous part of the hotspot track (>60 Ma, Walvis Ridge) mostly have tholeiitic compositions, which are not found in the Guyot Province.

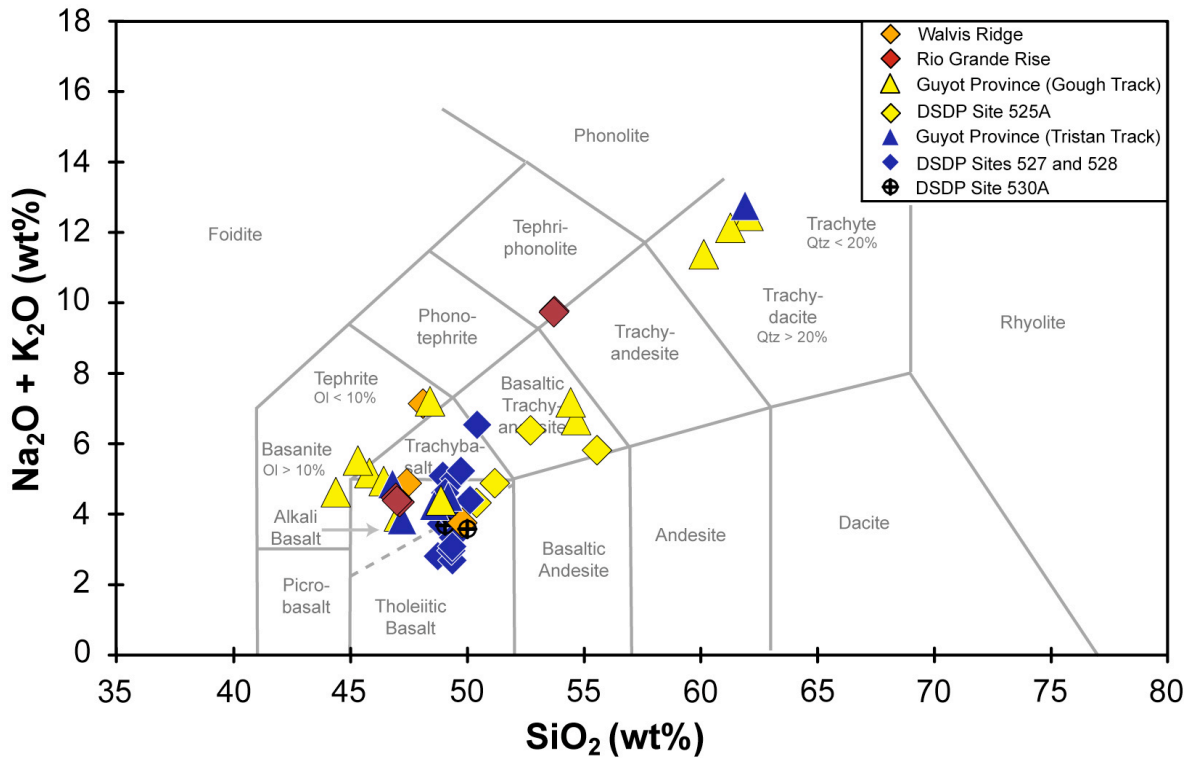


Fig. 3.2: Total alkali versus silica diagram (TAS diagram) of volcanic rocks from the Tristan-Gough volcanic track and the Rio Grande Rise after Le Maitre et al. (1989). Only samples with LOI (loss on ignition) <3.5 % are shown. Values are normalized to 100% on a volatile-free basis. Gray dashed line = subdivision line between alkali basalts and tholeiitic basalts after Macdonald and Katsura (1964). Qtz = Quartz, Ol = Olivine.

4.2. Trace elements

Primitive-mantle-normalized incompatible element compositions of samples from the Guyot Province, the Walvis Ridge and the Rio Grande Rise along with published data from Rohde et al. (2013a) are presented in Fig. 3.3. Only samples with MgO >4.5 wt% and LOI <5 % are shown. Although they possess a wide range in incompatible element concentrations, the majority display incompatible trace element signatures typical for oceanic intraplate basalts with a strong enrichment of highly to moderately incompatible

elements (e.g., $(\text{Nb}/\text{Zr})_N = 0.9\text{-}3.1$, $(\text{Nb}/\text{Y})_N = 1.0\text{-}14.5$; N refers to primitive-mantle normalization after Hofmann, 1988), enriched Light Rare Earth Element (LREE) compositions relative to Heavy (H) REE (e.g., $(\text{La}/\text{Yb})_N = 1.3\text{-}20.7$), HREE patterns with a negative slope (e.g. $(\text{Tb}/\text{Yb})_N = 1.0\text{-}15.8$) and a negative Pb anomaly (Fig. 3.3). SiO_2 forms an inverse correlation with $(\text{Tb}/\text{Yb})_N$ in the mafic samples (Fig. 3.4; $\text{MgO} > 4.5$ wt%).

Samples from the Guyot Province and the Walvis Ridge show some overlap, but the Guyot Province samples are characterized by a stronger enrichment in highly to moderately incompatible elements compared to the Walvis Ridge samples. These temporal differences in trace element composition along the Tristan-Gough volcanic track can also be seen in plots of sample age versus $(\text{La}/\text{Sm})_N$ and $(\text{Sm}/\text{Yb})_N$ (Fig. 3.5). Between ~115 and 60 Ma (along the Walvis Ridge), the $(\text{La}/\text{Sm})_N$ and $(\text{Sm}/\text{Yb})_N$ ratios are low (1.0-3.8 and 1.0-3.5, respectively) and begin to increase at ~55-60 Ma. In contrast to Walvis Ridge, the few samples from Rio Grande Rise display a smaller range in incompatible trace element composition, with slightly higher abundances of the moderately incompatible trace elements and overall steeper REE patterns. Some samples from the DSDP transect at the southwestern end of the Walvis Ridge (Sites 527 and 528) exhibit signatures more typical of E-MORB with less enrichment of highly to moderately incompatible elements and relatively flat REE patterns. DSDP Site 530A samples (not displayed on the incompatible trace element diagram), adjacent to the northeastern end of the Walvis Ridge, exhibit trace element patterns in between those for average E-MORB and average ocean island basalt (OIB). The samples from the Tristan-Gough hotspot track display typical EM-I-like trace element patterns (Weaver, 1991; Willbold and Stracke, 2006) with strong Ba enrichments relative to other LILE elements (e.g. $\text{Ba}/\text{La} = 8.8\text{-}20.5$) and generally low Nb/La (0.72-1.1) or U/Pb (0.12-0.63; see also Appendix IIIb). Compared to HIMU basalts with Nb/La $> \sim 1.2$, the mostly low Nb/La 0.72-1.1 and common lack of Nb and Ta peaks in the sample set suggest that EM basalts are less enriched in Nb and possibly Ta, as proposed by Willbold and Stracke (2006). Compared to HIMU basalts, the sample average exhibits higher Th/U (~4.2) and Rb/Nb (0.7) that are typical of EM basalts (Willbold and Stracke, 2006).

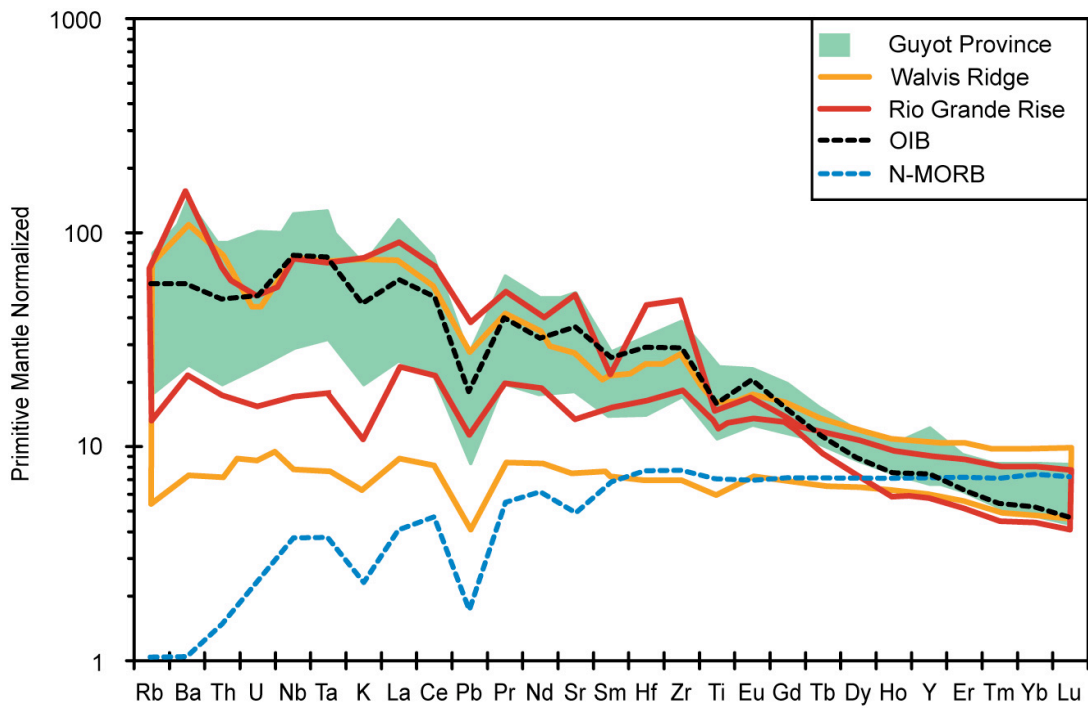


Fig. 3.3: Incompatible trace element diagram showing the arrays for the Walvis Ridge and the Guyot Province. The patterns include a compilation of the data generated for this study and published data from Rohde et al. (2013a). Only samples with MgO >4.5 wt% and LOI (loss on ignition) <5 % are shown. Concentrations are normalized to primitive mantle after Hofmann (1988). Incompatible patterns of average OIB and N-MORB are from Sun and McDonough (1989). Since the samples from DSDP Site 530A (north of the Walvis Ridge) cannot be clearly geographically attributed to the Walvis Ridge, they are excluded from the incompatible trace element diagram.

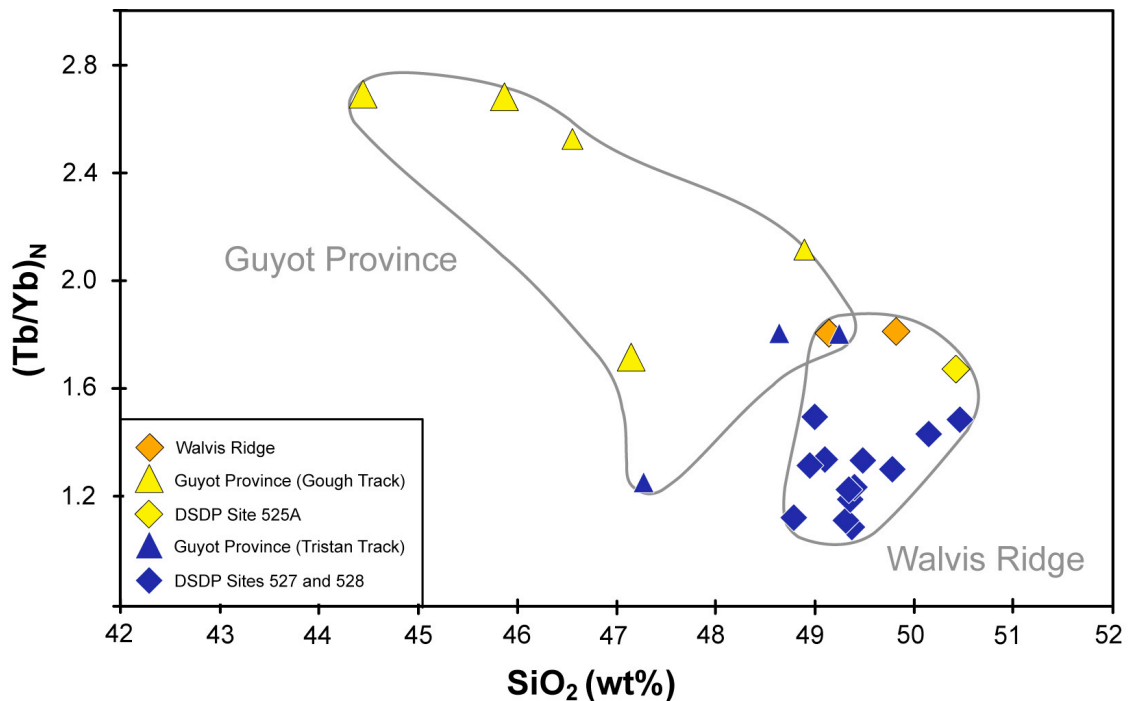


Fig. 3.4: SiO₂ versus (Tb/Yb)_N diagram including our data for the Guyot Province and the Walvis Ridge. Only samples with MgO >4.5 wt% and LOI (loss on ignition) <3.5 % are shown.

4.3. Sr-Nd-Pb-Hf isotopes

The samples from the Tristan-Gough hotspot track cover a wide range in Sr, Nd, Pb and Hf isotopic compositions (Fig. 3.6). Our new isotope data from the Guyot Province and the DSDP transect also plot into their respective isotopic domains, consistent with the plume zonation proposed by Rohde et al. (2013a). All new data from the Walvis Ridge and the Rio Grande Rise older than 72 Ma plot within the Gough field. The Rio Grande Rise samples and some of the other samples from the Walvis Ridge are isotopically as enriched as DSDP Site 525A; the EM-I archetype location of the South Atlantic (e.g., Richardson et al., 1982; Zindler and Hart, 1986). Two late-stage samples that are significantly younger than the surrounding rocks and much younger than expected from the age progression (one from the Walvis Ridge and one from the Rio Grande Rise) lie outside the Tristan and Gough isotopic domains (Appendix IIIb, Fig. 3.6; Rohde et al., 2013b).

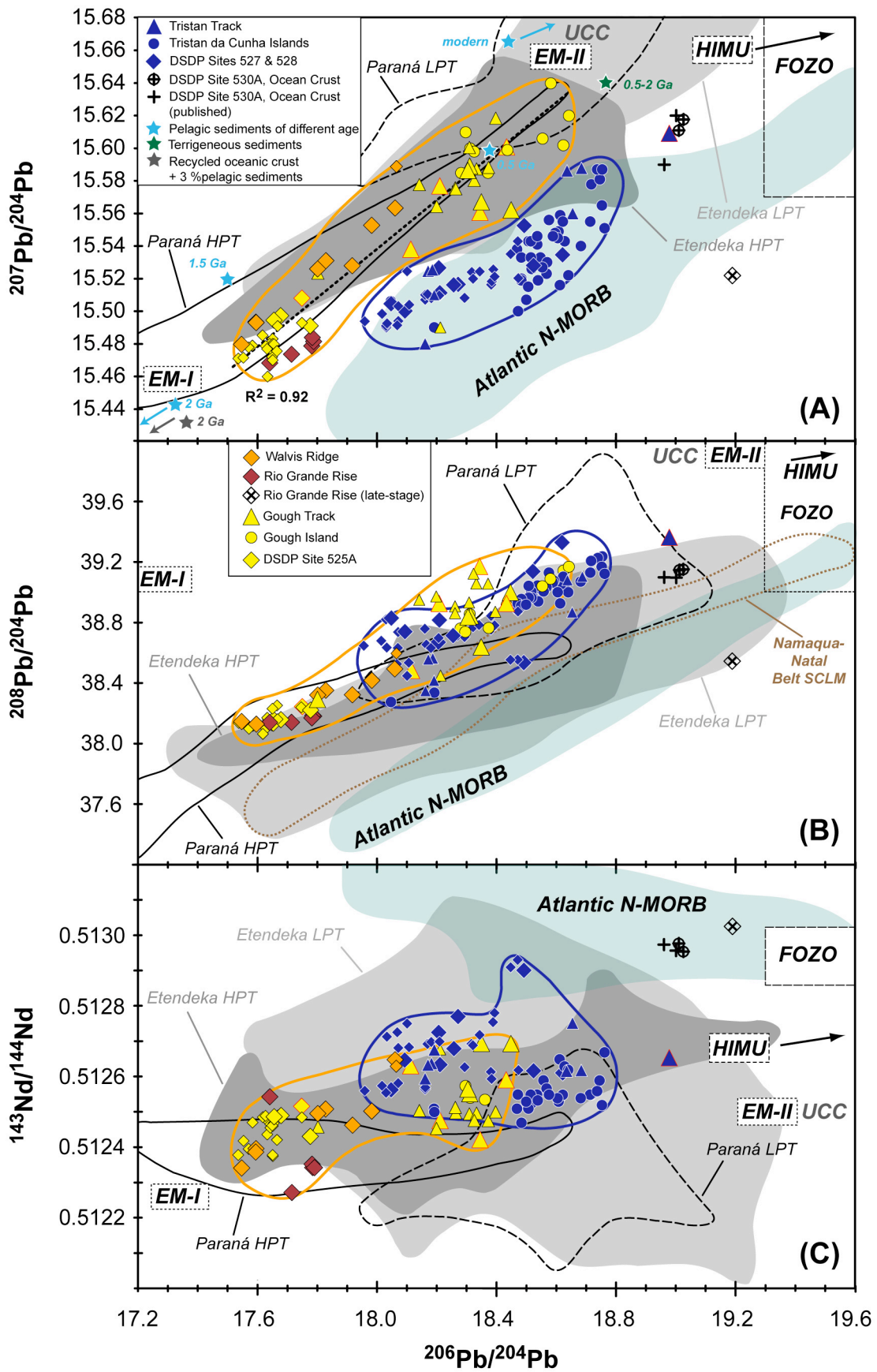


Fig. 3.6: Isotope variation diagrams for the Tristan-Gough hotspot track. Plots of (A) $^{206}\text{Pb}/^{204}\text{Pb}$ versus $^{207}\text{Pb}/^{204}\text{Pb}$, (B) $^{206}\text{Pb}/^{204}\text{Pb}$ versus $^{208}\text{Pb}/^{204}\text{Pb}$, (C) $^{206}\text{Pb}/^{204}\text{Pb}$ versus $^{143}\text{Nd}/^{144}\text{Nd}$, (D) $^{206}\text{Pb}/^{204}\text{Pb}$ versus $^{176}\text{Hf}/^{177}\text{Hf}$, (E) $^{206}\text{Pb}/^{204}\text{Pb}$ versus $^{87}\text{Sr}/^{86}\text{Sr}$, (F) $^{143}\text{Nd}/^{144}\text{Nd}$ versus $^{176}\text{Hf}/^{177}\text{Hf}$, (G) $^{87}\text{Sr}/^{86}\text{Sr}$ versus $^{143}\text{Nd}/^{144}\text{Nd}$ and (H) $^{87}\text{Sr}/^{86}\text{Sr}$ versus $^{176}\text{Hf}/^{177}\text{Hf}$. The diagrams include our isotope data from the Walvis Ridge, the Rio Grande Rise and the Guyot Province (represented by enlarged symbols). Evolved samples with $\text{MgO} < 1$ wt% are marked with a red border. The plots also include isotope data from the Guyot Province and the Walvis Ridge published by Rohde et al. (2013a) and published data from Tristan da Cunha and Gough island groups, the Tristan and Gough subtracks, from DSDP Sites 525A, 527, 528 and 530A and the Etendeka and Paraná CFBS compiled from GEOROC (<http://georoc.mpch-mainz.gwdg.de/georoc/>). These data are denoted with the same symbols but smaller in size. Data of Namaqua-Natal Belt SCLM from Class and Le Roex (2011). Data of the Rio Apa-Luis-Alves craton and Brasilia belt and São Francisco craton SCLM are from Gibson et al. (2005) are not shown due to purposes of visualization. Fields for FOZO and HIMU after Stracke et al. (2005) as well as EM-I and EM-II after Stracke et al. (2003) are also shown. Data from Atlantic N-MORB are compiled from the PetDB database (<http://www.petdb.org/>). There is no data for the dashed field next to the Atlantic N-MORB field in the $^{206}\text{Pb}/^{204}\text{Pb}$ versus $^{176}\text{Hf}/^{177}\text{Hf}$ diagram, but the size is estimated based on the $^{206}\text{Pb}/^{204}\text{Pb}$ versus $^{143}\text{Nd}/^{144}\text{Nd}$ and $^{143}\text{Nd}/^{144}\text{Nd}$ versus $^{176}\text{Hf}/^{177}\text{Hf}$ isotope diagrams. 2σ error for the samples analyzed in this study is equal or smaller than the symbol size. (A): Equation for best-fit correlation and correlation coefficient (R^2) for the Gough isotopic domain is displayed. Sample RC11-2RD #1 from the Rio Grande Rise is from the same dredge as the late-stage sample of Rohde et al. (2013b) and is therefore also considered to belong to the late-stage volcanic phase. It is not shown on the $^{87}\text{Sr}/^{86}\text{Sr}$ versus $^{143}\text{Nd}/^{144}\text{Nd}$ plot due to the low $^{87}\text{Sr}/^{86}\text{Sr}$ values. Samples DSDP Leg 74 527 39 1W 52-70 and AII-93-19-4 (late-stage sample; see Rohde et al., 2013b) exhibit higher $^{206}\text{Pb}/^{204}\text{Pb}$ values than the majority of the samples from DSDP Sites 527 and 528 and the Walvis Ridge, respectively, which we believe to result from U uptake during alteration on the seafloor and subsequent ingrowth of radiogenic Pb. Therefore these samples are not shown on the $^{206}\text{Pb}/^{204}\text{Pb}$ diagrams. The samples from DSDP Site 530A were recovered from the seafloor ~20 km north of the Walvis Ridge in the Angola Basin and are therefore not included in one of the Tristan-Gough isotopic domains. The MORB-like isotopic signatures of these samples are consistent with these samples being derived from spreading ridge type ocean crust of the Angola Basin.

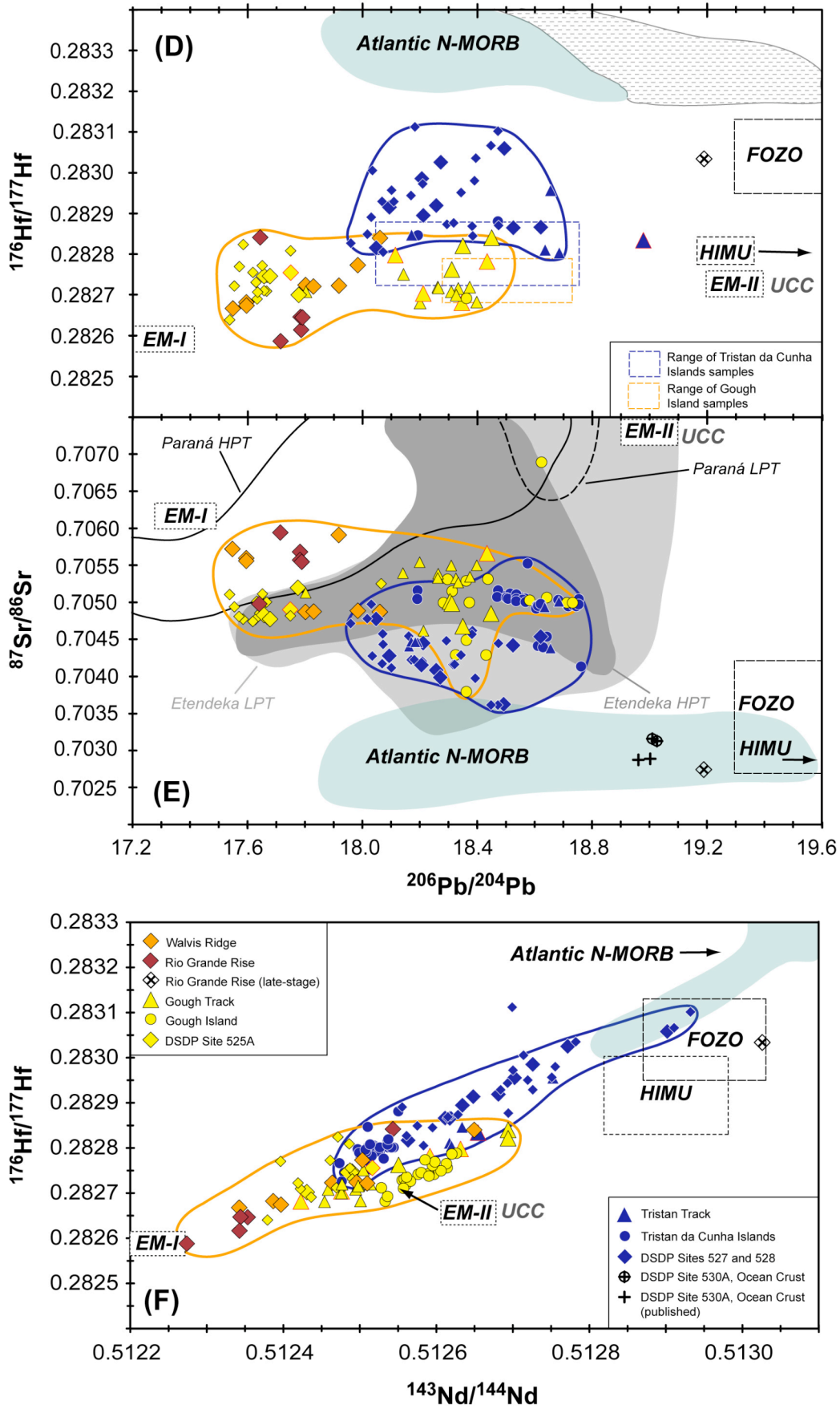


Fig. 3.6 (continued)

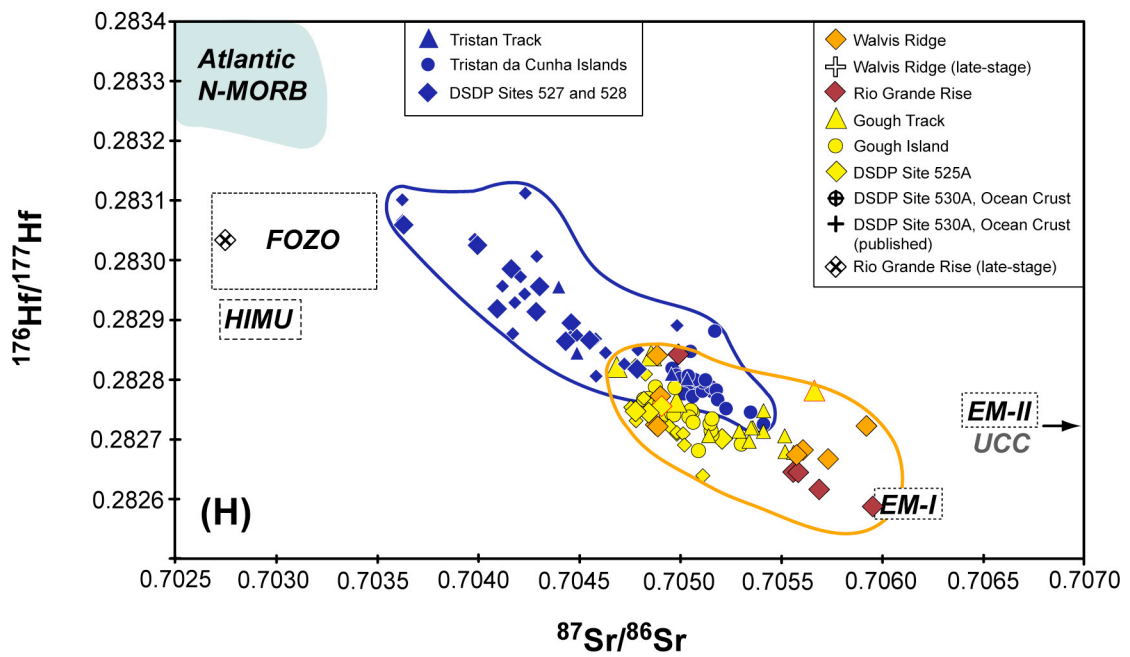
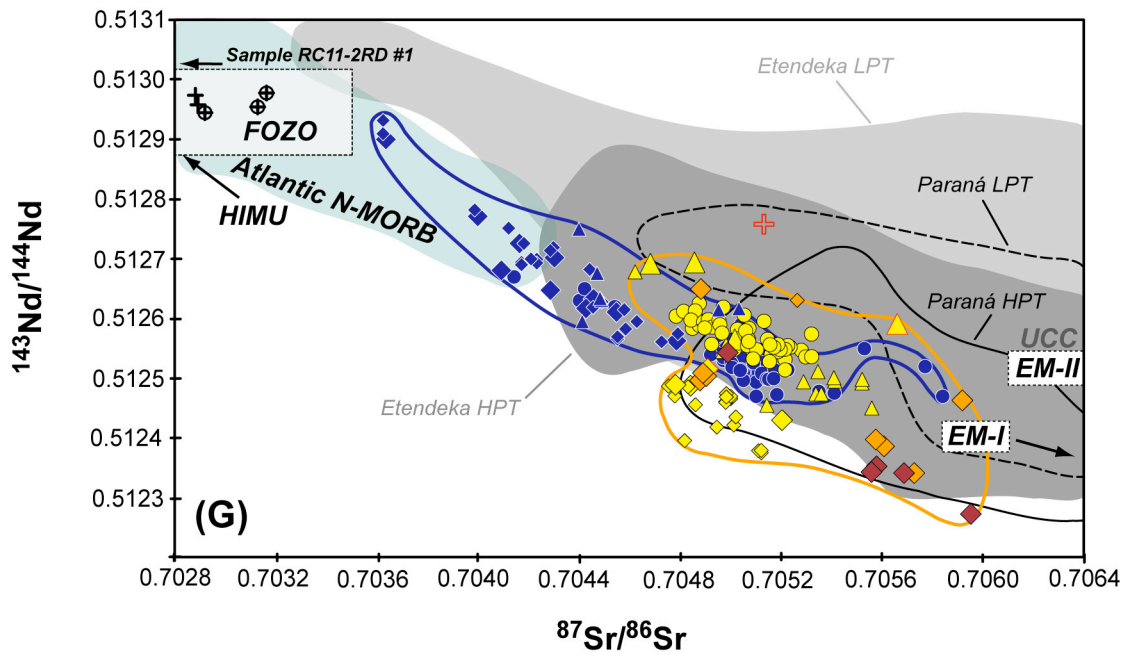


Fig. 3.6 (continued)

5. Discussion

5.1. Compositional variations along the Tristan-Gough hotspot track

5.1.1. Variations in geochemistry associated with the change from a ridge-centered to an intraplate hotspot

Systematic differences in the major and trace element compositions of the Tristan-Gough volcanic track can be observed on the African Plate (Walvis Ridge and Guyot Province). As noted above, the samples from the Walvis Ridge overall have more silica-saturated (including tholeiitic) compositions compared to the samples from the Guyot Province, which are silica-undersaturated, ranging from alkali basalt to basanite to trachyte. Whereas the Walvis Ridge rocks have low $(\text{Sm}/\text{Yb})_{\text{N}}$ and $(\text{Tb}/\text{Yb})_{\text{N}}$ and low $(\text{La}/\text{Sm})_{\text{N}}$ each of these ratios increase to the Tristan and Gough island groups from 55-60 Ma onwards (Fig. 3.4 and 3.5). The Walvis Ridge formed when the Tristan-Gough plume stem was located beneath the MAR. The greater extrusive volume and the major and trace element contents of the Walvis Ridge basalts compared to the Guyot Province rocks are consistent with higher degrees of melting (generating low $(\text{La}/\text{Sm})_{\text{N}}$) to shallower depths (high SiO_2 and low $(\text{Sm}/\text{Yb})_{\text{N}}$ and $(\text{Tb}/\text{Yb})_{\text{N}}$) producing larger amounts of melt as a result of plume-ridge interaction. In contrast to the Walvis Ridge (≥ 60 Ma), the Guyot Province (< 60 Ma) was formed in an intraplate setting. The change in morphology to smaller discrete ridges and seamounts, as well as the major and trace element compositions of the samples, indicate lower degrees of melting (high $(\text{La}/\text{Sm})_{\text{N}}$) at deeper average depths (low SiO_2 and high $(\text{Sm}/\text{Yb})_{\text{N}}$ and $(\text{Tb}/\text{Yb})_{\text{N}}$) generating lower volumes of melt, consistent with upwelling plume material being inhibited by a progressively thickening lithospheric cap (“lid effect”; Niu et al., 2011) as the MAR drifts westwards away from the hotspot. As shown above, the Rio Grande Rise samples have more alkalic compositions than the Walvis Ridge samples, exhibit steeper REE patterns and extend to higher moderately incompatible trace element abundances and ratios (Fig. 3.2 and 3.3). This may reflect the fact that the sampled part of the Rio Grande Rise was formed on thicker lithosphere further from the MAR.

The Gough subtrack is generally located on older lithosphere at a given distance along the hotspot track than the Tristan subtrack with a maximum difference at Gough and Tristan da Cunha island groups. In accordance with the “lid effect” model (Niu et al., 2011), the Gough subtrack volcanic rocks should have higher $(La/Sm)_N$ and $(Sm/Yb)_N$ ratios at a given part of the hotspot track compared to the Tristan subtrack rocks, but the two subtracks display similar incompatible element characteristics (Rohde et al., 2013a). As shown in Fig. 3.5, the $(La/Sm)_N$ ratios of both subtracks and the $(Sm/Yb)_N$ ratios of Gough and Tristan da Cunha Islands overlap (see also Appendix IIIb; Willbold and Stracke, 2006). In addition, the Tristan data extends to the highest values for $(La/Sm)_N$, opposite of what is expected. Therefore, the difference in lid thickness between the Gough and Tristan subtracks does not appear to cause systematic differences in the major and trace element geochemistry. To the contrary, the isotopic compositions of the Tristan and Gough subtracks are distinct on the uraniumogenic Pb isotope diagram over the last 70 Ma (Rohde et al., 2013a). On a plot of age versus $\Delta 7/4Pb$ (Fig. 3.5C), the $\Delta 7/4Pb$ remains constant for both subtracks. In conclusion, although the lid (lithospheric) thickness influences the major and trace element compositions, it cannot explain the differences in the isotopic composition of the two domains and the isotopic differences are the result of a chemically heterogeneous plume (Rohde et al., 2013a). The Tristan-Gough hotspot track shows bilateral, asymmetric zoning over the last 70 Ma, from the SW end of the Walvis Ridge through the Guyot Province to Tristan da Cunha and Gough island groups (Rohde et al., 2013a). The major purpose of this study was to see if the geochemical zonation can be traced through the earlier stages of plume stem evolution (i.e. ~70-114 Ma). Our new Sr-Nd-Pb-Hf data from the Guyot Province, the Walvis Ridge and the Rio Grande Rise provide new constraints on the long-term evolution of the Tristan-Gough plume system and on the composition and origin of the plume material older than 70 Ma. The nine newly analyzed, primarily evolved samples from the Gough subtrack, one sample from the Tristan subtrack and the samples from DSDP Sites 525A, 527 and 528 lie within their respective Gough and Tristan domains and thus confirm the bilateral zonation of the Tristan-Gough plume during the last 70 Ma years (Fig. 3.6). In contrast to the younger history of the hotspot, samples from the older (~70-114 Ma) part of the volcanic track (Walvis Ridge and Rio Grande Rise) do not show a geographic separation into the Tristan and Gough isotopic domains but instead they all have Gough-like isotopic signatures.

Since the plume was located beneath the MAR during prior to 60 Ma, we are surprised to find no geochemical evidence for Gough material interacting with the upper mantle, shifting Gough-type compositions towards the Atlantic N-MORB field.

As noted above, a change in major element composition and incompatible element ratios correlates with a change in morphology of the hotspot track from the more voluminous and continuous Walvis Ridge to the lower volume and more diffuse Guyot Province. A compositional difference also exists in isotopic composition between the Walvis Ridge and Guyot Province samples, which is most clearly seen in Pb isotopic composition. The Walvis Ridge (and Rio Grande Rise) samples have low $^{206}\text{Pb}/^{204}\text{Pb}$ (< 18.1), whereas the Guyot Province samples including Gough Island have high $^{206}\text{Pb}/^{204}\text{Pb}$ (> 18.1) with only one exception. The same general compositional shift can be seen in the Tristan domain data between 55 and 60 Ma ago, with Site 527 and 528 samples from the SW end of the Walvis Ridge (with ages of 58-67 Ma) having less radiogenic Pb than the Guyot Province samples (< 55 Ma). In conclusion, there is clear evidence for a change in composition coinciding with changes in morphology at ~ 55 -60 Ma (and ~ 10 -15 Ma after the beginning of plume zoning).

Our new results show that some samples from the oldest, northeastern part of the Walvis Ridge (~ 113 -114 Ma; Rohde et al., 2013b) and samples from the Rio Grande Rise, as well as some samples from the Paraná and Etendeka CFBs, have enriched EM-I-type compositions similar to the Site 525A samples, indicating that this type of enriched material was present both in the initial plume head stage and throughout the subsequent evolution of the Tristan-Gough plume to ≤ 70 Ma (Rohde et al., 2013b). Interestingly such enriched (EM-type) compositions have only been found while the plume was located beneath the MAR but have not been found thereafter in the Guyot Province during the youngest (< 60 Ma) history of the Tristan-Gough hotspot thus far. Therefore, the enriched continental-like compositions could reflect recycling of lower crust or lithospheric mantle at the spreading center that was delaminated or thermally eroded during Gondwana breakup (e.g. Hawkesworth et al., 1986). If the Walvis Ridge and Rio Grande Rise were formed through plume-ridge interaction, then recycled continental lithosphere must have dominated the composition of the lavas for ~ 70 Ma, masking the composition of the plume forming the flood basalts and the Tristan-Gough volcanic track. It is, however, difficult to explain spatial geochemical zonation of a hotspot track formed largely in an intraplate

setting over ~ 70 Ma (Rohde et al., 2013a) with shallow recycling of delaminated subcontinental lithosphere. Furthermore, based on geodynamic considerations, Class and Le Roex (2011) argued that African SCLM was most likely to be the source of the EM components of the hotspots in the South Atlantic, if it was derived from delamination of continental lithosphere during the break-up of Africa and South America. Class and Le Roex went on to show that African SCLM, however, does not have the appropriate isotopic composition, in particular on the thorogenic Pb isotope diagram, to be the source for the enriched rocks of the Gough subtrack, including DSDP site 525A (Fig. 3.6B). Therefore, shallow recycling of continental lithosphere does not appear to be the origin of either the pre- or post-60 Ma Gough signature since ~ 115 Ma. We believe that the chemical heterogeneity within the Tristan-Gough plume, both the Tristan and Gough compositions and the temporal variation within the Gough field, most likely reflects a chemically heterogeneous plume (see also Rohde et al., 2013a).

According to Gibson et al. (2005), variations in incompatible trace element composition and isotopic composition cannot be related to changes in lithospheric thickness and therefore to different degrees of partial melting to different depths. Instead, they argue that geochemical variations can be explained by the entrainment of compositionally variable mantle material into the plume. Gibson et al. (2005) suggested that the isotopic composition of the Tristan-Gough plume changed from a more EM-I-like to a more FOZO-like composition during its younger history. Although the compositional change at 55-60 Ma in both Gough and Tristan domain could have been related to a change in the composition of the upwelling plume material, the changes in major and trace element and Sr-Nd-Pb-Hf isotope chemistry correlate with the change from the MAR being located above the plume to an intraplate setting for the plume beneath the African Plate, suggesting that the “lid effect” may also be responsible for the change in chemistry of the two domain compositions. We will present a model below that can explain the observed temporal variations in geochemistry to variations in the thickness of the overlying lithosphere.

5.1.2. Are both Tristan and Gough components present in the plume head stage (Paraná and Etendeka flood basalts)?

We now evaluate the initial stage of the Tristan-Gough plume volcanism that formed the Paraná and Etendeka CFBs. We will begin by taking a look at the composition of the Paraná flood basalts. On the uraniumogenic Pb isotope diagram (Fig. 3.6A), the Paraná flood basalts overlap most of the Gough domain field. It has been argued by some that the elevated $^{207}\text{Pb}/^{204}\text{Pb}$ of the Paraná and Etendeka flood basalts reflects assimilation of continental crust (e.g. Ewart et al., 1998; Thompson et al., 2001). Since <70 Ma old lavas from the hotspot track (end of Walvis Ridge to active volcanic islands) clearly erupted on oceanic crust and cover much of the field for the flood basalts, it is tempting to argue that the high $\Delta 7/4\text{Pb}$ and $^{207}\text{Pb}/^{204}\text{Pb}$ of the plume head lavas is likely to reflect a source characteristic rather than continental crustal assimilation. Nevertheless, when we also take major and trace element compositions of the flood basalts into account in conjunction with their isotopic compositions, the Paraná basalts can be divided into high P_2O_5 and TiO_2 (HPT), with similar contents to ocean island basalts (OIB), and low P_2O_5 and TiO_2 (LPT) groups (e.g. Hawkesworth et al., 1986). The HPT group rocks consist primarily of basaltic rocks with low SiO_2 and relatively high MgO , whereas the LPT group ranges from basalts to rhyolites. The HPT group has high Ba/Nb , relatively unradiogenic Pb and Sr but radiogenic Nd isotopic compositions, compared to the LPT group (Fig. 3.6). The LPT group rocks also show a striking increase in Sr isotope ratios with increasing degree of differentiation (Mantovani et al., 1985). The LPT rocks therefore appear to have undergone upper crustal assimilation during shallow level fractionation.

On the $^{206}\text{Pb}/^{204}\text{Pb}$ versus $^{87}\text{Sr}/^{86}\text{Sr}$ and $^{143}\text{Nd}/^{144}\text{Nd}$ isotope correlation diagrams, the Gough domain field forms correlations extending from an EM-I-like component, characterized by radiogenic $^{207}\text{Pb}/^{204}\text{Pb}$, $^{208}\text{Pb}/^{204}\text{Pb}$ and $^{87}\text{Sr}/^{86}\text{Sr}$ but unradiogenic $^{206}\text{Pb}/^{204}\text{Pb}$, $^{143}\text{Nd}/^{144}\text{Nd}$ and $^{176}\text{Hf}/^{177}\text{Hf}$ isotope ratios, towards the radiogenic end of the N-MORB field or towards FOZO and/or HIMU. The Paraná field overlaps the EM-I-like end of the Gough array, specifically Walvis and Rio Grande Rise samples, but does not overlap the end of the Gough array with more radiogenic Pb, composed of the Guyot Province and Gough Island samples. Instead, the Paraná field trends towards more radiogenic Sr and less radiogenic Nd with more radiogenic Pb isotopic composition, or towards an enriched EM-II-type component. On the $^{87}\text{Sr}/^{86}\text{Sr}$ versus $^{143}\text{Nd}/^{144}\text{Nd}$ isotope

correlation diagram, the Paraná field overlaps the Gough domain field and also extends towards EM-II. On the thorogenic Pb isotope diagram, the Paraná basalts overlap the >60 Ma part of the Gough field, but fall below most of the <60 Ma part of the array. On the uranogenic Pb isotope diagram, the Paraná basalts also extend from the EM-I end of the Gough field towards an EM-II-type component, even though they also overlap much of the Gough field. These differences may reflect a different range in isotopic composition in the plume head than during the plume tail stage, but it is more likely that the deviation from the Gough domain field reflects interaction with EM-II-type material in the continental lithosphere, either in the upper crust or lithospheric mantle. Since the Rio Apa-Luis Alves, Brasilia Belt and São Francisco Craton SCLM do not form the appropriate endmember to explain Paraná samples with more radiogenic Pb (see Gibson et al., 2005), the upper crust is the most likely source of potential contamination to explain the trend to EM-II-like compositions.

Interestingly, the Etendeka flood basalt field is more extensive than that for the Paraná basalts. On the $^{206}\text{Pb}/^{204}\text{Pb}$ versus $^{87}\text{Sr}/^{86}\text{Sr}$ and $^{143}\text{Nd}/^{144}\text{Nd}$ and on the $^{87}\text{Sr}/^{86}\text{Sr}$ versus $^{143}\text{Nd}/^{144}\text{Nd}$ isotope diagrams, the Etendeka field covers most or all of the Tristan field and extends beyond Tristan into the N-MORB field. Furthermore, it covers some of the Gough field (mainly Guyot Province and Gough Island) on the $^{206}\text{Pb}/^{204}\text{Pb}$ versus $^{87}\text{Sr}/^{86}\text{Sr}$ diagram and almost the entire Gough field on the $^{206}\text{Pb}/^{204}\text{Pb}$ versus $^{143}\text{Nd}/^{144}\text{Nd}$ and the $^{87}\text{Sr}/^{86}\text{Sr}$ versus $^{143}\text{Nd}/^{144}\text{Nd}$ diagrams. Similar to the Paraná basalt field, Etendeka also extends towards the EM-II-type component. Although there is some Hf isotope data available from the Etendeka basalts, it is not available for the full range of Nd isotope data, but based on the available data, the relationship between Nd and Hf isotopes is consistent with the $^{87}\text{Sr}/^{86}\text{Sr}$ versus $^{143}\text{Nd}/^{144}\text{Nd}$ and $^{206}\text{Pb}/^{204}\text{Pb}$ versus $^{87}\text{Sr}/^{86}\text{Sr}$ and $^{143}\text{Nd}/^{144}\text{Nd}$ isotope diagrams. On the uranogenic and thorogenic Pb isotope diagrams, the Etendeka field overlaps most of the Gough field, extending to lower $\Delta 7/4\text{Pb}$ and $\Delta 8/4\text{Pb}$ than the Paraná field. On the thorogenic Pb isotope diagram, the Etendeka field overlaps the Tristan field and extends into the Atlantic N-MORB field. In summary, the Etendeka data is distinct from the Paraná data in that it requires a Tristan-type component in addition to an influence by the Gough component. If the trend to an EM-II-type of component also reflects lithospheric interaction as suggested above for the Paraná melts, then the Etendeka flood basalts could have been derived from a mixture of Gough- and Tristan-type of plume

components, whereas the Paraná flood basalts could be derived from a Walvis Ridge/Rio Grande Rise (>60 Ma hotspot track) type of Gough plume component.

5.2. Origin of the Gough and Tristan components

The entire volcanic evolution of the Tristan-Gough hotspot track can be explained by the presence of two distinct geochemical reservoirs (Gough and Tristan) in the plume. Rohde et al. (2013a) proposed that the Gough domain reflected the composition of the African LLSVP at the core-mantle boundary and that the Tristan domain represented the ambient depleted mantle around the African LLSVP or a mix between LLSVP and the surrounding ambient mantle. It is, however, important to evaluate if it would not simply be possible to mix Gough-type of composition with Atlantic N-MORB to derive the Tristan domain.

Volcanic rocks from the Tristan domain have compositions plotting between the Gough domain samples and Atlantic N-MORB field on most diagrams, e.g. on the uraniumogenic Pb isotope diagram, $^{206}\text{Pb}/^{204}\text{Pb}$ versus Sr, Nd, Hf, Nd versus Hf, and Sr versus Nd and Hf isotope diagrams (Fig. 3.6). On the thorogenic Pb isotope diagram, however, the Tristan domain falls almost completely within the Gough domain field. Since the Tristan samples on the thorogenic Pb isotope diagram are not shifted towards the N-MORB field, as is the case on the uraniumogenic Pb isotope diagram, mixing of Gough domain material with Atlantic N-MORB cannot generate the Tristan composition providing additional evidence that the Tristan domain composition is not generated through interaction of (deep) Gough-type plume material with depleted upper MORB-source mantle. Since no appropriate source material has been identified thus far in either the South Atlantic or from southern Africa or South America that fits the Tristan domain lavas, such material appears absent in the upper mantle or crust, suggesting that this material was transported within the plume from the lower mantle to the base of the African lithosphere. The Gough domain forms arrays on the isotope correlation diagrams that require the presence of at least two endmembers: 1) an EM-I-type of component with unradiogenic $^{206}\text{Pb}/^{204}\text{Pb}$ but $^{207}\text{Pb}/^{204}\text{Pb}$ and $^{208}\text{Pb}/^{204}\text{Pb}$ elevated above N-MORB with similar $^{206}\text{Pb}/^{204}\text{Pb}$ and with radiogenic Sr but unradiogenic Nd and Hf isotopic

compositions, and 2) a FOZO/HIMU-type component \pm EM-II with radiogenic Pb, Nd and Hf but relatively unradiogenic Sr isotopic composition (Fig. 3.6).

Several models have been suggested for the origin of the geochemical signatures of EM. These models involve deep origins for this enriched mantle anomaly (Castillo, 1988; Class and Le Roex, 2011; Stracke, 2012), shallow recycling of SCLM (e.g., Hawkesworth et al., 1986; Hoernle et al. 1991; Bizzi et al., 1995; Milner and Le Roex, 1996; Gibson et al., 2005; Geldmacher et al., 2008; Hoernle et al., 2011) or metasomatic processes (e.g., Salters and Sachi-Kocher, 2010), such as deeply recycled metasomatized oceanic lithosphere (Niu and O'Hara, 2003), intramantle metasomatism of peridotite with indirect or without involvement of sediments (Eiler et al., 1995) or derivation by introduction of small-volume melts and metasomatic fluids to an E-MORB source (Richardson et al., 1982). Proposed models for the origin of EM also include contributions by (lower) crustal material to the mantle (Tatsumi, 2000; Escrig et al., 2004; 2005; Hanan et al., 2004; Willbold and Stracke, 2006; 2010; Stracke, 2012), the formation from the residuum after melt extraction from primitive mantle (Roden et al., 1994), the involvement of recycled ancient pelagic sediments (Weaver et al., 1986) and the involvement of recycled oceanic crust including ancient pelagic or terrigenous sediments (White, 1985; Weaver, 1991).

Rohde et al. (2013a) proposed a deep (lower mantle) origin of the Gough source. They concluded it e.g. from the fact that it is difficult to derive a spatially zoned hotspot track of \sim 1700 km length, cutting fracture zones in the seafloor, through the shallow interaction of a plume with continental material. Furthermore, they noted that the African lithosphere, which was most likely located beneath the formation area of the Tristan-Gough basalts (Class and Le Roex, 2011), does not have the appropriate composition to account for the Gough isotopic signature. This is also inconsistent with a shallow origin. Instead, they interpret the Gough source to be derived from deep recycling of continental lithosphere beneath Brazil and Paraguay (lower crust and/or metasomatized mantle).

The second endmember has a FOZO/HIMU-type composition \pm EM-II. Although it has been proposed that FOZO could represent the composition of the lower mantle (Hart et al., 1992), more recently the first author favors an origin of FOZO through the recycling of oceanic crust (Stracke et al., 2005), as has also been proposed for the HIMU component with more radiogenic Pb isotopic compositions (e.g. Zindler and Hart, 1986). EM-II-type compositions can either reflect upper continental crust or recycled marine (pelagic)

sediments (Fig. 3.6A). Ancient pelagic sediments (0.5-2 Ga; Chauvel et al., 1992) would have the appropriate composition to contribute to the Gough isotopic signature (Fig. 3.6A) as also suggested by Weaver et al. (1986). Taken together this endmember is likely to reflect recycled oceanic crust including ancient pelagic sediments (e.g., Weaver, 1991; Chauvel et al., 1992). The enrichment in Ba relative to other LILE, expressed e.g. by high Ba/Th or Ba/La ratios, that can be observed for the Tristan-Gough samples, are also typical for pelagic sediments (Weaver, 1991). Therefore, the Gough array most likely reflects mixing of EM-I (lower crust, SCLM) and FOZO/HIMU (subducted oceanic crust) with a minor contribution of the EM-II component (marine sediments). A possible mechanism to explain the isotopic composition of the Gough source is subduction erosion or subduction-induced delamination of lower crust and SCLM (EM-I) (Kay and Kay, 1993; Kay et al., 1994; 2005) that sunk into the lower mantle, where it mixed with subducted oceanic crust (FOZO) including a certain amount of sediments (EM). Addition of basaltic melts converted to eclogite or pyroxene + garnet cumulates to the SCLM could have increased the density (Griffin et al., 2003; Schutt and Leshner, 2010) sufficiently to cause it to sink into the lower mantle. Or it may even have been dragged down by subducting oceanic crust.

The Tristan domain also forms arrays on the isotope correlation diagrams that are consistent with two component mixing of: 1) EM-I-type component with unradiogenic $^{206}\text{Pb}/^{204}\text{Pb}$ but $^{207}\text{Pb}/^{204}\text{Pb}$ and $^{208}\text{Pb}/^{204}\text{Pb}$ elevated above N-MORB with similar $^{206}\text{Pb}/^{204}\text{Pb}$ and with radiogenic Sr but unradiogenic Nd and Hf isotope ratios, and 2) FOZO/HIMU \pm EM-II-type mixed component with radiogenic Pb, Nd and Hf but relatively unradiogenic Sr isotope ratios. The EM-I-type component could be the same as or similar to the one required for the Gough component, but the FOZO/HIMU-type endmember contains less or no EM-II-type material.

Above we pointed out that the change from EM-I- to FOZO/HIMU \pm EM-II-type compositions between 55-60 Ma occurred at the same time as the change from a ridge-centered to an intraplate hotspot system and therefore that the lid affect may have played a role in the change in composition of the Gough, as well as the Tristan, domain. Assuming that both, the Gough and Tristan domains in the plume are heterogeneous, containing enriched plums (FOZO \pm EM-II, possibly young recycled oceanic crust, cf. Stracke et al. (2005), in the form of eclogite/garnet pyroxenite and marine sediments) within a more

refractory matrix (EM-I-type peridotitic material, e.g. SCLM), then at low degrees of melting under thicker lithosphere, the melts will preferentially sample the enriched plums of eclogite/pyroxenite with FOZO \pm EM-II-type compositions, whereas at higher degrees of melting beneath the ridge the more refractory EM-I-type peridotite will preferentially be sampled. Therefore, the “lid effect” can explain the temporal changes in composition at 55-60 Ma in both the Gough and Tristan domains, but not the zonation of the plume (presence of Tristan and Gough domains) during the last 70 Ma (see Rohde et al., 2013a) and the presence of only the Gough domain throughout the early history of the plume stem.

To summarize, we propose that the Gough compositional range reflects deep recycling of EM-type continental lithosphere and FOZO-type oceanic crust and EM-type sediments that possibly subducted into the lower mantle and are rising to the surface at the boundary of the LLSVP via the Tristan-Gough mantle plume. The Tristan compositional domain, which appears at ca. 70 Ma on the northwest side of the hotspot track, was formed through entrainment of ambient depleted lower mantle into the northwest side of the plume, possibly followed by mixing with the enriched Gough component derived from the LLSVP. The presence of the Tristan-type composition in the Etendeka flood basalts proves that this component was present in the plume source from the start, but that it either was not sampled or that evidence of its presence was wiped out when the MAR was located above the plume and the plume was able to upwell and melt extensively to shallow depths.

5.3. Evolution of the Tristan-Gough volcanic system

Recently published $^{40}\text{Ar}/^{39}\text{Ar}$ ages (Rohde et al., 2013b) confirm a progression to younger ages from the Etendeka and Paraná CFBs to the Tristan da Cunha and Gough island groups (O’Connor and Duncan, 1990; O’Connor and Le Roex, 1992), supporting the mantle plume hypothesis for the Tristan-Gough volcanic track. With the new isotopic and major and trace element data we can provide a continuous record of the Tristan-Gough mantle plume volcanism. In the following section we derive a geodynamic model for the evolution of the Tristan-Gough hotspot track.

Our new data suggest that the plume head contained both, the Gough and the Tristan components (Fig. 3.7A). Although there is no clear zonation observable, the Paraná and Etendeka CFB provinces both appear to have distinct isotopic compositions. The

Paraná CFBs are influenced by a Walvis Ridge/Rio Grande Rise (>60 Ma hotspot track) type of Gough component, whereas the Etendeka CFBs show an influence of a Tristan-type component in addition to an influence by the Gough component. The earlier (>70-115 Ma) part of the hotspot track (Walvis Ridge and Rio Grande Rise), formed above the early and presumably larger-diameter and thus more productive plume tail (Fig. 3.7B), shows no evidence of the Tristan component. The first clear evidence for zonation is found in the ~70 Ma DSDP Sites 525A, 527 and 528 (Fig. 3.7C). DSDP Sites 527 and 528 exhibit the Tristan isotopic signature generated by the entrainment of surrounding more depleted lower mantle material into the northwestern side of the upwelling plume. Shortly after the occurrence of the Tristan domain, the plume track bifurcated, forming distinct ridge-like structures that cross-cut fracture zones obliquely, suggesting that the plume conduit split into two arms (Fig. 3.7D). This implies a connection between plume zonation and bifurcation. The different zones/filaments in the plume could have had different physical properties, e.g. viscosity and density. Several geophysical mantle models (e.g., Ishii and Tromp 1999; 2004) suggest that the LLSVPs in the deep mantle are denser than the surrounding mantle. As shown by Rohde et al. (2013a) and confirmed by our study, the Gough source is interpreted to reflect the pure LLSVP composition and the Tristan source represents a mixture of this Gough source with ambient depleted lower mantle material. Since the Tristan component is „diluted“, it is most likely less dense than the Gough source, implying that the two different zones/filaments in the Tristan-Gough plume have different viscosities. It is unlikely, however, that these, probably relatively minor, differences in physical properties may have been the cause for the bifurcation of the plume conduit. Three-dimensional numerical experiments for the geochemically zoned Hawaiian plume by Kundargi and Hall (2012) demonstrated that melting and dehydration of upwelling peridotite within a plume can result in the formation of a residuum in form of a viscous plug. Consequently, the melts distribute to both sides of this plug leading to the formation of two spatially separated volcanic tracks with distinct composition. This is also a conceivable model for the bifurcation of the Tristan-Gough plume, resulting in the Gough and Tristan material rising up on opposite sides of a viscous plug. In order, to generate the distance of 400 km between the island groups of Tristan da Cunha and Gough, the viscous plug would need to have a similar dimension. Finally, the transition from ridge-like structures to individual volcanic edifices, with overall wider spacing with

decreasing age, may reflect the break-up of the plume into strings of blobs or pulses (Fig. 3.7D), which may be the natural consequence of weakening plume tail dynamics (see also Rohde et al., 2013b).

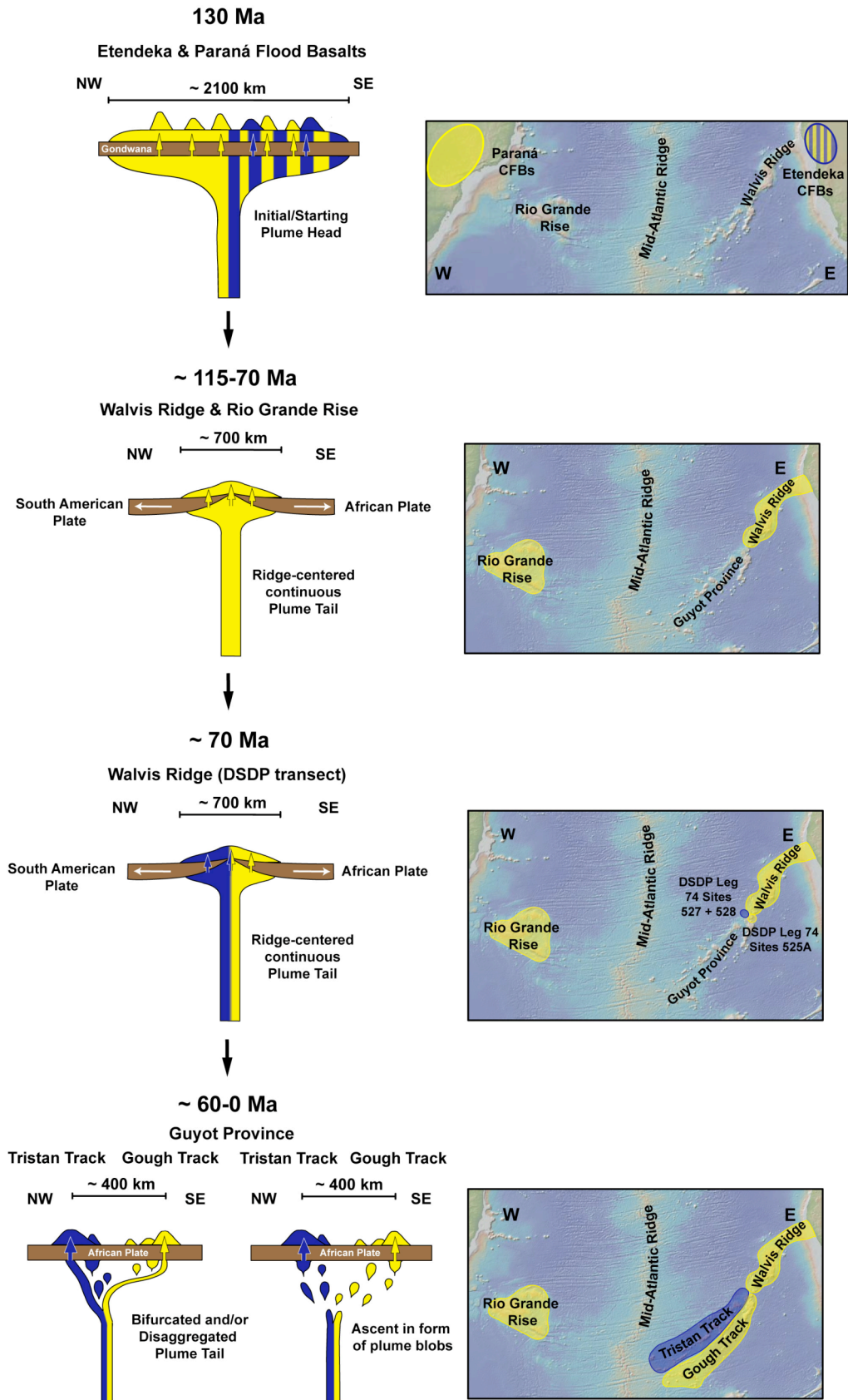


Fig. 3.7: Schematic model for the 130 Ma evolution of the Tristan-Gough hotspot track from the Etendeka/Paraná CFB provinces to the volcanically active island groups of Tristan da Cunha and Gough (modified after Rohde et al., 2013b). The zonation of the Guyot Province strikes northeast-southwest. Therefore the view is slightly oblique to the MAR. (A) ~130 Ma: The CFB provinces of Etendeka and Paraná

were generated by the initial Tristan-Gough plume head event. Although no zonation can be observed within the CFBs, the two different provinces are isotopically distinct. While the Paraná CFB province can be derived by a Walvis Ridge/Rio Grande Rise-type of Gough component, the Etendeka province can be derived by a mixture of Tristan- and Gough-type component. **(B)** ~115-70 Ma: The Walvis Ridge and the Rio Grande Rise originated from the early plume tail, when the MAR was located above a strong, productive plume conduit, directly after the plume head stage. The plume was not geochemically zoned during the Rio Grande Rise-Walvis Ridge stage. **(C)** The first clear evidence for zonation of the hotspot track and thus for the plume is found at DSDP Sites 525A, 527 and 528 (~70 Ma). ~70-60 Ma: The plume track bifurcated (at the time the Guyot Province began forming), suggesting a connection between plume zonation and bifurcation. **(D)** <~60 Ma: After the plume split, the Tristan arm formed a more pronounced and continuous subtrack. The more discontinuous nature of the Gough subtrack suggests that this plume arm was weaker and less stable. As the buoyancy flux decreased with age, the plume arms may eventually have broken up into strings of blobs, possibly the natural consequence of an aging and weakening zoned plume conduit.

5.4. Comparison of Tristan-Gough long-term history with that of Hawaii

The comparison of the long-term geochemical evolution of zoned hotspot tracks can provide insights into the cause and longevity of zonation in mantle plumes and offers the opportunity to identify at what stage of hotspot evolution zonation can appear and if there is a link between magmatic productivity and the onset of zonation.

The Hawaiian Islands consist of two parallel volcanic chains with distinct isotopic compositions (Kea and Loa trends; e.g., Abouchami et al., 2005; Weis et al., 2011). The compositional distinction, with the Loa component having higher $^{208}\text{Pb}/^{204}\text{Pb}$ at a given $^{206}\text{Pb}/^{204}\text{Pb}$, is thought to represent a geochemical zonation of the upwelling mantle plume and its source region (Abouchami et al., 2005; Kerr and Mériaux, 2004; Farnetani and Hofmann, 2009; 2010; Weis et al., 2011). Along the Hawaiian-Emperor hotspot chain the depleted Kea component can be traced through all the 80 Ma of hotspot evolution (Weis et al., 2011) and is even found in Kamchatka in 120-93 Ma old ophiolitic basalts believed to represent Emperor Seamounts accreted to the Kamchatkan forearc (Portnyagin et al., 2008). In contrast to the Kea component, the enriched Loa component can only be traced for 5 Ma (Weis et al., 2011). The Hawaiian plume rapidly migrated in a southward direction during 81-47 Ma forming the Emperor seamount chain (Tarduno et al., 2003). This rapid southward movement stopped at the hotspot track bend and before the formation of the Hawaiian seamount chain (<47 Ma; Tarduno et al., 2003). The first evidence for the enriched Loa component is found in 5 Ma old Hawaiian volcanic rocks, but since high-precision isotopic analyses are biased towards the last 5 Ma and the Emperor seamount chain (85-42 Ma) (Weis et al., 2011), the Loa component might also be found in 5-42 Ma

old Hawaiian seamounts (see also Portnyagin et al., 2008). The strong increase in Hawaiian hotspot activity during the last 30 Ma (Vidal and Bonneville, 2004) may indicate that increased eruption rates are associated with tapping the enriched component as a result of the plume moving into the LLSVP and tapping it at around 30 Ma. This means that the enriched LLSVP (presumably represented by the Loa component) might not be tapped in the early phase of the hotspot evolution. Consequently, since the Hawaiian plume may have been located north of the LLSVP during the early stages of its evolution, this might be the reason that no flood basalt province related to the initiation of the Hawaiian plume has been found thus far.

In contrast, the Tristan-Gough plume began with a flood basalt event, which we propose tapped the African LLSVP. In the case of the Tristan-Gough plume, the magma production rate decreased during hotspot evolution (White, 1993), which becomes obvious by the change from the voluminous Walvis Ridge to the diffuse Guyot Province. Consequently, there may be a connection between eruptive volumes and tapping of the LLSVP for both hotspots. We propose that the Hawaiian plume originally did not sample the Pacific LLSVP, but only began to do so sometime between 42-5 Ma, which was accompanied by an increase in the volume of eruptives. In contrast to Hawaii, the Tristan-Gough plume tapped the African LLSVP at the beginning of its history and thus was associated with a large, enriched plume head. As the plume stem weakened throughout the evolution of the hotspot, the Tristan reservoir began to play a more dominant role after ~70 Ma during the waning stages of the plume.

Castillo (1988) pointed out that there is a correlation between LLSVPs in the deep mantle and the enriched isotopic anomaly in the southern hemisphere, termed DUPAL anomaly by Hart (1984). Our samples exhibit this enriched EM-/DUPAL-type isotopic signature expressed by elevated $\Delta 7/4\text{Pb}$ values. In contrast to the Tristan-Gough hotspot, the enriched signature of the zoned Pacific hotspots is expressed by elevated $\Delta 8/4\text{Pb}$. Furthermore, both groups of zoned hotspots are characterized by relatively unradiogenic Nd. This suggests that the LLSVPs contain enriched EM-/DUPAL-type material with either elevated $\Delta 7/4\text{Pb}$ (Tristan-Gough) or elevated $\Delta 8/4\text{Pb}$ (Pacific zoned hotspots) values. Our isotopic Tristan-Gough data supports the connection between LLSVPs and the DUPAL geochemical anomaly.

6. Conclusion

To summarize, our new isotope and major and trace element data provide new constraints on the long-term evolution of the Tristan-Gough hotspot track between 70-132 Ma and on the origin and geochemical characteristics of the mantle sources contributing to the Tristan-Gough hotspot volcanism older than 70 Ma. In contrast to the bilateral long-term zonation of the Guyot Province (Rohde et al., 2013a), the Walvis Ridge and the Rio Grande Rise only exhibit enriched Gough-type isotopic compositions demonstrating that the Gough domain is the dominating mantle source in the early plume-tail stage. Although the Etendeka and Paraná CFBs, thought to represent the plume head stage, show the influence of lithospheric interaction, the Gough component can be recognized in both the Paraná and Etendeka flood basalts and the Tristan component also in the Etendeka flood basalts, indicating that both types of material were present in the plume source at the initiation of the plume. DSDP Site 525A has so far been the South Atlantic type locality for the EM-I endmember. Basalts from other parts of the Walvis Ridge and Rio Grande Rise, as well as the flood basalts, have similarly extreme compositions, indicating that the extreme EM-I-type composition at Site 525A is not only a local component sampled by the plume, but a major component in the Tristan-Gough plume. Our results confirm the lower mantle origin for the Tristan and Gough domains with the Gough component reflecting the composition of the African LLSVP and the Tristan component the surrounding depleted ambient lower mantle. The geochemical composition of the Gough domain can be derived through mixing of EM-I-type component (e.g., SCLM peridotite) (Rohde et al., 2013a) with FOZO-type component (subducted oceanic crust as eclogite) and a minor contribution of EM-II-type sediments. Subduction-induced delamination or subduction erosion and subsequent sinking of the removed SCLM into the lower mantle and mixing with subducted oceanic crust, or coupling between subducting oceanic lithosphere with delaminated/eroded SCLM, can explain the composition of the Gough domain, suggesting the presence of both continental and oceanic lithosphere in the African LLSVP (see also Rohde et al., 2013a). Since large sampling gaps of several hundreds of km exist along the Walvis Ridge and the Rio Grande Rise is very sparsely sampled, further sampling of these areas is needed to better define the mantle source characteristics of the early plume tail stage of the Tristan-Gough hotspot track.

A comparison with the zoned Hawaiian hotspot track reveals very different histories of evolution for mantle plumes. Although both zoned plumes are located above the margins of the African and Pacific LLSVPs, the onset of zonation can occur during different stages of plume evolution. Finally, tapping of the enriched LLSVP might be connected to elevated magma production rates.

Acknowledgments

This study was funded by the Deutsche Forschungsgemeinschaft (DFG) under grants HO 1833/17-1 and HO 1833/17-2 as part of the DFG Priority Program SPP 1375 “SAMPLE”. A special thank goes to Wilfried Jokat, Karsten Haase, Anton Le Roex, Roger Hekinian, Susan E. Humphris and John O’Connor for providing samples for this study. Stefan Jung, Jan Fietzke, Dieter Garbe-Schönberg, Silke Hauff, Ulrike Westernströer, Dagmar Rau and Petra Fiedler are thanked for their valuable analytical support.

References

- Abouchami, W., Hofmann, A.W., Galer, S.J.G., Frey, F.A., Eisele, J., and Feigenson, M., 2005, Lead isotopes reveal bilateral asymmetry and vertical continuity in the Hawaiian mantle plume: *Nature*, v. 434, p. 851-856, doi:10.1038/nature03402.
- Anderson, D.L., 2005, Scoring hotspots: the plume and plate paradigms, *in* Foulger, G.R., Natland, J.H., Presnall, D.C., and Anderson, D.L., eds., *Plates, Plumes, and Paradigms: Geological Society of America Special Paper 388*, p. 31-54.
- Baksi, A.K., 1999, Reevaluation of plate motion models based on hotspot tracks in the Atlantic and Indian Oceans: *Journal of Geology*, v. 107, p. 13-26.
- Baksi, A.K., 2007a, A quantitative tool for detecting alteration in undisturbed rocks and minerals - I: water, chemical weathering, and atmospheric argon, *in* Foulger, G.R., and Jurdy, D.M., eds., *Plates, Plumes and Planetary Processes: Geological Society of America Special Paper 430*, p. 285-303.
- Baksi, A.K., 2007b, A quantitative tool for detecting alteration in undisturbed rocks and minerals - II: application to argon ages related to hotspots, *in* Foulger, G.R., and Jurdy, D.M., eds., *Plates, Plumes and Planetary Processes: Geological Society of America Special Paper 430*, p. 305-333.
- Bizzi, L.A., De Wit, M.J., Smith, C.B., McDonald, I., and Armstrong, A., 1995, Heterogeneous enriched mantle materials and dupal-type magmatism along the SW margin of the São Francisco craton, Brazil: *Journal of Geodynamics*, v. 20, p. 469-491.
- Blichert-Toft, J., Chauvel, C., and Albarède, F., 1997, Separation of Hf and Lu for high-precision isotope analysis of rock samples by magnetic sector-multiple collector ICP-MS: *Contributions to Mineralogy and Petrology*, v. 127, p. 248-260.
- Castillo, P., 1988, The Dupal anomaly as a trace of the upwelling lower mantle: *Nature*,

v. 336, p. 667–670, doi:10.1038/336667a0.

Chauvel, C., Hofmann, A.W., and Vidal, P., 1992, HIMU-EM: The French Polynesian connection: *Earth and Planetary Science Letters*, v. 110, p. 99-119.

Chauvel, C., Maury, R.C., Blais, S., Lewin, E., Guillou, H., Guille, G., Rossi, P., and Gutscher, M.-A., 2012, The size of plume heterogeneities constrained by Marquesas isotopic stripes: *Geochemistry, Geophysics, Geosystems*, v. 13, Q07005, doi:10.1029/2012GC004123.

Clague, D.A., Dalrymple, G.B., 1987, The Hawaiian-Emperor volcanic chain, part I, *in* Decker, R.W., Wright, T.L., and Stauffer, P.H., eds., *Volcanism in Hawaii*: U.S. Geological Survey Professional Paper 1350, p. 5-54.

Class, C., and Le Roex, A., 2011, South Atlantic DUPAL anomaly-Dynamic and compositional evidence against a recent shallow origin: *Earth and Planetary Science Letters*, v. 305, p. 92– 102, doi:10.1016/j.epsl.2011.02.036.

Clouard, V., and Bonneville, A., 2005, Ages of seamounts, islands, and plateaus on the Pacific plate, *in* Foulger, G.R., Natland, J.H., Presnall, D.C., and Anderson, D.L., eds., *Plates, Plumes & Paradigms*: Geological Society of America Special Paper 388, p. 71-90.

Courtillot, V., Davaille, A., Besse, J., and Stock, J., 2003, Three distinct types of hotspots in the Earth's mantle: *Earth and Planetary Science Letters*, v. 205, p. 295-308.

DePaolo, D.J., and Manga, M., 2003, Deep origin of hotspots - the Mantle Plume Model: *Science*, v. 300, p. 920-921.

Duncan, R.A., 1981, Hotspots in the Southern Oceans - an absolute frame of reference for motion of Gondwana continents: *Tectonophysics*, v. 74, p. 29-42.

- Eiler, J.M., Farley, K.A., Valley, J.W., Stolper, E.M., Hauri, E.H., and Craig, H., 1995, Oxygen isotope evidence against bulk recycled sediment in the mantle sources of Pitcairn Island lavas: *Nature*, v. 377, p. 138-141.
- Escrig, S., Capmas, F., Dupré, B., and Allègre, C.J., 2004, Osmium isotopic constraints on the nature of the DUPAL anomaly from Indian mid-ocean-ridge basalts: *Nature*, v. 431, p. 59-63.
- Escrig, S., Doucelance, R., Moreira, M., and Allègre, C.J., 2005, Os isotope systematics in Fogo Island: Evidence for lower continental crust fragments under the Cape Verde Southern Islands: *Chemical Geology*, v. 219, p. 93-113.
- Ewart, A., Milner, S.C., Armstrong, R.A., and Duncan, A.R., 1998, Etendeka Volcanism of the Goboboseb Mountains and Messum Igneous Complex, Namibia. Part I: Geochemical Evidence of Early Cretaceous Tristan Plume Melts and the Role of Crustal Contamination in the Paraná Etendeka CFB: *Journal of Petrology*, v. 39, p. 191-25, doi: 10.1093/petroj/39.2.191.
- Fairhead, J.D., and Wilson, M., 2005, Plate tectonic processes in the South Atlantic Ocean: do we need deep mantle plumes? // Foulger, G.R., Natland, J.H., Presnall, D.C., and Anderson, D.L., eds., *Plates, Plumes, and Paradigms: Geological Society of America Special Paper 388*, p. 537-553.
- Farnetani, C.G., and Hofmann, A.W., 2009, Dynamics and internal structure of a lower mantle plume conduit: *Earth and Planetary Science Letters*, v. 282, p. 314-322, doi:10.1016/j.epsl.2009.03.035.
- Farnetani, C.G., and Hofmann, A.W., 2010, Dynamics and internal structure of the Hawaiian plume: *Earth and Planetary Science Letters*, v. 295, p. 231-240, doi: 10.1016/j.epsl.2010.04.005.
- Francheteau, J., Le Pichon, X., 1972, Marginal fracture zones as structural framework

of continental margins in South Atlantic Ocean: *American Association of Petroleum Geologists*, v. 56, p. 991-1007.

Galer, S.J.G., and O'Nions, R.K., 1985, Residence time of thorium, uranium and lead in the mantle with implications for mantle convection: *Nature*, v. 316, p. 778-782, doi:10.1038/316778a0.

Garbe-Schönberg, C.-D., 1993, Simultaneous determination of thirty-seven trace elements in twenty-eight international rock standards by ICP-MS: *Geostandards Newsletter*, v. 17, p. 81-97.

Geldmacher, J., Hanan, B.B., Blichert-Toft, J., Harpp, K., Hoernle, K., Hauff, F., Werner, R., and Kerr, A.C., 2003, Hafnium isotopic variations in volcanic rocks from the Caribbean Large Igneous Province and Galápagos hot spot tracks: *Geochemistry, Geophysics, Geosystems*, v. 4, 1062, doi:10.1029/2002GC000477.

Geldmacher, J., Hoernle, K., van den Bogaard, P., Duggen, S., and Werner, R., 2005, New $^{40}\text{Ar}/^{39}\text{Ar}$ age and geochemical data from seamounts in the Canary and Madeira volcanic provinces: support for the mantle plume hypothesis: *Earth and Planetary Science Letters*, v. 237, p. 85-101, doi:10.1016/j.epsl.2005.04.037.

Geldmacher, J., Hoernle, K., Klügel, A., van den Bogaard, P., and Bindemann, I., 2008, Geochemistry of a new enriched mantle type locality in the northern hemisphere: Implications for the origin of the EM-I source: *Earth and Planetary Science Letters*, v. 265, p. 167-182.

Gibson, S.A., Thompson, R.N., Day, J.A., Humphris, S.E., and Dickin, A.P., 2005, Melt-generation processes associated with the Tristan mantle plume: Constraints on the origin of EM-1: *Earth and Planetary Science Letters*, v. 237, p. 744-767, doi:10.1016/j.epsl.2005.06.015.

Griffin, W.L., O'Reilly, S.Y., Natapov, L.M., and Ryan, C.G., 2003, The evolution of

- lithospheric mantle beneath the Kalahari Craton and its margins: *Lithos*, v. 71, p. 215-241, doi:10.1016/j.lithos.2003.07.006.
- Hanan, B.B., Blichert-Toft, J., Pyle, D.G., and Christie, D.M., 2004, Contrasting origins of the upper mantle revealed by hafnium and lead isotopes from the Southeast Indian Ridge: *Nature*, v. 432, p. 91-94, doi:10.1038/nature03026.
- Hart, S.R., 1984, A large-scale isotope anomaly in the Southern Hemisphere mantle: *Nature*, v. 309, p. 753-757, doi:10.1038/309753a0.
- Hart, S.R., Hauri, E.H., Oschmann, L.A., and Whitehead, J.A., 1992, Mantle Plumes and Entrainment: Isotopic Evidence: *Science*, v. 256, p. 517-520, doi: 10.1126/science.256.5056.517.
- Harpp, K.S., Wanless, V.D., Otto, R.H., Hoernle, K., and Werner, R., 2005, The Cocos and Carnegie Aseismic Ridges: a Trace Element Record of Long-term Plume-Spreading Center Interaction: *Journal of Petrology*, v. 46, p. 109-133, doi:10.1093/petrology/egh064.
- Hawkesworth, C.J., Mantovani, M.S.M., Taylor, P.N., and Palacz, Z., 1986, Evidence from the Parana of south Brazil for a continental contribution to Dupal basalts: *Nature*, v. 322, p. 356-359, doi:10.1038/322356a0.
- Hoernle, K.A., and Tilton, G.R., 1991, Sr-Nd-Pb isotope data for Fuerteventura (Canary Islands) basal complex and subaerial volcanics: applications to magma genesis and evolution: *Schweizerische mineralogische und petrographische Mitteilungen*, v. 71, p. 3-18.
- Hoernle, K., Tilton, G., and Schmincke, H.-U., 1991, Sr-Nd-Pb isotopic evolution of Gran Canaria: Evidence for shallow enriched mantle beneath the Canary Islands: *Earth and Planetary Science Letters*, v. 106, p. 44-63.

- Hoernle, K., Schmincke, H.-U., 1993a, The petrology of the tholeiites through melilitite nephelinites on Gran Canaria, Canary Islands: crystal fractionation, accumulation, and depths of melting. *Journal of Petrology*, v. 34, p. 573-597.
- Hoernle, K., Schmincke, H.-U., 1993b, The role of partial melting in the 15-Ma geochemical evolution of Gran Canaria: a Blob Model for the Canary hotspot. *Journal of Petrology*, v. 34, p. 599-626.
- Hoernle, K., Werner, R., Phipps Morgan, J., Garbe- Schönberg, D., Bryce, J., and Mrazek, J., 2000, Existence of complex spatial zonation in the Galápagos plume for at least 14 m.y: *Geology*, v. 28, p. 435-438, doi:10.1130/0091-7613(2000)028<0435:EOCSZI>2.3.CO;2.
- Hoernle, K., Abt, D.L., Fischer, K.M., Nichols, H., Hauff, F., Abers, G.A., van den Bogaard, P., Heydolph, K., Alvarado, G., Protti, M., and Strauch, W., 2008, Arc-parallel flow in the mantle wedge beneath Costa Rica and Nicaragua: *Nature*, v. 451, p. 1094-1097, doi:10.1038/nature06550.
- Hoernle, K., Hauff, F., Kokfelt, T.F., Haase, K., Garbe- Schönberg, D., and Werner, R., 2011, On- and off-axis chemical heterogeneities along the South Atlantic Mid-Ocean-Ridge (5–11°S): Shallow or deep recycling of ocean crust and/ or intraplate volcanism?: *Earth and Planetary Science Letters*, v. 306, p. 86-97, doi:10.1016/j.epsl.2011.03.032.
- Hofmann, A.W., 1988, Chemical differentiation of the Earth: the relationship between mantle, continental crust, and oceanic crust: *Earth and Planetary Science Letters*, v. 90, p. 297-314.
- Huang, S., Hall, P.S., and Jackson, M.G., 2011, Geochemical zoning of volcanic chains associated with Pacific hotspots: *Nature Geoscience*, v. 4, p. 874-878, doi:10.1038/ngeo1263.

- Ishii, M., and Tromp, J., 1999, Normal-Mode and Free-Air Gravity Constraints on Lateral Variations in Velocity and Density of Earth's Mantle: *Science*, v. 285, p. 1231-1236, doi: 10.1126/science.285.5431.1231.
- Ishii, M., and Tromp, J., 2004, Constraining large-scale mantle heterogeneity using mantle and inner-core sensitive normal modes: *Physics of the Earth and Planetary Interiors*, v. 146, p. 113-124, doi:10.1016/j.pepi.2003.06.012.
- Kay, R.W., and Kay, S. Mahlburg, 1993, Delamination and delamination magmatism: *Tectonophysics*, v. 219, p. 177-189, doi:10.1016/0040-1951(93)90295-U.
- Kay, S. Mahlburg, Coira, B., and Viramonte, J., 1994, Young mafic back arc volcanic rocks as indicators of continental lithospheric delamination beneath the Argentine Puna plateau, central Andes: *Journal of Geophysical Research*, v. 99, p. 24323-24339, doi:10.1029/94JB00896.
- Kay, S. Mahlburg, Godoy, E., and Kurtz, A., 2005, Episodic arc migration, crustal thickening, subduction erosion, and magmatism in the south-central Andes: *Geological Society of America Bulletin*, v. 117, p. 67-88, doi:10.1130/B25431.1.
- Kerr, R.C., and Mériaux, C., 2004, Structure and dynamics of sheared mantle plumes: *Geochemistry, Geophysics, Geosystems*, v. 5, Q12009, doi:10.1029/2004GC000749.
- Kundargi, R., and Hall, P.S., 2012, Melting and dehydration within mantle plumes and the formation of sub-parallel volcanic trends at intra-plate hotspots: Analysis of physical properties on spatial and temporal evolution of viscous plug formation: American Geophysical Union Fall Meeting, San Francisco, Abstract.
- Lanphere, M.A., and Dalrymple, G.B., 2000, First-principles calibration of ^{38}Ar tracers: implications for the ages of $^{40}\text{Ar}/^{39}\text{Ar}$ fluence monitors: U.S. Geological Survey Professional Paper 1621, p. 1-10.

- Le Maitre, R.W., Bateman, P., Dudek, A., Keller, J., Lameyre, J., Le Bas, M.J., Sabine, P.A., Schmid, R., Sorensen, H., Streckeisen, A., Woolley, and A.R., Zanettin, B., 1989, A classification of igneous rocks and glossary of terms. Recommendations of the International Union of Geological Sciences Subcommittee on Systematics of Igneous Rocks: Blackwell Scientific Publications, Oxford.
- Lohmann, F.C., Hort, M., and Phipps Morgan, J., 2009, Flood basalts and ocean island basalts: A deep source or shallow entrainment?: *Earth and Planetary Science Letters*, v. 284, p. 553-563, doi:10.1016/j.epsl.2009.05.025.
- Macdonald, G.A., Katsura, T., 1964, Chemical composition of Hawaiian lavas: *Journal of Petrology*, v. 5, p. 82-133.
- Mantovani, M.S.M., Marques, L.S., De Sousa, M.A., Civetta, L., Atalla, L., and Innocenti, F., 1985, Trace Element and Strontium Isotope Constraints on the Origin and Evolution of Paraná Continental Flood Basalts of Santa Catarina State (Southern Brazil): *Journal of Petrology*, v. 26, p. 187-209, doi: 10.1093/petrology/26.1.187.
- Milner, S.C., and Le Roex, A.P., 1996, Isotope characteristics of the Okenyenya igneous complex, northwestern Namibia: constraints on the composition of the early Tristan plume and the origin of the EM 1 mantle component: *Earth and Planetary Science Letters*, v. 141, p. 277-291.
- Montelli, R., Nolet, G., Dahlen, F.A., and Masters, G., 2006, A catalogue of deep mantle plumes: New results from finite-frequency tomography: *Geochemistry, Geophysics, Geosystems*, v. 7, Q11007, doi:10.1029/2006GC001248.
- Morgan, W.J., 1971, Convection plumes in the lower mantle: *Nature*, v. 230, p. 42-43.
- Morgan, W.J., 1972, Plate motions and deep mantle convection: *Geological Society of America Memoirs*, v. 132, p. 7-22.

- Morgan, W.J., 1981, Hotspot tracks and the opening of the Atlantic and Indian Oceans, *in* Emiliani, C., ed., *The Sea: The Oceanic Lithosphere*, v. 7, p. 443-487.
- Müller, R.D., Royer, J.-Y., and Lawver, L.A., 1993, Revised plate motions relative to the hotspots from combined Atlantic and Indian Ocean hotspot tracks: *Geology*, v. 21, p. 275-278.
- Niu, Y., and O'Hara, M.J., 2003, Origin of ocean island basalts: A new perspective from petrology, geochemistry, and mineral physics considerations: *Journal of Geophysical Research*, v. 108, 2209, doi:10.1029/2002JB002048.
- Niu, Y., Wilson, M., Humphreys, E.R., and O'Hara, M.J., 2011, The Origin of Intra-plate Ocean Island Basalts (OIB): the Lid Effect and its Geodynamic Implications: *Journal of Petrology*, v. 52, p. 1443-1468, doi:10.1093/petrology/egr030.
- Norton, I.O., 2000, Global hotspot reference frames and plate motion, *in* Richards, M.A., Gordon, R.G., and van der Hilst, R.D., eds., *The History and Dynamics of Global Plate Motions: Geophysical Monograph Series*, v. 121, p. 339-357 (AGU).
- O'Connor, J.M., and Duncan, R.A., 1990, Evolution of the Walvis Ridge-Rio Grande Rise hot spot system: implications for African and South American plate motions over plumes: *Journal of Geophysical Research*, v. 95, p. 17,475-17,502.
- O'Connor, J.M., and Le Roex, A.P., 1992, South Atlantic hot spot-plume systems: 1. Distribution of volcanism in time and space: *Earth and Planetary Science Letters*, v. 113, p. 343-364.
- O'Connor, J.M., Stoffers, P., van den Bogaard, P., and McWilliams, M., 1999, First seamount age evidence for significantly slower African plate motion since 19 to 30 Ma: *Earth and Planetary Science Letters*, v. 171, p. 575-589.

- O'Connor, J.M., Stoffers, P., Wijbrans, J.R., and Worthington, T.J., 2007, Migration of widespread long-lived volcanism across the Galápagos Volcanic Province: evidence for a broad hotspot melting anomaly?: *Earth and Planetary Science Letters*, v. 263, p. 339-354.
- Payne, J.A., Jackson, M.G., and Hall, P.S., 2013, Parallel volcano trends and geochemical asymmetry of the Society Islands hotspot track: *Geology*, v. 41, p. 19-22, doi:10.1130/G33273.1.
- Portnyagin, M., Savelyev, D., Hoernle, K., Hauff, F., and Garbe-Schönberg, D., 2008, Mid-Cretaceous Hawaiian tholeiites preserved in Kamchatka: *Geology*, v. 36, p. 903-906, doi: 10.1130/G25171A.1.
- Renne, P.R., 2011, Continental flood basalts and biotic crises: does the Paraná-Etendeka exception prove the rule?: *Mineralogical Magazine*, v. 75, p. 1712.
- Renne, P.R., Glen, J.M., Milner, S.C., and Duncan, A.R., 1996, Age of Etendeka flood volcanism and associated intrusions in southwestern Africa: *Geology*, v. 24, p. 659-662.
- Richards, M.A., Duncan, R.A., and Courtillot, V.E., 1989, Flood basalts and hot-spot tracks: plume heads and tails: *Science*, v. 246, p. 103-107.
- Richardson, S.H., 1982, Correlated Nd, Sr and Pb isotope variation in Walvis Ridge basalts and implications for the evolution of their mantle source: *Earth and Planetary Science Letters*, v. 59, p. 327-342.
- Ritsema, J., van Heijst, H.J., and Woodhouse, J.H., 1999, Complex shear wave velocity structure imaged beneath Africa and Iceland: *Science*, v. 286, p. 1925-1928.
- Ritsema, J., Deuss, A., van Heijst, H.J., and Woodhouse, J.H., 2011, S40RTS: A degree-40 shearvelocity model for the mantle from new Rayleigh wave dispersion,

teleseismic traveltime and normal-mode splitting function measurements: *Geophysical Journal International*, v. 184, p. 1223–1236, doi:10.1111/j.1365-246X.2010.04884.x.

Roden, M.F., Trull, T., Hart, S.R., and Frey, F.A., 1994, New He, Nd, Pb, and Sr isotopic constraints on the constitution of the Hawaiian plume: Results from Koolau Volcano, Oahu, Hawaii, USA: *Geochimica et Cosmochimica Acta*, v. 58, p. 1431-1440.

Rohde, J., Hoernle, K., Hauff, F., Werner, R., O'Connor, J., Class, C., Garbe-Schönberg, D., and Jokat, W., 2013a, 70 Ma chemical zonation of the Tristan-Gough hotspot track: *Geology*, v. 41, p. 335-338, doi:10.1130/G33790.1.

Rohde, J.K., van den Bogaard, P., Hoernle, K., Hauff, F., and Werner, R., 2013b, Evidence for an age progression along the Tristan-Gough volcanic track from new $^{40}\text{Ar}/^{39}\text{Ar}$ ages on phenocryst phases: *Tectonophysics*, v. 604, p. 60-71, doi:10.1016/j.tecto.2012.08.026.

Salters, V.J.M., and Sachi-Kocher, A., 2010, An ancient metasomatic source for the Walvis Ridge basalts: *Chemical Geology*, v. 273, p. 151-167, doi:10.1016/j.chemgeo.2010.02.010.

Schutt, D.L., and Leshner, C.E., 2010, Compositional trends among Kaapvaal Craton garnet peridotite xenoliths and their effects on seismic velocity and density: *Earth and Planetary Science Letters*, v. 300, p. 367-373, doi:10.1016/j.epsl.2010.10.018.

Steinberger, B., and O'Connell, R.J., 1997, Changes of the Earth's rotation axis owing to advection of mantle density heterogeneities: *Nature*, v. 387, p. 169-173, doi:10.1038/387169a0.

- Stracke, A., 2012, Earth's heterogeneous mantle: A product of convection-driven interaction between crust and mantle: *Chemical Geology*, v. 330-331, p. 274-299, doi:10.1016/j.chemgeo.2012.08.007.
- Stracke, A., Bizimis, M., and Salters, V.J.M., 2003, Recycling oceanic crust: Quantitative constraints: *Geochemistry, Geophysics, Geosystems*, v. 4, 8003, doi:10.1029/2001GC000223.
- Stracke, A., Hofmann, A.W., and Hart, S.R., 2005, FOZO, HIMU, and the rest of the mantle zoo: *Geochemistry, Geophysics, Geosystems*, v. 6, Q05007, doi:10.1029/2004GC000824.
- Suetsugu, D., Isse, T., Tanaka, S., Obayashi, M., Shiobara, H., Sugioka, H., Kanazawa, T., Fukao, Y., Barruol, G., and Reymond, D., 2009, South Pacific mantle plumes imaged by seismic observation on islands and seafloor: *Geochemistry, Geophysics, Geosystems*, v. 10, Q11014, doi:10.1029/2009GC002533.
- Sun, S.-s., and McDonough, W.F., 1989, Chemical and isotopic systematics of oceanic basalts: implications for mantle composition and processes, *in* Saunders, A.D., and Norry, M.J., eds., *Magmatism in the Ocean Basins: Geological Society Special Publication 42*, p. 313-345, doi:10.1144/GSL.SP.1989.042.01.19.
- Tarduno, J.A., Duncan, R.A., Scholl, D.W., Cottrell, R.D., Steinberger, B., Thordarson, T., Kerr, B.C., Neal, C.R., Frey, F.A., Torii, M., and Carvallo, C., 2003, The Emperor Seamounts: Southward Motion of the Hawaiian Hotspot Plume in Earth's Mantle: *Science*, v. 301, p. 1064-1069, doi: 10.1126/science.1086442.
- Tatsumi, Y., 2000, Continental crust formation by crustal delamination in subduction zones and complementary accumulation of the enriched mantle I component in the mantle: *Geochemistry, Geophysics, Geosystems*, v. 1, 1053, doi: 10.1029/2000GC000094.

- Thompson, G., and Humphris, S.E., 1984, Petrology and geochemistry of rocks from the Walvis Ridge: Deep Sea Drilling Project Leg 74, sites 525, 527, and 528, *in* Moore, T.C., Rabinowitz, P.D., et al., eds., *Init. Repts. DSDP, 74*. U.S. Govt. Printing Office, Washington, p. 755-764.
- Thompson, R.N., Gibson, S.A., Dickin, A.P., and Smith, P.M., 2001, Early Cretaceous Basalt and Picrite Dykes of the Southern Etendeka Region, NW Namibia: Windiws into the Role of the Tristan Mntle Plume in Paraná-Etendeka Magmatism: *Journal of Petrology*, v. 42, p. 2049-2081, doi: 10.1093/petrology/42.11.2049.
- Vidal, V., and Bonneville, A., 2004, Variations of the Hawaiian hot spot activity revealed by variations in the magma production rate: *Journal of Geophysical Research*, v. 109, B03104, doi:10.1029/2003JB002559.
- Weaver, B., 1991, The origin of ocean island basalt end-member compositions: trace-element and isotopic constraints: *Earth and Planetary Science Letters*, v. 104, p. 381-397.
- Weaver, B.L., Wood, D.A., Tarney, J., and Joron, J.L., 1986, Role of subducted sediment in the genesis of ocean-island basalts: Geochemical evidence from South Atlantic Ocean islands: *Geology*, v. 14, p. 275-278.
- Weis, D., Garcia, M.O., Rhodes, J.M., Jellinek, M., and Scoates, J.S., 2011, Role of the deep mantle in generating the compositional asymmetry of the Hawaiian mantle plume: *Nature Geoscience*, v. 4, p. 831-838, doi:10.1038/ngeo1328.
- Werner, R., Hoernle, K., Barckhausen, U., and Hauff, F., 2003, Geodynamic evolution of the Galápagos hot spot system (Central East Pacific) over the past 20 m.y.: Constraints from morphology, geochemistry, and magnetic anomalies: *Geochemistry, Geophysics, Geosystems*, v. 4, 1108, doi:10.1029/2003GC000576.
- White, R.S., 1993, Melt production rates in mantle plumes: *Philosophical Transactions of*

the Royal Society A: Mathematical, Physical and Engineering Sciences, v. 342, p. 137-153, doi:10.1098/rsta.1993.0010.

White, W.M., 1985, Sources of oceanic basalts: Radiogenic isotopic evidence: *Geology*, v. 13, p. 115-118.

Willbold, M., and Stracke, A., 2006, Trace element composition of mantle end-members: Implications for recycling of oceanic and upper and lower continental crust: *Geochemistry, Geophysics, Geosystems*, v. 7, Q04004, doi:10.1029/2005GC001005.

Willbold, M., and Stracke, A., 2010, Formation of enriched mantle components by recycling of upper and lower continental crust: *Chemical Geology*, v. 276, p. 188-197.

Wilson, J.T., 1963, Evidence from Islands on the spreading of ocean floors: *Nature*, v. 197, p. 536-538.

Zindler, A., and Hart, S., 1986, Chemical Geodynamics: *Annual Review of Earth and Planetary Sciences*, v. 14, p. 493-571.

Appendices

Appendix I (CHAPTER I)

⁴⁰Ar/³⁹Ar analysis data

JD8fss MASS= J =	plagioclase 2.260 mg 3.48E-03		+/-		5.61E-06	(2 Sigma)	0.161 Percent				
STEP	POWER	40Ar/39Ar	37Ar/39Ar	36Ar/39Ar	Mol 39ArK	Ca/K	% 40ArA	Cum 39ArK	Age [Ma]	2 Sigma	A.I. (36/37)
1	3.00E-01	1.46E+04	1.34E+02	4.91E+01	3.78E-18	2.99E+02	9.91E+01	7.36E-04	7.33E+02	6.50E+02	1.28E-01
2	5.00E-01	4.30E+02	1.22E+01	1.39E+00	9.80E-17	2.43E+01	9.50E+01	1.98E-02	1.31E+02	2.64E+01	3.93E-02
3	8.00E-01	8.05E+01	1.35E+01	2.25E-01	2.62E-16	2.67E+01	8.04E+01	7.07E-02	9.75E+01	7.04E+00	5.66E-03
4	1.00E+00	2.29E+01	1.61E+01	3.06E-02	1.85E-16	3.21E+01	3.03E+01	1.07E-01	9.89E+01	3.44E+00	5.07E-04
5	1.20E+00	2.70E+01	1.63E+01	4.08E-02	1.55E-16	3.25E+01	3.68E+01	1.37E-01	1.05E+02	6.09E+00	7.16E-04
6	1.50E+00	2.32E+01	1.58E+01	2.70E-02	1.77E-16	3.13E+01	2.54E+01	1.71E-01	1.07E+02	4.21E+00	4.42E-04
7	2.00E+00	2.62E+01	1.68E+01	3.94E-02	1.96E-16	3.34E+01	3.61E+01	2.09E-01	1.04E+02	3.49E+00	6.63E-04
8	2.50E+00	2.20E+01	1.97E+01	2.12E-02	2.85E-16	3.94E+01	1.69E+01	2.65E-01	1.13E+02	2.21E+00	2.20E-04
9	3.00E+00	1.91E+01	2.00E+01	1.18E-02	1.02E-15	4.00E+01	4.57E+00	4.63E-01	1.13E+02	9.60E-01	5.09E-05
10	3.50E+00	1.91E+01	2.10E+01	1.14E-02	6.11E-16	4.20E+01	3.28E+00	5.81E-01	1.15E+02	1.29E+00	3.48E-05
11	4.00E+00	1.93E+01	2.04E+01	1.22E-02	5.92E-16	4.07E+01	4.91E+00	6.97E-01	1.14E+02	1.38E+00	5.44E-05
12	5.00E+00	1.91E+01	2.13E+01	1.17E-02	6.07E-16	4.25E+01	3.63E+00	8.15E-01	1.14E+02	1.28E+00	3.81E-05
13	6.00E+00	1.92E+01	2.12E+01	1.12E-02	2.87E-16	4.24E+01	2.91E+00	8.71E-01	1.15E+02	2.55E+00	3.06E-05
14	8.00E+00	1.89E+01	2.01E+01	1.08E-02	1.77E-16	4.02E+01	3.01E+00	9.05E-01	1.14E+02	3.55E+00	3.29E-05
15	1.00E+01	1.93E+01	2.06E+01	1.27E-02	2.89E-16	4.12E+01	5.60E+00	9.61E-01	1.13E+02	2.73E+00	6.16E-05
16	1.20E+01	2.08E+01	2.07E+01	1.27E-02	1.38E-16	4.14E+01	5.10E+00	9.88E-01	1.22E+02	5.23E+00	5.99E-05
17	1.50E+01	2.00E+01	1.50E+01	2.40E-03	2.35E-17	2.97E+01	-6.20E+00	9.93E-01	1.30E+02	2.48E+01	-9.79E-05
18	1.75E+01	2.04E+01	2.27E+01	6.96E-03	3.21E-17	4.54E+01	-4.40E+00	9.99E-01	1.32E+02	2.38E+01	-4.70E-05
19	2.00E+01	2.69E+01	3.64E+01	3.21E-02	5.93E-18	7.38E+01	1.76E+01	1.00E+00	1.39E+02	1.20E+02	1.53E-04
Total Gas Age =	1.13E+02		+/-		5.20E-01	Ma (2Sigma)					
Plateau age =	113.78±0.57 Ma (2s, including J-error of .161%) MSWD = 1.15, probability = 0.33, 75.2% of the 39Ar, steps 8 through 15										

JD8fs2 MASS= J =	plagioclase 3.350 mg 3.48E-03		+/-		5.61E-06	(2 Sigma)	0.161 Percent				
STEP	POWER	40Ar/39Ar	37Ar/39Ar	36Ar/39Ar	Mol 39ArK	Ca/K	% 40ArA	Cum 39ArK	Age [Ma]	2 Sigma	A.I. (36/37)
1	4.00E-01	4.50E+02	1.43E+01	1.47E+00	3.43E-16	2.84E+01	6.22E+01	4.32E-02	1.05E+02	1.36E+01	3.57E-02
2	6.00E-01	5.07E+01	1.36E+01	1.24E-01	3.84E-16	2.69E+01	6.87E+01	9.15E-02	9.81E+01	5.23E+00	3.02E-03
3	8.00E-01	4.00E+01	1.81E+01	8.28E-02	4.23E-16	3.61E+01	5.53E+01	1.22E-01	1.11E+02	5.04E+00	1.44E-03
4	1.00E+00	2.53E+01	1.58E+01	3.24E-02	2.10E-16	3.14E+01	2.97E+01	1.49E-01	1.10E+02	3.86E+00	5.61E-04
5	1.20E+00	1.88E+01	1.88E+01	1.16E-02	6.63E-16	3.76E+01	5.15E+00	2.32E-01	1.10E+02	1.42E+00	6.00E-05
6	1.50E+00	2.02E+01	2.01E+01	1.51E-02	6.74E-16	4.01E+01	9.09E+00	3.17E-01	1.14E+02	1.39E+00	1.07E-04
7	2.00E+00	1.90E+01	2.06E+01	1.11E-02	7.27E-16	4.11E+01	3.12E+00	4.09E-01	1.14E+02	1.49E+00	3.16E-05
8	2.50E+00	1.88E+01	2.05E+01	1.01E-02	9.03E-16	4.10E+01	1.72E+00	5.22E-01	1.14E+02	1.46E+00	1.81E-05
9	3.00E+00	1.87E+01	1.99E+01	1.03E-02	6.32E-16	3.98E+01	2.38E+00	6.02E-01	1.13E+02	2.16E+00	2.95E-05
10	4.00E+00	1.88E+01	2.01E+01	9.89E-03	6.33E-16	4.01E+01	1.65E+00	6.82E-01	1.15E+02	1.34E+00	1.78E-05
11	5.00E+00	1.89E+01	2.07E+01	1.04E-02	9.39E-16	4.13E+01	1.97E+00	8.00E-01	1.15E+02	1.10E+00	2.09E-05
12	6.00E+00	1.89E+01	1.99E+01	1.02E-02	8.28E-16	3.98E+01	2.17E+00	9.04E-01	1.15E+02	1.30E+00	2.39E-05
13	8.00E+00	1.93E+01	2.02E+01	1.17E-02	4.40E-16	4.03E+01	4.26E+00	9.60E-01	1.15E+02	2.01E+00	4.78E-05
14	1.00E+01	2.37E+01	1.51E+01	2.75E-02	1.39E-16	2.99E+01	2.60E+01	9.77E-01	1.08E+02	6.27E+00	4.81E-04
15	1.20E+01	1.88E+01	9.70E+00	1.07E-02	4.97E-17	1.92E+01	1.01E+01	9.84E-01	1.04E+02	1.34E+01	2.30E-04
16	1.35E+01	2.13E+01	1.74E+01	1.85E-02	1.50E-17	3.46E+01	1.50E+01	9.85E-01	1.12E+02	3.67E+01	2.16E-04
17	1.50E+01	3.05E+01	-9.63E+00	-9.25E-04	2.66E-18	-1.87E+01	3.22E+00	9.86E-01	1.25E+02	2.08E+02	-1.82E-04
18	2.00E+01	1.93E+01	6.74E+00	-9.07E-04	2.55E-17	1.33E+01	-5.94E+00	9.89E-01	1.25E+02	2.65E+01	-2.01E-04
19	2.25E+01	2.30E+02	1.12E+01	7.46E-01	7.44E-17	2.22E+01	9.51E+01	9.98E-01	6.98E+01	2.11E+01	2.31E-02
20	2.50E+01	3.20E+02	1.81E+01	9.92E-01	1.28E-17	3.60E+01	9.08E+01	1.00E+00	1.79E+02	8.43E+01	1.89E-02
Total Gas Age =	1.12E+02		+/-		4.69E-01	Ma (2Sigma)					
Plateau age =	114.46±0.54 Ma (2s, including J-error of .161%) MSWD = 0.43, probability = 0.88 72.8% of the 39Ar, steps 6 through 13										

JD9fss MASS= J =	plagioclase 2.125 mg 3.46E-03		+/-		5.83E-06	(2 Sigma)	0.169 Percent				
STEP	POWER	40Ar/39Ar	37Ar/39Ar	36Ar/39Ar	Mol 39ArK	Ca/K	% 40ArA	Cum 39ArK	Age [Ma]	2 Sigma	A.I. (36/37)
1	3.00E-01	1.13E+03	8.95E+00	3.71E+00	5.21E-17	1.77E+01	9.70E+01	2.00E-02	2.02E+02	5.08E+01	1.44E-01
2	5.00E-01	2.49E+02	1.34E+01	7.84E-01	1.29E-16	2.67E+01	9.24E+01	6.95E-02	1.16E+02	2.29E+01	2.01E-02
3	8.00E-01	8.87E+01	1.87E+01	2.53E-01	2.16E-16	3.73E+01	8.16E+01	1.52E-01	1.01E+02	8.97E+00	4.55E-03
4	1.00E+00	3.49E+01	2.21E+01	7.35E-02	1.35E-16	4.42E+01	5.40E+01	2.04E-01	9.95E+01	7.19E+00	1.00E-03
5	1.20E+00	2.79E+01	2.32E+01	5.13E-02	1.00E-16	4.64E+01	4.35E+01	2.42E-01	9.79E+01	8.44E+00	6.16E-04
6	1.50E+00	3.42E+01	2.50E+01	7.48E-02	1.42E-16	5.03E+01	5.51E+01	2.96E-01	9.57E+01	5.53E+00	8.86E-04
7	2.00E+00	2.84E+01	2.97E+01	5.50E-02	1.41E-16	5.98E+01	4.36E+01	3.50E-01	1.00E+02	4.38E+00	4.91E-04
8	2.50E+00	2.40E+01	4.39E+01	4.36E-02	3.25E-16	8.97E+01	2.99E+01	4.74E-01	1.06E+02	3.18E+00	1.92E-04
9	3.00E+00	2.08E+01	4.88E+01	3.51E-02	2.38E-16	1.00E+02	1.92E+01	5.65E-01	1.06E+02	4.64E+00	9.59E-05
10	3.50E+00	2.03E+01	5.05E+01	3.23E-02	2.94E-16	1.04E+02	1.46E+01	6.78E-01	1.10E+02	2.79E+00	6.89E-05
11	4.00E+00	2.01E+01	5.10E+01	3.20E-02	2.87E-16	1.05E+02	1.39E+01	7.88E-01	1.10E+02	3.23E+00	6.42E-05
12	5.00E+00	2.03E+01	5.39E+01	3.34E-02	2.04E-16	1.11E+02	1.40E+01	8.66E-01	1.11E+02	3.37E+00	6.18E-05
13	6.00E+00	1.92E+01	5.47E+01	2.72E-02	1.37E-16	1.13E+02	4.69E+00	9.18E-01	1.16E+02	4.78E+00	1.90E-05
14	8.00E+00	1.93E+01	5.44E+01	2.77E-02	1.34E-16	1.12E+02	5.68E+00	9.69E-01	1.16E+02	7.21E+00	2.34E-05
15	1.00E+01	1.94E+01	5.59E+01	2.65E-02	6.45E-17	1.16E+02	2.91E+00	9.94E-01	1.20E+02	9.53E+00	1.15E-05
16	1.20E+01	1.99E+01	4.83E+01	4.26E-02	1.10E-17	9.93E+01	3.16E+01	9.98E-01	8.70E+01	4.97E+01	1.53E-04
17	1.50E+01	2.31E+01	7.05E+01	1.44E-01	2.84E-18	1.48E+02	1.44E+02	9.99E-01	-6.95E+01	2.35E+02	5.56E-04
18	1.75E+01	2.74E+01	7.80E+01	2.43E-01	1.28E-18	1.65E+02	2.25E+02	1.00E+00	-2.47E+02	5.32E+02	9.30E-04
19	2.00E+01	5.63E+01	3.84E+02	1.10E+00	2.41E-19	1.18E+03	4.91E+02	1.00E+00	-7.10E+03	2.80E+04	8.47E-04
Total Gas Age =	1.08E+02		+/-		1.23E+00	Ma (2Sigma)					
Plateau age =	108.9±1.5 Ma (2s, including J-error of .169%) MSWD = 1.5, probability = 0.20 51.6% of the 39Ar, steps 8 through 12										

JD9fs2 MASS= J =	plagioclase 3.686 mg 3.46E-03		+/-		5.83E-06	(2 Sigma)	0.169 Percent				
STEP	POWER	40Ar/39Ar	37Ar/39Ar	36Ar/39Ar	Mol 39ArK	Ca/K	% 40ArA	Cum 39ArK	Age [Ma]	2 Sigma	A.I. (36/37)
1	4.00E-01	3.38E+02	1.39E+01	1.08E+00	5.55E-16	2.77E+01	9.38E+01	1.16E-01	1.28E+02	1.18E+01	2.68E-02
2	6.00E-01	5.78E+01	1.67E+01	1.53E-01	4.90E-16	3.32E+01	7.46E+01	2.19E-01	9.08E+01	3.88E+00	3.05E-03
3	8.00E-01	4.36E+01	2.75E+01	1.04E-01	2.41E-16	5.54E+01	6.25E+01	2.69E-01	1.02E+02	5.14E+00	1.16E-03
4	1.00E+00	3.68E+01	3.12E+01	8.34E-02	3.71E-16	6.31E+01	5.60E+01	3.47E-01	1.01E+02	4.19E+00	7.75E-04
5	1.20E+00	3.30E+01	3.72E+01	7.05E-02	1.54E-16	7.55E+01	4.84E+01	3.80E-01	1.07E+02	6.71E+00	5.06E-04
6	1.50E+00	2.14E+01	4.43E+01	3.51E-02	7.61E-16	9.05E+01	2.16E+01	5.39E-01	1.06E+02	1.87E+00	1.23E-04
7	2.00E+00	2.10E+01	4.73E+01	3.46E-02	6.36E-16	9.70E+01	1.94E+01	6.72E-01	1.07E+02	1.59E+00	1.01E-04
8	2.50E+00	2.15E+01	4.90E+01	3.66E-02	3.41E-16	1.01E+02	2.06E+01	7.44E-01	1.08E+02	3.32E+00	1.06E-04
9	3.00E+00	1.94E+01	5.09E+01	2.88E-02	2.71E-16	1.05E+02	9.69E+00	8.01E-01	1.11E+02	3.72E+00	4.30E-05
10	4.00E+00	1.91E+01	5.15E+01	2.67E-02	2.48E-16	1.06E					

JD10fss		plagioclase		MASS=		J =		0.169 Percent			
		1.981 mg		3.46E-03		+/-		5.83E-06 (2 Sigma)			
STEP	POWER	40Ar/39Ar	37Ar/39Ar	36Ar/39Ar	Mol 39ArK	Ca/K	% 40ArA	Cum 39ArK	Age [Ma]	2 Sigma	A.I. (36/37)
1	3.00E-01	2.93E+03	3.75E+01	9.75E+00	3.92E-17	7.62E+01	9.83E+01	9.47E-03	3.02E+02	6.36E+01	9.03E-02
2	5.00E-01	1.55E+02	1.48E+01	4.56E-01	2.58E-16	2.93E+01	8.58E+01	7.18E-02	1.34E+02	7.40E+00	1.06E-02
3	8.00E-01	4.16E+01	1.74E+01	8.47E-02	4.86E-16	3.47E+01	5.47E+01	1.89E-01	1.16E+02	3.11E+00	1.54E-03
4	1.00E+00	2.98E+01	1.91E+01	5.27E-02	1.88E-16	3.80E+01	4.39E+01	2.35E-01	1.03E+02	3.79E+00	8.09E-04
5	1.20E+00	2.55E+01	2.04E+01	3.39E-02	1.19E-16	4.09E+01	2.89E+01	2.64E-01	1.12E+02	6.19E+00	4.23E-04
6	1.50E+00	2.36E+01	2.11E+01	2.82E-02	2.59E-16	4.21E+01	2.37E+01	3.26E-01	1.11E+02	3.57E+00	3.13E-04
7	2.00E+00	2.19E+01	2.03E+01	2.12E-02	6.56E-16	4.06E+01	1.64E+01	4.85E-01	1.13E+02	1.78E+00	2.09E-04
8	2.50E+00	2.07E+01	2.24E+01	1.85E-02	1.92E-16	4.48E+01	1.23E+01	5.31E-01	1.12E+02	4.55E+00	1.33E-04
9	3.00E+00	2.11E+01	2.17E+01	1.81E-02	3.10E-16	4.34E+01	1.19E+01	6.06E-01	1.14E+02	2.93E+00	1.36E-04
10	3.50E+00	2.03E+01	2.22E+01	1.67E-02	4.74E-16	4.44E+01	1.01E+01	7.21E-01	1.13E+02	2.20E+00	1.08E-04
11	4.00E+00	2.02E+01	2.20E+01	1.67E-02	3.10E-16	4.41E+01	1.03E+01	7.96E-01	1.12E+02	2.27E+00	1.11E-04
12	5.00E+00	2.07E+01	2.22E+01	1.73E-02	3.65E-16	4.45E+01	1.07E+01	8.84E-01	1.14E+02	2.50E+00	1.16E-04
13	6.00E+00	2.16E+01	2.39E+01	2.10E-02	1.49E-16	4.80E+01	1.43E+01	9.20E-01	1.14E+02	5.51E+00	1.52E-04
14	8.00E+00	2.39E+01	2.22E+01	2.88E-02	1.53E-16	4.45E+01	2.36E+01	9.57E-01	1.12E+02	4.20E+00	2.98E-04
15	1.00E+01	2.72E+01	2.21E+01	4.23E-02	9.12E-17	4.41E+01	3.53E+01	9.79E-01	1.09E+02	9.46E+00	5.13E-04
16	1.20E+01	3.84E+01	1.75E+01	7.61E-02	5.10E-17	3.49E+01	5.27E+01	9.91E-01	1.11E+02	1.68E+01	1.36E-03
17	1.50E+01	8.50E+01	8.34E+00	2.31E-01	2.21E-17	1.65E+01	7.91E+01	9.97E-01	1.08E+02	3.92E+01	9.49E-03
18	1.75E+01	2.19E+02	2.01E+01	6.49E-01	9.13E-18	4.01E+01	8.64E+01	9.99E-01	1.08E+02	9.96E+01	1.11E-02
19	2.00E+01	5.49E+01	2.06E+00	1.27E-01	3.50E-18	4.04E+00	6.81E+01	1.00E+00	1.06E+02	1.63E+02	2.14E-02
20	2.25E+01	6.80E+01	-1.46E+00	4.09E-02	1.69E-18	-2.86E+00	1.80E+01	1.00E+00	3.17E+02	3.30E+02	-9.87E-03
Total Gas Age =	1.16E+02	+/-	8.33E-01	Ma (2Sigma)							
Plateau age =	112.83±0.93 Ma (2s, including J-error of .169%) MSWD = 0.51, probability = 0.85 69.3% of the 39Ar, steps 6 through 14										

JD11fss		plagioclase		MASS=		J =		0.169 Percent			
		2.207 mg		3.46E-03		+/-		5.83E-06 (2 Sigma)			
STEP	POWER	40Ar/39Ar	37Ar/39Ar	36Ar/39Ar	Mol 39ArK	Ca/K	% 40ArA	Cum 39ArK	Age [Ma]	2 Sigma	A.I. (36/37)
1	3.00E-01	2.68E+03	2.46E+01	8.90E+00	1.49E-16	4.93E+01	9.80E+01	3.13E-02	3.20E+02	7.21E+01	1.26E-01
2	5.00E-01	1.26E+02	1.42E+01	3.69E-01	7.24E-16	2.83E+01	8.52E+01	1.84E-01	1.14E+02	5.46E+00	8.87E-03
3	8.00E-01	3.74E+01	1.60E+01	7.64E-02	8.66E-16	3.18E+01	5.48E+01	3.66E-01	1.04E+02	2.98E+00	1.51E-03
4	1.00E+00	2.27E+01	2.08E+01	3.14E-02	2.33E-16	4.16E+01	2.89E+01	4.15E-01	9.99E+01	4.86E+00	3.71E-04
5	1.20E+00	2.12E+01	2.20E+01	2.45E-02	1.54E-16	4.40E+01	2.07E+01	4.48E-01	1.04E+02	4.26E+00	2.34E-04
6	1.50E+00	2.48E+01	2.20E+01	3.39E-02	2.84E-16	4.41E+01	2.89E+01	5.08E-01	1.09E+02	3.00E+00	3.28E-04
7	2.00E+00	2.27E+01	2.55E+01	2.70E-02	3.49E-16	5.13E+01	2.05E+01	5.81E-01	1.11E+02	2.17E+00	2.14E-04
8	2.50E+00	2.10E+01	2.94E+01	2.27E-02	5.55E-16	5.93E+01	1.37E+01	6.98E-01	1.12E+02	2.16E+00	1.15E-04
9	3.00E+00	2.03E+01	3.00E+01	2.06E-02	4.21E-16	6.05E+01	1.07E+01	7.87E-01	1.13E+02	2.76E+00	8.49E-05
10	3.50E+00	1.97E+01	2.99E+01	1.85E-02	1.84E-16	6.02E+01	8.05E+00	8.26E-01	1.13E+02	3.66E+00	3.25E-05
11	4.00E+00	2.73E+01	3.85E+01	4.54E-02	6.95E-17	7.84E+01	3.08E+01	8.40E-01	1.18E+02	1.31E+01	2.56E-04
12	5.00E+00	1.96E+01	3.59E+01	1.96E-02	8.48E-17	7.29E+01	5.62E+00	8.58E-01	1.15E+02	1.15E+01	3.57E-05
13	6.00E+00	1.94E+01	3.29E+01	1.88E-02	1.25E-16	6.65E+01	6.58E+00	8.84E-01	1.13E+02	5.24E+00	4.54E-05
14	8.00E+00	2.00E+01	3.15E+01	1.90E-02	2.21E-16	6.37E+01	7.53E+00	9.31E-01	1.15E+02	4.30E+00	5.59E-05
15	1.00E+01	1.97E+01	3.20E+01	1.75E-02	2.30E-16	6.47E+01	5.09E+00	9.79E-01	1.17E+02	4.15E+00	3.66E-05
16	1.20E+01	2.02E+01	3.97E+01	2.09E-02	3.10E-17	8.07E+01	5.07E+00	9.86E-01	1.20E+02	1.54E+01	3.00E-05
17	1.50E+01	2.18E+01	4.33E+01	2.99E-02	1.86E-17	8.85E+01	1.47E+01	9.90E-01	1.17E+02	2.79E+01	8.69E-05
18	1.75E+01	2.21E+01	3.74E+01	3.03E-02	3.28E-17	7.80E+01	1.84E+01	9.97E-01	1.13E+02	2.12E+01	1.28E-04
19	2.00E+01	3.07E+01	4.02E+01	6.20E-02	6.45E-18	8.18E+01	4.25E+01	9.98E-01	1.11E+02	8.91E+01	3.83E-04
20	2.25E+01	3.17E+01	3.32E+01	8.29E-02	8.53E-18	6.71E+01	6.38E+01	1.00E+00	7.23E+01	6.26E+01	7.17E-04
Total Gas Age =	1.17E+02	+/-	9.29E-01	Ma (2Sigma)							
Plateau age =	112.4±1.1 Ma (2s, including J-error of .169%) MSWD = 1.16, probability = 0.31 54.9% of the 39Ar, steps 6 through 18										

JD12fss		plagioclase		MASS=		J =		0.169 Percent			
		2.758 mg		3.46E-03		+/-		5.83E-06 (2 Sigma)			
STEP	POWER	40Ar/39Ar	37Ar/39Ar	36Ar/39Ar	Mol 39ArK	Ca/K	% 40ArA	Cum 39ArK	Age [Ma]	2 Sigma	A.I. (36/37)
1	3.00E-01	4.43E+02	1.52E+01	1.45E+00	3.03E-16	3.02E+01	9.62E+01	4.83E-02	1.03E+02	3.35E+01	3.29E-02
2	5.00E-01	8.65E+01	1.38E+01	2.51E-01	6.86E-16	2.74E+01	8.36E+01	1.58E-01	8.72E+01	7.03E+00	6.13E-03
3	8.00E-01	3.59E+01	1.53E+01	7.25E-02	1.12E-15	3.05E+01	5.41E+01	3.36E-01	1.01E+02	1.85E+00	1.48E-03
4	1.00E+00	3.11E+01	1.82E+01	5.51E-02	4.97E-16	3.62E+01	4.48E+01	4.15E-01	1.06E+02	3.48E+00	8.97E-04
5	1.20E+00	2.70E+01	2.00E+01	4.11E-02	3.20E-16	3.99E+01	3.53E+01	4.66E-01	1.08E+02	3.48E+00	5.59E-04
6	1.50E+00	2.63E+01	2.13E+01	3.74E-02	3.16E-16	4.26E+01	3.14E+01	5.16E-01	1.11E+02	2.56E+00	4.53E-04
7	2.00E+00	2.37E+01	2.62E+01	3.00E-02	5.83E-16	5.26E+01	2.31E+01	6.09E-01	1.13E+02	1.96E+00	2.45E-04
8	2.50E+00	2.29E+01	2.94E+01	2.92E-02	4.81E-16	5.92E+01	2.10E+01	6.86E-01	1.12E+02	3.32E+00	1.91E-04
9	3.00E+00	2.15E+01	2.71E+01	2.36E-02	7.30E-16	5.46E+01	1.59E+01	8.02E-01	1.12E+02	1.28E+00	1.48E-04
10	3.50E+00	2.05E+01	2.94E+01	2.01E-02	3.67E-16	5.33E+01	1.03E+01	8.61E-01	1.14E+02	2.49E+00	8.32E-05
11	4.00E+00	2.05E+01	3.28E+01	2.31E-02	2.16E-16	6.59E+01	1.25E+01	8.95E-01	1.12E+02	4.43E+00	9.22E-05
12	5.00E+00	2.02E+01	3.05E+01	1.98E-02	1.35E-16	6.15E+01	9.40E+00	9.17E-01	1.14E+02	4.65E+00	7.25E-05
13	6.00E+00	2.15E+01	3.07E+01	2.35E-02	1.91E-16	6.20E+01	1.37E+01	9.47E-01	1.15E+02	4.25E+00	1.12E-04
14	8.00E+00	2.18E+01	2.96E+01	2.52E-02	1.81E-16	5.97E+01	1.65E+01	9.76E-01	1.13E+02	3.30E+00	1.42E-04
15	1.00E+01	2.68E+01	2.94E+01	4.19E-02	9.07E-17	5.92E+01	3.20E+01	9.90E-01	1.13E+02	8.39E+00	3.41E-04
16	1.20E+01	2.32E+01	2.77E+01	1.70E-02	2.86E-17	5.58E+01	6.05E+00	9.95E-01	1.34E+02	2.19E+01	5.90E-05
17	1.50E+01	2.68E+01	2.16E+01	4.36E-02	1.95E-17	4.33E+01	3.75E+01	9.98E-01	1.04E+02	3.58E+01	5.43E-04
18	1.75E+01	2.68E+01	-9.97E+01	2.56E-02	2.68E-18	-1.79E+02	7.67E+01	9.98E-01	3.51E+01	2.64E+02	-2.42E-04
19	2.00E+01	3.05E+01	-7.18E+00	2.38E-02	5.72E-18	-1.40E+01	2.61E+01	9.99E-01	1.35E+02	1.13E+02	-1.30E-03
20	2.25E+01	2.29E+01	-2.62E+01	1.36E-02	4.79E-18	-5.02E+01	3.26E+01	1.00E+00	9.14E+01	1.28E+02	-3.33E-04
Total Gas Age =	1.07E+02	+/-	7.05E-01	Ma (2Sigma)							
Plateau age =	112.62±0.83 Ma (2s, including J-error of .169%) MSWD = 0.59, probability = 0.80 52.4% of the 39Ar, steps 6 through 15										

All93fss		K-feldspar		MASS=		J =		0.172 Percent			
		2.175 mg		3.46E-03		+/-		5.95E-06 (2 Sigma)			
STEP	POWER	40Ar/39Ar	37Ar/39Ar	36Ar/39Ar	Mol 39ArK	Ca/K	% 40ArA	Cum 39ArK	Age [Ma]	2 Sigma	A.I. (36/39)
1	6.00E-01	3.49E+03	1.16E-01	1.18E+01	5.22E-18	2.27E-01	9.96E+01	9.28E-05	7.62E+01	4.00E+02	4.08E+00
2	8.00E-01	1.06E+02	4.59E-02	3.20E-01	8.25E-17	9.00E-02	8.94E+01	1.56E-03	6.86E+01	1.90E+01	1.11E-01
3	1.00E+00	1.52E+01	1.09E-02	2.00E-02	3.87E-16	2.13E-02	3.90E+01	8.43E-03	5.68E+01	2.94E+00	6.91E-03
4	1.20E+00	1.27E+01	5.01E-03	1.21E-02	7.17E-16	9.83E-03	2.81E+01	2.12E-02	5.62E+01	1.33E+00	4.19E-03
5	1.50E+00	1.30E+01	3.40E-03	1.33E-02	1.39E-15	6.67E-03	3.01E+01	4.59E-02	5.59E+01	7.03E-01	4.59E-03
6	2.00E+00	9.27E+00	3.17E-03	1.04E-03	3.23E-15	6.22E-03	3.32E+00	1.03E-01	5.50E+01		

JD5fss MASS= J =		plagioclase 1.838 mg 3.50E-03		+/-		5.12E-06		(2 Sigma)		0.146 Percent	
STEP	POWER	40Ar/39Ar	37Ar/39Ar	36Ar/39Ar	Mol 39ArK	Ca/K	% 40ArA	Cum 39ArK	Age [Ma]	2 Sigma	A.I. (36/37)
1	3.00E-01	1.59E+03	4.62E+01	5.30E+00	5.14E-17	9.46E+01	9.81E+01	1.81E-02	1.87E+02	7.38E+01	3.98E-02
2	5.00E-01	2.31E+02	3.19E+01	7.62E-01	2.86E-16	6.44E+01	9.56E+01	1.19E-01	6.53E+01	1.57E+01	8.17E-03
3	8.00E-01	6.41E+01	2.75E+01	1.90E-01	5.30E-16	5.54E+01	8.20E+01	3.06E-01	7.33E+01	5.65E+00	2.25E-03
4	1.00E+00	5.93E+01	3.04E+01	1.73E-01	2.24E-16	6.13E+01	7.96E+01	3.84E-01	7.69E+01	6.02E+00	1.83E-03
5	1.20E+00	2.57E+01	3.08E+01	5.91E-02	1.58E-16	6.23E+01	5.22E+01	4.40E-01	7.83E+01	3.96E+00	5.12E-04
6	1.50E+00	3.76E+01	2.97E+01	1.01E-01	1.40E-16	6.00E+01	6.89E+01	4.89E-01	7.45E+01	8.59E+00	1.03E-03
7	2.00E+00	1.17E+01	3.05E+01	1.60E-02	2.39E-16	6.15E+01	6.47E+00	5.74E-01	7.00E+01	4.27E+00	2.90E-05
8	2.50E+00	1.18E+01	3.01E+01	1.54E-02	3.86E-16	6.08E+01	5.26E+00	7.10E-01	7.13E+01	2.54E+00	2.39E-05
9	3.00E+00	1.23E+01	3.66E+01	2.06E-02	2.73E-16	7.42E+01	1.07E+01	8.06E-01	7.05E+01	4.06E+00	4.21E-05
10	3.50E+00	1.19E+01	4.19E+01	1.95E-02	1.86E-16	8.55E+01	2.43E+00	8.71E-01	7.47E+01	3.98E+00	7.74E-06
11	4.00E+00	1.18E+01	3.87E+01	2.06E-02	2.18E-16	7.87E+01	9.02E+00	9.48E-01	6.88E+01	2.67E+00	3.20E-05
12	5.00E+00	1.17E+01	3.99E+01	1.87E-02	6.81E-17	8.12E+01	2.84E+00	9.72E-01	7.29E+01	1.06E+01	9.44E-06
13	6.00E+00	1.22E+01	4.16E+01	1.89E-02	3.68E-17	8.48E+01	1.37E+00	9.85E-01	7.72E+01	1.29E+01	4.36E-06
14	8.00E+00	1.23E+01	3.75E+01	2.26E-02	2.67E-17	7.62E+01	1.45E+01	9.95E-01	6.77E+01	1.75E+01	5.59E-05
15	1.00E+01	1.48E+01	5.47E+01	2.28E-02	5.93E-18	1.13E+02	-2.50E+00	9.97E-01	9.86E+01	6.05E+01	-8.35E-06
16	1.20E+01	1.42E+01	8.29E+01	1.72E-02	5.23E-18	1.76E+02	-4.01E+01	9.99E-01	1.32E+02	1.12E+02	-8.14E-05
17	1.50E+01	1.76E+01	8.43E+01	-2.32E-02	3.71E-18	1.80E+02	-1.02E+02	1.00E+00	2.28E+02	1.20E+02	-2.50E-04

Total Gas Age = 7.46E+01 +/- 1.26E+00 Ma (2Sigma)
 Plateau age = 71.0±1.4 Ma (2s, including J-error of .146%) MSWD = 1.01, probability = 0.43 55.7% of the 39Ar, steps 6 through 15

JD5fs2 MASS= J =		plagioclase 3.125 mg 3.50E-03		+/-		5.12E-06		(2 Sigma)		0.146 Percent	
STEP	POWER	40Ar/39Ar	37Ar/39Ar	36Ar/39Ar	Mol 39ArK	Ca/K	% 40ArA	Cum 39ArK	Age [Ma]	2 Sigma	A.I. (36/37)
1	4.00E-01	2.77E+02	2.56E+01	9.10E-01	8.33E-16	5.14E+01	9.60E+01	1.37E-01	7.11E+01	9.29E+00	1.22E-02
2	6.00E-01	4.36E+01	1.20E-01	1.20E-01	5.79E-16	4.34E+01	7.48E+01	2.33E-01	6.85E+01	4.89E+00	1.77E-03
3	8.00E-01	2.96E+01	2.48E+01	7.38E-02	4.20E-16	4.99E+01	6.27E+01	3.02E-01	7.01E+01	5.88E+00	8.79E-04
4	1.00E+00	4.82E+01	2.35E+01	1.32E-01	3.79E-16	4.70E+01	7.46E+01	3.64E-01	7.74E+01	4.96E+00	1.80E-03
5	1.20E+00	3.03E+01	2.32E+01	7.30E-02	4.04E-16	4.64E+01	6.12E+01	4.31E-01	7.44E+01	5.28E+00	9.43E-04
6	1.50E+00	1.58E+01	2.80E+01	2.73E-02	6.05E-16	6.63E+01	2.80E+01	5.30E-01	7.23E+01	7.23E+00	1.85E-04
7	2.00E+00	1.17E+01	2.68E+01	1.32E-02	6.16E-16	5.40E+01	3.53E+00	6.32E-01	7.16E+01	1.39E+00	1.78E-05
8	2.50E+00	1.19E+01	2.52E+01	1.42E-02	3.59E-16	5.75E+01	7.64E+00	6.91E-01	6.96E+01	2.41E+00	4.21E-05
9	3.00E+00	1.24E+01	2.71E+01	1.61E-02	4.06E-16	5.46E+01	9.99E+00	7.58E-01	7.07E+01	2.74E+00	5.32E-05
10	4.00E+00	1.26E+01	2.86E+01	1.76E-02	4.31E-16	5.75E+01	1.18E+01	8.29E-01	7.06E+01	2.19E+00	6.10E-05
11	5.00E+00	1.74E+01	2.88E+01	3.13E-02	3.79E-16	5.81E+01	3.16E+01	8.91E-01	7.55E+01	2.82E+00	2.23E-04
12	6.00E+00	2.99E+01	3.24E+01	7.49E-02	1.57E-16	6.56E+01	6.00E+01	9.17E-01	7.63E+01	6.27E+00	6.50E-04
13	8.00E+00	9.64E+01	2.35E+01	2.99E-01	1.18E-16	4.71E+01	8.86E+01	9.37E-01	6.97E+01	1.43E+01	4.28E-03
14	1.00E+01	6.89E+01	1.94E+01	1.95E-01	3.00E-17	3.87E+01	8.00E+01	9.42E-01	8.64E+01	2.84E+01	3.35E-03
15	1.20E+01	4.83E+01	2.01E+01	1.30E-01	4.87E-17	4.02E+01	7.44E+01	9.50E-01	7.79E+01	2.00E+01	2.10E-03
16	1.35E+01	5.94E+01	1.76E+01	1.74E-01	4.56E-17	3.51E+01	6.26E+01	9.57E-01	6.53E+01	1.53E+01	3.28E-03
17	1.50E+01	1.49E+01	2.49E+01	2.57E-02	1.50E-16	5.00E+01	2.92E+01	9.82E-01	6.72E+01	4.78E+00	2.06E-04
18	2.00E+01	2.49E+02	1.44E+00	8.30E-01	1.82E-17	2.83E+00	9.83E+01	9.85E-01	2.73E+01	7.00E+01	2.00E-01
19	2.25E+01	2.49E+02	1.51E+01	8.16E-01	5.76E-17	3.00E+01	9.63E+01	9.94E-01	5.87E+01	3.82E+01	1.87E-02
20	2.50E+01	1.08E+02	1.39E+01	3.40E-01	3.49E-17	2.76E+01	9.15E+01	1.00E+00	5.76E+01	2.63E+01	8.35E-03

Total Gas Age = 7.15E+01 +/- 7.96E-01 Ma (2Sigma)
 Plateau age = 71.40±0.88 Ma (2s, including J-error of .146%) MSWD = 1.6, probability = 0.14 59.6% of the 39Ar, steps 3 through 10

JD6fss MASS= J =		plagioclase 1.730 mg 3.50E-03		+/-		5.12E-06		(2 Sigma)		0.146 Percent	
STEP	POWER	40Ar/39Ar	37Ar/39Ar	36Ar/39Ar	Mol 39ArK	Ca/K	% 40ArA	Cum 39ArK	Age [Ma]	2 Sigma	A.I. (36/37)
1	5.00E-01	4.11E+02	3.12E+01	1.35E+00	1.90E-16	6.31E+01	9.58E+01	6.54E-02	1.09E+02	1.72E+01	1.49E-02
2	8.00E-01	4.51E+01	2.35E+01	1.23E-01	5.29E-16	4.71E+01	7.36E+01	2.48E-01	7.53E+01	3.49E+00	1.66E-03
3	1.00E+00	1.75E+01	2.45E+01	3.19E-02	2.55E-16	4.92E+01	3.55E+01	3.36E-01	7.16E+01	3.98E+00	2.98E-04
4	1.20E+00	1.38E+01	2.36E+01	1.81E-02	1.61E-16	4.74E+01	1.64E+01	3.92E-01	7.28E+01	5.15E+00	1.12E-04
5	1.50E+00	1.22E+01	2.98E+01	1.49E-02	2.41E-16	6.00E+01	4.22E+00	4.75E-01	7.41E+01	4.29E+00	2.00E-05
6	2.00E+00	1.22E+01	2.90E+01	1.60E-02	3.45E-16	5.85E+01	7.76E+00	5.94E-01	7.14E+01	2.46E+00	3.79E-05
7	2.50E+00	1.20E+01	2.70E+01	1.39E-02	4.61E-16	5.43E+01	5.01E+00	7.53E-01	7.22E+01	2.34E+00	2.58E-05
8	3.00E+00	1.18E+01	2.91E+01	1.46E-02	3.26E-16	5.86E+01	4.32E+00	8.65E-01	7.20E+01	2.44E+00	2.03E-05
9	3.50E+00	1.18E+01	2.76E+01	1.52E-02	1.29E-16	5.54E+01	7.63E+00	9.09E-01	6.94E+01	5.35E+00	3.82E-05
10	4.00E+00	1.30E+01	3.09E+01	3.13E-02	4.18E-17	6.24E+01	4.04E+01	9.24E-01	4.96E+01	1.06E+01	1.99E-04
11	5.00E+00	1.25E+01	3.38E+01	1.95E-02	1.09E-16	6.83E+01	1.10E+01	9.62E-01	7.12E+01	5.63E+00	4.77E-05
12	6.00E+00	1.33E+01	3.07E+01	2.31E-02	4.66E-17	6.21E+01	2.12E+01	9.78E-01	6.98E+01	9.68E+00	1.08E-04
13	8.00E+00	1.51E+01	3.48E+01	3.09E-02	4.94E-17	7.05E+01	3.05E+01	9.95E-01	6.70E+01	1.32E+01	1.55E-04
14	1.00E+01	4.53E+01	5.30E+01	1.23E-01	8.08E-18	1.09E+02	6.48E+01	9.97E-01	1.03E+02	6.17E+01	6.52E-04
15	1.20E+01	2.42E+02	7.75E+01	5.07E-01	1.51E-18	1.64E+02	5.77E+01	9.98E-01	5.91E+02	3.61E+02	2.12E-03
16	1.50E+01	1.83E+02	5.81E+01	5.37E-01	4.13E-18	1.20E+02	8.27E+01	9.99E-01	1.99E+02	1.77E+02	3.06E-03
17	1.75E+01	1.43E+03	6.48E+01	4.76E+00	9.68E-19	1.35E+02	9.80E+01	1.00E+00	1.79E+02	9.45E+02	2.54E-02

Total Gas Age = 7.53E+01 +/- 1.09E+00 Ma (2Sigma)
 Plateau age = 72.0±1.2 Ma (2s, including J-error of .146%) MSWD = 0.39, probability = 0.89 66.2% of the 39Ar, steps 3 through 9

971fss MASS= J =		plagioclase 3.295 mg 3.42E-03		+/-		6.67E-06		(2 Sigma)		0.195 Percent	
STEP	POWER	40Ar/39Ar	37Ar/39Ar	36Ar/39Ar	Mol 39ArK	Ca/K	% 40ArA	Cum 39ArK	Age [Ma]	2 Sigma	A.I. (36/37)
1	1.00E+00	7.86E+02	2.90E+02	2.76E+00	5.04E-18	7.81E+02	9.91E+01	6.25E-03	5.74E+01	1.67E+02	3.17E-03
2	1.20E+00	7.95E+02	2.82E+02	2.69E+00	5.14E-18	7.55E+02	9.55E+01	1.26E-02	2.79E+02	1.53E+02	3.17E-03
3	1.50E+00	7.61E+02	3.18E+02	2.66E+00	7.31E-18	8.92E+02	9.81E+01	2.17E-02	1.25E+02	2.09E+02	2.76E-03
4	2.00E+00	1.15E+02	2.07E+02	4.51E-01	2.75E-17	5.03E+02	9.20E+01	5.58E-02	6.90E+01	4.82E+01	6.05E-04
5	2.50E+00	3.74E+01	2.11E+02	1.90E-01	3.85E-17	5.16E+02	7.70E+01	1.04E-01	6.50E+01	2.58E+01	1.60E-04
6	3.00E+00	2.50E+01	2.43E+02	1.72E-01	1.41E-17	6.18E+02	7.61E+01	1.21E-01	4.72E+01	3.20E+01	9.19E-05
7	3.50E+00	2.43E+01	2.09E+02	1.54E-01	4.24E-17	5.10E+02	7.49E+01	1.74E-01	4.62E+01	2.67E+01	1.02E-04
8	4.00E+00	1.73E+01	2.16E+02	1.42E-01	2.59E-17	5.32E+02	7.93E+01	2.06E-01	2.75E+01	3.46E+01	7.43E-05
9	5.00E+00	1.35E+01	2.17E+02	1.15E-01	1.35E-16	5.36E+02	4.32E+01	3.73E-01	5.83E+01	1.16E+01	3.11E-05
10	6.00E+00	1.18E+01	2.14E+02	1.07E-01	2.65E-16	5.26E+02	3.14E+01	7.03E-01	6.15E+01	6.76E+00	2.01E-05
11	8.00E+00	1.22E+01	2.07E+02	1.08E-01	6.84E-17	5.05E+02	4.11E+01	7.88E-01	5.40E+01	1.54E+01	2.81E-05
12	1.00E+01	1.05E+01	2.05E+02	1.00E-01	1.15E-16	4.99E+02	2.76E+01	9.30E-01	5.74E+01	1.35E+01	1.63E-05
13	1.20E+01	1.08E+01	2.03E+02	1.17E-01	1.64E-17	4.92E+02	7.44E+01	9.51E-01	2.08E+01	5.03E+01	4.61E-05
14	1.50E+01	9.74E+00	2.35E+02	1.15E-01	3.56E-17	5.90E+02	3.50E+01	9.95E-01	4.94E+01	2.20E+01	1.68E-05
15	1.75E+01	8.47E+00	2.51E+02	5.83E-02	2.61E-18	6.45E+02	-1.83E+02	9.98E-01	1.84E+02	2.49E+02	-7.30E-05
16	2.00E+01	1.58E+01	8.36E+01	2.57E-01	1.28E-18	1.78E+02	4.10E+02	1.00E+00	-3.64E+02	6.25E+	

97Zfss MASS= J =	plagioclase 2.839 mg 3.42E-03	+/-	6.67E-06	(2 Sigma)	0.195 Percent						
STEP	POWER	40Ar/39Ar	37Ar/39Ar	36Ar/39Ar	Mol 39ArK	Ca/K	% 40ArA	Cum 39ArK	Age [Ma]	2 Sigma	A.I. (36/37)
1	1.00E+00	4.03E+02	1.93E+02	1.41E+00	2.13E-17	4.61E+02	9.70E+01	2.30E-02	9.01E+01	5.64E+01	2.39E-03
2	1.20E+00	1.22E+02	1.62E+02	4.59E-01	3.12E-17	3.74E+02	9.38E+01	5.67E-02	5.40E+01	4.23E+01	8.36E-04
3	1.50E+00	1.34E+02	1.76E+02	5.03E-01	4.16E-17	4.14E+02	9.37E+01	1.02E-01	6.15E+01	3.60E+01	8.40E-04
4	2.00E+00	3.48E+01	1.63E+02	1.55E-01	6.02E-17	3.78E+02	7.04E+01	1.67E-01	7.37E+01	1.27E+01	1.76E-04
5	2.50E+00	1.76E+01	1.67E+02	1.08E-01	4.18E-17	3.90E+02	5.74E+01	2.12E-01	5.40E+01	2.35E+01	7.07E-05
6	3.00E+00	1.53E+01	1.67E+02	9.64E-02	2.87E-17	3.89E+02	4.39E+01	2.43E-01	6.16E+01	2.11E+01	4.68E-05
7	3.50E+00	1.64E+01	1.80E+02	1.04E-01	8.38E-17	4.26E+02	4.33E+01	3.33E-01	6.76E+01	1.33E+01	4.59E-05
8	4.00E+00	2.17E+01	1.66E+02	1.20E-01	5.43E-17	3.85E+02	6.36E+01	3.92E-01	5.70E+01	1.39E+01	9.78E-05
9	5.00E+00	1.26E+01	1.70E+02	8.71E-02	1.27E-16	3.96E+02	2.88E+01	5.29E-01	6.47E+01	9.58E+00	2.48E-05
10	6.00E+00	1.69E+01	1.62E+02	9.66E-02	2.72E-16	3.75E+02	4.39E+01	8.22E-01	6.76E+01	7.36E+00	5.35E-05
11	8.00E+00	1.67E+01	1.60E+02	9.40E-02	1.39E-16	3.71E+02	4.10E+01	9.73E-01	7.04E+01	8.36E+00	5.00E-05
12	1.50E+01	3.33E+01	2.09E+02	5.82E-02	2.54E-18	5.11E+02	-3.03E+01	9.76E-01	3.06E+02	2.92E+02	-5.71E-05
13	2.00E+01	1.54E+01	1.76E+02	8.16E-02	1.37E-17	4.13E+02	7.76E+00	9.91E-01	1.02E+02	6.60E+01	7.65E-06
14	2.25E+01	1.46E+01	1.69E+02	5.49E-02	8.24E-18	3.95E+02	-4.01E+01	1.00E+00	1.44E+02	9.42E+01	-4.10E-05

Total Gas Age = 6.82E+01 +/- 3.87E+00 Ma (2Sigma)
Plateau age = 6.9±3.9 Ma (2s, including J-error of .195%) MSWD = 0.80, probability = 0.59 87.1% of the 39Ar, steps 4 through 11

5-3fss MASS= J =	plagioclase 2.206 mg 3.42E-03	+/-	6.67E-06	(2 Sigma)	0.195 Percent						
STEP	POWER	40Ar/39Ar	37Ar/39Ar	36Ar/39Ar	Mol 39ArK	Ca/K	% 40ArA	Cum 39ArK	Age [Ma]	2 Sigma	A.I. (36/37)
1	6.00E-01	1.27E+03	4.60E+01	4.29E+00	1.92E-17	9.43E+01	9.90E+01	6.51E-03	8.30E+01	1.66E+02	3.23E-02
2	8.00E-01	2.35E+02	3.88E+01	7.84E-01	7.50E-17	7.89E+01	9.64E+01	3.19E-02	5.40E+01	1.72E+01	6.88E-03
3	1.00E+00	6.98E+01	3.83E+01	2.33E-01	1.26E-16	7.79E+01	9.13E+01	7.46E-02	3.84E+01	1.06E+01	1.96E-03
4	1.20E+00	7.60E+01	4.39E+01	2.59E-01	1.20E-16	8.98E+01	9.31E+01	1.15E-01	3.33E+01	8.00E+00	1.90E-03
5	1.50E+00	7.22E+01	3.90E+01	2.37E-01	1.89E-16	7.93E+01	8.99E+01	1.79E-01	4.62E+01	9.76E+00	1.96E-03
6	2.00E+00	3.32E+01	4.07E+01	1.09E-01	2.45E-16	8.30E+01	8.11E+01	2.63E-01	3.98E+01	4.66E+00	7.77E-04
7	2.50E+00	1.57E+01	4.04E+01	5.10E-02	5.20E-16	8.23E+01	6.24E+01	4.39E-01	3.75E+01	1.71E+00	2.86E-04
8	3.00E+00	1.46E+01	4.09E+01	4.88E-02	7.70E-17	8.35E+01	6.24E+01	4.65E-01	3.47E+01	8.24E+00	2.61E-04
9	4.00E+00	2.34E+01	3.87E+01	7.78E-02	4.52E-16	7.86E+01	7.67E+01	6.19E-01	3.46E+01	2.05E+00	5.47E-04
10	5.00E+00	1.22E+01	3.89E+01	3.88E-02	2.63E-16	7.91E+01	5.23E+01	7.08E-01	3.70E+01	4.07E+00	1.93E-04
11	6.00E+00	1.04E+01	3.93E+01	3.36E-02	2.19E-16	8.00E+01	4.64E+01	7.82E-01	3.52E+01	2.06E+00	1.44E-04
12	8.00E+00	1.18E+01	4.15E+01	4.00E-02	1.59E-16	8.46E+01	5.43E+01	8.36E-01	3.43E+01	5.71E+00	1.82E-04
13	1.00E+01	9.59E+00	4.08E+01	3.09E-02	2.39E-16	8.32E+01	3.98E+01	9.18E-01	3.66E+01	3.77E+00	1.10E-04
14	1.20E+01	1.34E+01	4.08E+01	4.27E-02	1.45E-16	8.32E+01	5.47E+01	9.67E-01	3.84E+01	7.80E+00	2.11E-04
15	1.50E+01	7.86E+00	4.10E+01	2.62E-02	9.24E-17	8.36E+01	3.05E+01	9.98E-01	3.47E+01	8.16E+00	6.85E-05
16	2.00E+01	1.27E+01	4.81E+01	5.87E-02	5.69E-18	9.88E+01	8.73E+01	1.00E+00	1.04E+01	1.28E+02	2.70E-04

Total Gas Age = 3.78E+01 +/- 9.50E-01 Ma (2Sigma)
Plateau age = 36.07±0.99 Ma (2s, including J-error of .195%) MSWD = 0.86, probability = 0.55 73.5% of the 39Ar, steps 7 through 15

6-1fss MASS= J =	plagioclase 1.942 mg 3.42E-03	+/-	6.67E-06	(2 Sigma)	0.195 Percent						
STEP	POWER	40Ar/39Ar	37Ar/39Ar	36Ar/39Ar	Mol 39ArK	Ca/K	% 40ArA	Cum 39ArK	Age [Ma]	2 Sigma	A.I. (36/37)
1	1.00E+00	4.00E+02	3.99E+01	1.35E+00	1.09E-17	8.13E+01	9.84E+01	3.81E-03	4.08E+01	8.46E+01	1.16E-02
2	1.20E+00	9.74E+01	2.44E+01	3.24E-01	2.26E-17	4.89E+01	9.51E+01	1.16E-02	2.98E+01	4.27E+01	4.47E-03
3	1.50E+00	3.39E+01	2.99E+01	1.15E-01	5.95E-17	6.02E+01	8.90E+01	3.20E-02	2.35E+01	1.03E+01	1.19E-03
4	2.00E+00	2.38E+01	3.37E+01	7.58E-02	1.58E-16	6.83E+01	7.56E+01	8.62E-02	3.67E+01	5.63E+00	6.28E-04
5	2.50E+00	9.78E+00	3.43E+01	2.94E-02	4.72E-16	6.95E+01	4.30E+01	2.48E-01	3.51E+01	2.71E+00	1.44E-04
6	3.00E+00	6.65E+00	3.67E+01	2.08E-02	8.17E-16	7.46E+01	2.06E+01	5.28E-01	3.34E+01	1.41E+00	4.35E-05
7	4.00E+00	5.92E+00	3.52E+01	1.81E-02	5.81E-16	7.13E+01	1.30E+01	7.27E-01	3.25E+01	1.87E+00	2.35E-05
8	5.00E+00	6.16E+00	3.45E+01	1.90E-02	2.80E-16	6.98E+01	1.83E+01	8.24E-01	3.18E+01	3.24E+00	3.80E-05
9	6.00E+00	6.06E+00	3.70E+01	1.87E-02	2.22E-16	7.51E+01	1.16E+01	9.00E-01	3.39E+01	4.70E+00	2.21E-05
10	8.00E+00	5.97E+00	3.42E+01	1.66E-02	1.51E-16	6.92E+01	7.81E+00	9.51E-01	3.47E+01	5.14E+00	1.57E-05
11	1.00E+01	6.22E+00	4.26E+01	1.65E-02	7.40E-17	8.70E+01	-1.10E+01	9.77E-01	4.83E+01	1.00E+01	-1.93E-05
12	1.20E+01	6.04E+00	5.41E+01	-3.80E-03	1.30E-17	1.12E+02	-1.35E+02	9.81E-01	9.00E+01	5.66E+01	-1.78E-04
13	1.50E+01	5.87E+00	3.46E+01	1.61E-02	2.03E-17	7.00E+01	4.25E+00	9.88E-01	3.55E+01	3.22E+01	8.14E-06
14	2.00E+01	6.45E+00	4.06E+01	1.25E-02	3.44E-17	8.27E+01	-2.48E+01	1.00E+00	5.08E+01	2.03E+01	-4.67E-05

Total Gas Age = 3.16E+01 +/- 9.29E-01 Ma (2Sigma)
Plateau age = 33.40±0.95 Ma (2s, including J-error of .195%) MSWD = 1.4, probability = 0.22 89.1% of the 39Ar, steps 5 through 11

16956fss MASS= J =	K-feldspar 2.380 mg 3.42E-03	+/-	6.67E-06	(2 Sigma)	0.195 Percent						
STEP	POWER	40Ar/39Ar	37Ar/39Ar	36Ar/39Ar	Mol 39ArK	Ca/K	% 40ArA	Cum 39ArK	Age [Ma]	2 Sigma	A.I. (36/39)
1	2.00E-01	6.37E+02	2.45E+01	2.23E+00	3.56E-18	4.91E+01	1.03E+02	2.86E-05	-1.19E+02	3.58E+02	7.59E-01
2	3.00E-01	7.34E+01	1.63E+01	2.41E-01	2.75E-17	3.24E+01	9.42E+01	2.50E-04	2.63E+01	3.88E+01	8.01E-02
3	4.00E-01	2.18E+01	1.49E+00	6.39E-02	8.87E-17	2.93E+00	8.58E+01	9.64E-04	1.90E+01	9.51E+00	2.16E-02
4	6.00E-01	8.37E+00	-5.07E-02	1.39E-02	6.28E-16	-9.93E-02	4.90E+01	6.02E-03	2.61E+01	1.80E+00	4.75E-03
5	8.00E-01	5.50E+00	-8.78E-02	4.16E-03	1.21E-15	-1.72E-01	2.28E+01	1.58E-02	2.60E+01	6.19E-01	1.44E-03
6	1.00E+00	4.91E+00	1.24E-01	1.93E-03	1.87E-15	2.44E-01	1.13E+01	3.08E-02	2.66E+01	3.27E-01	6.40E-04
7	1.20E+00	4.96E+00	-8.63E-02	2.05E-03	1.88E-15	-1.69E-01	1.24E+01	4.59E-02	2.65E+01	4.10E-01	7.14E-04
8	1.50E+00	4.57E+00	6.13E-02	5.98E-04	3.61E-15	1.20E-01	3.70E+00	7.50E-02	2.69E+01	1.74E-01	1.95E-04
9	2.00E+00	5.37E+00	3.81E-02	3.16E-03	4.84E-15	7.47E-02	1.73E+01	1.14E-01	2.72E+01	2.07E-01	1.08E-03
10	2.50E+00	4.73E+00	7.15E-02	1.05E-03	4.80E-15	1.40E-01	6.40E+00	1.53E-01	2.71E+01	2.54E-01	3.50E-04
11	3.00E+00	4.45E+00	5.21E-02	2.10E-04	5.72E-15	1.02E-01	1.24E+00	1.99E-01	2.69E+01	1.53E-01	6.40E-05
12	4.00E+00	4.69E+00	6.02E-02	9.73E-04	6.37E-15	1.18E-01	5.97E+00	2.50E-01	2.69E+01	1.62E-01	3.24E-04
13	5.00E+00	4.45E+00	5.63E-02	1.43E-04	1.29E-14	1.10E-01	7.84E-01	3.53E-01	2.70E+01	8.74E-02	4.03E-05
14	6.00E+00	4.44E+00	7.24E-02	9.34E-05	3.10E-14	1.42E-01	4.10E-01	6.02E-01	2.70E+01	8.07E-02	2.10E-05
15	8.00E+00	4.46E+00	6.07E-02	1.63E-04	1.19E-14	1.19E-01	1.04E+00	6.98E-01	2.70E+01	1.01E-01	5.33E-05
16	1.00E+01	4.43E+00	6.92E-02	1.22E-04	2.04E-14	1.36E-01	6.11E-01	8.62E-01	2.69E+01	7.74E-02	3.13E-05
17	1.20E+01	4.52E+00	-6.15E-01	1.77E-03	2.44E-16	-1.21E+00	1.33E+01	8.64E-01	2.40E+01	2.71E+00	6.98E-04
18	1.50E+01	4.44E+00	8.77E-02	8.79E-05	1.22E-14	1.72E-01	3.29E-01	9.62E-01	2.70E+01	8.45E-02	1.68E-05
19	2.00E+01	4.46E+00	5.90E-02	1.65E-04	4.69E-15	1.16E-01	9.20E-01	1.00E+00	2.70E+01	1.74E-01	4.74E-05

Total Gas Age = 2.69E+01 +/- 3.35E-02 Ma (2Sigma)
Plateau age = 26.965±0.066 Ma (2s, including J-error of .195%) MSWD = 0.84, probability = 0.52 70.9% of the 39Ar, steps 11 through 16

3-1Bfss	plagioclase													
MASS=	2.201 mg													
J =	3.42E-03	+/-	6.67E-06	(2 Sigma)						0.195 Percent				
STEP	POWER	40Ar/39Ar	37Ar/39Ar	36Ar/39Ar	Mol 39ArK	Ca/K	% 40ArA	Cum 39ArK	Age [Ma]	2 Sigma	A.I. (36/37)			
1	8.00E-01	4.86E+02	6.36E+01	1.66E+00	1.86E-17	1.33E+02	9.93E+01	9.38E-03	2.27E+01	7.44E+01	8.94E-03			
2	1.00E+00	1.39E+02	5.06E+01	4.70E-01	3.48E-17	1.04E+02	9.50E+01	2.69E-02	4.41E+01	2.60E+01	3.08E-03			
3	1.20E+00	7.37E+01	5.76E+01	2.61E-01	4.63E-17	1.19E+02	9.45E+01	5.03E-02	2.60E+01	2.00E+01	1.42E-03			
4	1.50E+00	6.05E+01	5.52E+01	2.13E-01	7.72E-17	1.14E+02	9.20E+01	8.92E-02	3.13E+01	1.33E+01	1.19E-03			
5	2.00E+00	2.40E+01	5.47E+01	8.85E-02	1.25E-16	1.13E+02	7.94E+01	1.52E-01	3.18E+01	7.18E+00	4.09E-04			
6	2.50E+00	1.68E+01	5.39E+01	6.53E-02	1.54E-16	1.11E+02	7.32E+01	2.30E-01	2.90E+01	6.26E+00	2.68E-04			
7	3.00E+00	1.05E+01	5.32E+01	4.32E-02	2.33E-16	1.10E+02	5.54E+01	3.47E-01	3.01E+01	5.06E+00	1.29E-04			
8	4.00E+00	7.29E+00	5.48E+01	3.43E-02	5.81E-16	1.13E+02	4.14E+01	6.40E-01	2.76E+01	1.79E+00	6.45E-05			
9	5.00E+00	6.34E+00	6.18E+01	3.35E-02	2.27E-16	1.29E+02	2.91E+01	7.55E-01	2.92E+01	4.96E+00	3.48E-05			
10	6.00E+00	7.17E+00	6.27E+01	3.91E-02	1.59E-16	1.31E+02	4.72E+01	8.35E-01	2.46E+01	6.07E+00	6.30E-05			
11	8.00E+00	8.47E+00	5.76E+01	4.04E-02	1.44E-16	1.19E+02	5.24E+01	9.07E-01	2.61E+01	6.12E+00	9.03E-05			
12	1.00E+01	6.12E+00	5.47E+01	3.05E-02	8.88E-17	1.13E+02	3.06E+01	9.52E-01	2.74E+01	7.06E+00	3.99E-05			
13	1.20E+01	1.02E+01	2.22E+01	7.50E-02	8.53E-18	4.45E+01	1.89E+02	9.56E-01	-5.79E+01	7.76E+01	1.02E-03			
14	1.50E+01	5.82E+00	5.69E+01	3.26E-02	7.08E-17	1.18E+02	3.83E+01	9.92E-01	1.15E+01	4.58E+01	4.58E-05			
15	2.00E+01	6.55E+00	5.44E+01	2.79E-02	1.63E-17	1.12E+02	1.75E+01	1.00E+00	3.48E+01	3.37E+01	2.44E-05			
Total Gas Age =	2.80E+01	+/-	1.38E+00	Ma (2Sigma)										
Plateau age =	27.7±1.4 Ma (2s, including J-error of .195%) MSWD = 0.47, probability = 0.83 80% of the 39Ar, steps 6 through 12													
3-25fss	plagioclase													
MASS=	2.242 mg													
J =	3.42E-03	+/-	6.67E-06	(2 Sigma)						0.195 Percent				
STEP	POWER	40Ar/39Ar	37Ar/39Ar	36Ar/39Ar	Mol 39ArK	Ca/K	% 40ArA	Cum 39ArK	Age [Ma]	2 Sigma	A.I. (36/37)			
1	6.00E-01	4.87E+03	1.23E+02	1.64E+01	5.62E-18	2.72E+02	9.90E+01	2.44E-03	3.01E+02	3.12E+02	4.64E-02			
2	8.00E-01	6.88E+02	6.66E+01	2.28E+00	3.16E-17	1.39E+02	9.67E+01	1.62E-02	1.43E+02	5.10E+01	1.18E-02			
3	1.00E+00	2.29E+02	6.07E+01	7.69E-01	5.93E-17	1.26E+02	9.59E+01	4.20E-02	6.10E+01	2.79E+01	4.26E-03			
4	1.20E+00	5.85E+01	6.14E+01	2.03E-01	6.03E-17	1.28E+02	8.88E+01	6.82E-02	4.25E+01	1.80E+01	9.95E-04			
5	1.50E+00	4.58E+01	6.20E+01	1.69E-01	7.70E-17	1.29E+02	9.17E+01	1.02E-01	2.48E+01	1.34E+01	7.98E-04			
6	2.00E+00	3.02E+01	6.26E+01	1.08E-01	1.24E-16	1.30E+02	7.86E+01	1.56E-01	4.19E+01	1.02E+01	4.47E-04			
7	2.50E+00	1.34E+01	5.21E+01	5.44E-02	2.40E-16	1.07E+02	6.92E+01	2.60E-01	4.77E+01	2.82E+00	2.10E-04			
8	3.00E+00	1.99E+01	5.21E+01	7.52E-02	3.99E-16	1.07E+02	7.77E+01	4.33E-01	2.85E+01	4.00E+00	3.48E-04			
9	4.00E+00	1.25E+01	4.59E+01	4.84E-02	4.20E-16	9.40E+01	6.66E+01	6.16E-01	2.86E+01	3.72E+00	2.14E-04			
10	5.00E+00	1.01E+01	5.47E+01	4.40E-02	1.69E-16	1.13E+02	5.84E+01	6.89E-01	2.71E+01	6.36E+00	1.26E-04			
11	6.00E+00	7.38E+00	5.64E+01	3.62E-02	1.28E-16	1.17E+02	4.52E+01	7.45E-01	2.61E+01	4.78E+00	6.93E-05			
12	8.00E+00	9.22E+00	4.95E+01	3.86E-02	2.54E-16	1.02E+02	5.37E+01	8.55E-01	2.74E+01	3.76E+00	1.17E-04			
13	1.00E+01	5.14E+00	4.89E+01	2.39E-02	9.99E-17	1.01E+02	1.32E+01	8.98E-01	2.86E+01	7.18E+00	1.59E-05			
14	1.20E+01	6.11E+00	4.90E+01	3.30E-02	7.94E-17	1.01E+02	5.49E+01	9.33E-01	1.77E+01	9.01E+00	8.02E-05			
15	1.50E+01	5.63E+00	5.32E+01	2.82E-02	6.44E-17	1.10E+02	2.49E+01	9.61E-01	2.72E+01	1.15E+01	3.06E-05			
16	2.00E+01	6.21E+00	5.88E+01	3.47E-02	9.01E-17	1.22E+02	4.19E+01	1.00E+00	2.34E+01	6.90E+00	5.18E-05			
Total Gas Age =	3.11E+01	+/-	1.44E+00	Ma (2Sigma)										
Plateau age =	26.7±1.5 Ma (2s, including J-error of .195%) MSWD = 0.69, probability = 0.72 84.4% of the 39Ar, steps 7 through 16													
21-1mxs	matrix													
MASS=	1.703 mg													
J =	3.52E-03	+/-	6.52E-06	(2 Sigma)						0.185 Percent				
STEP	POWER	40Ar/39Ar	37Ar/39Ar	36Ar/39Ar	Mol 39ArK	Ca/K	% 40ArA	Cum 39ArK	Age [Ma]	2 Sigma	A.I. (36/37)			
1	1.25E-01	1.27E+02	3.30E+00	4.11E-01	2.07E-16	6.48E+00	9.53E+01	1.01E-02	3.79E+01	1.26E+01	4.37E-02			
2	2.00E-01	3.82E+01	5.68E+00	1.18E-01	2.41E-16	1.12E+01	8.99E+01	2.18E-02	2.46E+01	1.33E+01	7.19E-03			
3	3.00E-01	2.41E+01	5.75E+00	6.55E-02	1.86E-16	1.13E+01	7.72E+01	3.09E-02	3.47E+01	1.08E+01	3.86E-03			
4	4.00E-01	1.79E+01	3.40E+00	3.25E-02	2.52E-16	6.89E+00	5.12E+01	4.32E-02	5.49E+01	3.82E+00	3.21E-03			
5	5.00E-01	1.28E+01	2.53E+00	1.70E-02	4.75E-16	4.96E+00	3.66E+01	6.64E-02	5.10E+01	3.15E+00	2.21E-03			
6	6.00E-01	1.11E+01	2.75E+00	1.20E-02	8.97E-16	5.40E+00	2.89E+01	1.10E-01	4.94E+01	1.39E+01	1.39E-03			
7	7.00E-01	9.42E+00	2.85E+00	7.09E-03	1.03E-15	5.60E+00	1.83E+01	1.60E-01	4.83E+01	1.07E+00	7.20E-04			
8	8.00E-01	9.06E+00	3.30E+00	6.82E-03	1.15E-15	6.48E+00	1.75E+01	2.16E-01	4.70E+01	5.57E-01	5.73E-04			
9	9.00E-01	8.36E+00	3.31E+00	4.23E-03	1.80E-15	6.51E+00	9.81E+00	3.04E-01	4.74E+01	4.99E-01	2.95E-04			
10	1.00E+00	7.85E+00	3.32E+00	2.68E-03	1.49E-15	6.54E+00	4.57E+00	3.77E-01	4.71E+01	5.98E-01	1.28E-04			
11	1.10E+00	7.71E+00	3.44E+00	2.28E-03	1.40E-15	6.76E+00	2.91E+00	4.45E-01	4.71E+01	5.98E-01	7.75E-05			
12	1.20E+00	7.63E+00	3.27E+00	1.79E-03	1.66E-15	6.43E+00	1.33E+00	5.26E-01	4.73E+01	4.77E-01	3.67E-05			
13	1.35E+00	7.57E+00	3.42E+00	2.05E-03	1.58E-15	6.72E+00	2.13E+00	6.03E-01	4.66E+01	6.00E-01	5.58E-05			
14	1.50E+00	7.56E+00	3.26E+00	1.82E-03	1.66E-15	6.42E+00	1.48E+00	6.84E-01	4.68E+01	5.75E-01	4.05E-05			
15	2.00E+00	7.58E+00	3.46E+00	1.94E-03	3.07E-15	6.80E+00	1.63E+00	8.33E-01	4.69E+01	3.95E-01	4.21E-05			
16	3.00E+00	7.69E+00	3.38E+00	2.31E-03	3.14E-15	6.64E+00	3.14E+00	9.86E-01	4.68E+01	4.58E-01	4.88E-05			
17	5.00E+00	7.86E+00	3.18E+00	2.98E-03	2.72E-16	6.25E+00	5.93E+00	1.00E+00	4.65E+01	2.25E+00	1.74E-04			
Total Gas Age =	4.68E+01	+/-	1.64E-01	Ma (2Sigma)										
Plateau age =	47.01±0.20 Ma (2s, including J-error of .185%) MSWD = 0.97, probability = 0.46 78.4% of the 39Ar, steps 9 through 17													
25-4fss	K-feldspar													
MASS=	2.074 mg													
J =	3.46E-03	+/-	5.95E-06	(2 Sigma)						0.172 Percent				
STEP	POWER	40Ar/39Ar	37Ar/39Ar	36Ar/39Ar	Mol 39ArK	Ca/K	% 40ArA	Cum 39ArK	Age [Ma]	2 Sigma	A.I. (36/39)			
1	2.00E-01	2.55E+03	2.11E+00	8.07E+00	3.43E-19	4.15E+00	9.34E+01	4.19E-06	8.34E+02	2.20E+03	2.79E+00			
2	3.00E-01	7.20E+02	-2.82E-01	2.24E+00	2.28E-18	-5.54E-01	9.20E+01	3.21E-05	3.29E+02	3.86E+02	7.75E-01			
3	4.00E-01	4.64E+02	2.38E-02	1.60E+00	5.07E-18	4.66E-02	1.02E+02	9.40E-05	-5.22E+01	1.93E+02	5.53E-01			
4</														

10-11fss		plagioclase								0.195 Percent			
MASS=		2.500 mg											
J =		3.42E-03											
		+/-				6.67E-06				(2 Sigma)			
STEP	POWER	40Ar/39Ar	37Ar/39Ar	36Ar/39Ar	Mol 39ArK	Ca/K	% 40ArA	Cum 39ArK	Age [Ma]	2 Sigma	A.I. (36/37)		
1	1.25E-01	6.14E+02	-3.22E+01	1.83E+00	2.00E-18	-6.13E+01	8.90E+01	4.63E-04	3.66E+02	2.68E+02	-2.00E-02		
2	2.00E-01	4.09E+02	8.86E+00	1.31E+00	6.73E-18	1.75E+01	9.45E+01	2.02E-03	1.34E+02	1.15E+02	5.15E-02		
3	3.00E-01	1.54E+02	4.54E+00	4.87E-01	2.14E-17	8.93E+00	9.29E+01	6.99E-03	6.70E+01	4.96E+01	3.72E-02		
4	4.00E-01	6.77E+01	1.38E+01	2.09E-01	3.79E-17	2.74E+01	8.85E+01	1.58E-02	4.81E+01	2.89E+01	5.11E-03		
5	6.00E-01	3.36E+01	2.48E+01	9.84E-02	1.21E-16	4.98E+01	7.69E+01	4.38E-02	4.84E+01	7.77E+00	-1.23E-03		
6	8.00E-01	1.49E+01	3.05E+01	3.72E-02	1.45E-16	6.16E+01	4.73E+01	7.75E-02	4.90E+01	6.85E+00	2.71E-04		
7	1.00E+00	1.05E+01	2.88E+01	2.05E-02	1.64E-16	5.79E+01	2.21E+01	1.16E-01	5.09E+01	4.66E+00	9.43E-05		
8	1.20E+00	9.95E+00	3.09E+01	2.07E-02	1.40E-16	6.25E+01	2.09E+01	1.48E-01	4.93E+01	6.05E+00	7.88E-05		
9	1.50E+00	9.56E+00	2.92E+01	1.92E-02	2.46E-16	5.89E+01	1.94E+01	2.05E-01	4.81E+01	3.25E+00	7.44E-05		
10	2.00E+00	8.97E+00	3.01E+01	1.71E-02	5.23E-16	6.08E+01	1.24E+01	3.26E-01	4.92E+01	1.45E+00	4.32E-05		
11	2.50E+00	1.21E+01	3.00E+01	2.76E-02	1.08E-15	6.05E+01	3.52E+01	5.75E-01	4.90E+01	1.48E+00	1.67E-04		
12	3.00E+00	8.88E+00	2.99E+01	1.68E-02	5.18E-16	6.03E+01	1.20E+01	6.96E-01	4.89E+01	1.86E+00	4.17E-05		
13	4.00E+00	8.42E+00	3.13E+01	1.49E-02	3.82E-16	6.32E+01	3.97E+00	7.84E-01	5.06E+01	1.70E+00	1.22E-05		
14	5.00E+00	8.55E+00	3.14E+01	1.59E-02	2.55E-16	6.35E+01	7.16E+00	8.43E-01	4.97E+01	4.11E+00	2.26E-05		
15	6.00E+00	8.49E+00	3.17E+01	1.62E-02	3.08E-16	6.40E+01	7.76E+00	9.15E-01	4.91E+01	3.09E+00	2.41E-05		
16	8.00E+00	8.76E+00	2.98E+01	1.64E-02	2.19E-16	6.02E+01	1.08E+01	9.65E-01	4.89E+01	3.79E+00	3.69E-05		
17	1.00E+01	8.59E+00	3.24E+01	1.28E-02	7.47E-17	6.55E+01	-5.04E+00	9.83E-01	5.64E+01	7.70E+00	-1.61E-05		
18	1.20E+01	8.74E+00	2.51E+01	1.54E-02	4.09E-17	5.04E+01	1.48E+01	9.92E-01	4.64E+01	1.41E+01	6.03E-05		
19	1.50E+01	9.46E+00	3.31E+01	2.45E-02	2.17E-17	6.69E+01	3.09E+01	9.97E-01	4.11E+01	2.54E+01	1.04E-04		
20	2.00E+01	8.81E+00	2.45E+01	2.26E-02	1.19E-17	4.92E+01	3.98E+01	1.00E+00	3.32E+01	5.18E+01	1.68E-04		
Total Gas Age =	4.96E+01	+/-		7.02E-01	Ma (2Sigma)								
Plateau age =	49.37±0.71 Ma (2s, including J-error of .195%) MSWD = 0.59, probability = 0.88 95.6% of the 39Ar, steps 6 through 20												
32-2fss		plagioclase								0.195 Percent			
MASS=		2.114 mg											
J =		3.42E-03											
		+/-				6.67E-06				(2 Sigma)			
STEP	POWER	40Ar/39Ar	37Ar/39Ar	36Ar/39Ar	Mol 39ArK	Ca/K	% 40ArA	Cum 39ArK	Age [Ma]	2 Sigma	A.I. (36/37)		
1	8.00E-01	4.77E+02	9.69E+00	1.59E+00	4.61E-17	1.92E+01	9.83E+01	4.16E-03	5.05E+01	2.94E+01	5.69E-02		
2	1.00E+00	7.79E+01	7.01E+00	2.48E-01	1.29E-16	1.38E+01	9.27E+01	1.58E-02	3.50E+01	1.01E+01	1.21E-02		
3	1.20E+00	3.56E+01	8.56E+00	1.05E-01	1.34E-16	1.69E+01	8.39E+01	2.79E-02	3.53E+01	1.17E+01	4.11E-03		
4	1.50E+00	3.83E+01	8.52E+00	1.13E-01	1.83E-16	1.68E+01	8.44E+01	4.44E-02	3.68E+01	7.89E+00	4.47E-03		
5	2.00E+00	4.44E+01	8.85E+00	1.30E-01	2.06E-16	1.75E+01	8.40E+01	6.30E-02	4.37E+01	6.95E+00	4.99E-03		
6	2.50E+00	8.50E+00	8.25E+00	1.21E-02	1.60E-15	1.63E+01	2.93E+01	2.07E-01	3.70E+01	7.89E-01	3.55E-04		
7	3.00E+00	6.54E+00	7.67E+00	5.00E-03	1.50E-15	1.51E+01	7.31E+00	3.43E-01	3.72E+01	7.29E-01	7.30E-05		
8	4.00E+00	7.05E+00	7.51E+00	6.68E-03	8.96E-16	1.48E+01	1.41E+01	4.24E-01	3.72E+01	8.84E-01	1.55E-04		
9	5.00E+00	6.29E+00	7.44E+00	4.28E-03	2.55E-15	1.47E+01	4.68E+00	6.54E-01	3.68E+01	3.55E-01	4.62E-05		
10	6.00E+00	6.47E+00	7.67E+00	4.75E-03	1.52E-15	1.51E+01	6.26E+00	7.91E-01	3.72E+01	4.89E-01	6.17E-05		
11	8.00E+00	6.13E+00	7.29E+00	3.34E-03	1.23E-15	1.44E+01	5.90E-01	9.02E-01	3.74E+01	5.88E-01	5.48E-06		
12	1.00E+01	6.16E+00	7.29E+00	2.49E-03	2.39E-16	1.44E+01	-3.46E+00	9.24E-01	3.91E+01	3.08E+00	-3.48E-05		
13	1.20E+01	6.16E+00	7.56E+00	3.36E-03	6.55E-16	1.49E+01	1.26E-01	9.83E-01	3.78E+01	1.13E+00	8.52E-07		
14	1.50E+01	6.23E+00	7.51E+00	1.86E-03	1.64E-16	1.48E+01	-6.88E+00	9.98E-01	4.08E+01	3.96E+00	-6.75E-05		
15	2.00E+01	6.40E+00	1.46E+01	-7.62E-03	2.74E-17	2.90E+01	-6.50E+01	1.00E+00	6.47E+01	2.46E+01	-3.38E-04		
Total Gas Age =	3.74E+01	+/-		2.19E-01	Ma (2Sigma)								
Plateau age =	37.11±0.23 Ma (2s, including J-error of .195%) MSWD = 1.4, probability = 0.18 93.5% of the 39Ar, steps 6 through 14												
32-5fss		plagioclase								0.195 Percent			
MASS=		3.268 mg											
J =		3.42E-03											
		+/-				6.67E-06				(2 Sigma)			
STEP	POWER	40Ar/39Ar	37Ar/39Ar	36Ar/39Ar	Mol 39ArK	Ca/K	% 40ArA	Cum 39ArK	Age [Ma]	2 Sigma	A.I. (36/37)		
1	8.00E-01	6.32E+02	1.24E+01	2.11E+00	4.84E-17	2.45E+01	9.82E+01	4.91E-03	6.90E+01	8.21E+01	5.91E-02		
2	1.00E+00	1.31E+02	8.50E+00	4.14E-01	9.20E-17	1.68E+01	9.25E+01	1.12E-02	6.03E+01	1.47E+01	1.68E-02		
3	1.20E+00	5.65E+01	7.79E+00	1.70E-01	1.47E-16	1.54E+01	8.71E+01	2.13E-02	4.46E+01	5.37E+00	7.44E-03		
4	1.50E+00	2.66E+01	8.30E+00	7.47E-02	3.14E-16	1.64E+01	7.89E+01	4.28E-02	3.46E+01	3.92E+00	2.98E-03		
5	2.00E+00	1.26E+01	8.39E+00	2.36E-02	5.23E-16	1.66E+01	4.67E+01	7.86E-02	4.11E+01	1.97E+00	8.23E-04		
6	2.50E+00	6.62E+00	8.87E+00	5.74E-03	1.71E-15	1.75E+01	8.14E+00	1.96E-01	3.74E+01	4.76E-01	7.11E-05		
7	3.00E+00	6.80E+00	8.95E+00	6.72E-03	1.03E-15	1.77E+01	1.21E+01	2.66E-01	3.68E+01	5.87E-01	1.08E-04		
8	3.50E+00	6.34E+00	8.84E+00	5.22E-03	3.03E-15	1.75E+01	6.17E+00	4.74E-01	3.66E+01	3.14E-01	5.17E-05		
9	4.00E+00	6.33E+00	8.55E+00	4.95E-03	1.63E-15	1.69E+01	5.49E+00	5.86E-01	3.68E+01	4.63E-01	4.74E-05		
10	5.00E+00	8.55E+00	8.17E+00	1.28E-02	6.26E-16	1.61E+01	3.16E+01	6.29E-01	3.59E+01	1.23E+00	3.89E-04		
11	6.00E+00	6.14E+00	7.91E+00	3.75E-03	2.14E-15	1.56E+01	1.29E+00	7.75E-01	3.72E+01	5.24E-01	1.14E-05		
12	8.00E+00	6.11E+00	7.72E+00	3.74E-03	1.24E-15	1.52E+01	1.62E+00	8.60E-01	3.69E+01	8.18E-01	1.48E-05		
13	1.00E+01	6.09E+00	8.37E+00	3.95E-03	8.88E-16	1.65E+01	1.29E+00	9.21E-01	3.69E+01	1.08E+00	1.07E-05		
14	1.20E+01	6.11E+00	8.36E+00	3.39E-03	5.79E-16	1.65E+01	-1.43E+00	9.60E-01	3.81E+01	1.32E+00	-1.27E-05		
15	1.50E+01	6.57E+00	7.94E+00	5.66E-03	4.22E-16	1.57E+01	9.74E+00	9.89E-01	3.64E+01	1.94E+00	9.44E-05		
16	1.75E+01	6.07E+00	7.66E+00	4.60E-03	8.20E-17	1.51E+01	5.97E+00	9.95E-01	3.51E+01	7.98E+00	5.53E-05		
17	2.00E+01	6.18E+00	4.96E+00	5.01E-03	6.93E-17	9.77E+00	1.35E+01	1.00E+00	3.28E+01	1.16E+01	1.98E-04		
18	2.25E+01	6.58E+00	-1.55E+01	1.12E-02	4.10E-18	-3.00E+01	8.13E+01	1.00E+00	7.46E+00	1.96E+02	-4.05E-04		
Total Gas Age =	3.76E+01	+/-		1.83E-01	Ma (2Sigma)								
Plateau age =	36.87±0.20 Ma (2s, including J-error of .195%) MSWD = 1.6, probability = 0.099 92.1% of the 39Ar, steps 6 through 17												
979fss		plagioclase								0.195 Percent			
MASS=		2.901 mg											
J =		3.42E-03											
		+/-				6.67E-06				(2 Sigma)			
STEP	POWER	40Ar/39Ar	37Ar/39Ar	36Ar/39Ar	Mol 39ArK	Ca/K	% 40ArA	Cum 39ArK	Age [Ma]	2 Sigma	A.I. (36/37)		
1	4.00E-01	1.04E+03	4.87E+01	3.46E+00	8.68E-17	1.00E+02	9.75E+01	3.58E-02	1.62E+02	6.46E+01	2.46E-02		
2	6.00E-01	2.63E+02	5.43E+01	8.44E-01	1.59E-16	1.12E+02	9.22E+01	1.02E-01	1.28E+02	1.86E+01	5.25E-03		
3	8.00E-01	3.81E+01	5.95E+01	1.06E-01	1.53E-16	1.24E+02	6.19E+01	1.64E-01	9.23E+01	8.78E+00	4.67E-04		
4	1.00E+00	1.15E+02	6.20E+01	3.66E-01	1.52E-16	1.29E+02	8.70E+01	2.27E-01	9.52E+01	1.38E+01	1.90E-03		
5	1.20E+00	4.38E+01	6.25E+01	1.29E-01	1.22E-16	1.30E+02	6.88E+01	2.78E-01	8.74E+01	1.28E+01	5.67E-04		
6	1.50E+00	9.32E+01	6.28E+01	2.94E-01	1.35E-16	1.31E+02	8.43E+01	3.33E-01	9.34E+01	7.72E+00	1.47E-03		
7	2.00E+00	3.51E+01	6.09E+01	9.95E-02	1.76E-16	1.27E+02	6.11E+01	4.06E-01	9.81E+01	8.78E+00	4.15E-04		
8	2.50E+00	2.68E+01	5.71E+01	7.35E-02	2.86E-16	1.18E+02	5.33E+01	5.24E-01	7.99E+01	5.31E+00	2.95E-04		
9	3.00E+00	2.15E+01	6.83E+01	6.06E-02	2.02E-16	1.43E+02	4.19E+01	6.07E-01	8.06E+01	5.82E+00	1.55E-04		
10	4.00E+00	2.60E+01	6.31E+01	7.17E-02	3.42E-16	1.32E+02	4.99E+01	7.49E-01	8.33E+01	4.14E+00	2.42E-04		
11	5.00E+00	2.15E+01	6.21E+01	5.90E-02	2.24E-16	1.29E+02	4.34E+01	8.41E-01	7.80E+01	3.87E+00	1.77E-04		
12	6.00E+00	2.40E+01	6.52E+01	6.90E-02	1.42E-16	1.36E+02	4.95E+01	9.00E-01	7.80E+01	6.64E+00	2.14E-04		
13	8.00E+00	2.23E+01	6.66E+01	6.46E-02	1.98E-16	1.39E+02	4.68E+01	9.81E-01	7.62E+01	5.48E+00	1.84E-04		
14	1.00E+01	2.12E+01	7.81E+01	6.73E-02	3.53E-17	1.65E+02	4.58E+01	9.96E-01	7.47E+01	3.14E+01	1.46E-04		
15	1.20E+01	2.59E+01	1.16E+02	2.61E-01	1.57E-18	2.55E+02	2.40E+02	9.96E-01					

JD3fss MASS= J =	plagioclase 2.060 mg 3.48E-03	+/-	5.61E-06	(2 Sigma)	0.161 Percent						
STEP	POWER	40Ar/39Ar	37Ar/39Ar	36Ar/39Ar	Mol 39ArK	Ca/K	% 40ArA	Cum 39ArK	Age [Ma]	2 Sigma	A.I. (36/37)
1	5.96E-01	5.96E+02	2.03E+02	2.02E+00	7.39E-17	4.92E+02	9.57E+01	6.58E-02	1.90E+02	5.08E+01	3.31E-03
2	8.00E-01	2.27E+02	1.95E+02	8.01E-01	1.33E-16	4.69E+02	9.32E+01	1.84E-01	1.16E+02	1.97E+01	1.28E-03
3	1.00E+00	1.47E+02	1.31E+02	5.20E-01	6.73E-17	2.94E+02	9.27E+01	2.44E-01	7.57E+01	1.92E+01	1.22E-03
4	1.20E+00	8.98E+01	1.20E+02	3.09E-01	5.83E-17	2.66E+02	8.42E+01	2.96E-01	9.75E+01	1.95E+01	7.41E-04
5	1.50E+00	6.02E+01	1.96E+02	2.44E-01	6.63E-17	4.71E+02	7.72E+01	3.55E-01	1.03E+02	2.09E+01	2.79E-04
6	2.00E+00	4.40E+01	2.55E+02	2.22E-01	8.01E-17	6.59E+02	7.36E+01	4.26E-01	9.37E+01	9.77E+00	1.49E-04
7	2.50E+00	2.82E+02	2.47E+02	1.02E+00	8.82E-17	6.33E+02	9.56E+01	5.05E-01	9.87E+01	2.40E+01	1.28E-03
8	3.00E+00	2.22E+01	6.33E+01	5.99E-02	1.44E-16	1.32E+02	4.26E+01	6.33E-01	8.31E+01	6.99E+00	1.75E-04
9	3.50E+00	1.88E+01	6.14E+01	4.70E-02	7.41E-17	1.28E+02	3.14E+01	6.99E-01	8.39E+01	1.32E+01	1.13E-04
10	4.00E+00	1.66E+01	5.92E+01	4.41E-02	4.53E-17	1.23E+02	3.20E+01	7.39E-01	7.33E+01	1.87E+01	1.05E-04
11	5.00E+00	1.84E+01	6.47E+01	4.93E-02	8.27E-17	1.35E+02	3.34E+01	8.13E-01	8.02E+01	8.74E+00	1.11E-04
12	6.00E+00	1.57E+01	7.34E+01	4.34E-02	7.76E-17	1.55E+02	2.06E+01	8.82E-01	8.24E+01	8.85E+00	5.17E-05
13	8.00E+00	2.41E+01	6.11E+01	6.29E-02	1.38E-17	1.27E+02	4.42E+01	8.94E-01	8.73E+01	4.81E+01	2.04E-04
14	1.00E+01	1.76E+01	5.71E+01	4.04E-02	6.53E-17	1.18E+02	2.55E+01	9.52E-01	8.48E+01	1.35E+01	9.20E-05
15	1.20E+01	2.23E+01	6.05E+01	5.87E-02	4.11E-17	1.26E+02	4.24E+01	9.89E-01	8.38E+01	1.78E+01	1.84E-04
16	1.50E+01	3.21E+01	6.17E+01	9.39E-02	9.00E-18	1.28E+02	6.14E+01	9.97E-01	8.07E+01	8.09E+01	3.76E-04
17	1.75E+01	1.04E+02	4.42E+01	4.25E-01	1.93E-18	9.05E+01	1.15E+02	9.99E-01	-1.05E+02	3.97E+02	3.19E-03
18	2.00E+01	6.71E+02	8.40E+01	2.66E+00	3.54E-19	1.79E+02	1.16E+02	9.99E-01	-9.14E+02	2.37E+03	1.09E-02
19	2.25E+01	3.04E+02	2.15E+01	9.42E-01	9.95E-19	4.30E+01	9.06E+01	1.00E+00	1.75E+02	5.22E+02	1.51E-02

Total Gas Age = 9.64E+01 +/- 3.39E+00 Ma (2Sigma)
 Plateau age = 84.8±3.5 Ma (2s, including J-error of .161%) MSWD = 0.95, probability = 0.51 81.6% of the 39Ar, steps 3 through 19

JD3fs2 MASS= J =	plagioclase 2.210 mg 3.48E-03	+/-	5.61E-06	(2 Sigma)	0.161 Percent						
STEP	POWER	40Ar/39Ar	37Ar/39Ar	36Ar/39Ar	Mol 39ArK	Ca/K	% 40ArA	Cum 39ArK	Age [Ma]	2 Sigma	A.I. (36/37)
1	4.00E-01	1.39E+03	1.34E+02	4.65E+00	1.40E-16	3.00E+02	9.75E+01	1.02E-01	2.38E+02	6.05E+01	1.19E-02
2	6.00E-01	1.02E+02	7.00E+01	3.27E-01	1.40E-16	1.47E+02	8.53E+01	2.05E-01	9.83E+01	1.07E+01	1.47E-03
3	8.00E-01	1.16E+02	9.13E+01	3.88E-01	1.19E-16	1.96E+02	8.87E+01	2.92E-01	9.75E+01	1.51E+01	1.32E-03
4	1.00E+00	3.26E+01	1.34E+02	1.28E-01	1.25E-16	3.01E+02	6.26E+01	3.84E-01	8.56E+01	7.65E+00	1.79E-04
5	1.20E+00	1.23E+02	1.13E+02	4.32E-01	3.40E-17	2.48E+02	9.22E+01	4.09E-01	6.60E+01	4.38E+01	1.18E-03
6	1.50E+00	3.61E+01	8.71E+01	1.15E-01	1.09E-16	1.86E+02	6.27E+01	4.89E-01	9.00E+01	8.60E+00	3.02E-04
7	2.00E+00	8.26E+01	1.57E+02	3.05E-01	1.07E-16	3.62E+02	8.44E+01	5.67E-01	9.62E+01	1.70E+01	5.22E-04
8	2.50E+00	5.16E+01	8.48E+01	1.69E-01	2.11E-16	1.81E+02	7.51E+01	7.21E-01	8.55E+01	7.10E+00	5.39E-04
9	3.00E+00	5.75E+01	6.64E+01	1.77E-01	3.06E-17	1.39E+02	7.58E+01	7.44E-01	9.10E+01	2.95E+01	1.79E-04
10	4.00E+00	2.85E+01	6.50E+01	8.24E-02	7.84E-17	1.36E+02	5.56E+01	8.01E-01	8.28E+01	1.13E+01	2.87E-04
11	5.00E+00	3.81E+01	7.25E+01	1.16E-01	4.95E-17	1.52E+02	6.53E+01	8.37E-01	8.68E+01	1.77E+01	4.03E-04
12	6.00E+00	4.54E+01	7.48E+01	1.51E-01	2.42E-17	1.58E+02	7.71E+01	8.55E-01	6.90E+01	3.20E+01	5.50E-04
13	8.00E+00	1.88E+01	7.50E+01	5.41E-02	4.99E-17	1.58E+02	3.32E+01	8.92E-01	8.27E+01	1.52E+01	9.75E-05
14	1.00E+01	8.06E+01	8.00E+01	2.66E-01	4.32E-17	1.70E+02	8.44E+01	9.23E-01	8.32E+01	2.16E+01	1.00E-03
15	1.20E+01	3.10E+01	7.05E+01	9.17E-02	5.26E-17	1.48E+02	5.78E+01	9.62E-01	8.60E+01	1.68E+01	2.99E-04
16	1.35E+01	4.35E+01	5.73E+01	1.31E-01	1.15E-17	1.19E+02	7.20E+01	9.70E-01	7.91E+01	5.59E+01	6.42E-04
17	1.50E+01	1.96E+01	5.58E+01	7.34E-02	9.01E-18	1.15E+02	7.37E+01	9.77E-01	7.39E+01	6.52E+01	3.04E-04
18	2.00E+01	2.21E+01	6.80E+01	6.62E-02	1.63E-17	1.42E+02	4.83E+01	9.89E-01	7.51E+01	3.50E+01	1.85E-04
19	2.25E+01	1.80E+01	6.55E+01	5.87E-02	8.95E-18	1.37E+02	4.91E+01	9.95E-01	6.02E+01	6.91E+01	1.58E-04
20	2.50E+01	1.82E+01	6.46E+01	5.04E-02	6.28E-18	1.35E+02	3.56E+01	1.00E+00	7.68E+01	1.06E+02	1.18E-04

Total Gas Age = 1.02E+02 +/- 3.29E+00 Ma (2Sigma)
 Plateau age = 86.9±3.3 Ma (2s, including J-error of .161%) MSWD = 0.75, probability = 0.75 89.3% of the 39Ar, steps 2 through 19

981fss MASS= J =	plagioclase 2.713 mg 3.42E-03	+/-	6.67E-06	(2 Sigma)	0.195 Percent						
STEP	POWER	40Ar/39Ar	37Ar/39Ar	36Ar/39Ar	Mol 39ArK	Ca/K	% 40ArA	Cum 39ArK	Age [Ma]	2 Sigma	A.I. (36/37)
1	3.00E-01	9.45E+02	7.03E+01	3.16E+00	3.18E-17	1.48E+02	9.79E+01	1.55E-02	1.25E+02	7.91E+01	1.52E-02
2	4.00E-01	1.58E+02	6.11E+01	5.07E-01	8.33E-17	1.27E+02	8.99E+01	5.60E-02	1.02E+02	1.44E+01	2.69E-03
3	6.00E-01	6.34E+01	6.87E+01	1.96E-01	2.11E-16	1.44E+02	7.75E+01	1.59E-01	9.16E+01	9.31E+00	8.27E-04
4	8.00E-01	1.15E+02	7.60E+01	3.76E-01	2.05E-16	1.61E+02	8.81E+01	2.59E-01	8.90E+01	8.52E+00	1.54E-03
5	1.00E+00	3.68E+01	8.50E+01	1.17E-01	1.54E-16	1.81E+02	6.40E+01	3.34E-01	8.68E+01	1.10E+01	3.02E-04
6	1.20E+00	2.40E+01	7.05E+01	6.75E-02	1.17E-16	1.48E+02	4.49E+01	3.91E-01	8.52E+01	7.42E+00	1.76E-04
7	1.50E+00	2.99E+01	6.50E+01	8.41E-02	1.30E-16	1.36E+02	5.48E+01	4.54E-01	8.68E+01	9.72E+00	2.62E-04
8	2.00E+00	2.81E+01	6.42E+01	7.95E-02	2.65E-16	1.34E+02	5.38E+01	5.83E-01	8.33E+01	3.54E+00	7.27E-04
9	2.50E+00	2.20E+01	6.57E+01	5.83E-02	3.16E-16	1.37E+02	3.93E+01	7.37E-01	8.58E+01	3.95E+00	1.52E-04
10	3.00E+00	2.16E+01	7.31E+01	5.89E-02	1.40E-16	1.54E+02	3.65E+01	8.05E-01	8.88E+01	6.94E+00	1.25E-04
11	4.00E+00	2.07E+01	7.19E+01	5.41E-02	8.30E-17	1.51E+02	3.21E+01	8.45E-01	9.05E+01	1.10E+01	1.06E-04
12	5.00E+00	2.68E+01	7.00E+01	7.99E-02	1.39E-16	1.47E+02	5.40E+01	9.13E-01	7.97E+01	6.99E+00	2.39E-04
13	6.00E+00	2.50E+01	7.53E+01	6.96E-02	6.56E-17	1.59E+02	4.30E+01	9.45E-01	9.22E+01	1.29E+01	1.65E-04
14	8.00E+00	2.44E+01	7.29E+01	7.48E-02	6.82E-17	1.53E+02	5.17E+01	9.78E-01	7.62E+01	1.11E+01	2.00E-04
15	1.00E+01	2.37E+01	7.36E+01	7.71E-02	1.25E-17	1.55E+02	5.56E+01	9.84E-01	6.84E+01	5.78E+01	2.07E-04
16	1.20E+01	2.01E+01	3.50E+01	5.91E-02	1.43E-17	7.09E+01	6.42E+01	9.91E-01	4.53E+01	4.39E+01	4.27E-04
17	1.50E+01	2.23E+01	5.17E+01	6.17E-02	1.07E-17	1.06E+02	5.16E+01	9.96E-01	8.66E+01	6.92E+01	2.57E-04
18	2.00E+01	1.79E+01	5.28E+01	1.86E-02	7.40E-18	1.09E+02	-7.73E+00	1.00E+00	1.21E+02	7.50E+01	-3.06E-05

Total Gas Age = 8.73E+01 +/- 1.90E+00 Ma (2Sigma)
 Plateau age = 84.7±2.0 Ma (2s, including J-error of .195%) MSWD = 0.98, probability = 0.46 72.6% of the 39Ar, steps 5 through 15

JD2bts MASS= J =	biotite 1.904 mg 3.48E-03	+/-	5.61E-06	(2 Sigma)	0.161 Percent						
STEP	POWER	40Ar/39Ar	37Ar/39Ar	36Ar/39Ar	Mol 39ArK	Ca/K	% 40ArA	Cum 39ArK	Age [Ma]	2 Sigma	A.I. (36/37)
1	5.00E-02	1.81E+03	-4.32E+00	6.10E+00	1.29E-17	-8.44E+00	9.98E+01	9.34E-05	2.05E+01	1.81E+02	2.12E+00
2	1.00E-01	5.69E+02	-1.45E-02	1.91E+00	7.17E-17	-2.85E-02	9.93E+01	6.14E-04	2.60E+01	2.14E+01	6.65E-01
3	1.50E-01	6.83E+01	1.00E-01	2.03E-01	3.30E-16	1.97E-01	8.80E+01	3.01E-03	5.07E+01	6.52E+00	7.08E-02
4	2.00E-01	2.00E+01	4.01E-01	3.99E-02	1.52E-16	7.86E-01	5.87E+01	4.11E-03	5.11E+01	4.31E+00	1.38E-02
5	2.50E-01	1.96E+01	1.01E-01	3.98E-02	5.49E-16	1.97E-01	5.98E+01	8.09E-03	4.89E+01	2.28E+00	1.38E-02
6	3.00E-01	1.25E+01	-1.21E-01	1.63E-02	1.01E-15	-2.37E-01	3.87E+01	1.54E-02	4.73E+01	9.44E-01	5.69E-03
7	4.00E-01	9.48E+00	6.16E-02	6.57E-03	4.26E-15	1.21E-01	2.04E+01	4.64E-02	4.67E+01	3.53E-01	2.28E-03
8	5.00E-01	8.14E+00	5.97E-02	2.20E-03	8.28E-15	1.17E-01	7.89E+00	1.06E-01	4.64E+01	2.00E-01	7.56E-04
9	6.00E-01	7.78E+00	5.35E-02	1.04E-03	1.40E-14	1.05E-01	3.86E+00	2.08E-01	4.63E+01	1.22E-01	3.53E-04
10	7.00E-01	7.63E+00	5.03E-02	4.21E-04	1.78E-14	9.86E-02	1.55E+00	3.37E-01	4.65E+01	1.44E-01	1.39E-04
11	8.00E-01	7.64E+00	3.34E-02	4.61E-04	2.07E-14	6.55E-02	1.73E+00	4.88E-01	4.65E+01	1.08E-01	1.55E-04
12	9.00E-01	7.52E+00	5.32E-02	2.49E-04	1.47E-14	1.04E-01	8.87E-01	5.94E-01	4.62E+01	1.32E-01	7.85E-05
13	1.00E+00	7.54E+00	4.18E-02	3.34E-04	1.19E-14	8.19E-02	1.24E+00	6.81E-01	4.62E+01	1.54E-01	1.10E-04
14	1.10E+00	7.55E+00	3.35E-02</								

JD2bt2 MASS= J =	biotite 1.618 mg 3.48E-03	+/-	5.61E-06	(2 Sigma)	0.161 Percent						
STEP	POWER	40Ar/39Ar	37Ar/39Ar	36Ar/39Ar	Mol 39ArK	Ca/K	% 40ArA	Cum 39ArK	Age [Ma]	2 Sigma	A.I. (36/39)
1	5.00E-02	6.29E+02	8.83E-01	2.10E+00	5.89E-17	1.73E+00	9.87E+01	4.97E-04	5.24E+01	5.55E+01	7.31E-01
2	1.00E-01	4.54E+01	4.42E-01	1.29E-01	2.84E-16	8.66E-01	8.42E+01	2.90E-03	4.46E+01	6.24E+00	4.50E-02
3	1.50E-01	2.09E+01	8.02E-02	4.54E-02	1.13E-15	1.57E-01	6.42E+01	1.24E-02	4.64E+01	1.81E+00	1.58E-02
4	2.00E-01	9.16E+00	-3.01E-02	5.45E-03	1.77E-15	-5.90E-02	1.76E+01	2.73E-02	4.67E+01	7.01E-01	1.90E-03
5	2.50E-01	8.33E+00	-2.44E-02	2.80E-03	4.12E-15	-4.79E-02	9.98E+00	6.21E-02	4.65E+01	3.74E-01	9.79E-04
6	3.00E-01	7.82E+00	2.94E-02	1.24E-03	7.56E-15	5.77E-02	4.64E+00	1.26E-01	4.62E+01	2.31E-01	4.27E-04
7	4.00E-01	7.71E+00	2.36E-02	8.33E-04	2.08E-14	4.63E-02	3.16E+00	3.01E-01	4.62E+01	1.54E-01	2.86E-04
8	5.00E-01	7.56E+00	4.43E-02	4.80E-04	1.68E-14	8.68E-02	1.80E+00	4.43E-01	4.60E+01	1.27E-01	1.60E-04
9	6.00E-01	7.57E+00	9.30E-02	6.07E-04	1.11E-14	1.82E-01	2.21E+00	5.36E-01	4.59E+01	1.79E-01	1.97E-04
10	7.00E-01	7.52E+00	8.71E-02	4.26E-04	1.63E-14	1.71E-01	1.53E+00	6.74E-01	4.59E+01	1.44E-01	1.35E-04
11	8.00E-01	7.48E+00	2.41E-02	1.89E-04	1.60E-14	4.73E-02	7.06E-01	8.08E-01	4.60E+01	1.33E-01	6.21E-05
12	9.00E-01	7.50E+00	4.71E-02	1.85E-04	6.71E-15	9.23E-02	6.46E-01	8.65E-01	4.61E+01	2.22E-01	5.70E-05
13	1.00E+00	7.50E+00	-1.63E-01	5.81E-05	2.18E-15	-3.19E-01	5.12E-01	8.83E-01	4.62E+01	5.29E-01	4.52E-05
14	1.10E+00	7.50E+00	-7.25E-02	8.65E-05	3.90E-15	-1.42E-01	4.67E-01	9.16E-01	4.62E+01	3.31E-01	4.12E-05
15	1.20E+00	7.50E+00	-1.07E-01	1.17E-04	2.81E-15	-2.10E-01	6.47E-01	9.40E-01	4.62E+01	3.89E-01	5.72E-05
16	1.50E+00	7.50E+00	7.22E-02	2.75E-04	3.31E-15	1.42E-01	9.57E-01	9.68E-01	4.60E+01	3.16E-01	8.44E-05
17	3.00E+00	7.52E+00	-1.31E-01	1.41E-04	3.20E-15	-2.56E-01	7.82E-01	9.95E-01	4.62E+01	2.54E-01	6.92E-05
18	5.00E+00	7.49E+00	-2.01E+00	-2.23E-04	3.54E-16	-3.93E+00	2.62E+00	9.98E-01	4.51E+01	2.61E+00	2.31E-04
19	1.00E+01	8.11E+00	9.12E-01	-3.74E-02	1.40E-17	1.79E+00	-1.38E+02	9.98E-01	1.17E+02	6.35E+01	-1.32E-02
20	1.50E+01	7.64E+00	-1.31E+00	-8.88E-04	2.68E-16	-2.57E+00	-1.20E+00	1.00E+00	4.78E+01	3.39E+00	-1.07E-04
Total Gas Age =	4.61E+01	+/-	5.47E-02	Ma (2Sigma)							
Plateau age =	45.990±0.096 Ma (2s, including J-error of .161%) MSWD = 1.3, probability = 0.23 69.3% of the 39Ar, steps 8 through 17										

Appendix II (CHAPTER II)

Appendix II a

Analytical Methods

Rock powders and chips were prepared from the least altered inner parts of the samples. Trace element and isotope data for the samples along with background information are shown in Appendix II b, Table 1. Trace element concentrations were determined with an AGILENT 7500cs inductively coupled plasma mass spectrometer at the Institute of Geosciences at the Christian-Albrechts University of Kiel. International reference material BIR-1, BHVO-2 and BCR-2 were digested and measured along with the samples. Results for the standards together with an evaluation of accuracy and precision are provided in Appendix II b, Tables 2-5.

Sr-Nd-Pb isotope analyses were carried out by thermal ionization mass spectrometry at GEOMAR. Prior to dissolution, the rock chips were leached in warm 2N HCl at 70 °C for 1 hour and thereafter repeatedly rinsed in ELGA water. Sr-Pb analyses were carried out on a Finnigan MAT 262 RPQ2+ and Nd on a Thermo Fisher TRITON, both operating in static multi-collection mode. Sr and Nd isotopic ratios were normalized within run to $^{86}\text{Sr}/^{88}\text{Sr} = 0.1194$ and $^{146}\text{Nd}/^{144}\text{Nd} = 0.7219$ respectively and all errors are reported as 2 sigma of the mean. Reference material measured along with the samples were normalized for each sample tourret and gave $^{87}\text{Sr}/^{86}\text{Sr} = 0.710250 \pm 0.000014$ ($n = 23$; 2σ

external reproducibility) for NBS987 and $^{143}\text{Nd}/^{144}\text{Nd} = 0.511850 \pm 0.000008$ ($n = 18$; 2σ external reproducibility) for La Jolla. Pb isotope ratios were determined using a Pb double-spike (DS) technique described in Hoernle et al. (2011). Double spike corrected NBS981 values over the course of the study are $^{206}\text{Pb}/^{204}\text{Pb} = 16.9413 \pm 0.0019$, $^{207}\text{Pb}/^{204}\text{Pb} = 15.4995 \pm 0.0019$, $^{208}\text{Pb}/^{204}\text{Pb} = 36.7241 \pm 0.0048$ ($n = 30$; 2σ external reproducibility). Total Pb chemistry blanks were 10-20pg and thus considered negligible. Hf isotopes were determined on a VG Axiom multi-collector ICPMS (MC-ICPMS) at GEOMAR operating in static mode. Our in-house SPEX Hf ICP standard solution (Lot #9) yields an averaged, JMC475-normalized value of $^{176}\text{Hf}/^{177}\text{Hf} = 0.282173 \pm 0.000008$ ($n = 132$). Additional references on the details of the geochemical methods are provided in Appendix II e.

We plot the measured, rather than the initial, isotopic ratios for the following reasons: 1) The samples display an age range of ~ 100 Ma and are thus difficult to compare at a common age without making additional assumptions, such as parent/daughter ratios of the source. 2) Parent and daughter element concentrations or ratios are not available for most of the published data and would need to be assumed to make age corrections. 3) The relatively low parent/daughter ratios (e.g. U/Pb; see Appendix II b) result in negligible radiogenic ingrowth (e.g. Fig. 2A), and thus the Gough and Tristan subtracks still form distinct fields on isotope correlation diagrams when initial isotopic ratios are plotted.

Appendix II b

Trace element and isotope data

Table 1: Trace element and Sr-Nd-Pb-Hf isotope data of samples from the Guyot Province and the Walvis Ridge

Appendix IIIb (Table 1) Trace element and Sr-Nd-Pb-Hf isotope data of samples from the Guyot Province and the Walvis Ridge

Sample	Tristan Track					
	AII-93-3-1B	AII-93-3-25	AII-93-3-25*	AII-93-5-3	AII-93-6-1	PS69/435-1-DR 27-1
Rock Type	Alkali Basalt	Alkali Basalt	Alkali Basalt	Alkali Basalt	Tephrite	Alkali Basalt
Ar/Ar Age (Ma)	27	27	27	36	33	42
Lat. (°)	-37.10	-37.10	-37.10	-34.29	-34.35	-32.9
Long. (°)	-7.78	-7.78	-7.78	-5.03	-4.98	-5.15
Depth (m.b.s.l.)	2600-2000	2600-2000	2600-2000	3100-3000	2360-2460	2400-2290
Cruise	R/V Atlantis II (AII-93)	R/V Atlantis II (AII-93)	R/V Atlantis II (AII-93)	R/V Atlantis II (AII-93)	R/V Atlantis II (AII-93)	R/V Polarstern ANT-XXIII/5
Li (ppm)	32.0	36.7	37.4	25.9	37.5	28.2
Sc (ppm)	33.7	33.2	33.5	25.5	22.7	35.6
V (ppm)	291	291	288	279	222	236
Cr (ppm)	56.8	56.6	56.0	20.0	29.9	237
Co (ppm)	45.5	40.4	40.0	24.1	17.5	42.7
Ni (ppm)	41.2	41.6	41.7	19.3	20.9	136
Cu (ppm)	46.7	44.8	44.6	47.8	23.3	62.8
Zn (ppm)	118	129	128	124	124	102
Ga (ppm)	21.3	21.4	21.1	22.8	17.9	19.8
Rb (ppm)	22.9	35.7	35.8	19.5	28.7	9.29
Sr (ppm)	441	434	430	571	587	334
Y (ppm)	27.4	26.5	26.5	58.8	55.9	34.5
Zr (ppm)	170	167	164	237	240	168
Nb (ppm)	25.8	24.8	24.8	42.5	41.7	17.9
Cs (ppm)	1.98	3.34	3.37	0.441	0.469	0.249
Ba (ppm)	351	347	344	433	396	146
La (ppm)	26.2	25.6	26.0	65.3	52.3	15.5
Ce (ppm)	54.9	53.7	53.9	81.7	84.6	35.2
Pr (ppm)	6.83	6.68	6.76	12.9	10.8	4.81
Nd (ppm)	28.6	27.9	28.4	51.9	43.6	21.1
Sm (ppm)	6.49	6.35	6.41	10.1	8.95	5.35
Eu (ppm)	2.38	2.33	2.34	3.20	2.90	1.85
Gd (ppm)	6.56	6.37	6.48	10.5	8.97	5.97
Tb (ppm)	0.990	0.962	0.979	1.54	1.31	0.990
Dy (ppm)	5.71	5.53	5.66	9.04	7.70	6.29
Ho (ppm)	1.09	1.05	1.07	1.83	1.56	1.29
Er (ppm)	2.80	2.72	2.74	4.88	4.25	3.58
Tm (ppm)	0.386	0.373	0.381	0.690	0.603	0.531
Yb (ppm)	2.41	2.34	2.38	4.33	3.87	3.45
Lu (ppm)	0.348	0.336	0.344	0.658	0.591	0.523
Hf (ppm)	4.18	4.01	4.09	5.94	5.68	3.76
Ta (ppm)	1.63	1.57	1.62	2.71	2.63	1.12
Pb (ppm)	1.98	1.91	1.95	3.20	3.11	1.47
Th (ppm)	2.76	2.65	2.73	4.48	4.25	1.59
U (ppm)	0.626	0.478	0.487	1.00	1.16	0.468

Sample	AII-93-3-1B	AII-93-3-25	AII-93-3-25*	AII-93-5-3	AII-93-6-1	PS69/435-1-DR 27-1
⁸⁷ Sr/ ⁸⁶ Sr _m	0.704480	0.704486		0.704951	0.705032	0.704396
±2σ	5	5		5	5	5
⁸⁷ Rb/ ⁸⁶ Sr	0.150	0.238		0.099	0.141	0.080
⁸⁷ Sr/ ⁸⁶ Sr _m	0.704422	0.704395		0.704900	0.704966	0.704349
¹⁴³ Nd/ ¹⁴⁴ Nd _m	0.512637	0.512633		0.512616	0.512619	0.512752
±2σ	3	3		3	3	3
εNd	-0.02	-0.09		-0.43	-0.38	2.22
¹⁴⁷ Sm/ ¹⁴⁴ Nd	0.137	0.137		0.118	0.123	0.152
¹⁴³ Nd/ ¹⁴⁴ Nd _{in}	0.512613	0.512609		0.512588	0.512592	0.512710
εNd _{in}	0.19	0.11		-0.07	-0.07	2.46
²⁰⁶ Pb/ ²⁰⁴ Pb _m	18.1835	18.1691		18.6339	18.6823	18.6531
±2σ	14	9		10	12	9
²⁰⁷ Pb/ ²⁰⁴ Pb _m	15.5256	15.5248		15.5862	15.5879	15.5602
±2σ	12	8		10	11	9
²⁰⁸ Pb/ ²⁰⁴ Pb _m	38.5721	38.5632		39.0848	39.1117	38.8756
±2σ	32	19		28	28	26
²⁰⁷ Pb/ ²⁰⁶ Pb _m	0.85383	0.85446		0.83645	0.83437	0.83419
±2σ	1	1		2	1	1
²⁰⁸ Pb/ ²⁰⁶ Pb _m	2.12127	2.12246		2.09752	2.09352	2.08414
±2σ	3	3		6	4	6
²³⁸ U/ ²⁰⁴ Pb	20.00	15.83		20.11	24.03	20.42
²³⁵ U/ ²⁰⁴ Pb	0.15	0.11		0.15	0.17	0.15
²³² Th/ ²⁰⁴ Pb	91.14	90.52		92.91	90.73	71.56
²³² Th/ ²³⁸ U	4.56	5.72		4.62	3.78	3.50
²⁰⁶ Pb/ ²⁰⁴ Pb _{in}	18.100	18.103		18.521	18.559	18.520
²⁰⁷ Pb/ ²⁰⁴ Pb _{in}	15.522	15.522		15.581	15.582	15.554
²⁰⁸ Pb/ ²⁰⁴ Pb _{in}	38.450	38.442		38.919	38.963	38.727
²⁰⁷ Pb/ ²⁰⁶ Pb _{in}	0.858	0.857		0.841	0.840	0.840
²⁰⁸ Pb/ ²⁰⁶ Pb _{in}	2.124	2.124		2.101	2.099	2.091
delta 7/4	6.3	6.4		7.5	7.2	4.7
delta 8/4	96.1	97.0		92.9	89.8	69.7
²⁰⁸ Pb*/ ²⁰⁶ Pb*	1.02	1.03		1.03	1.03	1.01
¹⁷⁶ Hf/ ¹⁷⁷ Hf _m	-	0.282848		0.282812	0.282805	0.282957
±2σ	-	6		3	3	7
εHf	-	2.67		1.40	1.15	6.55
¹⁷⁶ Lu/ ¹⁷⁷ Hf	-	0.012012		0.015901	0.014919	0.019929
¹⁷⁶ Hf/ ¹⁷⁷ Hf _{in}	-	0.282841		0.282801	0.282795	0.282941
εHf _{in}	-	3.06		1.83	1.57	6.93

Gough Track						
Sample	AII-93-10-11	AII-93-14-1	AII-93-14-19	PS69/419-1-DR 20-1	PS69/419-1-DR 20-1**	PS69/421-2-DR 23-1
Rock Type	Alkali Basalt	Mugearite	Mugearite	Alkali Basalt	Alkali Basalt	Tephrite
Ar/Ar Age (Ma)	49	51	51	53	53	47
Lat. (°)	-34.34	-31.99	-31.99	-31.53	-31.53	-33.35
Long. (°)	-1.57	2.39	2.39	2.02	2.02	2.12
Depth (m.b.s.l.)	2300-2000	2300-1600	2300-1600	2600-2240	2600-2240	1970-1660
Cruise	R/V Atlantis II (AII-93)	R/V Atlantis II (AII-93)	R/V Atlantis II (AII-93)	R/V Polarstern ANT-XXIII/5	R/V Polarstern ANT-XXIII/5	R/V Polarstern ANT-XXIII/5
Li (ppm)	11.6	19.9	38.2	54.0		8.38
Sc (ppm)	28.8	21.3	20.6	23.6		21.0
V (ppm)	368	165	159	215		263
Cr (ppm)	28.0	123	124	121		163
Co (ppm)	40.5	30.1	52.8	18.7		28.5
Ni (ppm)	31.0	63.5	156	44.1		88.1
Cu (ppm)	113	35.0	33.1	51.6		35.7
Zn (ppm)	133	144	118	251		129
Ga (ppm)	24.0	24.4	23.7	24.7		25.2
Rb (ppm)	32.0	31.8	37.7	15.8		55.1
Sr (ppm)	494	437	446	375		827
Y (ppm)	30.4	30.8	29.9	31.0		33.0
Zr (ppm)	261	213	215	342		349
Nb (ppm)	29.6	31.1	31.1	42.3		54.8
Cs (ppm)	1.30	0.409	1.45	0.421		0.221
Ba (ppm)	350	1229	1278	371		827
La (ppm)	37.6	36.5	36.2	39.5		59.0
Ce (ppm)	80.8	77.1	75.2	79.3		114
Pr (ppm)	9.81	9.51	9.32	11.4		13.5
Nd (ppm)	40.1	39.8	38.6	45.4		51.9
Sm (ppm)	8.60	8.69	8.45	9.57		10.3
Eu (ppm)	2.78	4.07	3.98	2.97		3.15
Gd (ppm)	8.15	8.46	8.07	8.81		9.22
Tb (ppm)	1.19	1.22	1.18	1.31		1.30
Dy (ppm)	6.62	6.72	6.52	7.20		6.85
Ho (ppm)	1.21	1.23	1.19	1.29		1.22
Er (ppm)	3.03	3.04	2.95	3.21		2.99
Tm (ppm)	0.411	0.407	0.396	0.431		0.396
Yb (ppm)	2.47	2.46	2.41	2.63		2.36
Lu (ppm)	0.347	0.354	0.343	0.369		0.334
Hf (ppm)	6.46	4.95	4.95	7.46		7.92
Ta (ppm)	1.93	1.92	1.87	2.55		3.29
Pb (ppm)	3.43	3.38	3.35	4.33		5.28
Th (ppm)	3.61	3.33	3.30	5.17		6.93
U (ppm)	0.762	0.765	0.705	0.684		1.37

Sample	AII-93-10-11	AII-93-14-1	AII-93-14-19	PS69/419-1-DR 20-1	PS69/419-1-DR 20-1**	PS69/421-2-DR 23-1
$^{87}\text{Sr}/^{86}\text{Sr}_m$	0.705143	0.705345	0.705411	0.705289		0.705558
$\pm 2\sigma$	4	4	5	4		5
$^{87}\text{Rb}/^{86}\text{Sr}$	0.187	0.211	0.245	0.122		0.193
$^{87}\text{Sr}/^{86}\text{Sr}_m$	0.705012	0.705192	0.705234	0.705198		0.705430
$^{143}\text{Nd}/^{144}\text{Nd}_m$	0.512458	0.512513	0.512498	0.512498		0.512454
$\pm 2\sigma$	3	3	3	3		3
ϵNd	-3.50	-2.43	-2.73	-2.74		-3.60
$^{147}\text{Sm}/^{144}\text{Nd}$	0.129	0.132	0.132	0.127		0.120
$^{143}\text{Nd}/^{144}\text{Nd}_{in}$	0.512417	0.512469	0.512454	0.512454		0.512417
ϵNd_{in}	-3.08	-2.01	-2.30	-2.27		-3.14
$^{206}\text{Pb}/^{204}\text{Pb}_m$	17.8006	18.2603	18.2621	18.3314		18.1975
$\pm 2\sigma$	11	11	7	9		8
$^{207}\text{Pb}/^{204}\text{Pb}_m$	15.5234	15.5758	15.5752	15.5875		15.5644
$\pm 2\sigma$	10	13	7	11		9
$^{208}\text{Pb}/^{204}\text{Pb}_m$	38.2917	38.8708	38.9081	39.0642		38.9756
$\pm 2\sigma$	27	43	22	34		28
$^{207}\text{Pb}/^{206}\text{Pb}_m$	0.87207	0.85299	0.85287	0.85032		0.85530
$\pm 2\sigma$	1	2	1	2		2
$^{208}\text{Pb}/^{206}\text{Pb}_m$	2.15114	2.12871	2.13054	2.13100		2.14180
$\pm 2\sigma$	5	12	5	9		7
$^{238}\text{U}/^{204}\text{Pb}$	13.95	14.40	13.43	10.10		16.54
$^{235}\text{U}/^{204}\text{Pb}$	0.10	0.10	0.10	0.07		0.12
$^{232}\text{Th}/^{204}\text{Pb}$	68.33	64.83	64.88	78.82		86.53
$^{232}\text{Th}/^{238}\text{U}$	4.90	4.50	4.83	7.81		5.23
$^{206}\text{Pb}/^{204}\text{Pb}_{in}$	17.694	18.146	18.155	18.248		18.077
$^{207}\text{Pb}/^{204}\text{Pb}_{in}$	15.518	15.570	15.570	15.584		15.559
$^{208}\text{Pb}/^{204}\text{Pb}_{in}$	38.126	38.707	38.744	38.857		38.774
$^{207}\text{Pb}/^{206}\text{Pb}_{in}$	0.877	0.858	0.858	0.854		0.861
$^{208}\text{Pb}/^{206}\text{Pb}_{in}$	2.155	2.133	2.134	2.129		2.145
delta 7/4	10.3	10.5	10.5	10.9		10.1
delta 8/4	114.4	116.7	120.2	127.5		134.8
$^{208}\text{Pb}^*/^{206}\text{Pb}^*$	1.04	1.05	1.05	1.06		1.07
$^{176}\text{Hf}/^{177}\text{Hf}_m$	0.282708	0.282720	0.282718	0.282716	0.282727	0.282681
$\pm 2\sigma$	3	6	8	3	6	3
ϵHf	-2.25	-1.85	-1.93	-1.97	-1.59	-3.21
$^{176}\text{Lu}/^{177}\text{Hf}$	0.007704	0.010249	0.009937	0.007090	0.007090	0.006051
$^{176}\text{Hf}/^{177}\text{Hf}_{in}$	0.282701	0.282710	0.282708	0.282709	0.282720	0.282676
ϵHf_{in}	-1.40	-1.05	-1.12	-1.03	-0.64	-2.34

Gough Track

Sample	PS69/421-2-DR 23-1*	PS69/422-1-DR 24-1	PS69/423-1-DR 25-1a	PS69/423-1-DR 25-2	PS69/440-1-DR 32-2
Rock Type	Tephrite	Nephelinite	Alkali Basalt	Hawaiite	Alkali Basalt
Ar/Ar Age (Ma)	47	47	46	46	37
Lat. (°)	-33.35	-34.01	-34.92	-34.92	-37.48
Long. (°)	2.12	0.96	0.55	0.55	-2.43
Depth (m.b.s.l.)	1970-1660	2040-1940	2075-1900	2075-1900	1890-1390
Cruise	R/V Polarstern ANT-XXIII/5	R/V Polarstern ANT-XXIII/5	R/V Polarstern ANT-XXIII/5	R/V Polarstern ANT-XXIII/5	R/V Polarstern ANT-XXIII/5
Li (ppm)	8.43	45.5	31.4	22.2	27.4
Sc (ppm)	21.3	21.0	24.6	24.0	20.8
V (ppm)	265	221	227	230	268
Cr (ppm)	164	324	360	337	186
Co (ppm)	28.6	34.5	29.5	28.4	35.2
Ni (ppm)	89.7	91.0	85.8	109	111
Cu (ppm)	36.0	72.0	32.6	37.2	35.6
Zn (ppm)	131	155	142	154	131
Ga (ppm)	25.4	16.0	19.9	19.8	23.8
Rb (ppm)	55.7	22.1	29.6	41.4	20.0
Sr (ppm)	840	361	898	844	919
Y (ppm)	33.2	37.4	47.8	55.8	27.5
Zr (ppm)	353	236	330	309	265
Nb (ppm)	55.4	53.0	62.4	62.0	43.5
Cs (ppm)	0.223	0.549	0.642	0.790	0.229
Ba (ppm)	833	709	854	861	623
La (ppm)	59.4	67.5	71.6	74.2	42.9
Ce (ppm)	115	105	124	120	90.9
Pr (ppm)	13.6	12.4	15.1	15.4	11.0
Nd (ppm)	52.5	47.2	58.3	60.1	44.7
Sm (ppm)	10.4	8.74	10.8	11.2	9.32
Eu (ppm)	3.19	2.63	3.32	3.37	3.03
Gd (ppm)	9.34	8.19	10.0	10.5	8.32
Tb (ppm)	1.30	1.12	1.40	1.46	1.14
Dy (ppm)	6.92	5.95	7.65	8.12	6.00
Ho (ppm)	1.24	1.11	1.46	1.59	1.06
Er (ppm)	3.02	2.79	3.81	4.09	2.56
Tm (ppm)	0.400	0.361	0.516	0.549	0.331
Yb (ppm)	2.42	2.16	3.18	3.30	1.98
Lu (ppm)	0.336	0.313	0.467	0.481	0.276
Hf (ppm)	8.07	5.52	7.69	7.29	6.12
Ta (ppm)	3.37	3.13	3.76	3.73	2.72
Pb (ppm)	5.42	4.85	4.23	5.31	3.95
Th (ppm)	7.03	6.11	6.96	7.03	4.26
U (ppm)	1.42	1.66	2.03	1.51	0.953

Rock Type	PS69/421-2-DR 23-1 *	PS69/422-1-DR 24-1	PS69/423-1-DR 25-1a	PS69/423-1-DR 25-2	PS69/440-1-DR 32-2
⁸⁷ Sr/ ⁸⁶ Sr _m		0.705409	0.705337	0.705357	0.705519
±2σ		5	5	5	5
⁸⁷ Rb/ ⁸⁶ Sr		0.177	0.095	0.142	0.063
⁸⁷ Sr/ ⁸⁶ Sr _{in}		0.705291	0.705275	0.705264	0.705486
¹⁴³ Nd/ ¹⁴⁴ Nd _m		0.512504	0.512476	0.512476	0.512495
±2σ		3	2	3	3
εNd		-2.61	-3.16	-3.15	-2.80
¹⁴⁷ Sm/ ¹⁴⁴ Nd		0.111	0.112	0.112	0.125
¹⁴³ Nd/ ¹⁴⁴ Nd _{in}		0.512470	0.512442	0.512443	0.512464
εNd _{in}		-2.10	-2.67	-2.66	-2.46
²⁰⁶ Pb/ ²⁰⁴ Pb _m		18.1401	18.3236	18.3711	18.3079
±2σ		9	7	8	5
²⁰⁷ Pb/ ²⁰⁴ Pb _m		15.5777	15.5803	15.5883	15.6007
±2σ		8	8	9	5
²⁰⁸ Pb/ ²⁰⁴ Pb _m		38.9557	39.1268	39.0655	38.9339
±2σ		19	26	26	13
²⁰⁷ Pb/ ²⁰⁶ Pb _m		0.85875	0.85029	0.84853	0.85213
±2σ		1	1	1	1
²⁰⁸ Pb/ ²⁰⁶ Pb _m		2.14749	2.13532	2.12647	2.12662
±2σ		2	6	5	3
²³⁸ U/ ²⁰⁴ Pb		21.83	30.69	18.20	15.42
²³⁵ U/ ²⁰⁴ Pb		0.16	0.22	0.13	0.11
²³² Th/ ²⁰⁴ Pb		82.80	108.76	87.51	71.16
²³² Th/ ²³⁸ U		3.79	3.54	4.81	4.62
²⁰⁶ Pb/ ²⁰⁴ Pb _{in}		17.980	18.104	18.241	18.219
²⁰⁷ Pb/ ²⁰⁴ Pb _{in}		15.570	15.570	15.582	15.597
²⁰⁸ Pb/ ²⁰⁴ Pb _{in}		38.763	38.879	38.866	38.804
²⁰⁷ Pb/ ²⁰⁶ Pb _{in}		0.866	0.860	0.854	0.856
²⁰⁸ Pb/ ²⁰⁶ Pb _{in}		2.156	2.148	2.131	2.130
delta 7/4		12.0	10.3	10.6	12.5
delta 8/4		139.7	134.7	122.8	117.3
²⁰⁸ Pb*/ ²⁰⁶ Pb*		1.07	1.07	1.06	1.05
¹⁷⁶ Hf/ ¹⁷⁷ Hf _m		0.282752	0.282700	0.282720	0.282709
±2σ		4	5	5	8
εHf		-0.72	-2.54	-1.83	-2.24
¹⁷⁶ Lu/ ¹⁷⁷ Hf		0.008146	0.008721	0.009446	0.006459
¹⁷⁶ Hf/ ¹⁷⁷ Hf _{in}		0.282744	0.282692	0.282712	0.282704
εHf _{in}		0.08	-1.77	-1.09	-1.57

	Gough Track	Walvis Ridge
Sample	PS69/440-1-DR 32-5b	AII-93-21-1
Rock Type	Tephrite	Alkali Basalt
Ar/Ar Age (Ma)	37	90
Lat. (°)	-37.48	-25.44
Long. (°)	-2.43	6.70
Depth (m.b.s.l.)	1890-1390	3200-2600
Cruise	R/V Polarstern ANT-XXIII/5	R/V Atlantis II (AII-93)
Li (ppm)	30.3	17.0
Sc (ppm)	22.1	43.7
V (ppm)	294	362
Cr (ppm)	139	24.5
Co (ppm)	34.1	25.1
Ni (ppm)	94.8	44.5
Cu (ppm)	34.7	209
Zn (ppm)	161	146
Ga (ppm)	23.9	22.8
Rb (ppm)	31.4	36.0
Sr (ppm)	935	388
Y (ppm)	30.2	32.5
Zr (ppm)	235	189
Nb (ppm)	38.6	16.6
Cs (ppm)	1.18	1.31
Ba (ppm)	656	169
La (ppm)	39.2	18.8
Ce (ppm)	79.2	41.7
Pr (ppm)	9.91	5.75
Nd (ppm)	41.1	25.4
Sm (ppm)	8.81	6.16
Eu (ppm)	2.98	2.10
Gd (ppm)	8.11	6.56
Tb (ppm)	1.12	1.05
Dy (ppm)	5.99	6.31
Ho (ppm)	1.07	1.22
Er (ppm)	2.63	3.25
Tm (ppm)	0.343	0.458
Yb (ppm)	2.05	2.89
Lu (ppm)	0.292	0.416
Hf (ppm)	5.58	4.25
Ta (ppm)	2.40	1.12
Pb (ppm)	3.96	1.97
Th (ppm)	3.47	1.69
U (ppm)	1.39	0.556

Sample	PS69/440-1-DR 32-5b	AII-93-21-1
$^{87}\text{Sr}/^{86}\text{Sr}_m$	0.705519	0.705262
$\pm 2\sigma$	4	5
$^{87}\text{Rb}/^{86}\text{Sr}$	0.097	0.269
$^{87}\text{Sr}/^{86}\text{Sr}_m$	0.705468	0.704918
$^{143}\text{Nd}/^{144}\text{Nd}_m$	0.512501	0.512631
$\pm 2\sigma$	2	3
ϵNd	-2.67	-0.14
$^{147}\text{Sm}/^{144}\text{Nd}$	0.129	0.146
$^{143}\text{Nd}/^{144}\text{Nd}_m$	0.512470	0.512545
ϵNd_m	-2.35	0.44
$^{206}\text{Pb}/^{204}\text{Pb}_m$	18.3953	18.0632
$\pm 2\sigma$	6	9
$^{207}\text{Pb}/^{204}\text{Pb}_m$	15.6186	15.5888
$\pm 2\sigma$	5	9
$^{208}\text{Pb}/^{204}\text{Pb}_m$	38.8704	38.5971
$\pm 2\sigma$	13	25
$^{207}\text{Pb}/^{206}\text{Pb}_m$	0.84905	0.86301
$\pm 2\sigma$	1	2
$^{208}\text{Pb}/^{206}\text{Pb}_m$	2.11306	2.13678
$\pm 2\sigma$	2	7
$^{238}\text{U}/^{204}\text{Pb}$	22.48	17.88
$^{235}\text{U}/^{204}\text{Pb}$	0.16	0.13
$^{232}\text{Th}/^{204}\text{Pb}$	57.77	56.30
$^{232}\text{Th}/^{238}\text{U}$	2.57	3.15
$^{206}\text{Pb}/^{204}\text{Pb}_m$	18.266	17.812
$^{207}\text{Pb}/^{204}\text{Pb}_m$	15.613	15.577
$^{208}\text{Pb}/^{204}\text{Pb}_m$	38.765	38.346
$^{207}\text{Pb}/^{206}\text{Pb}_m$	0.855	0.875
$^{208}\text{Pb}/^{206}\text{Pb}_m$	2.122	2.153
$\delta 7/4$	13.4	14.0
$\delta 8/4$	100.3	113.2
$^{208}\text{Pb}^*/^{206}\text{Pb}^*$	1.03	1.04
$^{176}\text{Hf}/^{177}\text{Hf}_m$	0.282683	-
$\pm 2\sigma$	4	-
ϵHf	-3.16	-
$^{176}\text{Lu}/^{177}\text{Hf}$	0.007500	-
$^{176}\text{Hf}/^{177}\text{Hf}_m$	0.282677	-
ϵHf_m	-2.51	-

Isotopes: Internal errors are shown for the last significant digit(s).

Ar/Ar ages in regular font are from Rohde et al. (2012).

Ages in italics are estimated based on linear age-distance relationships of published age data from Rohde et al. (2012).

*ICPMS replicate analyses on separate sample dissolution

**MC-ICPMS replicate analyses on separate sample dissolution

$^{208}\text{Pb}^*/^{206}\text{Pb}^* =$

$[(^{208}\text{Pb}/^{204}\text{Pb})_{\text{sample}} - (^{208}\text{Pb}/^{204}\text{Pb})_{\text{Earth initial}}] / [(^{206}\text{Pb}/^{204}\text{Pb})_{\text{sample}} - (^{206}\text{Pb}/^{204}\text{Pb})_{\text{Earth initial}}]$;
after Galer and O'Nions, 1985.

$\delta 7/4$ and $\delta 8/4$ = deviation of $^{207}\text{Pb}/^{204}\text{Pb}$ and $^{208}\text{Pb}/^{204}\text{Pb}$ from the Northern Hemisphere Reference Line (NHRL) as defined in Hart, 1984.

Table 2: Reproducibility and accuracy of ICP-MS trace element data for BIR-1

Appendix IIb (Table 2)		Reproducibility and accuracy of ICP-MS trace element data for BIR-1						
# Analysis/ Element	#1	#2	#3	Mean	Std. dev. ($\pm 1\sigma$ abs)	Std. dev. ($\pm 1\sigma$ %)	Ref. Value ¹	Rel. dev. (%)
Li (ppm)	3.19	3.23	2.79	3.07	0.24	7.9	3.4	9.6
Sc (ppm)	44.3	40.5	33.5	39.4	5.45	13.8	44	10.4
V (ppm)	311	308	312	310	2.30	0.7	313	0.8
Cr (ppm)	374	386	389	383	7.96	2.1	382	-0.2
Co (ppm)	51.5	51.9	52.1	51.8	0.30	0.6	51.4	-0.8
Ni (ppm)	166	159	161	162	3.24	2.0	166	2.4
Cu (ppm)	125	113	113	117	7.01	6.0	126	6.9
Zn (ppm)	70.2	66.8	67.8	68.2	1.75	2.6	71	3.9
Ga (ppm)	16.0	15.3	15.2	15.5	0.47	3.0	16	3.1
Rb (ppm)	0.233	0.157	0.120	0.170	0.06	34.0	0.212	19.8
Sr (ppm)	107	105	99	104	4.27	4.1	104	0.2
Y (ppm)	15.8	14.8	14.0	14.8	0.92	6.2	16	7.2
Zr (ppm)	14.7	13.6	13.5	13.9	0.66	4.7	14	0.5
Nb (ppm)	0.525	0.539	0.537	0.533	0.01	1.5	0.55	3.0
Cs (ppm)	0.006	0.003	0.002	0.004	0.002	57.5	0.005	26.8
Ba (ppm)	6.33	6.05	5.92	6.10	0.21	3.4	5.83	-4.6
La (ppm)	0.585	0.579	0.564	0.576	0.01	1.9	0.62	7.1
Ce (ppm)	1.86	1.87	1.83	1.85	0.02	1.1	1.95	4.9
Pr (ppm)	0.363	0.368	0.358	0.363	0.005	1.4	0.38	4.4
Nd (ppm)	2.33	2.37	2.32	2.34	0.03	1.2	2.5	6.4
Sm (ppm)	1.08	1.10	1.07	1.08	0.02	1.4	1.1	1.6
Eu (ppm)	0.513	0.517	0.501	0.510	0.01	1.6	0.54	5.5
Gd (ppm)	1.74	1.77	1.73	1.75	0.02	1.2	1.85	5.5
Tb (ppm)	0.349	0.356	0.346	0.350	0.01	1.5	0.36	2.7
Dy (ppm)	2.52	2.54	2.47	2.51	0.04	1.5	2.5	-0.4
Ho (ppm)	0.562	0.561	0.541	0.555	0.01	2.2	0.57	2.7
Er (ppm)	1.61	1.61	1.54	1.59	0.04	2.4	1.7	6.7
Tm (ppm)	0.244	0.243	0.233	0.240	0.01	2.5	0.26	7.8
Yb (ppm)	1.62	1.59	1.52	1.58	0.05	3.2	1.65	4.5
Lu (ppm)	0.244	0.241	0.229	0.238	0.01	3.5	0.26	8.5
Hf (ppm)	0.551	0.558	0.550	0.553	0.005	0.8	0.581	4.8
Ta (ppm)	0.040	0.046	0.046	0.044	0.003	7.5	0.035	-26.0
Pb (ppm)	2.98	3.00	2.91	2.97	0.05	1.6	3.08	3.7
Th (ppm)	0.029	0.030	0.028	0.029	0.001	2.6	0.03	3.2
U (ppm)	0.012	0.010	0.010	0.011	0.001	11.0	0.01	-9.0

¹Preferred values of Hoernle et al. (2011).

Table 3: Reproducibility and accuracy of ICP-MS trace element data for BHVO-2

**Appendix IIb
(Table 3)**

Reproducibility and accuracy of ICP-MS trace element data for BHVO-2

# Analysis/ Element	#1	#2	#3	Mean	Std. dev. ($\pm 1\sigma$ abs)	Std. dev. ($\pm 1\sigma$ %)	Ref. value ¹	Rel. dev. (%)	Ref. Value (U.S. Geological Survey)
Li (ppm)	4.52	4.53	4.09	4.38	0.2	5.6	4.6	4.8	5
Sc (ppm)	32.7	31.8	30.4	31.6	1.2	3.6	31.8	0.5	32
V (ppm)	322	316	314	317	3.9	1.2	317*	-0.1	317
Cr (ppm)	293	295	294	294	1.2	0.4	289	-1.7	280
Co (ppm)	45.0	44.1	43.9	44.3	0.6	1.3	45*	1.6	45
Ni (ppm)	119	116	117	117	1.3	1.1	119*	1.4	119
Cu (ppm)	134	125	127	129	5.0	3.9	127*	-1.4	127
Zn (ppm)	104	104	104	104	0.3	0.3	103*	-1.0	103
Ga (ppm)	22.4	21.8	21.7	22.0	0.4	1.8	21.7*	-1.2	21.7
Rb (ppm)	9.32	9.26	8.30	8.96	0.6	6.4	9.2	2.6	9.8
Sr (ppm)	387	389	380	385	4.5	1.2	395	2.5	389
Y (ppm)	25.7	25.6	24.9	25.4	0.4	1.7	25.5	0.5	26
Zr (ppm)	170	174	175	173	2.6	1.5	174	0.4	172
Nb (ppm)	17.7	18.3	18.3	18.1	0.3	1.9	18*	-0.5	18
Cs (ppm)	0.108	0.104	0.074	0.096	0.02	19.2	0.11	13.1	
Ba (ppm)	132	132	132	132	0.5	0.4	130*	-1.6	130
La (ppm)	15.4	15.2	15.1	15.3	0.1	0.9	15.2	-0.4	15
Ce (ppm)	38.3	37.6	37.3	37.7	0.5	1.4	38*	0.7	38
Pr (ppm)	5.39	5.41	5.35	5.38	0.03	0.5	5.3	-1.5	
Nd (ppm)	24.4	24.9	24.8	24.7	0.3	1.2	25*	1.2	25
Sm (ppm)	6.13	6.19	6.15	6.16	0.03	0.5	6.2*	0.7	6.2
Eu (ppm)	2.07	2.08	2.07	2.07	0.01	0.4	2.06	-0.7	
Gd (ppm)	6.21	6.24	6.19	6.22	0.02	0.4	6.3*	1.3	6.3
Tb (ppm)	0.935	0.954	0.938	0.943	0.01	1.1	0.93	-1.4	0.9
Dy (ppm)	5.36	5.41	5.29	5.36	0.1	1.1	5.25	-2.0	
Ho (ppm)	0.983	0.984	0.974	0.98	0.01	0.6	0.99	1.0	1.04
Er (ppm)	2.44	2.46	2.43	2.44	0.02	0.7	2.5	2.2	
Tm (ppm)	0.328	0.329	0.323	0.327	0.004	1.1	0.34	4.0	
Yb (ppm)	2.00	2.00	1.96	1.98	0.02	1.1	2*	0.9	2.0
Lu (ppm)	0.280	0.278	0.272	0.276	0.004	1.5	0.28*	1.3	0.28
Hf (ppm)	4.33	4.16	4.19	4.23	0.1	2.1	4.07	-3.8	4.1
Ta (ppm)	1.10	1.13	1.13	1.12	0.02	1.6	1.13	0.5	1.4
Pb (ppm)	1.67	1.99	1.58	1.74	0.2	12.6	1.7	-2.6	
Th (ppm)	1.19	1.21	1.15	1.18	0.03	2.4	1.21	2.4	1.2
U (ppm)	0.409	0.419	0.421	0.416	0.01	1.6	0.41	-1.5	

¹Preferred values of the ICP-MS laboratory at the Institute of Geosciences at the Christian-Albrechts University of Kiel
 * equivalent to the certified values of the U.S. Geological Survey (http://crustal.usgs.gov/geochemical_reference_standards/)

Table 4: Accuracy of ICP-MS trace element data for BCR-2

# Analysis/ Element	Accuracy of ICP-MS trace element data for BCR-2		
	BCR-2	Ref. Value ¹	Rel. dev. (%)
Li (ppm)	8.88	9.00	1.3
Sc (ppm)	34.9	33.0	-5.7
V (ppm)	420	416	-1.0
Cr (ppm)	19.5	18.0	-8.2
Co (ppm)	37.7	37.0	-1.9
Ni (ppm)	12.1	12.3	1.7
Cu (ppm)	20.3	19.0	-6.9
Zn (ppm)	133	127	-5.1
Ga (ppm)	23.4	23.0	-1.6
Rb (ppm)	48.5	47.5	-2.2
Sr (ppm)	339	343	1.1
Y (ppm)	35.8	37.0	3.2
Zr (ppm)	189	186	-1.8
Nb (ppm)	12.0	12.6	4.4
Cs (ppm)	1.15	1.10	-4.2
Ba (ppm)	664	680	2.3
La (ppm)	25.2	25.0	-0.7
Ce (ppm)	52.9	53.0	0.2
Pr (ppm)	6.83	6.75	-1.2
Nd (ppm)	28.9	28.4	-1.8
Sm (ppm)	6.59	6.64	0.8
Eu (ppm)	1.95	1.98	1.7
Gd (ppm)	6.75	6.78	0.3
Tb (ppm)	1.05	1.07	2.2
Dy (ppm)	6.36	6.41	0.8
Ho (ppm)	1.28	1.31	2.1
Er (ppm)	3.48	3.66	4.8
Tm (ppm)	0.519	0.540	4.0
Yb (ppm)	3.36	3.44	2.4
Lu (ppm)	0.500	0.507	1.4
Hf (ppm)	4.71	4.85	2.8
Ta (ppm)	0.727	0.740	1.7
Pb (ppm)	10.7	11.0	2.8
Th (ppm)	5.67	5.95	4.8
U (ppm)	1.61	1.69	4.6

¹Reference values are from GeoReM
(<http://georem.mpch-mainz.gwdg.de/>)

Table 5: Reproducibility of ICP-MS trace element data based on sample replicates

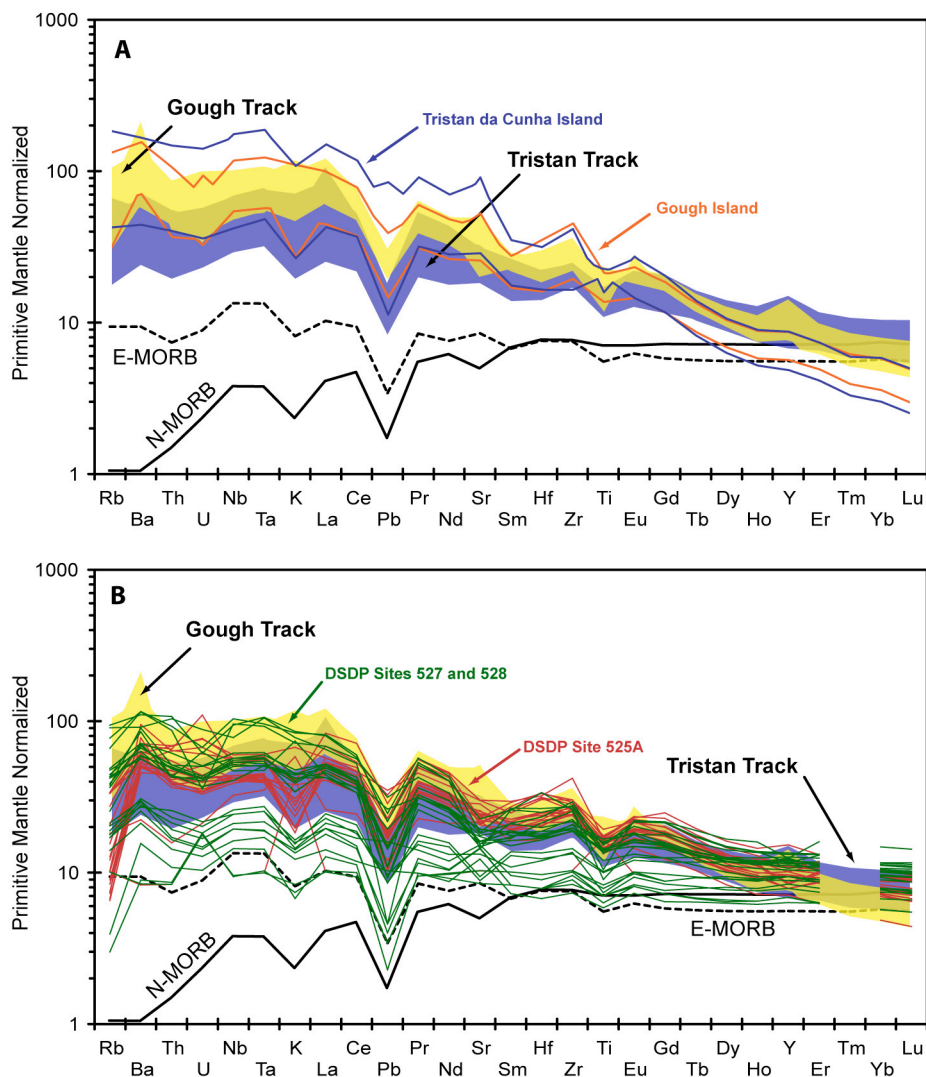
Appendix IIb
(Table 5) Reproducibility of ICP-MS trace element data based on sample replicates

# Analysis/ Element	AII-93-3-25 (1)	AII-93-3-25 (2)	Diff. (%)	PS69/421-2- DR 23-1 (1)	PS69/421-2- DR 23-1 (2)	Diff. (%)
Li (ppm)	36.7	37.4	-1.8	8.38	8.43	-0.5
Sc (ppm)	33.2	33.5	-0.8	21.0	21.3	-1.6
V (ppm)	291	288	0.8	263	265	-1.0
Cr (ppm)	56.6	56.0	0.9	163	164	-0.9
Co (ppm)	40.4	40.0	0.8	28.5	28.6	-0.4
Ni (ppm)	41.6	41.7	-0.1	88.1	89.7	-1.9
Cu (ppm)	44.8	44.6	0.5	35.7	36.0	-0.9
Zn (ppm)	129	128	0.8	129	131	-1.8
Ga (ppm)	21.4	21.1	1.3	25.2	25.4	-0.9
Rb (ppm)	35.7	35.8	-0.5	55.1	55.7	-1.1
Sr (ppm)	434	430	0.9	827	840	-1.6
Y (ppm)	26.5	26.5	-0.1	33.0	33.2	-0.4
Zr (ppm)	167	164	1.5	349	353	-1.3
Nb (ppm)	24.8	24.8	0.0	54.8	55.4	-1.1
Cs (ppm)	3.34	3.37	-0.8	0.221	0.223	-0.9
Ba (ppm)	347	344	0.9	827	833	-0.7
La (ppm)	25.6	26.0	-1.6	59.0	59.4	-0.6
Ce (ppm)	53.7	53.9	-0.4	114	115	-0.9
Pr (ppm)	6.68	6.76	-1.2	13.5	13.6	-0.9
Nd (ppm)	27.9	28.4	-2.0	51.9	52.5	-1.1
Sm (ppm)	6.35	6.41	-1.0	10.3	10.4	-0.8
Eu (ppm)	2.33	2.34	-0.4	3.15	3.19	-1.4
Gd (ppm)	6.37	6.48	-1.7	9.22	9.34	-1.3
Tb (ppm)	0.962	0.979	-1.8	1.30	1.30	-0.1
Dy (ppm)	5.53	5.66	-2.3	6.85	6.92	-1.0
Ho (ppm)	1.05	1.07	-2.3	1.22	1.24	-1.7
Er (ppm)	2.72	2.74	-0.8	2.99	3.02	-1.1
Tm (ppm)	0.373	0.381	-2.0	0.396	0.400	-1.1
Yb (ppm)	2.34	2.38	-1.9	2.36	2.42	-2.6
Lu (ppm)	0.336	0.344	-2.4	0.334	0.336	-0.6
Hf (ppm)	4.01	4.09	-2.0	7.92	8.07	-1.8
Ta (ppm)	1.57	1.62	-2.7	3.29	3.37	-2.6
Pb (ppm)	1.91	1.95	-2.2	5.28	5.42	-2.8
Th (ppm)	2.65	2.73	-3.0	6.93	7.03	-1.4
U (ppm)	0.478	0.487	-1.8	1.37	1.42	-3.7

Appendix II c

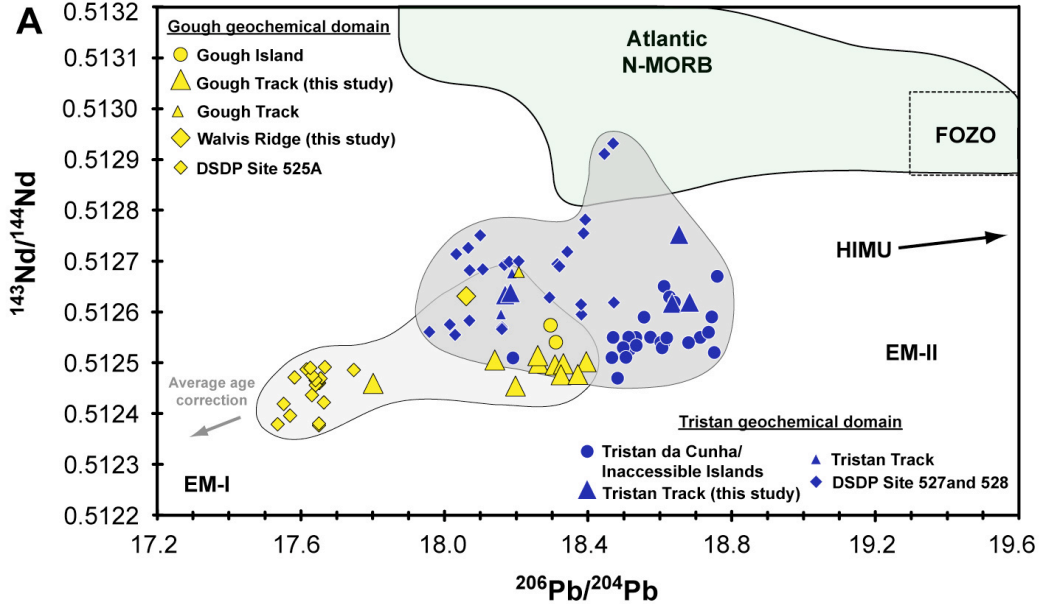
Multi-element diagrams

Incompatible element diagrams for Tristan and Gough subtrack samples including Tristan and Gough Islands and DSDP Sites 525A, 527 and 528. The diagrams include our data from the Guyot Province and published data for A: Tristan da Cunha and Gough Islands (Willbold and Stracke, 2006) and for B: DSDP Sites 525A, 527 and 528 (Salters and Sachi-Kocher, 2010). Values are primitive mantle normalized (Hofmann, 1988). N-MORB and E-MORB are also shown (Sun and McDonough, 1989). The incompatible element data for the Tristan and Gough subtracks do not show any systematic differences but instead largely overlap. References are provided in Appendix II e.



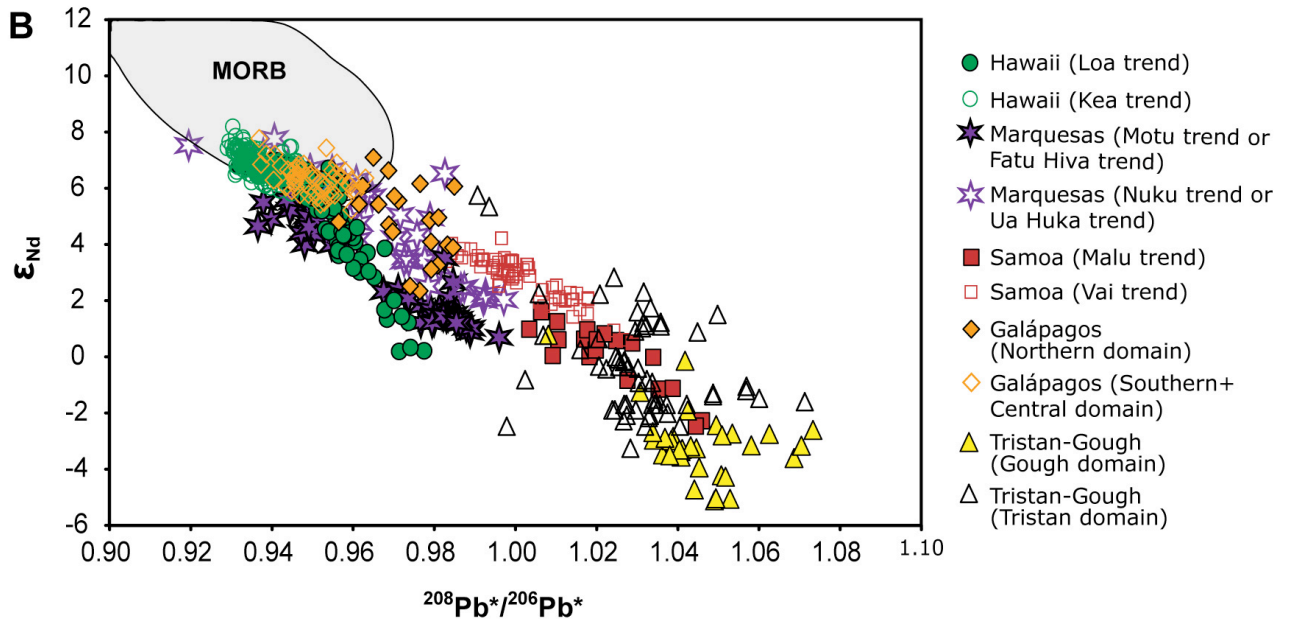
Appendix II d

(A) *Pb-Nd isotope variation diagram*



$^{206}\text{Pb}/^{204}\text{Pb}$ versus $^{143}\text{Nd}/^{144}\text{Nd}$ demonstrating that the Gough subtrack generally has less radiogenic Pb and Nd isotopic compositions (i.e. more enriched isotopic composition) than the Tristan subtrack. The Gough domain includes data from Gough Island and seamount/ridge chain in the Guyot Province, DSDP Site 525A and one dredge site on the Walvis Ridge. The Tristan domain includes data from Tristan da Cunha and Inaccessible Islands, the Tristan seamount/ridge chain in the Guyot Province and DSDP Sites 527 and 528 on the Walvis Ridge (published data compiled from GEOROC (<http://georoc.mpch-mainz.gwdg.de/georoc/>)). Gray arrow shows average reduction in isotopic ratios resulting from age correction for our Tristan and Gough data. Field for FOZO (Stracke et al., 2005) is also shown. Enriched mantle (EM-I and EM-II) from (Stracke et al., 2003). Data from Atlantic NMORB are compiled from PetDB (<http://www.petdb.org/>). References are provided in Appendix II e.

(B) $^{208}\text{Pb}^*/^{206}\text{Pb}^*$ versus ϵNd plot for the Tristan-Gough and zoned Pacific hotspots



Base data for Hawaii, the Marquesas, Samoa and Galápagos compiled from GEOROC (<http://georoc.mpch-mainz.gwdg.de/georoc/>). Data for the Tristan domain include our data from the Tristan subtrack and published data (Tristan da Cunha Islands, Tristan subtrack and DSDP Sites 527 and 528) compiled from GEOROC (<http://georoc.mpch-mainz.gwdg.de/georoc/>). Data for the Gough domain include our data from the Gough subtrack and the Walvis Ridge and published data (Gough Island, Gough subtrack and DSDP Site 525A) compiled from GEOROC (<http://georoc.mpch-mainz.gwdg.de/georoc/>). MORB data are compiled from PetDB (<http://www.petdb.org/>). Nomenclature of the Marquesan geochemical domains is from Huang et al. (2011) and Chauvel et al. (2012), respectively. References are provided in Appendix II e.

Appendix II e

Additional references

References for methods section

- Hoernle, K., Hauff, F., Kokfelt, T. F., Haase, K., Garbe-Schönberg, D., and Werner, R., 2011, On- and off-axis chemical heterogeneities along the South Atlantic Mid-Ocean-Ridge (5-11°S): Shallow or deep recycling of ocean crust and/or intraplate volcanism?: *Earth and Planetary Science Letters*, v. 306, p. 86-97.
- Hoernle, K., Hauff, F., Werner, R., van den Bogaard, P., Gibbons, A. D., Conrad, S., and Müller, R. D., 2011, Origin of Indian Ocean Seamount Province by shallow recycling of continental lithosphere: *Nature Geoscience*, v. 4, p. 883-887.
- Brandl, P.A., Beier, C., Regelous, M., Abouchami, W., Haase, K.M., Garbe-Schönberg, D., and Galer, S.J.G., 2012, Volcanism on the flanks of the East Pacific Rise: Quantitative constraints on mantle heterogeneity and melting processes: *Chemical Geology*, v. 298-299, p. 41-56.

References for Supplementary Information

- Hofmann, A. W., 1988, Chemical differentiation of the Earth: the relationship between mantle, continental crust, and oceanic crust: *Earth and Planetary Science Letters*, v. 90, p. 297-314.
- Huang, S., Hall, P. S., and Jackson, M. G., 2011, Geochemical zoning of volcanic chains associated with Pacific hotspots: *Nature Geoscience*, v. 4, p. 874-878.
- Salters, V. J. M., and Sachi-Kocher, A., 2010, An ancient metasomatic source for the Walvis Ridge basalts: *Chemical Geology*, v. 273, p. 151-167.
- Stracke, A., Bizimis, M., and Salters, V. J., 2003, M. Recycling oceanic crust: Quantitative constraints: *Geochemistry Geophysics Geosystems*, v. 4, no. 3, 8003, doi:10.1029/2001GC000223.
- Stracke, A., Hofmann, A. W., and Hart, S. R., 2005, FOZO, HIMU, and the rest of the mantle zoo. *Geochemistry Geophysics Geosystems*, v. 6, no. 5, Q05007, doi:10.1029/2004GC000824.
- Sun, S.-s. & McDonough, W. F., 1989, Chemical and isotopic systematics of oceanic basalts: implications for mantle composition and processes, *in* Saunders, A. D., and Norry, M. J., eds., *Magmatism in the Ocean Basins*: London, Geological Society [London] Special Publication 42, p. 313-345.

Willbold, M., and Stracke, A., 2006, Trace element composition of mantle endmembers: Implications for recycling of oceanic and upper and lower continental crust: *Geochemistry Geophysics Geosystems*, v. 7, no. 4, Q04004, doi:10.1029/2005GC001005.

Chauvel, C., Maury, R.C., Blais, S., Lewin, E., Guillou, H., Guille, G., Rossi, P., and Gutscher, M.-A., 2012, The size of plume heterogeneities constrained by Marquesas isotopic stripes: *Geochemistry Geophysics Geosystems*, v. 13, no. 1, Q07005, doi:10.1029/2012GC004123.

Appendix III (CHAPTER III)

Appendix III a

Major and selected trace element data

Table 1: Major and selected trace element data for the Walvis Ridge, the Rio Grande Rise and the Guyot Province

**Appendix IIIa
(Table 1)**

Major and selected trace element data for samples from the Walvis Ridge, the Rio Grande Rise and the Guyot Province

Sample	Tristan Track	Gough Track									Walvis Ridge	
	AK-1695-6	AII-93-11-8	PS69/420-1-DR 21-1	PS69/423-1-DR 25-4	PS69/424-1-DR 26-1	V29-9-1	AG51-6-1	AG51-6-5	AG51-7-1	AG51-7-2	DSDP Leg 74 525 A 53 2W 91-102	DSDP Leg 74 525 A 53 3W 87-97
Rock type	Trachyte	Trachyte	Trachyte	Trachyte	Picrobasalt	Alkali Basalt	Trachyte	Trachyte	Tephrite	Trachy-basalt	Basaltic Trachyandesite	Trachybasalt
Lab Method	1 XRF	1 XRF	1 XRF	1 XRF	1 XRF	2 ICP-ES	2 ICP-ES	2 ICP-ES	2 ICP-ES	2 ICP-ES	2 ICP-ES	2 ICP-ES
Major Elements (wt%)												
SiO ₂	60.9	59.5	60.7	60.7	39.6	45.9	61.0	61.2	43.1	44.9	53.5	43.2
TiO ₂	0.540	0.500	0.20	0.700	4.08*	3.70	0.420	0.440	4.02	3.94	2.61	2.16
Al ₂ O ₃	17.3	16.7	18.3	18.0	15.0	14.1	17.7	17.6	12.6	12.6	21.1	17.9
Fe ₂ O ₃	6.02	7.66	4.40	4.47	15.8	14.4	4.64	4.66	11.8	11.8	4.31	6.02
MnO	0.080	0.120	0.100	0.160	0.100	0.170	0.190	0.260	0.140	0.140	0.020	0.120
MgO	0.240	0.690	0.530	0.720	8	4.87	0.620	0.590	10.7	10.1	0.830	0.930
CaO	0.500	2.30	1.20	1.94	10.3	10.0	1.38	1.40	9.05	8.67	7.90	14.3
Na ₂ O	6.00	5.19	5.75	5.33	1.41	2.84	5.94	5.92	2.60	2.84	4.25	3.64
K ₂ O	6.50	6.00	6.34	6.64	0.930	0.920	6.39	6.31	1.84	2.16	1.33	0.980
P ₂ O ₅	0.190	0.170	0.090	0.370	0.610	0.540	0.220	0.230	1.09	0.830	0.320	0.290
LOI	0.990	1.18	2.08	0.690	4.54	2.30	1.30	1.10	3	2	3.50	10.2
TOTAL	99.32	100.06	99.65	99.68	100.64	99.65	99.77	99.74	99.40	99.37	99.71	99.75
Trace Elements (ppm)												
Co	15.0	BDL	BDL	<3	61.0	37.9	5.10	17.2	51.6	51.6	104	53.8
Cr	BDL	BDL	BDL	<3	501							
Ni	6.00	BDL	BDL	12.0	266							
Cu												
Sc						34.0	5.00	5.00	22.0	22.0	42.0	51.0
V	90.0	14.0	<6	35.0	347							
Zn	132	183	129	97.0	203							
Nb	111.0	109	226	151	70.0	28.5	148	141	46.6	46.8	17.4	15.6
Ga	36.0	33.0	36.0	29.0	21.0							
Rb	130	123	204	176.0	16.0							
Ba	192	942	BDL	227	533	214	98.0	118	822	825	318	280
Sr	19.0	69.0	29.0	226	957	430	84.0	87.1	1034	983	449	415
Y	41.0	49.0	41.0	14.0	31.0	36.2	35.7	36.5	30.5	30.8	29.9	35.5
Zr	575	694	1272	738	362	234	1035	933	319	345	233	183

1 = GEOMAR Helmholtz-Zentrum für Ozeanforschung Kiel; 2 = Acme Analytical Laboratories Ltd.; 3 = Mineralogisch-Petrographisches Institut, Universität Hamburg.

* = Element concentrations in excess of the XRF calibration lines; BDL = Below detection limit

Walvis Ridge

Sample	DSDP Leg 74 525 A 56 2W 68-79	DSDP Leg 74 525 A 56 2W 128-134	DSDP Leg 74 525 A 56 5W 42-53	DSDP Leg 74 525 A 57 2W 91-103	DSDP Leg 74 525 A 57 5W 141-148	DSDP Leg 74 525 A 58 1W 98-110	DSDP Leg 74 525 A 59 1W 110-119	DSDP Leg 74 525 A 60 4W 88-102
Rock type	Alkali Basalt	Tholeiitic Basalt	Tholeiitic Basalt	Alkali Basalt	Alkali Basalt	Alkali Basalt	Tholeiitic Basalt	Alkali Basalt
Lab Method	2 ICP-ES	2 ICP-ES	2 ICP-ES	2 ICP-ES	2 ICP-ES	2 ICP-ES	2 ICP-ES	2 ICP-ES
Major Elements (wt%)								
SiO ₂	43.8	47.3	49.1	49.3	48.6	43.6	49.0	46.2
TiO ₂	2.25	2.32	2.38	2.65	2.42	2.35	2.64	2.66
Al ₂ O ₃	13.8	13.5	14.0	15.7	14.1	13.9	14.8	15.6
Fe ₂ O ₃	11.9	12.6	11.7	10.1	12.1	8.78	10.5	8.11
MnO	0.230	0.130	0.120	0.110	0.120	0.170	0.100	0.140
MgO	4	6	5.04	4.03	5.51	1.90	4.92	2
CaO	12.5	9.8	9.29	9.30	9.04	13.8	8.71	12.2
Na ₂ O	3.00	2.83	3.15	3.47	3.14	3.02	3.19	3.40
K ₂ O	0.980	0.610	0.980	1.22	1.01	1.19	0.500	0.850
P ₂ O ₅	0.300	0.300	0.320	0.380	0.330	0.330	0.330	0.320
LOI	7.10	4.60	3.60	3.50	3.30	10.7	5.00	7.90
TOTAL	99.70	99.71	99.74	99.73	99.69	99.76	99.65	99.70
Trace Elements (ppm)								
Co	33.6	35.2	38.6	39.3	38.4	56.7	37.8	55.6
Cr								
Ni								
Cu								
Sc	33.0	35.0	35.0	36.0	34.0	34.0	38.0	38.0
V								
Zn								
Nb	19.5	18.8	19.8	22.6	20.4	20.6	21.1	23.4
Ga								
Rb								
Ba	293	297	328	375	314	339	290	359
Sr	440	437	432	484	420	458	492	536
Y	35.3	28.0	30.8	33.6	31.2	33.7	38.9	40.0
Zr	196	198	208	243	215	218	238	254

Walvis Ridge								
Sample	DSDP Leg 74 525 A 63 2W 59-78	DSDP Leg 74 527 39 1W 52-70	DSDP Leg 74 527 41 1W 47-63	DSDP Leg 74 527 41 5W 95-105	DSDP Leg 74 527 42 4W 59-68	DSDP Leg 74 527 43 4W 59-73	DSDP Leg 74 527 44 4W 59-72	DSDP Leg 74 528 40 2W 73-85
Rock type	Basaltic Trachyandesite	Alkali Basalt	Tholeiitic Basalt	Tholeiitic Basalt	Trachybasalt	Trachybasalt	Alkali Basalt	Tholeiitic Basalt
Lab	2	2	2	2	2	2	2	2
Method	ICP-ES	ICP-ES	ICP-ES	ICP-ES	ICP-ES	ICP-ES	ICP-ES	ICP-ES
Major Elements (wt%)								
SiO ₂	51.0	47.8	49.1	48.6	47.5	47.8	47.8	48.1
TiO ₂	3.09	1.91	1.22	1.42	2.47	2.43	2.47	1.22
Al ₂ O ₃	15.3	14.9	15.5	16.0	14.1	14.2	13.7	15.3
Fe ₂ O ₃	9.73	13.0	11.6	9.8	13.5	13.7	13.6	10.3
MnO	0.130	0.130	0.180	0.190	0.220	0.190	0.190	0.160
MgO	3.20	6.91	6.48	7.01	6.77	6.41	5.75	6.86
CaO	7.46	8.30	12.5	12.4	6.15	6.68	9.01	12.5
Na ₂ O	3.95	3.37	2.40	2.74	3.80	3.63	3.44	2.52
K ₂ O	2.21	0.430	0.250	0.190	1.20	1.21	1.03	0.460
P ₂ O ₅	0.670	0.210	0.110	0.120	0.370	0.420	0.360	0.140
LOI	2.90	2.70	0.400	1.10	3.70	3.10	2.40	2.40
TOTAL	99.66	99.65	99.73	99.65	99.66	99.70	99.71	99.79
Trace Elements (ppm)								
Co	44.7	54.9	48.1	52.0	41.2	44.6	44.6	44.9
Cr								
Ni								
Cu								
Sc	27.0	46.0	43.0	49.0	33.0	33.0	36.0	43.0
V								
Zn								
Nb	32.7	14.2	7.20	5.00	29.3	31.1	27.9	10.4
Ga								
Rb								
Ba	568	177	82.0	46.0	353	376	341	147
Sr	520	207	147	188	289	309	319	248
Y	52.5	42.4	27.9	31.5	39.1	42.8	39.4	23.9
Zr	373	128	65.4	85.7	185	183	164	76.9

Walvis Ridge

Sample	DSDP Leg 74 528 42 1W 29-45	DSDP Leg 74 528 42 5W 31-46	DSDP Leg 74 528 43 2W 80-98	DSDP Leg 74 528 44 3W 96-130	DSDP Leg 74 528 45 2W 109-119	DSDP Leg 74 528 47 2W 103-117	DSDP Leg 74 528 47 3W 66-80	WALVIS III DR04-35	V29-11-1	CIR 139D-2	CIR 139D-3
Rock type	Basaltic Trachyandesite	Tholeiitic Basalt	Tholeiitic Basalt	Alkali Basalt	Alkali Basalt	Trachybasalt	Trachybasalt	Trachybasalt	Basaltic Trachyandesite	Tholeiitic Basalt	Tholeiitic Basalt
Lab	2	2	2	2	2	2	2	2	2	2	2
Method	ICP-ES	ICP-ES	ICP-ES	ICP-ES	ICP-ES	ICP-ES	ICP-ES	ICP-ES	ICP-ES	ICP-ES	ICP-ES
Major Elements (wt%)											
SiO ₂	48.5	47.6	48.0	48.7	47.3	47.3	48.1	45.3	52.1	47.5	48.4
TiO ₂	2.49	1.07	1.46	1.88	1.73	2.70	2.41	2.04	4.04	2.06	2.04
Al ₂ O ₃	14.6	17.8	15.2	14.6	14.7	13.9	14.6	17.7	15.1	16.1	16.5
Fe ₂ O ₃	12.3	9.45	11.2	11.2	10.8	13.7	12.1	13.5	12.9	11.6	10.7
MnO	0.200	0.140	0.150	0.200	0.210	0.210	0.220	0.120	0.110	0.120	0.120
MgO	5.57	5.70	6.44	6.09	7.44	5.77	5.55	2.32	3.93	4.96	4.57
CaO	5.66	13.0	11.3	9.8	10.7	7.69	8.20	7.05	0.93	10.4	10.9
Na ₂ O	4.01	2.35	2.68	3.19	2.76	3.66	3.81	3.16	4.27	2.80	2.73
K ₂ O	2.25	0.390	0.550	1.06	0.83	1.24	1.21	1.54	0.58	0.77	0.90
P ₂ O ₅	0.520	0.130	0.200	0.260	0.210	0.420	0.410	0.930	0.580	0.300	0.260
LOI	3.50	2.20	2.50	2.70	3.10	3.10	3.20	6.10	5.30	3.10	2.70
TOTAL	99.67	99.79	99.69	99.68	99.71	99.68	99.72	99.76	99.81	99.75	99.75
Trace Elements (ppm)											
Co	33.1	35.8	43.5	41.8	45.2	37.7	40.0	30.1	18.9	54.7	52.2
Cr											
Ni											
Cu											
Sc	24.0	37.0	38.0	38.0	40.0	33.0	34.0	39.0	38.0	32.0	31.0
V											
Zn											
Nb	37.7	7.30	15.8	22.0	19.0	20.2	27.9	14.9	26.1	15.4	16.4
Ga											
Rb											
Ba	621	125	195	303	248	447	385	186	114	229	235
Sr	334	227	290	289	294	344	329	415	121	536	514
Y	38.8	22.7	24.8	31.2	28.5	39.3	38.5	49.0	38.5	26.0	27.2
Zr	218	60.3	90.9	141	115	158	171	166	271	149	158

Sample	Walvis Ridge								DSDP Site 530 A		
	AII-93-19-4	CH19 DR3-2	CH19 DR3-22	CH19 DR4-1	CH19 DR4-2	CH19 DR4-3	CH19 DR4-H2	WALDA-002-CH19-DR4-03	DSDP Leg 75 530 A 106 1W 4-10	DSDP Leg 75 530 A 107 3W 37-45	DSDP Leg 75 530 A 108 3W 78-84
Rock type	Trachyte	Tephrite	Alkali Basalt	Basaltic Andesite	Basaltic Trachyandesite	Basaltic Trachyandesite	Basaltic Trachyandesite	Basaltic Trachyandesite	Alkali Basalt	Tholeiitic Basalt	Tholeiitic Basalt
Lab	1	2	2	2	2	2	2	2	3	3	3
Method	XRF	ICP-ES	ICP-ES	ICP-ES	ICP-ES	ICP-ES	ICP-ES	ICP-ES	XRF	XRF	XRF
Major Elements (wt%)											
SiO ₂	57.7	46.8	46.3	51.3	51.0	50.7	50.9	50.8	42.4	48.7	46.9
TiO ₂	0.330	3.60	1.20	3.29	2.65	2.65	2.63	2.62	2.12	1.70	1.68
Al ₂ O ₃	19.7	16.4	16.9	15.6	17.7	18.3	18.0	18.1	17.2	15.3	15.2
Fe ₂ O ₃	3	15.5	10.4	9.73	9.33	8.99	9.23	8.98	11.6	11.4	10.0
MnO	0.140	0.250	0.160	0.150	0.070	0.090	0.090	0.060	0.53	0.260	0.200
MgO	0.93	1.82	7.29	3.03	2.43	2.45	2.29	2.71	7.01	6.61	7.10
CaO	0.24	5.39	7.73	7.43	7.42	6.83	7.40	7.18	7.33	9.7	10.7
Na ₂ O	4.97	3.27	2.68	3.59	3.29	3.36	3.24	3.33	2.79	2.84	3.00
K ₂ O	6.04	3.65	1.58	0.99	1.74	1.89	1.89	1.80	0.240	0.650	0.530
P ₂ O ₅	0.040	0.540	0.130	0.420	0.380	0.380	0.400	0.370	0.320	0.250	0.240
LOI	5.82	2.50	5.30	4.20	3.70	4.10	3.60	3.80	7.59	2.57	3.17
TOTAL	99.44	99.65	99.68	99.73	99.70	99.71	99.73	99.74	99.15	99.86	98.71
Trace Elements (ppm)											
Co	<2	32.0	27.7	42.9	28.0	35.0	27.6	32.8	52.0	37.0	34.0
Cr	BDL								118	115	117
Ni	6.00								98.0	62.0	99.0
Cu									105	82.0	103
Sc		38.0	29.0	39.0	38.0	36.0	38.0	37.0	38.0	38.0	37.0
V	35.0								370	326	299
Zn	91.0								114	100	78.0
Nb	337	23.1	5.80	22.6	21.6	22.4	22.9	23.3	20.0	14.0	14.0
Ga	25.0								3.00	5.00	2.00
Rb	201								2	16.0	13.0
Ba	183	302	141	265	284	294	306	279	175	126	135
Sr	264	313	304	396	431	423	433	428	259	241	269
Y	BDL	34.4	15.2	42.2	29.4	28.3	34.7	30.7	28.0	33.0	28.0
Zr	991	284	76.8	278	219	224	236	228	148	104	103

Rio Grande Rise

Sample	RC11-2RD 1	RC11-2RD P5	RC11-2RD P9	RC16-11RD 1	RC16-11RD 2	RC16-11RD 3	RC16-12RD 1	RC16-12RD 2	RC16-12RD 3
Rock type	Alkali Basalt	Phonotephrite	Phonotephrite	Alkali Basalt	Alkali Basalt	Alkali Basalt	Trachybasalt	Tephriphonolite	Tephriphonolite
Lab Method	2 ICP-ES	2 ICP-ES	2 ICP-ES	2 ICP-ES	2 ICP-ES	2 ICP-ES	2 ICP-ES	2 ICP-ES	2 ICP-ES
Major Elements (wt%)									
SiO ₂	43.2	43.8	43.1	45.7	45.8	45.5	46.4	51.8	52.0
TiO ₂	3.46	0.79	3.01	2.50	2.50	2.49	2.08	3.13	3.12
Al ₂ O ₃	17.5	15.0	16.7	14.2	14.2	14.3	15.1	18.5	18.6
Fe ₂ O ₃	13.0	6.04	8.46	10.7	10.8	10.8	9.02	5.62	5.73
MnO	0.200	0.200	0.080	0.150	0.150	0.150	0.140	0.080	0.080
MgO	4.02	5.23	4.54	8.44	8.37	8.09	8.45	1.85	1.88
CaO	9.6	7.62	5.06	10.5	10.6	10.7	8.01	4.63	4.61
Na ₂ O	3.01	3.50	2.99	2.31	2.33	2.25	2.63	3.45	3.48
K ₂ O	0.870	5.28	5.87	1.94	1.86	2.05	2.26	5.96	5.93
P ₂ O ₅	1.10	0.330	0.93	0.610	0.61	0.60	0.64	1.29	1.30
LOI	3.70	11.9	8.90	2.40	2.40	2.60	4.80	3.10	2.80
TOTAL	99.60	99.63	99.57	99.48	99.50	99.50	99.53	99.44	99.51
Trace Elements (ppm)									
Co	37.1	11.4	30.4	42.0	45.2	41.7	35.1	17.8	16.3
Cr									
Ni									
Cu									
Sc	25.0	2.00	9.00	28.0	28.0	28.0	22.0	12.0	13.0
V									
Zn									
Nb	47.4	71.6	69.3	36.8	36.0	36.0	45.8	65.6	66.8
Ga									
Rb									
Ba	308	1121	1289	896	913	913	893	1610	1445
Sr	838	649	746	867	879	904	661	1116	1017
Y	35.3	21.4	28.3	23.6	23.6	24.1	22.7	38.2	33.5
Zr	321	417	376	229	267	462	272	486	445

Sample	Rio Grande Rise		
	DSDP Leg 72 516 F 126 3W 56-73	DSDP Leg 72 516 F 127 3W 59-76	DSDP Leg 72 516 F 128 2W 63-84
Rock type	Alkali Basalt	Tholeiitic Basalt	Tholeiitic Basalt
Lab	2	2	2
Method	ICP-ES	ICP-ES	ICP-ES
Major Elements (wt%)			
SiO ₂	39.4	43.5	48.4
TiO ₂	2.58	2.46	2.20
Al ₂ O ₃	15.0	14.5	13.2
Fe ₂ O ₃	10.9	12.0	12.7
MnO	0.130	0.090	0.170
MgO	2.83	4.43	5.53
CaO	12.2	8.44	9.85
Na ₂ O	2.85	2.95	2.64
K ₂ O	0.230	0.280	0.320
P ₂ O ₅	0.290	0.280	0.250
LOI	13.4	10.8	4.40
TOTAL	99.76	99.70	99.73
Trace Elements (ppm)			
Co	45.9	70.7	48.8
Cr			
Ni			
Cu			
Sc	47.0	44.0	4.00
V			
Zn			
Nb	12.4	12.1	10.7
Ga			
Rb			
Ba	95.0	124	132
Sr	352	377	270
Y	39.6	30.2	37.7
Zr	204	190	177

Appendix III b

Trace element and isotope data

Table 1: Trace element and Sr-Nd-Pb-Hf isotope data for the Walvis Ridge, the Rio Grande Rise and the Guyot Province

Appendix IIIb Trace element and Sr-Nd-Pb-Hf isotope data for samples from the Tristan-Gough hotspot track and the Rio Grande Rise
(Table 1)

Sample	Tristan Track		Gough Track			
	AK-1695-6 ^{a++}	AII-93-11-8 ^{a++}	PS69/420-1-DR 21-1 ^{a++}	PS69/420-1-DR 21-1 **	PS69/423-1-DR 25-4 ^{a++}	PS69/424-1-DR 26-1 ^{a++}
Rock Type	Trachyte	Trachyte	Trachyte	Trachyte	Trachyte	Picrobasalt
Ar/Ar Age (Ma)	27	47	47	47	46	46.5
Lat. (°)	-36.45	-32.97	-32.81	-32.81	-34.92	-34.92
Long. (°)	-7.81	-0.02	2.55	2.55	0.55	0.55
Cruise	(R/V Akademik Kurchatov)	AII-93 (R/V Atlantis II)	ANT-XXIII/5 (R/V Polarstern)	ANT-XXIII/5 (R/V Polarstern)	ANT-XXIII/5 (R/V Polarstern)	ANT-XXIII/5 (R/V Polarstern)
Li (ppm)	8.37	14.4	16.0		15.7	70.2
Sc (ppm)	5.65	14.2	2.19		3.17	34.9
V (ppm)	86.4	4.36	1.54		28.0	340
Cr (ppm)	4.96	4.50	4.54		9.09	483
Co (ppm)	23.2	0.414	0.374		5.66	42.1
Ni (ppm)	28.4	2.90	2.41		41.1	247
Cu (ppm)	11.7	4.52	5.58		28.6	84.2
Zn (ppm)	116	158	114		89.0	207
Ga (ppm)	33.0	33.2	30.2		26.1	18.5
Rb (ppm)	120	110	183		159	11.9
Sr (ppm)	22.3	73.4	29.6		220	948
Y (ppm)	45.8	52.5	56.9		24.3	33.1
Zr (ppm)	568	718	1251		608	377
Nb (ppm)	98.6	90.5	201		130.01	75.2
Ba (ppm)	226	1009	8.96		258	506
La (ppm)	90.0	85.8	172		102	54.3
Ce (ppm)	156	172	293		173	114
Pr (ppm)	19.0	20.8	29.8		17.3	13.6
Nd (ppm)	68.5	79.5	92.0		54.1	53.8
Sm (ppm)	12.6	15.6	13.7		8.24	10.7
Eu (ppm)	2.41	4.62	0.615		1.75	3.32
Gd (ppm)	11.0	13.8	11.0		6.42	9.57
Tb (ppm)	1.68	2.10	1.70		0.907	1.33
Dy (ppm)	9.62	11.8	9.84		4.75	7.12
Ho (ppm)	1.85	2.16	1.97		0.874	1.27
Er (ppm)	4.99	5.59	5.64		2.29	3.13
Tm (ppm)	0.735	0.786	0.860		0.319	0.412
Yb (ppm)	4.79	5.03	5.77		2.04	2.51
Lu (ppm)	0.694	0.732	0.884		0.291	0.353
Hf (ppm)	13.6	16.6	26.0		18.0	8.80
Ta (ppm)	5.83	5.41	13.3		9.19	4.56
Pb (ppm)	6.29	7.45	10.6		15.1	4.54
Th (ppm)	11.3	9.21	31.1		27.6	7.47
U (ppm)	1.80	0.687	2.67		1.25	1.34

	AK-1695-6 ^{a++}	AII-93-11-8 ^{a++}	PS69/420-1-DR 21-1 ^{a++}	PS69/420-1-DR 21-1 **	PS69/423-1-DR 25-4 ^{a++}	PS69/424-1-DR 26-1 ^{a++}
⁸⁷ Sr/ ⁸⁶ Sr _m	-	-	-	-	-	0.704856
±2σ	-	-	-	-	-	5
⁸⁷ Rb/ ⁸⁶ Sr	-	-	-	-	-	0.036
⁸⁷ Sr/ ⁸⁶ Sr _{in}	-	-	-	-	-	0.704832
¹⁴³ Nd/ ¹⁴⁴ Nd _m	0.512654	0.512631	0.512423	0.512426	0.512476	0.512694
±2σ	3	3	5	3	2	3
εNd	0.32	-0.13	-4.20	-4.13	-3.16	1.09
¹⁴⁷ Sm/ ¹⁴⁴ Nd	0.110	0.118	0.089	0.089	0.092	0.120
¹⁴³ Nd/ ¹⁴⁴ Nd _{in}	0.512635	0.512595	0.512395	0.512399	0.512448	0.512657
εNd _{in}	0.62	0.34	-3.56	-3.49	-2.55	1.54
²⁰⁶ Pb/ ²⁰⁴ Pb _m	18.9762	18.1120	18.3429	18.3496	18.2090	18.4471
±2σ	6	11	6	9	13	6
²⁰⁷ Pb/ ²⁰⁴ Pb _m	15.6093	15.5381	15.5607	15.5632	15.5770	15.5623
±2σ	7	13	5	10	15	6
²⁰⁸ Pb/ ²⁰⁴ Pb _m	39.3651	38.4782	39.1694	39.1976	38.9231	38.9972
±2σ	22	43	15	32	50	17
²⁰⁷ Pb/ ²⁰⁶ Pb _m	0.82257	0.85789	0.84833	0.84815	0.85546	0.84362
±2σ	1	2	1	2	3	1
²⁰⁸ Pb/ ²⁰⁶ Pb _m	2.07445	2.12446	2.13540	2.13616	2.13758	2.11400
±2σ	6	11	3	9	13	4
²³⁸ U/ ²⁰⁴ Pb	18.51	5.83	16.07	16.08	5.28	18.88
²³⁵ U/ ²⁰⁴ Pb	0.13	0.04	0.12	0.12	0.04	0.14
²³² Th/ ²⁰⁴ Pb	120.59	80.71	193.37	193.46	120.71	108.73
²³² Th/ ²³⁸ U	6.52	13.85	12.03	12.03	22.88	5.76
²⁰⁶ Pb/ ²⁰⁴ Pb _{in}	18.899	18.069	18.225	18.232	18.171	18.310
²⁰⁷ Pb/ ²⁰⁴ Pb _{in}	15.606	15.536	15.555	15.558	15.575	15.556
²⁰⁸ Pb/ ²⁰⁴ Pb _{in}	39.204	38.290	38.719	38.747	38.648	38.747
²⁰⁷ Pb/ ²⁰⁶ Pb _{in}	0.826	0.860	0.853	0.853	0.857	0.850
²⁰⁸ Pb/ ²⁰⁶ Pb _{in}	2.074	2.119	2.124	2.125	2.127	2.116
delta 7/4	6.1	8.4	8.1	8.3	11.2	7.2
delta 8/4	79.6	95.4	136.6	138.6	128.1	106.8
²⁰⁸ Pb*/ ²⁰⁶ Pb*	1.02	1.02	1.07	1.08	1.06	1.04
¹⁷⁶ Hf/ ¹⁷⁷ Hf _m	0.282835	0.282799	0.282682	-	0.282704	0.282841
±2σ	3	4	3	-	3	6
εHf	2.23	0.94	-3.19	-	-2.41	2.45
¹⁷⁶ Lu/ ¹⁷⁷ Hf	0.007346	0.006319	0.004868	-	0.002325	0.005744
¹⁷⁶ Hf/ ¹⁷⁷ Hf _{in}	0.282831	0.282793	0.282677	-	0.282702	0.282836
εHf _{in}	2.70	1.81	-2.28	-	-1.44	3.32

Gough Track							Walvis Ridge	
Sample	PS69/424-1-DR 26-1 **	V29-9-1^a	AG51-6-1^a	AG51-6-5^a	AG51-7-1^a	AG51-7-2^a	DSDP Site 525 A	
							DSDP Leg 74 525 A	DSDP Leg 74 525 A
							53 2W 91-102^a	53 3W 87-97^a
Rock Type	Picrobasalt	Alkali Basalt	Trachyte	Trachyte	Tephrite	Trachybasalt	Basaltic Trachyandesite	Trachybasalt
Ar/Ar Age (Ma)	46.5	47		8	8	8	71	
Lat. (°)	-34.92	-32.63			-40.17	-40.17	-29.07	-29.07
Long. (°)	0.55	1.12			-8.55	-8.55	2.99	2.99
Cruise	ANT-XXIII/5 (R/V Polarstern)	VM 29 (R/V Vema)	51 (R/V S. A. Agulhas)	51 (R/V S. A. Agulhas)	51 (R/V S. A. Agulhas)	51 (R/V S. A. Agulhas)	DSDP Leg 74 (R/V Glomar Challenger)	DSDP Leg 74 (R/V Glomar Challenger)
Li (ppm)		18.5	17.7	18.5	23.4	13.1	7.19	4.38
Sc (ppm)		33.1	5.29	4.99	20.7	21.3	42.1	49.9
V (ppm)		420	8.79	16.6	228	228	413	318
Cr (ppm)		28.1	0.341	0.254	250	263	314	264
Co (ppm)		37.1	3.28	14.8	46.4	46.5	95.4	50.7
Ni (ppm)		27.4	14.5	22.1	220	217	50.1	47.2
Cu (ppm)		57.4	3.95	5.69	24.1	25.9	168	116
Zn (ppm)		164	130.32	116	117	119	192	75.6
Ga (ppm)		25.5	32.9	32.8	18.6	20.2	28.9	24.7
Rb (ppm)		11.5	145	151	31.1	42.2	27.6	16.2
Sr (ppm)		420	79.5	73.7	871	851	397	375
Y (ppm)		39.7	37.3	34.2	29.8	28.9	29.1	34.1
Zr (ppm)		281	1032	867	341	353	237	190
Nb (ppm)		31.5	146	141	46.8	46.6	16.8	14.4
Ba (ppm)		237	106	111	765	750	316	273
La (ppm)		29.6	120	116	50.1	49.3	22.1	22.2
Ce (ppm)		62.8	208	209	98.1	98.1	47.3	47.4
Pr (ppm)		8.47	22.9	22.5	12.3	12.2	6.01	6.14
Nd (ppm)		37.1	78.4	77.0	51.4	50.6	26.2	27.2
Sm (ppm)		8.47	13.0	12.7	10.2	10.1	6.28	6.81
Eu (ppm)		2.74	1.95	1.91	3.07	3.03	2.19	2.30
Gd (ppm)		8.56	10.1	9.74	8.96	8.86	6.47	7.34
Tb (ppm)		1.30	1.47	1.40	1.20	1.19	1.01	1.18
Dy (ppm)		7.63	7.96	7.44	6.26	6.18	6.01	7.16
Ho (ppm)		1.46	1.41	1.30	1.08	1.07	1.15	1.38
Er (ppm)		3.79	3.62	3.32	2.59	2.57	3.02	3.69
Tm (ppm)		0.527	0.509	0.460	0.331	0.330	0.431	0.529
Yb (ppm)		3.34	3.23	2.95	1.96	1.95	2.72	3.45
Lu (ppm)		0.491	0.460	0.427	0.280	0.275	0.387	0.495
Hf (ppm)		6.41	23.6	22.2	7.59	7.62	5.60	4.57
Ta (ppm)		1.88	8.71	8.74	2.56	2.55	0.924	0.815
Pb (ppm)		2.98	14.0	13.9	4.36	4.40	3.16	2.57
Th (ppm)		2.66	25.1	25.2	4.62	4.61	2.56	2.24
U (ppm)		0.568	2.15	1.78	0.894	0.945	0.589	0.467

	PS69/424-1-DR 26-1 **	V29-9-1 ^a	AG51-6-1 ^a	AG51-6-5 ^a	AG51-7-1 ^a	AG51-7-2 ^a	DSDP Leg 74 525 A	DSDP Leg 74 525 A
							53 2W 91-102 ^a	53 3W 87-97 ^a
⁸⁷ Sr/ ⁸⁶ Sr _m	0.705237	0.704681		0.705660	0.705014	0.704982	0.704909	
±2σ	5	5		5	3	5	6	
⁸⁷ Rb/ ⁸⁶ Sr	0.036	0.079		5.946	0.103	0.143	0.201	
⁸⁷ Sr/ ⁸⁶ Sr _{in}	0.705213	0.704629		0.704985	0.705002	0.704966	s	
¹⁴³ Nd/ ¹⁴⁴ Nd _m	0.512691	0.512694		0.512591	0.512565	0.512551	0.512516	
±2σ	2	3		3	3	3	2	
εNd	1.04	1.10		-0.91	-1.42	-1.70	-2.37	
¹⁴⁷ Sm/ ¹⁴⁴ Nd	0.12	0.138		0.100	0.119	0.120	0.144	
¹⁴³ Nd/ ¹⁴⁴ Nd _{in}	0.512655	0.512652		0.512586	0.512559	0.512544	0.512449	
εNd _{in}	1.49	1.45		-0.81	-1.34	-1.63	-1.90	
²⁰⁶ Pb/ ²⁰⁴ Pb _m	18.4376	18.3477		18.4323	18.3014	18.3086	17.7478	
±2σ	19	14		13	23	7	6	
²⁰⁷ Pb/ ²⁰⁴ Pb _m	15.5543	15.5671		15.6010	15.5863	15.5892	15.5081	
±2σ	16	12		15	19	8	7	
²⁰⁸ Pb/ ²⁰⁴ Pb _m	38.9548	38.6352		38.9192	38.8299	38.8399	38.2496	
±2σ	40	32		49	49	27	23	
²⁰⁷ Pb/ ²⁰⁶ Pb _m	0.84361	0.84845		0.84639	0.85164	0.85147	0.87380	
±2σ	2	1		2	2	2	1	
²⁰⁸ Pb/ ²⁰⁶ Pb _m	2.11278	2.10573		2.11146	2.12169	2.12141	2.15518	
±2σ	6	5		13	8	8	6	
²³⁸ U/ ²⁰⁴ Pb	18.86	12.11		8.20	13.06	13.68	11.66	
²³⁵ U/ ²⁰⁴ Pb	0.14	0.09		0.06	0.09	0.10	0.08	
²³² Th/ ²⁰⁴ Pb	108.64	58.59		119.86	69.70	68.93	52.35	
²³² Th/ ²³⁸ U	5.76	4.84		14.61	5.34	5.04	4.49	
²⁰⁶ Pb/ ²⁰⁴ Pb _{in}	18.301	18.259		18.422	18.285	18.292	17.619	
²⁰⁷ Pb/ ²⁰⁴ Pb _{in}	15.548	15.563		15.601	15.586	15.588	15.502	
²⁰⁸ Pb/ ²⁰⁴ Pb _{in}	38.705	38.499		38.872	38.802	38.813	38.065	
²⁰⁷ Pb/ ²⁰⁶ Pb _{in}	0.850	0.852		0.847	0.852	0.852	0.880	
²⁰⁸ Pb/ ²⁰⁶ Pb _{in}	2.115	2.108		2.110	2.122	2.122	2.161	
delta 7/4	6.5	8.7		11.2	11.1	11.4	9.3	
delta 8/4	103.7	82.6		100.7	107.7	107.8	116.6	
²⁰⁸ Pb*/ ²⁰⁶ Pb*	1.04	1.01		1.03	1.04	1.04	1.04	
¹⁷⁶ Hf/ ¹⁷⁷ Hf _m	-	0.282822		0.282783	-	0.282763	0.282756	
±2σ	-	4		5	-	5	5	
εHf	-	1.78		0.37	-	-0.31	-0.56	
¹⁷⁶ Lu/ ¹⁷⁷ Hf	-	0.010970		0.002753	-	0.005180	0.009901	
¹⁷⁶ Hf/ ¹⁷⁷ Hf _{in}	-	0.282812		0.282782	-	0.282762	0.282743	
εHf _{in}	-	2.50		0.54	-	-0.16	0.57	

Walvis Ridge						
Sample	DSDP Site 525 A					
	DSDP Leg 74 525 A 56 2W 68-79 ^a	DSDP Leg 74 525 A 56 2W 68-79 ^a *	DSDP Leg 74 525 A 56 2W 128-134 ^a	DSDP Leg 74 525 A 56 2W 128-134 ^a *	DSDP Leg 74 525 A 56 5W 42-53 ^a	DSDP Leg 74 525 A 57 2W 91-103 ^a
Rock Type	Alkali Basalt	Alkali Basalt	Tholeiitic Basalt	Tholeiitic Basalt	Tholeiitic Basalt	Alkali Basalt
Ar/Ar Age (Ma)			71			
Lat. (°)	-29.07	-29.07	-29.07	-29.07	-29.07	-29.07
Long. (°)	2.99	2.99	2.99	2.99	2.99	2.99
Cruise	DSDP Leg 74 (R/V Glomar Challenger)	DSDP Leg 74 (R/V Glomar Challenger)	DSDP Leg 74 (R/V Glomar Challenger)	DSDP Leg 74 (R/V Glomar Challenger)	DSDP Leg 74 (R/V Glomar Challenger)	DSDP Leg 74 (R/V Glomar Challenger)
Li (ppm)	7.38	7.33	9.64	9.71	8.28	8.66
Sc (ppm)	31.4	32.0	33.1	33.6	33.6	34.3
V (ppm)	293	301	305	315	312	332
Cr (ppm)	38.4	38.8	37.6	37.9	37.7	37.2
Co (ppm)	30.8	31.0	29.8	30.0	35.4	35.8
Ni (ppm)	22.7	22.9	19.7	19.8	24.2	25.2
Cu (ppm)	58.4	58.7	57.9	57.5	60.7	60.9
Zn (ppm)	92.0	94.5	104	104	96.3	114
Ga (ppm)	20.3	20.6	20.8	21.1	21.8	24.2
Rb (ppm)	13.3	13.3	4.31	4.33	15.1	14.2
Sr (ppm)	389	392	411	414	396	446
Y (ppm)	33.8	34.1	27.6	27.8	30.3	33.9
Zr (ppm)	204	205	212	213	226	263
Nb (ppm)	18.2	18.5	18.5	18.5	20.0	22.9
Ba (ppm)	306	310	309	308	332	384
La (ppm)	25.9	26.1	22.3	22.3	26.3	29.7
Ce (ppm)	55.0	55.1	49.3	49.2	56.0	63.8
Pr (ppm)	6.90	6.98	6.39	6.40	7.07	8.05
Nd (ppm)	29.6	29.7	27.7	27.6	30.1	34.2
Sm (ppm)	6.60	6.64	6.25	6.28	6.63	7.50
Eu (ppm)	2.14	2.15	2.14	2.13	2.18	2.48
Gd (ppm)	6.87	6.89	6.35	6.33	6.66	7.57
Tb (ppm)	1.06	1.06	0.960	0.957	1.01	1.14
Dy (ppm)	6.36	6.38	5.62	5.59	5.99	6.75
Ho (ppm)	1.25	1.25	1.07	1.07	1.15	1.30
Er (ppm)	3.32	3.33	2.75	2.74	3.00	3.39
Tm (ppm)	0.465	0.469	0.370	0.376	0.417	0.473
Yb (ppm)	2.93	2.96	2.33	2.33	2.65	2.98
Lu (ppm)	0.438	0.439	0.340	0.340	0.388	0.438
Hf (ppm)	4.77	4.77	5.03	4.99	5.21	5.95
Ta (ppm)	1.02	1.01	1.05	1.05	1.10	1.27
Pb (ppm)	2.47	2.71	2.61	2.56	2.50	2.53
Th (ppm)	2.43	2.41	2.54	2.50	2.65	3.04
U (ppm)	0.614	0.615	0.528	0.526	0.596	0.757

	DSDP Leg 74 525 A	DSDP Leg 74 525 A	DSDP Leg 74 525 A	DSDP Leg 74 525 A	DSDP Leg 74 525 A	DSDP Leg 74 525 A
	56 2W 68-79 ^a	56 2W 68-79 ^a *	56 2W 128-134 ^a	56 2W 128-134 ^a *	56 5W 42-53 ^a	57 2W 91-103 ^a
⁸⁷ Sr/ ⁸⁶ Sr _m			0.704780			
±2σ			5			
⁸⁷ Rb/ ⁸⁶ Sr			0.030			
⁸⁷ Sr/ ⁸⁶ Sr _m			0.704749			
¹⁴³ Nd/ ¹⁴⁴ Nd _m			0.512490			
±2σ			2			
εNd			-2.89			
¹⁴⁷ Sm/ ¹⁴⁴ Nd			0.136			
¹⁴³ Nd/ ¹⁴⁴ Nd _{in}			0.512427			
εNd _{in}			-2.34			
²⁰⁶ Pb/ ²⁰⁴ Pb _m			17.6759			
±2σ			8			
²⁰⁷ Pb/ ²⁰⁴ Pb _m			15.4972			
±2σ			9			
²⁰⁸ Pb/ ²⁰⁴ Pb _m			38.1620			
±2σ			28			
²⁰⁷ Pb/ ²⁰⁶ Pb _m			0.87674			
±2σ			2			
²⁰⁸ Pb/ ²⁰⁶ Pb _m			2.15899			
±2σ			8			
²³⁸ U/ ²⁰⁴ Pb			12.65			
²³⁵ U/ ²⁰⁴ Pb			0.09			
²³² Th/ ²⁰⁴ Pb			62.77			
²³² Th/ ²³⁸ U			4.96			
²⁰⁶ Pb/ ²⁰⁴ Pb _{in}			17.536			
²⁰⁷ Pb/ ²⁰⁴ Pb _{in}			15.491			
²⁰⁸ Pb/ ²⁰⁴ Pb _{in}			37.941			
²⁰⁷ Pb/ ²⁰⁶ Pb _{in}			0.883			
²⁰⁸ Pb/ ²⁰⁶ Pb _{in}			2.164			
delta 7/4			9.0			
delta 8/4			116.5			
²⁰⁸ Pb*/ ²⁰⁶ Pb*			1.04			
¹⁷⁶ Hf/ ¹⁷⁷ Hf _m			0.282748			
±2σ			4			
εHf			-0.85			
¹⁷⁶ Lu/ ¹⁷⁷ Hf			0.009705			
¹⁷⁶ Hf/ ¹⁷⁷ Hf _{in}			0.282735			
εHf _{in}			0.29			

Walvis Ridge						
Sample	DSDP Site 525 A					
	DSDP Leg 74 525 A	DSDP Leg 74 525 A	DSDP Leg 74 525 A	DSDP Leg 74 525 A	DSDP Leg 74 525 A	DSDP Leg 74 525 A
	57 5W 141-148 ^a	57 5W 141-148 ^{**}	58 1W 98-110 ^a	59 1W 110-111 ^b	60 4W 88-102 ^a	63 2W 59-78 ^a
Rock Type	Alkali Basalt	Alkali Basalt	Alkali Basalt	Tholeiitic Basalt	Alkali Basalt	Basaltic Trachyandesite
Ar/Ar Age (Ma)	72	72				72
Lat. (°)	-29.07	-29.07	-29.07	-29.07	-29.07	-29.07
Long. (°)	2.99	2.99	2.99	2.99	2.99	2.99
Cruise	DSDP Leg 74 (R/V Glomar Challenger)	DSDP Leg 74 (R/V Glomar Challenger)	DSDP Leg 74 (R/V Glomar Challenger)	DSDP Leg 74 (R/V Glomar Challenger)	DSDP Leg 74 (R/V Glomar Challenger)	DSDP Leg 74 (R/V Glomar Challenger)
Li (ppm)	8.35		5.32		9.06	7.74
Sc (ppm)	32.9		33.3	38.0	37.5	27.0
V (ppm)	313		303	401	359	327
Cr (ppm)	48.5		36.8		51.6	38.1
Co (ppm)	34.3		52.0	37.8	47.0	38.9
Ni (ppm)	25.5		42.2	19.2	51.8	28.7
Cu (ppm)	55.7		57.8	67.2	73.2	42.1
Zn (ppm)	99.0		106	97.0	103	112
Ga (ppm)	22.0		21.2	23.8	24.4	26.9
Rb (ppm)	13.5		18.4	2.70	5.83	23.5
Sr (ppm)	396		427	492	480	448
Y (ppm)	31.7		33.3	38.9	37.7	49.4
Zr (ppm)	232		235	238	259	383
Nb (ppm)	20.3		20.3	21.1	21.0	30.0
Ba (ppm)	341		344	290	353	532
La (ppm)	26.9		29.6	29.3	29.9	50.0
Ce (ppm)	57.6		62.4	68.4	64.5	102
Pr (ppm)	7.25		7.82	8.11	8.13	12.7
Nd (ppm)	30.8		33.1	34.8	34.7	52.3
Sm (ppm)	6.83		7.20	7.23	7.70	10.9
Eu (ppm)	2.23		2.30	2.40	2.50	3.21
Gd (ppm)	6.90		7.31	7.73	7.92	10.7
Tb (ppm)	1.05		1.11	1.24	1.22	1.62
Dy (ppm)	6.20		6.58	6.87	7.28	9.47
Ho (ppm)	1.20		1.28	1.38	1.41	1.83
Er (ppm)	3.13		3.37	3.66	3.70	4.84
Tm (ppm)	0.437		0.479	0.520	0.509	0.682
Yb (ppm)	2.77		3.08	3.16	3.20	4.34
Lu (ppm)	0.410		0.453	0.470	0.464	0.646
Hf (ppm)	5.30		5.29	6.30	5.88	8.46
Ta (ppm)	1.13		1.11	1.40	1.17	1.67
Pb (ppm)	1.74		2.80		3.36	4.27
Th (ppm)	2.67		2.72	3.00	3.05	4.83
U (ppm)	0.621		0.781	0.800	0.737	2.24

	DSDP Leg 74 525 A	DSDP Leg 74 525 A	DSDP Leg 74 525 A	DSDP Leg 74 525 A	DSDP Leg 74 525 A	DSDP Leg 74 525 A
	57 5W 141-148 ^a	57 5W 141-148 **	58 1W 98-110 ^a	59 1W 110-119 ^b	60 4W 88-102 ^a	63 2W 59-78 ^a
⁸⁷ Sr/ ⁸⁶ Sr _m	0.704841	-	-	-	-	0.705201
±2σ	5	-	-	-	-	6
⁸⁷ Rb/ ⁸⁶ Sr	0.098	-	-	-	-	0.151
⁸⁷ Sr/ ⁸⁶ Sr _{in}	0.704741	-	-	-	-	0.705047
¹⁴³ Nd/ ¹⁴⁴ Nd _m	0.512489	-	-	-	-	0.512431
±2σ	3	-	-	-	-	3
εNd	-2.91	-	-	-	-	-4.04
¹⁴⁷ Sm/ ¹⁴⁴ Nd	0.133	-	-	-	-	0.125
¹⁴³ Nd/ ¹⁴⁴ Nd _{in}	0.512426	-	-	-	-	0.512372
εNd _{in}	-2.33	-	-	-	-	-3.39
²⁰⁶ Pb/ ²⁰⁴ Pb _m	17.6544	-	-	-	-	17.7753
±2σ	6	-	-	-	-	10
²⁰⁷ Pb/ ²⁰⁴ Pb _m	15.4945	-	-	-	-	15.4910
±2σ	7	-	-	-	-	12
²⁰⁸ Pb/ ²⁰⁴ Pb _m	38.1603	-	-	-	-	38.2252
±2σ	22	-	-	-	-	35
²⁰⁷ Pb/ ²⁰⁶ Pb _m	0.87765	-	-	-	-	0.87149
±2σ	1	-	-	-	-	2
²⁰⁸ Pb/ ²⁰⁶ Pb _m	2.16152	-	-	-	-	2.15047
±2σ	6	-	-	-	-	9
²³⁸ U/ ²⁰⁴ Pb	22.33	-	-	-	-	32.81
²³⁵ U/ ²⁰⁴ Pb	0.16	-	-	-	-	0.24
²³² Th/ ²⁰⁴ Pb	99.16	-	-	-	-	73.17
²³² Th/ ²³⁸ U	4.44	-	-	-	-	2.23
²⁰⁶ Pb/ ²⁰⁴ Pb _{in}	17.404	-	-	-	-	17.407
²⁰⁷ Pb/ ²⁰⁴ Pb _{in}	15.483	-	-	-	-	15.474
²⁰⁸ Pb/ ²⁰⁴ Pb _{in}	37.806	-	-	-	-	37.964
²⁰⁷ Pb/ ²⁰⁶ Pb _{in}	0.890	-	-	-	-	0.889
²⁰⁸ Pb/ ²⁰⁶ Pb _{in}	2.172	-	-	-	-	2.181
delta 7/4	9.0	-	-	-	-	7.3
delta 8/4	118.9	-	-	-	-	110.8
²⁰⁸ Pb*/ ²⁰⁶ Pb*	1.04	-	-	-	-	1.03
¹⁷⁶ Hf/ ¹⁷⁷ Hf _m	0.282747	0.282754	-	-	-	0.282702
±2σ	4	5	-	-	-	6
εHf	-0.90	-0.63	-	-	-	-2.48
¹⁷⁶ Lu/ ¹⁷⁷ Hf	0.011078	0.011078	-	-	-	0.010944
¹⁷⁶ Hf/ ¹⁷⁷ Hf _{in}	0.282731	0.282739	-	-	-	0.282687
εHf _{in}	0.19	0.46	-	-	-	-1.38

Walvis Ridge							
Sample	DSDP Site 527						
	DSDP Leg 74 527	DSDP Leg 74 527	DSDP Leg 74 527	DSDP Leg 74 527	DSDP Leg 74 527	DSDP Leg 74 527	DSDP Leg 74 527
	39 1W 52-70 ^a	41 1W 47-63 ^a	41 5W 95-105 ^a	41 5W 95-105 **	42 4W 59-68 ^b	43 4W 59-73 ^a	44 4W 59-72 ^a
Rock Type	Alkali Basalt	Tholeiitic Basalt	Tholeiitic Basalt	Tholeiitic Basalt	Trachybasalt	Trachybasalt	Alkali Basalt
Ar/Ar Age (Ma)	67	67	67	67		67	67
Lat. (°)	-28.04	-28.04	-28.04	-28.04	-28.04	-28.04	-28.04
Long. (°)	1.76	1.76	1.76	1.76	1.76	1.76	1.76
Cruise	DSDP Leg 74 (R/V Glomar Challenger)	DSDP Leg 74 (R/V Glomar Challenger)	DSDP Leg 74 (R/V Glomar Challenger)	DSDP Leg 74 (R/V Glomar Challenger)	DSDP Leg 74 (R/V Glomar Challenger)	DSDP Leg 74 (R/V Glomar Challenger)	DSDP Leg 74 (R/V Glomar Challenger)
Li (ppm)	16.7	6.31	11.2			12.3	9.13
Sc (ppm)	43.4	40.9	46.5		33.0	30.9	33.9
V (ppm)	465	327	331		408	346	362
Cr (ppm)	75.0	88.2	303			14.3	18.5
Co (ppm)	46.7	40.9	44.7		41.2	39.2	41.1
Ni (ppm)	50.4	50.3	85.6		13.3	17.9	21.0
Cu (ppm)	214	160	177		60.3	72.7	90.3
Zn (ppm)	109	83.5	77.1		88.0	108	105
Ga (ppm)	20.7	17.3	17.9		20.8	21.0	20.9
Rb (ppm)	7.46	3.45	2.85		16.5	21.5	17.0
Sr (ppm)	165	138	170		289	278	303
Y (ppm)	38.5	27.2	29.9		39.1	41.4	39.6
Zr (ppm)	123	67.7	88.4		185	196	182
Nb (ppm)	13.5	6.88	4.79		29.3	29.0	27.0
Ba (ppm)	160	82.4	44.7		353	380	352
La (ppm)	13.1	7.00	5.48		28.3	30.3	27.6
Ce (ppm)	28.1	15.37	13.5		62.2	61.3	56.0
Pr (ppm)	3.70	2.09	2.05		7.05	7.46	6.80
Nd (ppm)	17.1	10.1	10.6		29.5	30.9	28.3
Sm (ppm)	4.71	2.98	3.47		6.10	6.92	6.38
Eu (ppm)	1.67	1.12	1.33		2.10	2.29	2.15
Gd (ppm)	5.87	3.87	4.58		6.74	7.58	7.09
Tb (ppm)	1.04	0.690	0.807		1.16	1.22	1.15
Dy (ppm)	6.92	4.68	5.38		6.65	7.64	7.19
Ho (ppm)	1.47	1.00	1.12		1.43	1.56	1.46
Er (ppm)	4.14	2.82	3.08		3.96	4.28	4.02
Tm (ppm)	0.618	0.423	0.449		0.580	0.616	0.576
Yb (ppm)	4.10	2.80	2.89		3.43	4.02	3.77
Lu (ppm)	0.627	0.426	0.434		0.530	0.607	0.564
Hf (ppm)	3.26	1.90	2.42		4.90	4.71	4.40
Ta (ppm)	0.740	0.380	0.272		1.80	1.61	1.48
Pb (ppm)	0.803	1.14	0.704			1.30	1.16
Th (ppm)	1.58	0.731	0.586		3.90	3.64	3.28
U (ppm)	0.89	0.174	0.236		0.900	0.801	0.729

	DSDP Leg 74 527	DSDP Leg 74 527	DSDP Leg 74 527	DSDP Leg 74 527	DSDP Leg 74 527	DSDP Leg 74 527	DSDP Leg 74 527
	39 1W 52-70 ^a	41 1W 47-63 ^a	41 5W 95-105 ^a	41 5W 95-105 **	42 4W 59-68 ^b	43 4W 59-73 ^a	44 4W 59-72 ^a
⁸⁷ Sr/ ⁸⁶ Sr _m	0.704300	0.704161	0.703633	0.703649		0.704547	0.704427
±2σ	6	12	6	6		6	5
⁸⁷ Rb/ ⁸⁶ Sr	0.131	0.072	0.048	0.048		0.224	0.162
⁸⁷ Sr/ ⁸⁶ Sr _m	0.704175	0.704092	0.703587	0.703603		0.704334	0.704273
¹⁴³ Nd/ ¹⁴⁴ Nd _m	0.512702	0.512726	0.512901	0.512915		0.512611	0.512617
±2σ	3	3	3	3		2	3
εNd	1.25	1.71	5.14	5.41		-0.53	-0.40
¹⁴⁷ Sm/ ¹⁴⁴ Nd	0.166	0.178	0.196	0.196		0.135	0.136
¹⁴³ Nd/ ¹⁴⁴ Nd _{in}	0.512629	0.512648	0.512815	0.512829		0.512552	0.512558
εNd _{in}	1.51	1.87	5.14	5.41		0.00	0.12
²⁰⁶ Pb/ ²⁰⁴ Pb _m	19.7562	18.2048	18.4908	18.5096		18.6188	18.5224
±2σ	14	13	10	19		8	11
²⁰⁷ Pb/ ²⁰⁴ Pb _m	15.6122	15.5267	15.5527	15.5506		15.5347	15.5281
±2σ	12	14	9	17		8	12
²⁰⁸ Pb/ ²⁰⁴ Pb _m	39.2337	38.6715	38.5336	38.5262		39.3297	39.1353
±2σ	34	44	24	46		25	36
²⁰⁷ Pb/ ²⁰⁶ Pb _m	0.79024	0.85289	0.84111	0.84014		0.83436	0.83834
±2σ	2	2	1	2		1	2
²⁰⁸ Pb/ ²⁰⁶ Pb _m	1.98589	2.12425	2.08394	2.08142		2.11236	2.11287
±2σ	6	11	5	8		7	8
²³⁸ U/ ²⁰⁴ Pb	72.06	9.68	21.31	21.31		39.54	40.36
²³⁵ U/ ²⁰⁴ Pb	0.52	0.07	0.15	0.15		0.29	0.29
²³² Th/ ²⁰⁴ Pb	132.88	42.05	54.65	54.66		185.66	187.58
²³² Th/ ²³⁸ U	1.84	4.35	2.56	2.56		4.70	4.65
²⁰⁶ Pb/ ²⁰⁴ Pb _{in}	19.003	18.104	18.268	18.287		18.206	18.101
²⁰⁷ Pb/ ²⁰⁴ Pb _{in}	15.577	15.522	15.542	15.540		15.515	15.508
²⁰⁸ Pb/ ²⁰⁴ Pb _{in}	38.793	38.532	38.352	38.345		38.713	38.512
²⁰⁷ Pb/ ²⁰⁶ Pb _{in}	0.820	0.857	0.851	0.850		0.852	0.857
²⁰⁸ Pb/ ²⁰⁶ Pb _{in}	2.041	2.128	2.099	2.097		2.126	2.128
delta 7/4	-2.0	6.2	5.7	5.3		2.5	2.9
delta 8/4	-27.9	103.5	55.1	52.1		119.3	111.5
²⁰⁸ Pb*/ ²⁰⁶ Pb*	0.93	1.03	0.99	0.98		1.06	1.05
¹⁷⁶ Hf/ ¹⁷⁷ Hf _m	0.282957	0.282987	0.283060	-		0.282867	0.282866
±2σ	4	5	4	-		5	5
εHf	6.53	7.59	10.19	-		3.37	3.33
¹⁷⁶ Lu/ ¹⁷⁷ Hf	0.027570	0.032222	0.025662	-		0.018453	0.018377
¹⁷⁶ Hf/ ¹⁷⁷ Hf _{in}	0.282921	0.282945	0.283027	-		0.282843	0.282843
εHf _{in}	6.79	7.64	10.54	-		4.04	4.01

Walvis Ridge						
Sample	DSDP Site 528					
	DSDP Leg 74 528 40 2W 73-85 ^a	DSDP Leg 74 528 42 1W 29-45 ^a	DSDP Leg 74 528 42 1W 29-45 ^{**}	DSDP Leg 74 528 42 5W 31-46 ^a	DSDP Leg 74 528 43 2W 80-98 ^a	DSDP Leg 74 528 44 3W 96-130 ^b
Rock Type	Tholeiitic Basalt	Basaltic Trachyandesite	Basaltic Trachyandesite	Tholeiitic Basalt	Tholeiitic Basalt	Alkali Basalt
Ar/Ar Age (Ma)		58	58	58	67	
Lat. (°)	-28.53	-28.53	-28.53	-28.53	-28.53	-28.53
Long. (°)	2.32	2.32	2.32	2.32	2.32	2.32
Cruise	DSDP Leg 74 (R/V Glomar Challenger)	DSDP Leg 74 (R/V Glomar Challenger)	DSDP Leg 74 (R/V Glomar Challenger)	DSDP Leg 74 (R/V Glomar Challenger)	DSDP Leg 74 (R/V Glomar Challenger)	DSDP Leg 74 (R/V Glomar Challenger)
Li (ppm)	7.25	13.0		5.96	7.95	
Sc (ppm)	40.6	22.7		35.0	36.2	38.0
V (ppm)	283	344		274	313	374
Cr (ppm)	75.6	4.38		120	46.1	
Co (ppm)	40.6	33.1		35.7	42.0	41.8
Ni (ppm)	52.3	10.5		64.5	43.8	22.7
Cu (ppm)	144	35.4		123	148	116
Zn (ppm)	71.8	115		72.4	83.4	79.0
Ga (ppm)	17.0	22.4		16.8	18.1	19.5
Rb (ppm)	9.16	38.4		7.27	5.30	12.5
Sr (ppm)	235	308		208	274	289
Y (ppm)	23.8	41.5		23.7	26.1	31.2
Zr (ppm)	80.3	263		68.5	102.57	141.1
Nb (ppm)	10.3	48.2		9.36	15.7	22.0
Ba (ppm)	155	654		128	208	303
La (ppm)	10.8	45.5		8.87	14.5	19.6
Ce (ppm)	22.5	89.2		18.5	30.0	44.7
Pr (ppm)	2.86	10.5		2.37	3.76	5.19
Nd (ppm)	12.6	41.3		10.7	16.2	22.2
Sm (ppm)	3.19	8.24		2.85	3.90	4.89
Eu (ppm)	1.18	2.56		1.06	1.38	1.74
Gd (ppm)	3.83	8.28		3.53	4.41	5.56
Tb (ppm)	0.648	1.28		0.619	0.731	0.940
Dy (ppm)	4.26	7.80		4.15	4.65	5.72
Ho (ppm)	0.886	1.55		0.878	0.967	1.17
Er (ppm)	2.48	4.17		2.48	2.68	3.38
Tm (ppm)	0.363	0.593		0.368	0.392	0.480
Yb (ppm)	2.40	3.79		2.43	2.60	2.89
Lu (ppm)	0.363	0.563		0.372	0.391	0.430
Hf (ppm)	2.15	5.94		1.86	2.52	3.90
Ta (ppm)	0.566	2.57		0.511	0.858	1.20
Pb (ppm)	1.00	4.87		1.83	1.65	
Th (ppm)	1.26	6.39		1.07	1.71	3.20
U (ppm)	0.284	0.830		0.255	0.435	0.600

	DSDP Leg 74 528	DSDP Leg 74 528	DSDP Leg 74 528	DSDP Leg 74 528	DSDP Leg 74 528	DSDP Leg 74 528
	40 2W 73-85 ^a	42 1W 29-45 ^a	42 1W 29-45 **	42 5W 31-46 ^a	43 2W 80-98 ^a	44 3W 96-130 ^b
⁸⁷ Sr/ ⁸⁶ Sr _m		0.704785	0.704751	0.703996	0.704092	
±2σ		5	5	6	5	
⁸⁷ Rb/ ⁸⁶ Sr		0.361	0.361	0.101	0.056	
⁸⁷ Sr/ ⁸⁶ Sr _{in}		0.704488	0.704454	0.703913	0.704039	
¹⁴³ Nd/ ¹⁴⁴ Nd _m		0.512563	0.512563	0.512771	0.512681	
±2σ		3	3	3	3	
εNd		-1.46	-1.45	2.60	0.84	
¹⁴⁷ Sm/ ¹⁴⁴ Nd		0.120	0.120	0.160	0.145	
¹⁴³ Nd/ ¹⁴⁴ Nd _{in}		0.512517	0.512518	0.512710	0.512617	
εNd _{in}		-0.90	-0.89	2.86	1.28	
²⁰⁶ Pb/ ²⁰⁴ Pb _m		18.0458	18.0330	18.2698	18.2553	
±2σ		7	0	20	18	
²⁰⁷ Pb/ ²⁰⁴ Pb _m		15.5046	15.5033	15.5165	15.5161	
±2σ		8	12	17	17	
²⁰⁸ Pb/ ²⁰⁴ Pb _m		38.8273	38.8175	38.7332	38.7148	
±2σ		21	41	42	45	
²⁰⁷ Pb/ ²⁰⁶ Pb _m		0.85918	0.85972	0.84930	0.84995	
±2σ		2	3	2	2	
²⁰⁸ Pb/ ²⁰⁶ Pb _m		2.15160	2.15258	2.12006	2.12074	
±2σ		6	12	5	7	
²³⁸ U/ ²⁰⁴ Pb		10.82	18.00	8.84	16.71	
²³⁵ U/ ²⁰⁴ Pb		0.08	0.13	0.06	0.12	
²³² Th/ ²⁰⁴ Pb		86.11	82.27	38.14	67.89	
²³² Th/ ²³⁸ U		7.96	4.57	4.31	4.06	
²⁰⁶ Pb/ ²⁰⁴ Pb _{in}		17.948	17.870	18.190	18.081	
²⁰⁷ Pb/ ²⁰⁴ Pb _{in}		15.500	15.496	15.513	15.508	
²⁰⁸ Pb/ ²⁰⁴ Pb _{in}		38.580	38.581	38.624	38.489	
²⁰⁷ Pb/ ²⁰⁶ Pb _{in}		0.864	0.867	0.853	0.858	
²⁰⁸ Pb/ ²⁰⁶ Pb _{in}		2.150	2.159	2.123	2.129	
delta 7/4		5.7	5.8	4.5	4.6	
delta 8/4		138.3	138.9	101.8	101.7	
²⁰⁸ Pb ₃ / ²⁰⁶ Pb ₃ *		1.07	1.07	1.03	1.03	
¹⁷⁶ Hf/ ¹⁷⁷ Hf _m		0.282818	-	0.283027	0.282920	
±2σ		5	-	5	4	
εHf		1.62	-	9.02	5.24	
¹⁷⁶ Lu/ ¹⁷⁷ Hf		0.013595	-	0.028640	0.022238	
¹⁷⁶ Hf/ ¹⁷⁷ Hf _{in}		0.282802	-	0.282995	0.282891	
εHf _{in}		2.39	-	9.20	5.74	

Walvis Ridge						
DSDP Site 528						
Sample	DSDP Leg 74 528	DSDP Leg 74 528	DSDP Leg 74 528	DSDP Leg 74 528	All-93-19-4 ^a	All-93-19-4 ^a *
	45 2W 109-119 ^a	45 2W 109-119 ^a *	47 2W 103-117 ^b	47 3W 66-80 ^a		
Rock Type	Alkali Basalt	Alkali Basalt	Trachybasalt	Trachybasalt	Trachyte	Trachyte
Ar/Ar Age (Ma)	67	67		67	55	55
Lat. (°)	-28.53	-28.53	-28.53	-28.53	-26.48	-26.48
Long. (°)	2.32	2.32	2.32	2.32	6.25	6.25
Cruise	DSDP Leg 74 (R/V Glomar Challenger)	DSDP Leg 74 (R/V Glomar Challenger)	DSDP Leg 74 (R/V Glomar Challenger)	DSDP Leg 74 (R/V Glomar Challenger)	AII-93 (R/V Atlantis II)	AII-93 (R/V Atlantis II)
Li (ppm)	16.3	16.3		10.1	47.2	47.4
Sc (ppm)	37.7	38.0	33.0	33.0	1.97	1.99
V (ppm)	329	327	433	364	34.1	34.02
Cr (ppm)	66.5	75.9		35.6	<0.5	<0.5
Co (ppm)	41.4	41.5	37.7	38.6	<0.1	<0.1
Ni (ppm)	55.9	56.0	19.1	29.7	23.2	23.1
Cu (ppm)	120	120	69.6	81.6	20.8	21.0
Zn (ppm)	81.2	81.3	100	110	77.3	77.8
Ga (ppm)	17.8	18.1	18.9	21.0	21.1	21.4
Rb (ppm)	11.9	12.0	16.2	20.9	183	187
Sr (ppm)	271	274	344	321	247	250
Y (ppm)	28.5	28.6	39.3	39.5	7.23	7.38
Zr (ppm)	126	127	158	190	1004	1018
Nb (ppm)	18.2	18.3	20.2	28.5	344	348
Ba (ppm)	268	273	447	402	173	177
La (ppm)	18.3	18.3	24.2	30.2	17.0	17.5
Ce (ppm)	37.3	37.3	50.9	61.1	27.8	28.6
Pr (ppm)	4.57	4.58	6.36	7.38	3.77	3.89
Nd (ppm)	19.2	19.3	28.9	30.6	12.1	12.4
Sm (ppm)	4.54	4.50	6.10	6.74	1.97	2.03
Eu (ppm)	1.58	1.58	2.29	2.26	0.543	0.558
Gd (ppm)	5.07	5.07	6.86	7.30	1.58	1.62
Tb (ppm)	0.827	0.833	1.20	1.18	0.240	0.248
Dy (ppm)	5.24	5.25	6.75	7.44	1.36	1.40
Ho (ppm)	1.07	1.07	1.39	1.51	0.266	0.273
Er (ppm)	2.92	2.92	3.76	4.19	0.800	0.807
Tm (ppm)	0.426	0.422	0.610	0.611	0.133	0.134
Yb (ppm)	2.76	2.78	3.53	3.98	0.963	0.979
Lu (ppm)	0.417	0.421	0.530	0.598	0.151	0.152
Hf (ppm)	3.18	3.16	4.20	4.55	16.8	16.9
Ta (ppm)	1.00	1.00	1.50	1.55	10.2	10.4
Pb (ppm)	2.15	2.07		2.46	7.46	7.62
Th (ppm)	2.33	2.33	3.20	3.59	46.9	47.6
U (ppm)	0.449	0.448	0.800	0.800	2.76	2.81

	DSDP Leg 74 528	DSDP Leg 74 528	DSDP Leg 74 528	DSDP Leg 74 528	All-93-19-4 ^a	All-93-19-4 ^a *
	45 2W 109-119 ^a	45 2W 109-119 ^a *	47 2W 103-117 ^b	47 3W 66-80 ^a		
⁸⁷ Sr/ ⁸⁶ Sr _m	0.704285			0.704456	0.705130	
±2σ	6			6	5	
⁸⁷ Rb/ ⁸⁶ Sr	0.127			0.188	2.143	
⁸⁷ Sr/ ⁸⁶ Sr _{in}	0.704164			0.704277	0.703455	
¹⁴³ Nd/ ¹⁴⁴ Nd _m	0.512648			0.512634	0.512758	
±2σ	3			3	3	
εNd	0.20			-0.07	2.34	
¹⁴⁷ Sm/ ¹⁴⁴ Nd	0.142			0.132	0.098	
¹⁴³ Nd/ ¹⁴⁴ Nd _{in}	0.512586			0.512576	0.512723	
εNd _{in}	0.66			0.48	3.03	
²⁰⁶ Pb/ ²⁰⁴ Pb _m	18.0917			18.2089	20.4260	
±2σ	18			10	15	
²⁰⁷ Pb/ ²⁰⁴ Pb _m	15.5001			15.5113	15.7215	
±2σ	19			10	13	
²⁰⁸ Pb/ ²⁰⁴ Pb _m	38.7408			38.8174	40.8126	
±2σ	54			26	38	
²⁰⁷ Pb/ ²⁰⁶ Pb _m	0.85675			0.85185	0.76968	
±2σ	3			2	2	
²⁰⁸ Pb/ ²⁰⁶ Pb _m	2.14135			2.13179	1.99807	
±2σ	14			7	6	
²³⁸ U/ ²⁰⁴ Pb	13.23			20.69	24.95	
²³⁵ U/ ²⁰⁴ Pb	0.10			0.15	0.18	
²³² Th/ ²⁰⁴ Pb	71.00			95.88	437.41	
²³² Th/ ²³⁸ U	5.37			4.63	17.53	
²⁰⁶ Pb/ ²⁰⁴ Pb _{in}	17.954			17.993	20.212	
²⁰⁷ Pb/ ²⁰⁴ Pb _{in}	15.494			15.501	15.711	
²⁰⁸ Pb/ ²⁰⁴ Pb _{in}	38.505			38.499	39.621	
²⁰⁷ Pb/ ²⁰⁶ Pb _{in}	0.863			0.862	0.777	
²⁰⁸ Pb/ ²⁰⁶ Pb _{in}	2.145			2.140	1.960	
delta 7/4	4.8			4.6	1.6	
delta 8/4	124.1			117.6	49.1	
²⁰⁸ Pb [*] / ²⁰⁶ Pb [*]	1.05			1.05	1.02	
¹⁷⁶ Hf/ ¹⁷⁷ Hf _m	0.282916			0.282896	-	
±2σ	4			6	-	
εHf	5.08			4.39	-	
¹⁷⁶ Lu/ ¹⁷⁷ Hf	0.018798			0.018849	-	
¹⁷⁶ Hf/ ¹⁷⁷ Hf _{in}	0.282891			0.282872	-	
εHf _{in}	5.74			5.05	-	

Walvis Ridge

Sample	V29-11-1^a	CIR 139D-2^a	CIR 139D-2^a *	CIR 139D-3^a	Walvis III DR04-35^a	CH19 DR3-2^a	CH19 DR3-22^b	CH19 DR4-1^a
Rock Type	Basaltic Trachyandesite	Tholeiitic Basalt	Tholeiitic Basalt	Tholeiitic Basalt	Trachybasalt	Tephrite	Alkali Basalt	Basaltic Andesite
Ar/Ar Age (Ma)	85	85		85	79	114		113
Lat. (°)	-26.15	-26.45	-26.45	-26.45	-27.26	-19.37	-19.37	-19.85
Long. (°)	5.58	5.89	5.89	5.89	4.39	9.33	9.33	9.02
Cruise	VM 29 (R/V Vema)	CIRCE (R/V Argo)	CIRCE (R/V Argo)	CIRCE (R/V Argo)		CH19 (R/V Jean Charcot)	CH19 (R/V Jean Charcot)	CH19 (R/V Jean Charcot)
Li (ppm)	41.0	22.9	23.0	17.2	22.8	26.4		292
Sc (ppm)	38.2	31.9	31.9	31.9	39.3	38.5	29.0	38.5
V (ppm)	398	295	292	292	227	596	199	430
Cr (ppm)	12.0	92.2	92.7	90.3	202	71.7		54.1
Co (ppm)	19.2	51.0	50.5	45.3	27.7	32.6	27.7	43.0
Ni (ppm)	41.0	73.5	73.2	50.5	47.2	50.9	131	28.0
Cu (ppm)	68.4	62.7	63.0	140	110	291	46.6	40.7
Zn (ppm)	109	122	123	119	156	249	92.0	154
Ga (ppm)	25.2	21.4	21.2	22.0	20.7	26.6	15.4	25.0
Rb (ppm)	9.81	15.1	15.0	18.9	27.3	52.8	15.5	12.3
Sr (ppm)	131	493	490	425	425	322	304	395
Y (ppm)	42.6	25.2	25.3	23.6	50.4	37.3	15.2	45.1
Zr (ppm)	318	146	145	159	179	323	76.8	309
Nb (ppm)	28.7	14.7	14.8	14.5	14.2	24.1	5.80	23.8
Ba (ppm)	129	208	210	243	201	338	141	289
La (ppm)	43.8	20.2	20.3	18.4	27.3	29.8	8.70	32.4
Ce (ppm)	86.3	43.2	43.3	40.87	38.7	61.6	20.8	70.4
Pr (ppm)	11.6	5.62	5.63	5.36	6.52	8.73	2.59	9.34
Nd (ppm)	48.4	24.1	24.1	23.6	28.8	38.12	12.1	40.6
Sm (ppm)	10.3	5.52	5.51	5.41	6.92	9.12	3.02	9.54
Eu (ppm)	3.41	1.88	1.89	1.88	2.29	2.94	1.13	3.09
Gd (ppm)	9.72	5.61	5.62	5.43	7.91	9.10	3.16	9.73
Tb (ppm)	1.41	0.846	0.847	0.817	1.24	1.36	0.520	1.50
Dy (ppm)	8.21	4.94	4.94	4.79	7.61	7.79	3.01	8.82
Ho (ppm)	1.60	0.933	0.936	0.898	1.55	1.44	0.570	1.69
Er (ppm)	4.26	2.41	2.41	2.32	4.14	3.69	1.53	4.43
Tm (ppm)	0.606	0.334	0.333	0.318	0.585	0.517	0.210	0.622
Yb (ppm)	3.90	2.06	2.07	1.98	3.71	3.34	1.37	3.97
Lu (ppm)	0.567	0.296	0.294	0.287	0.546	0.477	0.190	0.568
Hf (ppm)	7.14	3.58	3.61	3.88	4.27	7.46	1.90	7.16
Ta (ppm)	1.59	0.824	0.834	0.834	0.808	1.40	0.400	1.38
Pb (ppm)	4.00	2.18	2.20	1.83	1.94	4.62		2.87
Th (ppm)	3.10	1.65	1.65	1.65	1.78	2.93	0.700	3.03
U (ppm)	0.767	0.300	0.298	0.266	0.655	0.972	0.200	1.85

	V29-11-1 ^a	CIR 139D-2 ^a	CIR 139D-2 ^a *	CIR 139D-3 ^a	Walvis III DR04-35 ^a	CH19 DR3-2 ^a	CH19 DR3-22 ^b	CH19 DR4-1 ^a
⁸⁷ Sr/ ⁸⁶ Sr _m	0.704901	0.704878		0.704887	0.704882	0.705919		0.705728
±2σ	5	5		0	5	5		5
⁸⁷ Rb/ ⁸⁶ Sr	0.217	0.089		0.116	0.186	0.474		0.090
⁸⁷ Sr/ ⁸⁶ Sr _{in}	0.704639	0.704771		0.704747	0.704673	0.705151		0.705584
¹⁴³ Nd/ ¹⁴⁴ Nd _m	0.512503	0.512496		0.512509	0.512649	0.512464		0.512342
±2σ	3	3		0	3	3		2
εNd	-2.64	-2.78		-2.51	0.22	-3.40		-5.78
¹⁴⁷ Sm/ ¹⁴⁴ Nd	0.128	0.138		0.138	0.145	0.144		0.141
¹⁴³ Nd/ ¹⁴⁴ Nd _{in}	0.512431	0.512419		0.512433	0.512575	0.512356		0.512237
εNd _{in}	-1.90	-2.14		-1.87	0.74	-2.63		-4.98
²⁰⁶ Pb/ ²⁰⁴ Pb _m	17.9811	17.8002		17.8275	18.0587	17.9161		17.5458
±2σ	10	22		0	8	9		5
²⁰⁷ Pb/ ²⁰⁴ Pb _m	15.5529	15.5259		15.5310	15.5635	15.5279		15.4796
±2σ	9	24		0	9	10		5
²⁰⁸ Pb/ ²⁰⁴ Pb _m	38.4227	38.3248		38.3558	38.4937	38.3254		38.1510
±2σ	25	69		0	25	35		12
²⁰⁷ Pb/ ²⁰⁶ Pb _m	0.86495	0.87223		0.87118	0.86183	0.86670		0.88224
±2σ	2	4		0	2	2		1
²⁰⁸ Pb/ ²⁰⁶ Pb _m	2.13683	2.15305		2.15149	2.13159	2.13916		2.17437
±2σ	6	16		0	7	10		3
²³⁸ U/ ²⁰⁴ Pb	12.08	8.62		9.12	21.29	13.23		40.26
²³⁵ U/ ²⁰⁴ Pb	0.09	0.06		0.07	0.15	0.10		0.29
²³² Th/ ²⁰⁴ Pb	50.42	48.97		58.48	59.91	41.18		68.05
²³² Th/ ²³⁸ U	4.18	5.68		6.41	2.81	3.11		1.69
²⁰⁶ Pb/ ²⁰⁴ Pb _{in}	17.821	17.686		17.706	17.796	17.680		16.834
²⁰⁷ Pb/ ²⁰⁴ Pb _{in}	15.545	15.520		15.525	15.551	15.516		15.445
²⁰⁸ Pb/ ²⁰⁴ Pb _{in}	38.210	38.118		38.109	38.259	38.093		37.769
²⁰⁷ Pb/ ²⁰⁶ Pb _{in}	0.872	0.878		0.877	0.874	0.878		0.918
²⁰⁸ Pb/ ²⁰⁶ Pb _{in}	2.144	2.155		2.152	2.150	2.155		2.244
delta 7/4	11.3	10.5		10.8	11.5	9.5		8.7
delta 8/4	105.7	117.7		117.5	103.4	103.8		131.1
²⁰⁸ Pb _{*/206} Pb*	1.03	1.04		1.04	1.03	1.03		1.05
¹⁷⁶ Hf/ ¹⁷⁷ Hf _m	0.282774	0.282725		0.282723	0.282841	0.282724		0.282668
±2σ	5	6		5	6	4		5
εHf	0.08	-1.66		-1.74	2.44	-1.71		-3.68
¹⁷⁶ Lu/ ¹⁷⁷ Hf	0.011379	0.011861		0.010591	0.018316	0.009157		0.011377
¹⁷⁶ Hf/ ¹⁷⁷ Hf _{in}	0.282756	0.282706		0.282705	0.282813	0.282703		0.282643
εHf _{in}	1.35	-0.42		-0.43	3.25	0.16		-2.00

Walvis Ridge					North of Walvis Ridge	
Sample	CH19 DR4-2 ^a	CH19 DR4-3 ^b	CH19 DR4-H2 ^b	WALDA-002- CH19-DR4-03 ^a	DSDP Site 530 A	
					DSDP Leg 75 530 A 106 1W 4-10 ^{at}	DSDP Leg 75 530 A 107 3W 37-45 ^{at}
Rock Type	Basaltic Trachyandesite	Basaltic Trachyandesite	Basaltic Trachyandesite	Basaltic Trachyandesite	Alkali Basalt	Tholeiitic Basalt
Ar/Ar Age (Ma)	112			113	100	100
Lat. (°)	-19.85	-19.85	-19.85	-19.85	-19.19	-19.19
Long. (°)	9.02	9.02	9.02	9.02	9.39	9.39
Cruise	CH19 (R/V Jean Charcot)	CH19 (R/V Jean Charcot)	CH19 (R/V Jean Charcot)	WALDA-002 (CH19) (R/V Jean Charcot)	DSDP Leg 75 (R/V Glomar Challenger)	DSDP Leg 75 (R/V Glomar Challenger)
Li (ppm)	29.7			42.4	48.6	11.2
Sc (ppm)	36.7	36.0	38.0	37.1	38.2	37.4
V (ppm)	321	343	343	331	330	309
Cr (ppm)	168			178	110	112
Co (ppm)	27.0	35.0	27.6	31.8	47.2	34.5
Ni (ppm)	45.0	40.9	28.1	46.6	80.5	53.9
Cu (ppm)	37.0	41.1	10.4	81.2	68.6	63.6
Zn (ppm)	164	229	129	219	117	104
Ga (ppm)	23.0	21.2	22.5	23.0	19.4	19.1
Rb (ppm)	21.1	19.5	24.4	20.6	1.88	17.6
Sr (ppm)	406	423	433	438	282	239
Y (ppm)	32.1	28.3	34.7	30.5	28.8	30.6
Zr (ppm)	253	224	236	247	166	131
Nb (ppm)	22.3	22.4	22.9	22.5	24.7	17.0
Ba (ppm)	309	294	306	306	177	121
La (ppm)	26.0	25.3	26.9	27.2	18.8	13.3
Ce (ppm)	57.2	59.3	62.4	58.7	40.4	29.0
Pr (ppm)	7.38	7.03	7.65	7.56	5.17	3.85
Nd (ppm)	31.5	30.5	33.6	31.5	22.4	17.5
Sm (ppm)	6.96	6.68	6.66	6.96	5.28	4.45
Eu (ppm)	2.46	2.35	2.33	2.41	1.77	1.52
Gd (ppm)	6.90	6.45	7.04	6.81	5.55	5.16
Tb (ppm)	1.06	1.02	1.10	1.02	0.900	0.862
Dy (ppm)	6.24	5.61	5.97	5.94	5.64	5.58
Ho (ppm)	1.18	1.08	1.23	1.13	1.15	1.14
Er (ppm)	3.05	2.98	3.28	2.92	3.18	3.15
Tm (ppm)	0.420	0.410	0.450	0.408	0.486	0.459
Yb (ppm)	2.62	2.60	2.78	2.58	3.32	3.01
Lu (ppm)	0.381	0.370	0.410	0.370	0.505	0.454
Hf (ppm)	5.81	5.40	5.90	5.63	3.93	3.13
Ta (ppm)	1.27	1.50	1.20	1.28	1.42	0.952
Pb (ppm)	6.21			4.77	2.05	1.75
Th (ppm)	2.23	2.50	2.30	2.21	1.88	1.28
U (ppm)	1.02	1.10	1.30	0.968	0.622	0.325

	CH19 DR4-2 ^a	CH19 DR4-3 ^b	CH19 DR4-H2 ^b	WALDA-002- CH19-DR4-03 ^a	DSDP Leg 75 530 A 106 1W 4-10 ³⁺	DSDP Leg 75 530 A 107 3W 37-45 ³⁺
⁸⁷ Sr/ ⁸⁶ Sr _m	0.705607			0.705574	0.702920	0.703164
±2σ	5			6	3	3
⁸⁷ Rb/ ⁸⁶ Sr	0.150			0.136	0.019	0.213
⁸⁷ Sr/ ⁸⁶ Sr _{in}	0.705369			0.705356	0.702893	0.702861
¹⁴³ Nd/ ¹⁴⁴ Nd _m	0.512387			0.512397	0.512944	0.512977
±2σ	3			3	4	3
εNd	-4.90			-4.70	5.97	6.62
¹⁴⁷ Sm/ ¹⁴⁴ Nd	0.133			0.133	0.142	0.153
¹⁴³ Nd/ ¹⁴⁴ Nd _{in}	0.512289			0.512299	0.512851	0.512877
εNd _{in}	-3.99			-3.78	6.67	7.17
²⁰⁶ Pb/ ²⁰⁴ Pb _m	17.5932			17.5942	-	19.0106
±2σ	11			7	-	14
²⁰⁷ Pb/ ²⁰⁴ Pb _m	15.4933			15.4930	-	15.6105
±2σ	15			9	-	13
²⁰⁸ Pb/ ²⁰⁴ Pb _m	38.1276			38.1328	-	39.1428
±2σ	49			28	-	39
²⁰⁷ Pb/ ²⁰⁶ Pb _m	0.88064			0.88057	-	0.82115
±2σ	3			2	-	2
²⁰⁸ Pb/ ²⁰⁶ Pb _m	2.16717			2.16735	-	2.05900
±2σ	14			8	-	9
²³⁸ U/ ²⁰⁴ Pb	10.27			12.67	-	11.99
²³⁵ U/ ²⁰⁴ Pb	0.07			0.09	-	0.09
²³² Th/ ²⁰⁴ Pb	23.17			29.96	-	48.80
²³² Th/ ²³⁸ U	2.26			2.36	-	4.07
²⁰⁶ Pb/ ²⁰⁴ Pb _{in}	17.413			17.370	-	18.823
²⁰⁷ Pb/ ²⁰⁴ Pb _{in}	15.485			15.482	-	15.602
²⁰⁸ Pb/ ²⁰⁴ Pb _{in}	37.999			37.965	-	38.901
²⁰⁷ Pb/ ²⁰⁶ Pb _{in}	0.889			0.891	-	0.829
²⁰⁸ Pb/ ²⁰⁶ Pb _{in}	2.182			2.186	-	2.067
delta 7/4	9.5			9.5	-	5.9
delta 8/4	123.0			123.4	-	53.2
²⁰⁸ Pb*/ ²⁰⁶ Pb*	1.04			1.04	-	1.00
¹⁷⁶ Hf/ ¹⁷⁷ Hf _m	0.282683			0.282675	-	-
±2σ	5			5	-	-
εHf	-3.14			-3.42	-	-
¹⁷⁶ Lu/ ¹⁷⁷ Hf	0.009403			0.009423	-	-
¹⁷⁶ Hf/ ¹⁷⁷ Hf _{in}	0.282663			0.282655	-	-
εHf _{in}	-1.32			-1.59	-	-

	North of Walvis Ridge		Rio Grande Rise					
Sample	DSDP Site 530 A		RC11-2RD # 1 ^a	RC11-2RDP5 ^a	RC11-2RD P9 ^b	RC16-11 RD #1 ^a	RC16-11RD #2 ^a	RC16-11RD #2 **
	DSDP Leg 75 530	DSDP Leg 75 530						
	A 108 3W 78-84 ^{a+}	A 108 3W 78-84 ^{**+}						
Rock Type	Tholeiitic Basalt	Tholeiitic Basalt	Alkali Basalt	Phonotephrite	Phonotephrite	Alkali Basalt	Alkali Basalt	Alkali Basalt
Ar/Ar Age (Ma)	100	100	46			86	86	86
Lat. (°)	-19.19	-19.19	-30.42	-30.42	-30.42	-30.43	-30.43	-30.43
Long. (°)	9.39	9.39	-35.97	-35.97	-35.97	-36.02	-36.02	-36.02
Cruise	DSDP Leg 75 (R/V Glomar Challenger)	DSDP Leg 75 (R/V Glomar Challenger)	RC11 (R/V Robert D. Conrad)	RC11 (R/V Robert D. Conrad)	RC11 (R/V Robert D. Conrad)	RC16 (R/V Robert D. Conrad)	RC16 (R/V Robert D. Conrad)	RC16 (R/V Robert D. Conrad)
Li (ppm)	12.8		29.2	20.6		15.9	16.3	
Sc (ppm)	37.0		25.0	2.02	9.00	28.1	27.1	
V (ppm)	292		303	63.0	248	272	270	
Cr (ppm)	111		125	0.54		242	238	
Co (ppm)	28.9		33.3	10.4	30.4	42.5	40.7	
Ni (ppm)	87.6		46.7	25.1	53.1	91.7	85.9	
Cu (ppm)	75.7		41.9	6.67	5.50	46.9	46.1	
Zn (ppm)	84.5		145	66.3	71.0	85.9	89.2	
Ga (ppm)	18.1		22.7	18.2	23.3	19.8	20.0	
Rb (ppm)	11.7		9.01	133	143	35.1	33.0	
Sr (ppm)	263		803	596	746	903	853	
Y (ppm)	27.4		32.9	19.7	28.3	24.5	23.8	
Zr (ppm)	129		317	445	376	244	247	
Nb (ppm)	17.9		47.7	71.3	69.3	38.1	37.1	
Ba (ppm)	142		301	1092	1289	945	927	
La (ppm)	13.3		37.0	75.4	78.0	48.6	46.3	
Ce (ppm)	29.3		77.0	135	167	97.1	96.3	
Pr (ppm)	3.86		9.67	13.1	17.7	11.8	11.5	
Nd (ppm)	17.2		40.3	42.8	67.3	46.5	45.9	
Sm (ppm)	4.28		8.60	6.03	10.7	8.40	8.33	
Eu (ppm)	1.47		2.79	1.69	2.99	2.55	2.55	
Gd (ppm)	4.80		8.13	4.77	9.22	7.21	7.04	
Tb (ppm)	0.794		1.17	0.644	1.19	0.967	0.939	
Dy (ppm)	5.09		6.55	3.52	5.99	5.11	4.99	
Ho (ppm)	1.04		1.20	0.667	1.07	0.916	0.900	
Er (ppm)	2.89		3.08	1.83	2.82	2.27	2.23	
Tm (ppm)	0.424		0.428	0.267	0.390	0.304	0.300	
Yb (ppm)	2.76		2.69	1.77	2.36	1.87	1.82	
Lu (ppm)	0.414		0.390	0.269	0.330	0.264	0.261	
Hf (ppm)	3.11		6.67	8.56	8.80	5.47	5.49	
Ta (ppm)	1.02		2.73	4.17	3.80	2.06	2.01	
Pb (ppm)	1.62		2.26	10.6		5.42	5.47	
Th (ppm)	1.38		3.19	13.6	10.1	4.29	4.20	
U (ppm)	0.443		1.44	2.25	2.10	0.896	0.869	

	DSDP Leg 75 530	DSDP Leg 75 530	RC11-2RD # 1 ^a	RC11-2RDP5 ^a	RC11-2RD P9 ^b	RC16-11 RD #1 ^a	RC16-11RD #2 ^a	RC16-11RD #2 **
	A 108 3W 78-84 ^{a+}	A 108 3W 78-84 ^{**+}						
⁸⁷ Sr/ ⁸⁶ Sr _m	0.703127	0.703090	0.702747			0.705578	0.705557	0.705572
±2σ	3	3	6			6	5	5
⁸⁷ Rb/ ⁸⁶ Sr	0.129	0.129	0.032			0.112	0.112	0.112
⁸⁷ Sr/ ⁸⁶ Sr _{in}	0.702944	0.702907	0.702726			0.705441	0.705421	0.705436
¹⁴³ Nd/ ¹⁴⁴ Nd _m	0.512954	0.512958	0.513026			0.512353	0.512344	0.512358
±2σ	3	3	3			1	2	2
εNd	6.17	6.23	7.57			-5.56	-5.74	-5.47
¹⁴⁷ Sm/ ¹⁴⁴ Nd	0.150	0.150	0.128			0.109	0.109	0.109
¹⁴³ Nd/ ¹⁴⁴ Nd _{in}	0.512856	0.512860	0.512987			0.512292	0.512282	0.512296
εNd _{in}	6.77	6.83	7.97			-4.59	-4.78	-4.51
²⁰⁶ Pb/ ²⁰⁴ Pb _m	19.0262	19.0219	19.1872			17.7807	17.7866	17.7844
±2σ	10	9	82			7	9	14
²⁰⁷ Pb/ ²⁰⁴ Pb _m	15.6174	15.6161	15.5220			15.4787	15.4813	15.4776
±2σ	10	10	65			7	11	18
²⁰⁸ Pb/ ²⁰⁴ Pb _m	39.1486	39.1388	38.5490			38.1734	38.1861	38.1795
±2σ	30	32	162			20	31	58
²⁰⁷ Pb/ ²⁰⁶ Pb _m	0.82084	0.82096	0.80897			0.87054	0.87039	0.87029
±2σ	2	2	4			1	2	3
²⁰⁸ Pb/ ²⁰⁶ Pb _m	2.05762	2.05757	2.00910			2.14691	2.14690	2.14679
±2σ	7	8	8			5	9	15
²³⁸ U/ ²⁰⁴ Pb	17.60	17.60	40.89			10.35	9.95	9.95
²³⁵ U/ ²⁰⁴ Pb	0.13	0.13	0.30			0.08	0.07	0.07
²³² Th/ ²⁰⁴ Pb	56.55	56.54	93.86			51.28	49.64	49.63
²³² Th/ ²³⁸ U	3.21	3.21	2.30			4.95	4.99	4.99
²⁰⁶ Pb/ ²⁰⁴ Pb _{in}	18.751	18.747	18.894			17.642	17.653	17.651
²⁰⁷ Pb/ ²⁰⁴ Pb _{in}	15.604	15.603	15.508			15.472	15.475	15.471
²⁰⁸ Pb/ ²⁰⁴ Pb _{in}	38.868	38.858	38.335			37.955	37.974	37.968
²⁰⁷ Pb/ ²⁰⁶ Pb _{in}	0.832	0.832	0.821			0.877	0.877	0.877
²⁰⁸ Pb/ ²⁰⁶ Pb _{in}	2.073	2.073	2.029			2.151	2.151	2.151
delta 7/4	6.4	6.3	-4.9			6.0	6.2	5.9
delta 8/4	51.9	51.4	-27.5			105.0	105.5	105.1
²⁰⁸ Pb _{in} / ²⁰⁶ Pb _{in} *	1.00	0.99	0.92			1.03	1.03	1.03
¹⁷⁶ Hf/ ¹⁷⁷ Hf _m	-	-	0.283035			0.282646	0.282647	-
±2σ	-	-	5			5	5	-
εHf	-	-	9.30			-4.44	-4.42	-
¹⁷⁶ Lu/ ¹⁷⁷ Hf	-	-	0.008377			0.006917	0.006811	-
¹⁷⁶ Hf/ ¹⁷⁷ Hf _{in}	-	-	0.283028			0.282635	0.282636	-
εHf _{in}	-	-	10.08			-2.90	-2.87	-

Rio Grande Rise							
Sample	RC16-11RD #3 ^b	RC16-12RD #1 ^a	RC16-12RD #2 ^b	RC16-12 RD #3 ^a	DSDP Leg 72 516 F	DSDP Site 516 F	DSDP Leg 72 516 F
					126 3W 56-73 ^a	127 3W 59-76 ^a	128 2W 63-84 ^a
Rock Type	Alkali Basalt	Trachybasalt	Tephriphonolite	Tephriphonolite	Alkali Basalt	Tholeiitic Basalt	Tholeiitic Basalt
Ar/Ar Age (Ma)		86		86			86
Lat. (°)	-30.43	-30.43	-30.43	-30.43	-30.28	-30.28	-30.28
Long. (°)	-36.02	-36.02	-36.02	-36.02	-35.29	-35.29	-35.29
Cruise	RC16 (R/V Robert D. Conrad)	RC16 (R/V Robert D. Conrad)	RC16 (R/V Robert D. Conrad)	RC16 (R/V Robert D. Conrad)	DSDP Leg 72 (R/V Glomar Challenger)	DSDP Leg 72 (R/V Glomar Challenger)	DSDP Leg 72 (R/V Glomar Challenger)
Li (ppm)		61.3		28.7	8.67	11.2	6.49
Sc (ppm)	28.0	21.4	12.0	14.8	45.8	43.5	38.3
V (ppm)	270	211	228	209	418	404	350
Cr (ppm)		286		62.3	37.1	36.7	35.5
Co (ppm)	41.7	33.6	17.8	18.9	41.7	64.6	43.8
Ni (ppm)	68.1	119	15.6	40.5	36.8	49.9	41.1
Cu (ppm)	45.0	39.6	4.00	11.0	236	202	198
Zn (ppm)	66.0	94.1	96.0	115	128	97.7	120
Ga (ppm)	20.4	19.9	24.4	25.6	23.6	23.0	20.4
Rb (ppm)	36.2	32.9	93.0	83.1	2.40	2.95	7.11
Sr (ppm)	904	631	1116	1115	318	357	247
Y (ppm)	24.1	22.6	38.2	34.1	38.3	30.8	35.7
Zr (ppm)	462	315	486	484	210	202	180
Nb (ppm)	36.0	47.3	65.6	67.0	12.5	12.1	10.5
Ba (ppm)	913	907	1610	1458	97.1	138	132
La (ppm)	44.5	56.0	98.0	94.7	16.8	14.8	14.7
Ce (ppm)	97.2	112	219	187	40.0	35.8	34.6
Pr (ppm)	11.0	12.8	24.0	22.2	5.56	4.98	4.81
Nd (ppm)	44.4	48.5	91.4	83.6	26.0	23.2	22.5
Sm (ppm)	7.74	8.08	14.0	13.9	6.86	6.03	5.96
Eu (ppm)	2.40	2.34	3.83	3.87	2.28	2.07	2.00
Gd (ppm)	6.81	6.60	11.8	11.0	7.61	6.54	6.72
Tb (ppm)	0.960	0.879	1.45	1.44	1.22	1.05	1.10
Dy (ppm)	4.82	4.63	7.67	7.38	7.56	6.37	6.83
Ho (ppm)	0.810	0.842	1.30	1.30	1.49	1.23	1.36
Er (ppm)	2.25	2.14	3.72	3.25	3.90	3.22	3.64
Tm (ppm)	0.320	0.291	0.490	0.433	0.543	0.452	0.519
Yb (ppm)	1.95	1.82	2.79	2.69	3.38	2.93	3.37
Lu (ppm)	0.280	0.264	0.410	0.375	0.491	0.425	0.494
Hf (ppm)	12.0	6.59	12.4	10.2	5.07	5.00	4.44
Ta (ppm)	2.00	2.57	3.90	3.56	0.720	0.700	0.616
Pb (ppm)		6.60		9.98	2.14	2.03	1.99
Th (ppm)	4.90	5.64	9.80	8.49	1.67	1.63	1.42
U (ppm)	1.00	0.785	2.50	2.07	0.369	0.352	0.313

	RC16-11RD #3 ^b	RC16-12RD #1 ^a	RC16-12RD #2 ^b	RC16-12 RD #3 ^a	DSDP Leg 72 516 F 126 3W 56-73 ^a	DSDP Leg 72 516 F 127 3W 59-76 ^a	DSDP Leg 72 516 F 128 2W 63-84 ^a
⁸⁷ Sr/ ⁸⁶ Sr _m		0.705687		0.705952			0.704988
±2σ		5		5			6
⁸⁷ Rb/ ⁸⁶ Sr		0.151		0.216			0.083
⁸⁷ Sr/ ⁸⁶ Sr _{in}		0.705503		0.705689			0.704886
¹⁴³ Nd/ ¹⁴⁴ Nd _m		0.512342		0.512273			0.512543
±2σ		3		3			2
εNd		-5.77		-7.11			-1.85
¹⁴⁷ Sm/ ¹⁴⁴ Nd		0.100		0.100			0.159
¹⁴³ Nd/ ¹⁴⁴ Nd _{in}		0.512286		0.512217			0.512453
εNd _{in}		-4.72		-6.05			-1.44
²⁰⁶ Pb/ ²⁰⁴ Pb _m		17.7822		17.7127			17.6396
±2σ		7		6			5
²⁰⁷ Pb/ ²⁰⁴ Pb _m		15.4839		15.4736			15.4681
±2σ		9		7			5
²⁰⁸ Pb/ ²⁰⁴ Pb _m		38.1913		38.1437			38.1425
±2σ		27		23			12
²⁰⁷ Pb/ ²⁰⁶ Pb _m		0.87075		0.87359			0.87690
±2σ		2		2			1
²⁰⁸ Pb/ ²⁰⁶ Pb _m		2.14773		2.15347			2.16232
±2σ		7		7			4
²³⁸ U/ ²⁰⁴ Pb		7.45		12.94			9.84
²³⁵ U/ ²⁰⁴ Pb		0.05		0.09			0.07
²³² Th/ ²⁰⁴ Pb		55.30		54.94			46.21
²³² Th/ ²³⁸ U		7.42		4.25			4.69
²⁰⁶ Pb/ ²⁰⁴ Pb _{in}		17.682		17.539			17.507
²⁰⁷ Pb/ ²⁰⁴ Pb _{in}		15.479		15.465			15.462
²⁰⁸ Pb/ ²⁰⁴ Pb _{in}		37.956		37.909			37.945
²⁰⁷ Pb/ ²⁰⁶ Pb _{in}		0.875		0.882			0.883
²⁰⁸ Pb/ ²⁰⁶ Pb _{in}		2.147		2.161			2.167
delta 7/4		6.5		6.3			6.5
delta 8/4		106.6		110.2			118.9
²⁰⁸ Pb*/ ²⁰⁶ Pb*		1.03		1.03			1.04
¹⁷⁶ Hf/ ¹⁷⁷ Hf _m		0.282616		0.282588			0.282843
±2σ		6		4			5
εHf		-5.50		-6.51			2.50
¹⁷⁶ Lu/ ¹⁷⁷ Hf		0.005750		0.005249			0.015970
¹⁷⁶ Hf/ ¹⁷⁷ Hf _{in}		0.282607		0.282579			0.282816
εHf _{in}		-3.89		-4.87			3.51

^aTrace element data from the Institute of Geosciences at the Christian-Albrechts University of Kiel

^bTrace element data from Acme Analytical Laboratories Ltd.

BDL = Below detection limit

* Trace element replicate analyses on separate sample dissolution

** Isotope replicate analyses on separate sample dissolution

Isotopes: Internal errors are shown for the last significant digit(s).

Ar/Ar ages in regular font are from Rohde et al. (2012)

Ages in italics are estimated based on linear age-distance relationships of published age data from Rohde et al. (2012).

$^{208}\text{Pb}^*/^{206}\text{Pb}^* = [(^{208}\text{Pb}/^{204}\text{Pb})_{\text{sample}} - (^{208}\text{Pb}/^{204}\text{Pb})_{\text{Earth initial}}] / [(^{206}\text{Pb}/^{204}\text{Pb})_{\text{sample}} - (^{206}\text{Pb}/^{204}\text{Pb})_{\text{Earth initial}}]$; after Galer and O'Nions, 1985, Nature, v. 316, p. 778-782.

delta 7/4 and delta 8/4 = deviation of $^{207}\text{Pb}/^{204}\text{Pb}$ and $^{208}\text{Pb}/^{204}\text{Pb}$ from the Northern Hemisphere reference line (NHRL) as defined in Hart, 1984, Nature, v. 309, p. 753-757.

+

Sr ratios measure on a Thermo Fisher TRITON TIMS

++

Hf ratios measure on a VG Axiom MC-ICPMS

Appendix III c

Data quality (major elements)

Table 1: Reproducibility and accuracy of XRF major element data for several international reference standards (GEOMAR Helmholtz Centre for Ocean Research Kiel)

Appendix IIIc Reproducibility and accuracy of XRF major element data for several international reference materials (Table 1)														
(GEOMAR Helmholtz Centre for Ocean Research Kiel)														
Element	JB-2 (1)	JB-2 (2)	Mean	Std. dev. ($\pm 1\sigma$ abs)	Std. dev. ($\pm 1\sigma$ %)	JB-2*	Rel. dev. (%)	JB-3 (1)	JB-3 (2)	Mean	Std. dev. ($\pm 1\sigma$ abs)	Std. dev. ($\pm 1\sigma$ %)	JB-3*	Rel. dev. (%)
SiO ₂	53.07	53.03	53.05	0.03	0.05	53.2	0.3	50.8	50.8	50.8	0.00	0.00	51.04	0.5
TiO ₂	1.17	1.17	1.17	0.00	0.00	1.19	1.7	1.41	1.41	1.41	0.00	0.00	1.45	2.8
Al ₂ O ₃	14.82	14.77	14.80	0.04	0.24	14.67	-0.9	17.21	17.21	17.2	0.00	0.00	16.89	-1.9
Fe ₂ O ₃	14.46	14.45	14.46	0.01	0.05	14.34	-0.8	11.96	11.98	12.0	0.01	0.12	11.88	-0.8
MnO	0.21	0.21	0.21	0.00	0.00	0.2	-5.0	0.17	0.17	0.17	0.00	0.00	0.16	-6.3
MgO	4.72	4.71	4.72	0.01	0.15	4.66	-1.2	5.22	5.20	5.21	0.01	0.27	5.2	-0.2
CaO	9.91	9.89	9.90	0.01	0.14	9.89	-0.1	9.77	9.75	9.76	0.01	0.14	9.86	1.0
Na ₂ O	2.05	2.03	2.04	0.01	0.69	2.03	-0.5	2.76	2.76	2.76	0.00	0.00	2.82	2.1
K ₂ O	0.42	0.41	0.42	0.01	1.70	0.42	1.2	0.77	0.77	0.77	0.00	0.00	0.78	1.3
P ₂ O ₅	0.1	0.1	0.1	0.00	0.00	0.1	0.0	0.30	0.29	0.30	0.01	2.40	0.29	-1.7
SUM	100.93	100.77						100.4	100.3					

Element	JA-2 (1)	JA-2 (2)	Mean	Std. dev. ($\pm 1\sigma$ abs)	Std. dev. ($\pm 1\sigma$ %)	JA-2*	Rel. dev. (%)	JR-1 (1)	JR-1 (2)	Mean	Std. dev. ($\pm 1\sigma$ abs)	Std. dev. ($\pm 1\sigma$ %)	JR-1*	Rel. dev. (%)
SiO ₂	56.12	56.24	56.18	0.08	0.15	56.18	0.0	74.98	74.92	74.95	0.04	0.06	75.41	0.6
TiO ₂	0.67	0.67	0.67	0.00	0.00	0.67	0.0	0.11	0.11	0.11	0.00	0.00	0.1	-10.0
Al ₂ O ₃	15.41	15.45	15.43	0.03	0.18	15.32	-0.7	12.75	12.84	12.80	0.06	0.50	12.89	0.7
Fe ₂ O ₃	6.35	6.38	6.37	0.02	0.33	6.14	-3.7	0.85	0.85	0.85	0.00	0.00	0.96	11.5
MnO	0.11	0.11	0.11	0.00	0.00	0.11	0.0	0.11	0.10	0.11	0.01	6.73	0.1	-5.0
MgO	7.97	8.04	8.01	0.05	0.62	7.68	-4.2	0.14	0.14	0.14	0.00	0.00	0.09	-55.6
CaO	6.25	6.26	6.26	0.01	0.11	6.48	3.5	0.69	0.70	0.70	0.01	1.02	0.63	-10.3
Na ₂ O	3.02	2.98	3.00	0.03	0.94	3.08	2.6	4.15	4.11	4.13	0.03	0.68	4.1	-0.7
K ₂ O	1.75	1.75	1.75	0.00	0.00	1.8	2.8	4.44	4.46	4.45	0.01	0.32	4.41	-0.9
P ₂ O ₅	0.16	0.15	0.16	0.01	4.56	0.15	-3.3	0.03	0.03	0.03	0.00	0.00	0.02	-50.0
SUM	97.81	98.03						98.25	98.26					

BDL = Below detection limit

* Working values are from Govindaraju, 1994, Geostandards Newsletter, Special Issue, v. 18, p. 1 - 158

Table 2: Accuracy of XRF major element data for several international reference standards (Institute of Mineralogy and Petrography at the University of Hamburg)

Appendix IIIc (Table 2)			Accuracy of XRF major element data for several international reference materials (Institute of Mineralogy and Petrography at the University of Hamburg)																	
Element	JGB-1	JGB-1*	Rel. dev. (%)	JB-3	JB-3*	Rel. dev. (%)	JB-2	JB-2*	Rel. dev. (%)	JA-3	JA-3*	Rel. dev. (%)	JG-3	JG-3*	Rel. dev. (%)	JG-2	JG-2*	Rel. dev. (%)		
SiO ₂	43.59	43.44	-0.3	50.17	51.04	1.7	53.46	53.2	-0.5	61.92	62.26	0.5	66.4	67.1	1.0	76.61	76.95	0.4		
Al ₂ O ₃	17.71	17.66	-0.3	17.1	16.89	-1.2	14.83	14.67	-1.1	15.75	15.57	-1.2	15.47	15.52	0.3	12.43	12.41	-0.2		
Fe ₂ O ₃	15.38	15.16	-1.5	11.82	11.88	0.5	14.45	14.34	-0.8	6.56	6.59	0.5	3.7	3.73	0.8	0.92	0.92	0.0		
MnO	0.19	0.17	-11.8	0.17	0.16	-6.3	0.21	0.2	-5.0	0.1	0.106	5.7	0.07	0.072	2.8	0.02	0.015	-33.3		
MgO	7.71	7.83	1.5	5.01	5.2	3.7	4.53	4.66	2.8	3.66	3.65	-0.3	1.77	1.79	1.1	0.05	0.04	-25.0		
CaO	11.79	11.98	1.6	9.57	9.86	2.9	9.83	9.89	0.6	6.27	6.28	0.2	3.74	3.76	0.5	0.7	0.8	12.5		
Na ₂ O	1.25	1.23	-1.6	3.11	2.82	-10.3	2.08	2.03	-2.5	3.1	3.17	2.2	4.01	4.03	0.5	3.61	3.55	-1.7		
K ₂ O	0.23	0.24	4.2	0.76	0.78	2.6	0.42	0.42	0.0	1.39	1.41	1.4	2.61	2.63	0.8	4.68	4.72	0.8		
TiO ₂	1.62	1.62	0.0	1.42	1.45	2.1	1.19	1.19	0.0	0.7	0.68	-2.9	0.48	0.48	0.0	0.05	0.04	-25.0		
P ₂ O ₅	0.06	0.05	-20.0	0.28	0.29	3.4	0.09	0.1	10.0	0.11	0.11	0.0	0.13	0.12	-8.3	0.01	0.002	-400		
SUM	99.53			99.41			101.09			99.56			98.38			99.08				

* Working values are from Govindaraju, 1994, Geostandards Newsletter, Special Issue, v. 18, p. 1 - 158

Table 3: Accuracy of ICP-ES major element data for several international reference standards (Acme Analytical Laboratories Ltd.)

Appendix IIIc (Table 3)			Accuracy of ICP-ES major element data for several international reference materials (Acme Analytical Laboratories Ltd.)											
Element	BIR-1	BIR-1*	Rel. dev. (%)	BHVO-2	BHVO-2*	Rel. dev. (%)	BCR-2	BCR-2*	Rel. dev. (%)	AGV-2	AGV-2*	Rel. dev. (%)		
SiO ₂	47.91	47.7	-0.4	49.8	49.9	0.2	53.87	54.1	0.4	58.9	59.3	0.6		
Al ₂ O ₃	15.12	15.4	1.8	13.37	13.5	1.0	13.6	13.5	-0.7	16.90	16.91	0.1		
Fe ₂ O ₃	11.4	11.3	-0.9	12.26	12.3	0.3	13.64	13.8	1.2	6.62	6.69	1.0		
MgO	9.98	9.7	-2.9	7.43	7.23	-2.8	3.62	3.59	-0.8	1.77	1.79	1.1		
CaO	13.27	13.4	1.0	11.45	11.4	-0.4	7.11	7.12	0.1	5.19	5.20	0.2		
Na ₂ O	1.79	1.81	1.1	2.22	2.22	0.0	3.13	3.16	0.9	4.21	4.19	-0.5		
K ₂ O	0.02	0.03	33.3	0.52	0.52	0.0	1.81	1.79	-1.1	2.95	2.88	-2.4		
TiO ₂	0.96	0.97	1.0	2.76	2.73	-1.1	2.24	2.26	0.9	1.03	1.05	1.9		
P ₂ O ₅	0.030	0.027	-11.1	0.26	0.27	3.7	0.35	0.35	0.0	0.47	0.48	2.1		
MnO	0.170	0.176	3.4	0.17	0.17	0.0	0.2	0.2	0.0	0.1	0.1	0.0		
SUM	100.65			100.24			99.57			98.16				

* Preferred values of GeoReM (Geological and Environmental Reference Materials; <http://georem.mpch-mainz.gwdg.de/>)

Appendix III d

Data quality (trace elements)

Table 1a and b: *Reproducibility and accuracy of ICP-MS trace element data for BIR-1*

Appendix III d (Table 1a)		Reproducibility and accuracy of ICP-MS trace element data for BIR-1 (Institute of Geosciences at the Christian-Albrechts University of Kiel)											
# Analysis/ Element	# 1	# 2	# 3	# 4	# 5	# 6	# 7	Mean	Std. dev. ($\pm 1\sigma$ abs)	Std. dev. ($\pm 1\sigma$ %)	Ref. Value ¹	Rel. dev. (%)	
Li (ppm)	3.19	3.23	2.79	3.20	3.24	3.39	3.37	3.20	0.20	6.2	3.2	-0.1	
Sc (ppm)	44.3	40.5	33.5	43.2	43.4	44.0	43.5	41.8	3.85	9.2	43	2.8	
V (ppm)	311	308	312	320	325	318	331	318	8.12	2.6	319	0.4	
Cr (ppm)	374	386	389	386	388	388	390	386	5.44	1.4	391	1.4	
Co (ppm)	51.5	51.9	52.1	51.6	51.7	51.3	51.6	51.7	0.26	0.5	52	0.6	
Ni (ppm)	166	159	161	165	165	164	164	163	2.35	1.4	166	1.5	
Cu (ppm)	125	113	113	121	122	124	123	120	4.97	4.1	119	-1.0	
Zn (ppm)	70.2	66.8	67.8	70.0	70.5	71.1	70.7	69.6	1.64	2.4	72	3.4	
Ga (ppm)	16.0	15.3	15.2	16.1	16.1	16.0	15.9	15.8	0.39	2.5	15.3	-3.3	
Rb (ppm)	0.233	0.157	0.120	0.219	0.226	0.211	0.209	0.197	0.04	21.3	0.2	1.7	
Sr (ppm)	107	105	99	111	112	105	105	106	4.24	4.0	109	2.5	
Y (ppm)	15.8	14.8	14.0	15.4	15.7	15.5	15.2	15.2	0.64	4.2	15.6	2.6	
Zr (ppm)	14.7	13.6	13.5	13.9	14.0	14.4	13.9	14.0	0.42	3.0	14	0.0	
Nb (ppm)	0.525	0.539	0.537	0.561	0.564	0.526	0.519	0.539	0.02	3.3	0.55	2.1	
Ba (ppm)	6.33	6.05	5.92	6.15	6.22	6.27	6.10	6.15	0.14	2.3	7.14	13.9	
La (ppm)	0.585	0.579	0.564	0.482	0.493	0.619	0.608	0.561	0.05	9.6	0.615	8.7	
Ce (ppm)	1.86	1.87	1.83	1.86	1.87	1.90	1.88	1.87	0.02	1.1	1.92	2.7	
Pr (ppm)	0.363	0.368	0.358	0.376	0.377	0.372	0.370	0.369	0.01	1.8	0.37	0.2	
Nd (ppm)	2.33	2.37	2.32	2.41	2.44	2.43	2.41	2.39	0.05	1.9	2.38	-0.2	
Sm (ppm)	1.08	1.10	1.07	1.11	1.11	1.12	1.10	1.10	0.02	1.7	1.12	1.9	
Eu (ppm)	0.513	0.517	0.501	0.521	0.529	0.530	0.523	0.519	0.01	1.9	0.53	2.1	
Gd (ppm)	1.74	1.77	1.73	1.81	1.83	1.83	1.80	1.79	0.04	2.2	1.87	4.4	
Tb (ppm)	0.349	0.356	0.346	0.359	0.363	0.358	0.355	0.355	0.01	1.7	0.36	1.4	
Dy (ppm)	2.52	2.54	2.47	2.57	2.60	2.59	2.55	2.55	0.05	1.8	2.51	-1.5	
Ho (ppm)	0.562	0.561	0.541	0.569	0.574	0.572	0.567	0.564	0.01	2.0	0.56	-0.7	
Er (ppm)	1.61	1.61	1.54	1.63	1.64	1.64	1.62	1.61	0.03	2.1	1.66	2.9	
Tm (ppm)	0.244	0.243	0.233	0.247	0.248	0.247	0.244	0.244	0.01	2.1	0.25	2.6	
Yb (ppm)	1.62	1.59	1.52	1.64	1.65	1.64	1.63	1.61	0.05	2.9	1.65	2.2	
Lu (ppm)	0.244	0.241	0.229	0.247	0.250	0.255	0.253	0.246	0.01	3.6	0.25	1.8	
Hf (ppm)	0.551	0.558	0.550	0.58	0.58	0.58	0.58	0.568	0.01	2.6	0.582	2.4	
Ta (ppm)	0.040	0.046	0.046	0.045	0.044	0.036	0.036	0.042	0.005	10.8	0.0357	-17.1	
Pb (ppm)	2.98	3.00	2.91	2.82	3.25	3.10	2.97	3.00	0.14	4.6	3.1	3.1	
Th (ppm)	0.029	0.030	0.028	0.029	0.031	0.031	0.033	0.030	0.002	5.3	0.032	5.9	
U (ppm)	0.012	0.010	0.010	0.012	0.012	0.013	0.011	0.012	0.001	9.0	0.01	-16.0	

¹Preferred values of GeoReM (Geological and Environmental Reference Materials; <http://georem.mpch-mainz.gwdg.de/>)

Appendix III d Accuracy of ICP-MS trace element data for BIR-1
(Table 1b) (Acme Analytical Laboratories Ltd.)

Element	BIR-1	Ref. Value ¹	Rel. dev. (%)
Li (ppm)		3.2	
Sc (ppm)	44.0	43	-2.3
V (ppm)	331	319	-3.8
Cr (ppm)		391	
Co (ppm)	51.7	52	0.6
Ni (ppm)	119.5	166	28.0
Cu (ppm)	112.6	119	5.4
Zn (ppm)	48	72	33.3
Ga (ppm)	15.1	15.3	1.3
Rb (ppm)	BDL	0.2	
Sr (ppm)	115.5	109	-6.0
Y (ppm)	15.5	15.6	0.6
Zr (ppm)	17.2	14	-22.9
Nb (ppm)	0.3	0.55	45.5
Ba (ppm)	7	7.14	2.0
La (ppm)	0.7	0.615	-13.8
Ce (ppm)	2.0	1.92	-4.2
Pr (ppm)	0.39	0.37	-5.4
Nd (ppm)	2.4	2.38	-0.8
Sm (ppm)	1.04	1.12	7.1
Eu (ppm)	0.51	0.53	3.8
Gd (ppm)	1.72	1.87	8.0
Tb (ppm)	0.38	0.36	-5.6
Dy (ppm)	2.40	2.51	4.4
Ho (ppm)	0.56	0.56	0.0
Er (ppm)	1.65	1.66	0.6
Tm (ppm)	0.26	0.25	-4.0
Yb (ppm)	1.63	1.65	1.2
Lu (ppm)	0.24	0.25	4.0
Hf (ppm)	0.7	0.582	-20.3
Ta (ppm)	BDL	0.0357	
Th (ppm)	BDL	0.032	
U (ppm)	BDL	0.01	

BDL = Below detection limit

¹Preferred values of GeoReM (Geological and Environmental Reference Materials; <http://georem.mpch-mainz.gwdg.de/>)

Table 2 a and b: *Reproducibility and accuracy of ICP-MS trace element data for BHVO-2*

Appendix III d
(Table 2a)

Reproducibility and accuracy of ICP-MS trace element data for BHVO-2
(Institute of Geosciences at the Christian-Albrechts University of Kiel)

# Analysis/ Element	# 1	# 2	# 3	# 4	# 5	# 6	# 7	Mean	Std. dev. ($\pm 1\sigma$ abs)	Std. dev. ($\pm 1\sigma$ %)	Ref. value ¹	Rel. dev. (%)
Li (ppm)	4.52	4.53	4.09	4.59	4.63	4.71	4.68	4.53	0.207	4.6	4.8	5.5
Sc (ppm)	32.7	31.8	30.4	32.6	32.1	31.4	31.0	31.7	0.826	2.6	32	0.9
V (ppm)	322	316	314	321	320	317	318	318	2.71	0.9	317	-0.4
Cr (ppm)	293	295	294	295	288	292	286	292	3.40	1.2	280	-4.3
Co (ppm)	45.0	44.1	43.9	44.8	44.1	43.2	42.8	44.0	0.797	1.8	45	2.3
Ni (ppm)	119	116	117	123	121	115	114	118	3.20	2.7	119	1.0
Cu (ppm)	134	125	127	136	134	133	132	132	4.23	3.2	127	-3.7
Zn (ppm)	104	104	104	106	104	108	105	105	1.62	1.5	103	-1.9
Ga (ppm)	22.4	21.8	21.7	22.3	21.9	22.1	22.0	22.0	0.260	1.2	22	-0.2
Rb (ppm)	9.32	9.26	8.30	9.61	9.48	9.56	9.50	9.29	0.453	4.9	9.11	-2.0
Sr (ppm)	387	389	380	405	401	381	378	389	10.6	2.7	396	1.8
Y (ppm)	25.7	25.6	24.9	25.9	25.6	25.4	25.3	25.5	0.334	1.3	26	2.0
Zr (ppm)	170	174	175	171	169	180	175	174	3.72	2.1	172	-0.9
Nb (ppm)	17.7	18.3	18.3	17.9	17.7	17.8	17.7	17.9	0.280	1.6	18.1	1.1
Ba (ppm)	132	132	132	133	131	133	132	132	0.751	0.6	131	-0.9
La (ppm)	15.4	15.2	15.1	15.6	15.4	15.2	15.1	15.3	0.187	1.2	15.2	-0.8
Ce (ppm)	38.3	37.6	37.3	38.3	37.8	37.2	37.2	37.7	0.486	1.3	37.5	-0.5
Pr (ppm)	5.39	5.41	5.35	5.42	5.37	5.27	5.27	5.35	0.062	1.2	5.35	-0.1
Nd (ppm)	24.4	24.9	24.8	24.9	24.6	24.8	24.7	24.7	0.190	0.8	24.5	-0.9
Sm (ppm)	6.13	6.19	6.15	6.22	6.12	6.11	6.11	6.15	0.044	0.7	6.07	-1.3
Eu (ppm)	2.07	2.08	2.07	2.09	2.07	2.08	2.07	2.08	0.009	0.4	2.07	-0.3
Gd (ppm)	6.21	6.24	6.19	6.29	6.21	6.22	6.19	6.22	0.035	0.6	6.24	0.3
Tb (ppm)	0.935	0.954	0.938	0.950	0.941	0.925	0.920	0.938	0.012	1.3	0.92	-1.9
Dy (ppm)	5.36	5.41	5.29	5.43	5.37	5.28	5.27	5.35	0.062	1.2	5.31	-0.7
Ho (ppm)	0.983	0.984	0.974	1.00	0.99	0.971	0.968	0.98	0.010	1.0	0.98	0.0
Er (ppm)	2.44	2.46	2.43	2.46	2.45	2.41	2.42	2.44	0.019	0.8	2.54	4.0
Tm (ppm)	0.328	0.329	0.323	0.331	0.330	0.324	0.323	0.327	0.004	1.1	0.33	1.0
Yb (ppm)	2.00	2.00	1.96	2.03	2.01	1.96	1.96	1.99	0.026	1.3	2	0.7
Lu (ppm)	0.280	0.278	0.272	0.283	0.281	0.279	0.281	0.279	0.004	1.3	0.274	-1.8
Hf (ppm)	4.33	4.16	4.19	4.36	4.33	4.35	4.40	4.30	0.089	2.1	4.36	1.3
Ta (ppm)	1.10	1.13	1.13	1.05	1.05	1.02	1.02	1.07	0.050	4.7	1.14	5.8
Pb (ppm)	1.67	1.99	1.58	1.56	1.90	1.89	1.66	1.75	0.174	9.9	1.6	-9.2
Th (ppm)	1.19	1.21	1.15	1.13	1.18	1.17	1.18	1.17	0.025	2.2	1.22	3.9
U (ppm)	0.409	0.419	0.421	0.413	0.413	0.418	0.414	0.415	0.004	1.0	0.403	-3.0

¹Preferred values of GeoReM (Geological and Environmental Reference Materials; <http://georem.mpch-mainz.gwdg.de/>)

Appendix III d Accuracy of ICP-MS trace element data for BHVO-2
(Table 2b) (Acme Analytical Laboratories Ltd.)

Element	BHVO-2	Ref. value ¹	Rel. dev. (%)
Li (ppm)		4.8	
Sc (ppm)	32	32	0.0
V (ppm)	329	317	-3.8
Cr (ppm)		280	
Co (ppm)	43.2	45	4.0
Ni (ppm)	34.8	119	70.8
Cu (ppm)	82.1	127	35.4
Zn (ppm)	45	103	56.3
Ga (ppm)	22.7	22	-3.2
Rb (ppm)	9.0	9.11	1.2
Sr (ppm)	411.8	396	-4.0
Y (ppm)	25.1	26	3.5
Zr (ppm)	164.2	172	4.5
Nb (ppm)	17.3	18.1	4.4
Ba (ppm)	134	131	-2.3
La (ppm)	14.4	15.2	5.3
Ce (ppm)	37.6	37.5	-0.3
Pr (ppm)	5.14	5.35	3.9
Nd (ppm)	23.8	24.5	2.9
Sm (ppm)	5.79	6.07	4.6
Eu (ppm)	1.97	2.07	4.8
Gd (ppm)	5.93	6.24	5.0
Tb (ppm)	0.97	0.92	-5.4
Dy (ppm)	5.02	5.31	5.5
Ho (ppm)	0.93	0.98	5.1
Er (ppm)	2.44	2.54	3.9
Tm (ppm)	0.33	0.33	0.0
Yb (ppm)	1.88	2	6.0
Lu (ppm)	0.27	0.274	1.5
Hf (ppm)	5.1	4.36	-17.0
Ta (ppm)	1.1	1.14	3.5
Th (ppm)	1.6	1.22	-31.1
U (ppm)	0.5	0.403	-24.1

¹Preferred values of GeoReM (Geological and Environmental Reference Materials;
<http://georem.mpch-mainz.gwdg.de/>)

Table 3 a and b: *Reproducibility and accuracy of ICP-MS trace element data for BCR-2*

Appendix III d
(Table 3a)

Reproducibility and accuracy of ICP-MS trace element data for BCR-2
(Institute of Geosciences at the Christian-Albrechts University of Kiel)

# Analysis/ Element	# 1	# 2	Mean	Std. dev. ($\pm 1\sigma$ abs)	Std. dev. ($\pm 1\sigma$ %)	Ref. Value ¹	Rel. dev. (%)
Li (ppm)	8.88	9.04	8.96	0.114	1.3	9*	0.4
Sc (ppm)	34.9	33.7	34.3	0.847	2.5	33	-3.9
V (ppm)	420	410	415	7.38	1.8	416	0.2
Cr (ppm)	19.5	19.9	19.7	0.291	1.5	18	-9.3
Co (ppm)	37.7	37.1	37.4	0.432	1.2	37	-1.1
Ni (ppm)	12.1	11.2	11.6	0.647	5.6	18*	35.4
Cu (ppm)	20.3	18.7	19.5	1.13	5.8	21*	7.1
Zn (ppm)	133	134	134	0.583	0.4	127	-5.4
Ga (ppm)	23.4	22.7	23.0	0.495	2.1	23	-0.1
Rb (ppm)	48.5	48.9	48.7	0.260	0.5	46.9	-3.9
Sr (ppm)	339	349	344	7.13	2.1	340	-1.3
Y (ppm)	35.8	35.5	35.7	0.198	0.6	37	3.6
Zr (ppm)	189	190	190	0.244	0.1	184	-3.0
Nb (ppm)	12.0	12.1	12.1	0.043	0.4	12.6	4.1
Ba (ppm)	664	687	675	15.6	2.3	677	0.2
La (ppm)	25.2	26.0	25.6	0.606	2.4	24.9	-2.8
Ce (ppm)	52.9	53.3	53.1	0.319	0.6	52.9	-0.4
Pr (ppm)	6.83	6.97	6.90	0.095	1.4	6.7	-3.0
Nd (ppm)	28.9	29.3	29.1	0.293	1.0	28.7	-1.3
Sm (ppm)	6.59	6.70	6.64	0.077	1.2	6.58	-0.9
Eu (ppm)	1.95	1.97	1.96	0.013	0.7	1.96	0.2
Gd (ppm)	6.75	6.81	6.78	0.040	0.6	6.75	-0.5
Tb (ppm)	1.05	1.07	1.06	0.019	1.8	1.07	0.9
Dy (ppm)	6.36	6.51	6.44	0.109	1.7	6.41	-0.4
Ho (ppm)	1.28	1.30	1.29	0.015	1.1	1.28	-1.0
Er (ppm)	3.48	3.54	3.51	0.036	1.0	3.66	4.1
Tm (ppm)	0.519	0.521	0.520	0.002	0.3	0.54	3.8
Yb (ppm)	3.36	3.41	3.39	0.038	1.1	3.38	-0.1
Lu (ppm)	0.500	0.504	0.502	0.003	0.7	0.503	0.2
Hf (ppm)	4.71	4.84	4.78	0.092	1.9	4.9	2.5
Ta (ppm)	0.727	0.712	0.720	0.011	1.6	0.74	2.8
Pb (ppm)	10.7	9.96	10.33	0.514	5.0	11	6.1
Th (ppm)	5.67	5.79	5.73	0.091	1.6	5.7	-0.5
U (ppm)	1.61	1.65	1.63	0.027	1.7	1.69	3.4

¹Preferred values of GeoReM (Geological and Environmental Reference Materials; <http://georem.mpch-mainz.gwdg.de/>)

*Information Values

Appendix III d Accuracy of ICP-MS trace element data for BCR-2
(Table 3b) (Acme Analytical Laboratories Ltd.)

Element	BCR-2	Ref. Value ¹	Rel. dev. (%)
Li (ppm)		9*	
Sc (ppm)	33.0	33	0.0
V (ppm)	405	416	2.6
Cr (ppm)		18	
Co (ppm)	35.3	37	4.6
Ni (ppm)	7.30	18*	59.4
Cu (ppm)	20.2	21*	3.8
Zn (ppm)	79.0	127	37.8
Ga (ppm)	21.2	23	7.8
Rb (ppm)	46.4	46.9	1.1
Sr (ppm)	352	340	-3.6
Y (ppm)	33.1	37	10.5
Zr (ppm)	208	184	-12.9
Nb (ppm)	11.1	12.6	11.9
Ba (ppm)	686	677	-1.3
La (ppm)	24.1	24.9	3.2
Ce (ppm)	52.3	52.9	1.1
Pr (ppm)	6.43	6.7	4.0
Nd (ppm)	27.9	28.7	2.8
Sm (ppm)	5.97	6.58	9.3
Eu (ppm)	1.75	1.96	10.7
Gd (ppm)	6.33	6.75	6.2
Tb (ppm)	1.03	1.07	3.7
Dy (ppm)	5.95	6.41	7.2
Ho (ppm)	1.21	1.28	5.5
Er (ppm)	3.40	3.66	7.1
Tm (ppm)	0.490	0.54	9.3
Yb (ppm)	3.10	3.38	8.3
Lu (ppm)	0.470	0.503	6.6
Hf (ppm)	5.90	4.9	-20.4
Ta (ppm)	0.600	0.74	18.9
Th (ppm)	6.40	5.7	-12.3
U (ppm)	1.70	1.69	-0.6

¹Preferred values of GeoReM (Geological and Environmental Reference Materials;
<http://georem.mpch-mainz.gwdg.de/>)

*Information Values

Table 4:

*Accuracy of ICP-MS trace element data for AGV-2***Appendix III d** Accuracy of ICP-MS trace element data for AGV-2
(Acme Analytical Laboratories Ltd.)

Element	AGV-2	Ref. Value ¹	Rel. dev. (%)
Li (ppm)		11	
Sc (ppm)	12.0	13	7.7
V (ppm)	118	122	3.3
Cr (ppm)		16	
Co (ppm)	15.6	16	2.5
Ni (ppm)	11.8	20	41.0
Cu (ppm)	53.7	53	-1.3
Zn (ppm)	65.0	86	24.4
Ga (ppm)	19.4	20	3.0
Rb (ppm)	68.6	66.3	-3.5
Sr (ppm)	673	661	-1.8
Y (ppm)	19.2	19	-1.1
Zr (ppm)	284	230	-23.4
Nb (ppm)	12.3	14.5	15.2
Ba (ppm)	1131	1130	-0.1
La (ppm)	36.8	37.9	2.9
Ce (ppm)	70.7	68.6	-3.1
Pr (ppm)	7.85	7.84	-0.1
Nd (ppm)	29.6	30.5	3.0
Sm (ppm)	5.19	5.49	5.5
Eu (ppm)	1.44	1.53	5.9
Gd (ppm)	4.51	4.52	0.2
Tb (ppm)	0.620	0.64	3.1
Dy (ppm)	3.39	3.47	2.3
Ho (ppm)	0.660	0.65	-1.5
Er (ppm)	1.66	1.81	8.3
Tm (ppm)	0.240	0.26	7.7
Yb (ppm)	1.57	1.62	3.1
Lu (ppm)	0.240	0.247	2.8
Hf (ppm)	7.40	5	-48.0
Ta (ppm)	0.600	0.87	31.0
Th (ppm)	6.40	6.1	-4.9
U (ppm)	2.00	1.86	-7.5

¹Preferred values of GeoReM (Geological and Environmental Reference Materials;
<http://georem.mpch-mainz.gwdg.de/>)

Table 5: Reproducibility of ICP-MS trace element data

Appendix III d
(Table 5)

Reproducibility of ICP-MS trace element data evaluated from different sample dissolutions
(Institute of Geosciences at the Christian-Albrechts University of Kiel)

# Analysis/ Element	CIR 139D-2 (1)	CIR 139D-2 (2)	Diff. (%)	DSDP Leg 74 525 A 56 2W 68-79 (1)	DSDP Leg 74 525 A 56 2W 68-79 (2)	Diff. (%)	DSDP Leg 74 525 A 56 2W 128-134 (1)	DSDP Leg 74 525 A 56 2W 128-134 (2)	Diff. (%)	DSDP Leg 74 528 45 2W 109-119 (1)	DSDP Leg 74 528 45 2W 109-119 (2)	Diff. (%)	AII-93-19-4 (1)	AII-93-19-4 (2)	Diff. (%)
Li (ppm)	22.9	23.0	-0.5	7.33	7.38	-0.6	9.71	9.64	0.7	16.3	16.3	0.3	47.2	47.4	-0.5
Sc (ppm)	31.9	31.9	0.1	32.0	31.4	1.9	33.6	33.1	1.3	38.0	37.7	0.7	1.97	1.99	-1.1
V (ppm)	295	292	0.9	301	293	2.8	315	305	3.3	327	329	-0.3	34.1	34.02	0.3
Cr (ppm)	92.2	92.7	-0.5	38.8	38.4	1.1	37.9	37.6	0.8	75.9	66.5	12.3	<0.5	<0.5	
Co (ppm)	51.0	50.5	1.0	31.0	30.8	0.6	30.0	29.8	0.5	41.5	41.4	0.3	<0.1	<0.1	
Ni (ppm)	73.5	73.2	0.4	22.9	22.7	1.1	19.8	19.7	0.0	56.0	55.9	0.2	23.2	23.1	0.2
Cu (ppm)	62.7	63.0	-0.4	58.7	58.4	0.5	57.5	57.9	-0.6	120	120	0.1	20.8	21.0	-1.1
Zn (ppm)	122	123	-1.2	94.5	92.0	2.7	104	104	0.4	81.3	81.2	0.2	77.3	77.8	-0.7
Ga (ppm)	21.4	21.2	0.8	20.6	20.3	1.6	21.1	20.8	1.2	18.1	17.8	1.5	21.1	21.4	-1.5
Rb (ppm)	15.1	15.0	0.2	13.3	13.3	0.7	4.33	4.31	0.6	12.0	11.9	0.7	183	187	-2.2
Sr (ppm)	493	490	0.5	392	389	0.9	414	411	0.8	274	271	1.2	247	250	-1.2
Y (ppm)	25.2	25.3	-0.2	34.1	33.8	0.8	27.8	27.6	0.9	28.6	28.5	0.2	7.23	7.38	-2.0
Zr (ppm)	146	145	0.7	205	204	0.8	213	212	0.4	127	126	0.4	1004	1018	-1.5
Nb (ppm)	14.7	14.8	-0.3	18.5	18.2	1.4	18.5	18.5	0.4	18.3	18.2	0.7	344	348	-1.2
Ba (ppm)	208	210	-0.8	310	306	1.3	308	309	-0.4	273	268	1.7	173	177	-2.0
La (ppm)	20.2	20.3	-0.3	26.1	25.9	0.7	22.3	22.3	0.2	18.3	18.3	-0.1	17.0	17.5	-2.8
Ce (ppm)	43.2	43.3	-0.1	55.1	55.0	0.2	49.2	49.3	-0.1	37.3	37.3	0.1	27.8	28.6	-2.7
Pr (ppm)	5.62	5.63	-0.3	6.98	6.90	1.2	6.40	6.39	0.2	4.58	4.57	0.2	3.77	3.89	-3.2
Nd (ppm)	24.1	24.1	0.3	29.7	29.6	0.3	27.6	27.7	-0.3	19.3	19.2	0.6	12.1	12.4	-2.8
Sm (ppm)	5.52	5.51	0.2	6.64	6.60	0.6	6.28	6.25	0.5	4.50	4.54	-0.9	1.97	2.03	-2.8
Eu (ppm)	1.88	1.89	-0.5	2.15	2.14	0.7	2.13	2.14	-0.2	1.58	1.58	-0.6	0.543	0.558	-2.7
Gd (ppm)	5.61	5.62	-0.3	6.89	6.87	0.4	6.33	6.35	-0.3	5.07	5.07	-0.1	1.58	1.62	-2.8
Tb (ppm)	0.846	0.847	-0.1	1.06	1.06	0.1	0.957	0.960	-0.3	0.833	0.827	0.6	0.240	0.248	-3.0
Dy (ppm)	4.94	4.94	0.1	6.38	6.36	0.3	5.59	5.62	-0.4	5.25	5.24	0.2	1.36	1.40	-2.3
Ho (ppm)	0.933	0.936	-0.4	1.25	1.25	0.5	1.07	1.07	0.0	1.07	1.07	0.7	0.266	0.273	-2.7
Er (ppm)	2.41	2.41	0.0	3.33	3.32	0.2	2.74	2.75	-0.3	2.92	2.92	-0.2	0.800	0.807	-0.9
Tm (ppm)	0.334	0.333	0.2	0.469	0.465	0.8	0.376	0.370	1.7	0.422	0.426	-1.0	0.133	0.134	-0.8
Yb (ppm)	2.06	2.07	-0.3	2.96	2.93	0.9	2.33	2.33	-0.4	2.78	2.76	0.5	0.963	0.979	-1.6
Lu (ppm)	0.296	0.294	1.0	0.439	0.438	0.0	0.340	0.340	-0.3	0.421	0.417	1.1	0.151	0.152	-0.9
Hf (ppm)	3.58	3.61	-0.7	4.77	4.77	0.0	4.99	5.03	-0.7	3.16	3.18	-0.7	16.8	16.9	-0.6
Ta (ppm)	0.824	0.834	-1.2	1.01	1.02	-0.3	1.05	1.05	0.0	1.00	1.00	0.1	10.2	10.4	-2.5
Pb (ppm)	2.18	2.20	-0.7	2.71	2.47	8.8	2.56	2.61	-1.9	2.07	2.15	-3.8	7.46	7.62	-2.2
Th (ppm)	1.65	1.65	-0.4	2.41	2.43	-0.8	2.50	2.54	-1.4	2.33	2.33	0.0	46.9	47.6	-1.7
U (ppm)	0.300	0.298	0.6	0.615	0.614	0.2	0.526	0.528	-0.4	0.448	0.449	-0.2	2.76	2.81	-1.7

Table 6:

Machine reproducibility

Appendix III d
(Table 6)Machine reproducibility evaluated from same sample dissolution
(Institute of Geosciences at the Christian-Albrechts University of Kiel)

# Analysis/ Element	PS69/424-1- DR 26-1 (1)	PS69/424-1- DR 26-1 (2)	PS69/424-1- DR 26-1 (3)	Std. dev. ($\pm 1\sigma\%$)	DSDP Leg 74 525 A 60 4W 88-102 (1)	DSDP Leg 74 525 A 60 4W 88-102 (2)	DSDP Leg 74 525 A 60 4W 88-102 (3)	DSDP Leg 74 525 A 60 4W 88-102 (4)	DSDP Leg 74 525 A 60 4W 88-102 (5)	DSDP Leg 74 525 A 60 4W 88-102 (6)	Std. dev. ($\pm 1\sigma\%$)
Li (ppm)	70.22	68.52	67.90	1.7	8.97	9.06	8.89	8.89	8.84	8.80	1.1
Sc (ppm)	34.88	34.23	34.38	1.0	37.8	37.5	36.7	37.3	37.3	37.4	1.0
V (ppm)	339.85	333.93	335.12	0.9	363	359	357	361	360	363	0.6
Cr (ppm)	482.59	481.27	480.82	0.2	52.7	51.6	50.7	51.4	51.6	51.5	1.3
Co (ppm)	42.12	41.30	40.72	1.7	48.1	47.0	46.4	46.5	46.7	46.7	1.3
Ni (ppm)	247.42	244.59	241.39	1.2	53.2	51.8	51.1	51.1	51.4	51.4	1.5
Cu (ppm)	84.21	82.15	80.78	2.1	74.5	73.2	72.0	72.3	72.7	72.8	1.2
Zn (ppm)	206.60	203.90	200.20	1.6	104	103	103	103	102	103	0.5
Ga (ppm)	18.45	18.32	17.76	2.0	24.4	24.4	24.4	24.6	24.5	24.4	0.3
Rb (ppm)	11.94	11.87	11.75	0.8	5.78	5.83	5.82	5.88	5.88	5.88	0.7
Sr (ppm)	948.37	951.17	932.04	1.1	472	480	479	484	483	491	1.3
Y (ppm)	33.11	33.11	32.44	1.2	37.6	37.7	37.7	37.8	37.8	38.1	0.5
Zr (ppm)	377.33	372.52	370.04	1.0	257	259	260	263	262	265	1.0
Nb (ppm)	75.18	73.26	73.46	1.4	21.1	21.0	20.9	20.9	20.9	21.0	0.4
Ba (ppm)	506.28	504.10	512.85	0.9	344	353	355	360	362	365	2.2
La (ppm)	54.32	53.86	54.57	0.7	30.0	29.9	30.1	30.1	30.2	30.2	0.4
Ce (ppm)	113.95	114.25	116.93	1.4	64.1	64.5	64.7	64.6	64.6	64.8	0.4
Pr (ppm)	13.63	13.57	13.63	0.2	8.10	8.13	8.16	8.16	8.16	8.15	0.3
Nd (ppm)	53.76	53.51	53.86	0.3	34.4	34.7	34.7	34.6	34.6	34.7	0.3
Sm (ppm)	10.73	10.64	10.82	0.8	7.61	7.70	7.66	7.64	7.62	7.67	0.4
Eu (ppm)	3.32	3.29	3.32	0.7	2.49	2.50	2.50	2.49	2.49	2.50	0.3
Gd (ppm)	9.57	9.45	9.61	0.9	7.90	7.92	7.93	7.88	7.89	7.90	0.2
Tb (ppm)	1.33	1.32	1.34	0.5	1.21	1.22	1.22	1.22	1.21	1.22	0.3
Dy (ppm)	7.12	7.05	7.14	0.7	7.25	7.28	7.32	7.30	7.30	7.28	0.3
Ho (ppm)	1.27	1.26	1.27	0.6	1.41	1.41	1.41	1.41	1.41	1.41	0.3
Er (ppm)	3.13	3.08	3.14	0.9	3.67	3.70	3.71	3.70	3.69	3.68	0.3
Tm (ppm)	0.41	0.41	0.42	0.6	0.504	0.509	0.509	0.508	0.512	0.509	0.5
Yb (ppm)	2.51	2.46	2.49	0.9	3.17	3.20	3.17	3.19	3.17	3.16	0.5
Lu (ppm)	0.35	0.35	0.36	0.7	0.459	0.464	0.464	0.462	0.465	0.457	0.7
Hf (ppm)	8.80	8.60	8.70	1.1	5.85	5.88	5.95	5.93	5.89	5.83	0.8
Ta (ppm)	4.56	4.55	4.61	0.7	1.16	1.17	1.17	1.18	1.17	1.16	0.7
Pb (ppm)	4.54	4.52	4.57	0.5	3.36	3.36	3.37	3.38	3.36	3.34	0.4
Th (ppm)	7.47	7.29	7.40	1.2	3.07	3.05	3.04	3.04	3.02	2.99	0.9
U (ppm)	1.34	1.32	1.33	0.7	0.743	0.737	0.739	0.738	0.728	0.720	1.1

Appendix III e

Sample replicates (isotope measurements)

Table 1: Replicates using same sample material and leaching method

Appendix IIIe (Table 1)								
Replicates using same sample material and leaching method								
Sample	⁸⁷ Sr/ ⁸⁶ Sr	¹⁴³ Nd/ ¹⁴⁴ Nd	²⁰⁴ Pb/ ²⁰⁶ Pb	²⁰⁷ Pb/ ²⁰⁶ Pb	²⁰⁸ Pb/ ²⁰⁶ Pb	²⁰⁶ Pb/ ²⁰⁴ Pb	²⁰⁷ Pb/ ²⁰⁴ Pb	²⁰⁸ Pb/ ²⁰⁴ Pb
Standard	<i>NBS987</i>	<i>La Jolla</i>	<i>NBS981</i>	<i>NBS981</i>	<i>NBS981</i>	<i>NBS981</i>	<i>NBS981</i>	<i>NBS981</i>
Average	0.710250	0.511850	0.059026	0.91486	2.16771	16.9416	15.4992	36.7246
2sigma	0.000013	0.000007	0.000009	0.00007	0.00009	0.0024	0.0024	0.0061
2sigma array	0.000026	0.000014	0.000017	0.00013	0.00019	0.0049	0.0049	0.0122
N=	42	25	18	18	18	18	18	18
PS69/420-1-DR 21-1		0.512426	0.054517	0.84833	2.13540	18.3429	15.5607	39.1694
PS69/420-1-DR 21-1_Rep		0.512426	0.054497	0.84815	2.13616	18.3496	15.5632	39.1976
Average		0.512426	0.054507	0.84824	2.13578	18.3462	15.5619	39.1835
Delta		0.000000	0.000020	0.00018	-0.00076	-0.0067	-0.0024	-0.0282
Delta within 2 sigma array?		yes	no	no	no	no	yes	no
DSDP Leg 74 528 42 1W 29-45	0.704785	0.512563	0.055415	0.85918	2.15160	18.0458	15.5046	38.8273
DSDP Leg 74 528 42 1W 29-45_Rep	0.704751	0.512563	0.055454	0.85972	2.15258	18.0330	15.5033	38.8175
Average	0.704768	0.512563	0.055434	0.85945	2.15209	18.0394	15.5039	38.8224
Delta	-0.000033	0.000000	0.000039	0.00054	0.00098	-0.0128	-0.0013	-0.0098
Delta within 2 sigma array?	no	yes	no	no	no	no	yes	yes
AII-93-5-3	0.704951	0.512616	0.053666	0.83645	2.09752	18.6339	15.5862	39.0848
AII-93-5-3_Rep	0.704968	0.512621	0.053680	0.83660	2.09766	18.6288	15.5848	39.0768
Average	0.704959	0.512618	0.053673	0.83652	2.09759	18.6313	15.5855	39.0808
Delta	0.000018	0.000005	0.000015	0.00015	0.00015	-0.0051	-0.0015	-0.0080
Delta within 2 sigma array?	yes	yes	yes	yes	yes	yes	yes	yes
PS69/419-1-DR 20-1	0.705289	0.512498	0.054551	0.85032	2.13100	18.3314	15.5875	39.0642
PS69/419-1-DR 20-1_Rep	0.705298	0.512496	0.054643	0.85131	2.13262	18.3006	15.5795	39.0282
Average	0.705294	0.512497	0.054597	0.85081	2.13181	18.3160	15.5835	39.0462
Delta	0.000009	-0.000002	0.000092	0.00099	0.00162	-0.0308	-0.0080	-0.0360
Delta within 2 sigma array?	yes	yes	no	no	no	no	no	no
PS69/440-1-DR 32-2	0.705519	0.512495	0.054621	0.85213	2.12662	18.3079	15.6007	38.9339
PS69/440-1-DR 32-2_Rep	0.705522	0.512499	0.054622	0.85199	2.12652	18.3077	15.5980	38.9318
Average	0.705521	0.512497	0.054622	0.85206	2.12657	18.3078	15.5993	38.9329
Delta	0.000004	0.000004	0.000000	-0.00014	-0.00010	-0.0001	-0.0026	-0.0021
Delta within 2 sigma array?	yes	yes	yes	yes	yes	yes	yes	yes
Sample	⁸⁷Sr/⁸⁶Sr	¹⁴³Nd/¹⁴⁴Nd	²⁰⁴Pb/²⁰⁶Pb	²⁰⁷Pb/²⁰⁶Pb	²⁰⁸Pb/²⁰⁶Pb	²⁰⁶Pb/²⁰⁴Pb	²⁰⁷Pb/²⁰⁴Pb	²⁰⁸Pb/²⁰⁴Pb
DSDP Leg 74 527 41 5W 95-105	0.703633	0.512901	0.054081	0.84111	2.08394	18.4908	15.5527	38.5336
DSDP Leg 74 527 41 5W 95-105_Rep	0.703649	0.512915	0.054026	0.84014	2.08142	18.5096	15.5506	38.5262
Average	0.703641	0.512908	0.054054	0.84062	2.08268	18.5002	15.5516	38.5299
Delta	-0.000016	-0.000014	0.000055	0.00097	0.00252	-0.0188	0.0021	0.0074
Delta within 2 sigma array?	yes	yes	no	no	no	no	no	yes
RC16-11RD # 2	0.705557	0.512344	0.056222	0.87039	2.14690	17.7866	15.4813	38.1861
RC16-11RD # 2_Rep	0.705572	0.512358	0.056229	0.87029	2.14679	17.7844	15.4776	38.1795
Average	0.705565	0.512351	0.056226	0.87034	2.14685	17.7855	15.4795	38.1828
Delta	-0.000015	-0.000014	-0.000007	0.00010	0.00011	0.0022	0.0037	0.0066
Delta within 2 sigma array?	yes	yes	yes	yes	yes	yes	yes	yes
DSDP Leg 75 530 A 108 3W 78-84	0.703127	0.512954	0.052559	0.82084	2.05762	19.0262	15.6174	39.1486
DSDP Leg 75 530 A 108 3W 78-84_Rep	0.703090	0.512958	0.052571	0.82096	2.05757	19.0219	15.6161	39.1388
Average	0.703109	0.512956	0.052565	0.82090	2.05759	19.0240	15.6168	39.1437
Delta	-0.000037	0.000003	0.000012	0.00012	-0.00005	-0.0043	-0.0013	-0.0098
Delta within 2 sigma array?	no	yes	yes	yes	yes	yes	yes	yes
AII-93-3-25	0.704486	0.512633	0.055039	0.85446	2.12246	18.1691	15.5248	38.5632
AII-93-3-25_Rep	0.704514	0.512633	0.055046	0.85462	2.12259	18.1665	15.5255	38.5599
Average	0.704500	0.512633	0.055043	0.85454	2.12253	18.1678	15.5251	38.5615
Delta	0.000028	0.000000	0.000008	0.00016	0.00012	-0.0026	0.0008	-0.0033
Delta within 2 sigma array?	no	yes	yes	no	yes	yes	yes	yes
PS69/424-1-DR 26-1	0.704856	0.512694	0.054209	0.84362	2.11400	18.4471	15.5623	38.9972
PS69/424-1-DR 26-1_Rep	0.705237	0.512691	0.054237	0.84361	2.11278	18.4376	15.5543	38.9548
Average	0.705046	0.512693	0.054223	0.84362	2.11339	18.4424	15.5583	38.9760
Delta	0.000382	-0.000003	0.000028	0.00000	-0.00121	-0.0095	-0.0080	-0.0424
Delta within 2 sigma array?	no	yes	no	yes	no	no	no	no

Appendix IV

Additional Major and selected trace element data

Table 1: Additional major and selected trace element data for the Walvis Ridge and the Guyot Province

Appendix IV
(Table 1)

Additional major and selected trace element data for the Walvis Ridge and the Guyot Province

Sample	Tristan Track					Gough Track										Walvis Ridge
	AII-93-3-1B	AII-93-3-25	AII-93-5-3	AII-93-6-1	PS69/435-1-DR 27-1	AII-93-10-11	AII-93-14-1	AII-93-14-19	PS69/419-1-DR 20-1	PS69/421-2-DR 23-1	PS69/422-1-DR 24-1	PS69/423-1-DR 25-1a	PS69/423-1-DR 25-2	PS69/440-1-DR 32-2	PS69/440-1-DR 32-5b	AII-93-21-1
Rock type	Alkali Basalt	Alkali Basalt	Alkali Basalt	Tephrite	Alkali Basalt	Alkali Basalt	Basaltic Trachy-andesite	Basaltic Trachy-andesite	Alkali Basalt	Tephrite	Foidite	Alkali Basalt	Tephrite	Alkali Basalt	Tephrite	Alkali Basalt
Lab Method	1 XRF	1 XRF	1 XRF	1 XRF	1 XRF	1 XRF	1 XRF	1 XRF	1 XRF	1 XRF	1 XRF	1 XRF	1 XRF	1 XRF	1 XRF	1 XRF
Major Elements (wt%)																
SiO ₂	47.9	48.7	45.6	43.0	46.6	48.5	53.8	53.7	48.5	47.6	30.2	43.9	43.5	45.9	44.0	46.3
TiO ₂	2.79	2.72	2.98	2.93	1.94	3.86*	2.16	2.05	2.59	3.40	2.73	3.29	3.31	3.89*	4.1*	2.39
Al ₂ O ₃	15.7	15.9	17.0	17.4	17.9	13.6	16.6	16.5	17.6	16.7	10.4	15.0	15.1	16.1	16.9	16.3
Fe ₂ O ₃	12.0	10.9	12.3	10.6	12.0	15.1	8.06	7.90	12.3	12.3	10.1	10.7	11.7	12.8	13.0	16.1
MnO	0.160	0.120	0.120	0.120	0.170	0.160	0.090	0.120	0.120	0.120	0.180	0.100	0.100	0.130	0.120	0.090
MgO	4.98	5.14	3.42	2.05	6.16	4.48	3.15	3.37	4.21	2.08	4.89	4.44	3.73	5.01	3.06	3.33
CaO	10.3	10.5	9.7	9.6	9.8	8.69	7.33	7.52	6.45	7.72	22.5	11.7	11.6	8.90	8.89	7.81
Na ₂ O	3.00	3.19	3.20	3.87	3.11	2.83	4.09	3.86	2.74	3.46	1.07	2.28	2.26	3.24	3.34	3.03
K ₂ O	1.13	1.22	1.52	2.09	0.600	1.46	2.92	2.63	1.58	3.58	1.11	2.12	2.85	1.58	1.92	1.71
P ₂ O ₅	0.490	0.470	1.57*	3.39*	0.330	0.500	0.540	0.490	0.290	1.11	2.4*	2.34*	1.5*	1.01	1.65*	0.550
LOI	1.69	1.74	2.29	4.16	1.82	1.48	1.37	1.87	3.92	2.02	13.2	3.79	4.45	1.74	2.79	2.99
TOTAL	100.18	100.55	99.73	99.18	100.43	100.64	100.12	100.03	100.37	100.07	98.86	99.61	100.11	100.24	99.71	100.58
Trace Elements (ppm)																
Co	51.0	49.0	33.0	23.0	48.0	48.0	27.0	51.0	27.0	37.0	44.0	40.0	40.0	44.0	40.0	33.0
Cr	48.0	47.0	<16	26.0	239	22.0	114	113	120	154	265	348	347	178	135	18.0
Ni	33.0	37.0	9.00	12.0	135	21.0	48.0	122	40	60.0	118	78.0	95.0	99.0	80.0	33.0
Cu																
Sc																
V	301	292	286	221	249	368	173	162	228	282	234	236	245	274	304	376
Zn	123	134	127	129	103	133	154	124	258	132	168	141	154	126	156	150
Nb	23.0	22.0	41.0	41.0	16.0	28.0	32.0	32.0	42.0	57.0	67.0	64.0	63.0	38.0	38.0	13.0
Ga	22.0	24.0	27.0	18.0	23.0	28.0	31.0	27.0	28.0	26.0	24.0	17.0	22.0	26.0	28.0	23.0
Rb	29.0	45.0	25.0	35.0	16.0	37.0	39.0	45.0	23.0	58.0	27.0	38.0	50.0	23.0	38.0	40.0
Ba	307	314	437	379	154	349	1205	1227	383	812	654	884	870	637	690	166
Sr	466	451	604	612	342	518	454	477	409	833	375	915	859	942	946	381
Y	25.0	20.0	53.0	51.0	30.0	27.0	26.0	26.0	29.0	32.0	34.0	44.0	49.0	25.0	28.0	29.0
Zr	173	161	254	266	161	279	205	213	298	382	269	353	341	281	262	173

1 = GEOMAR Helmholtz-Zentrum für Ozeanforschung Kiel

* = Element concentrations in excess of the XRF calibration lines; BDL = Below detection limit

CURRICULUM VITAE

Joana Kristin Rohde,
née Deppe

Date of birth: 02.07.1981
Place of birth: Hamburg, Germany
Nationality: German
Marital status: married

PROFESSIONAL EXPERIENCE

- since 11/2009* Research assistant at GEOMAR Helmholtz Centre for Ocean Research Kiel within the DFG project WALVIS I (Ar/Ar Geochronology and Geochemistry of existing samples from the Walvis Ridge and Rio Grande Rise), Research Division: Dynamics of the Ocean Floor, Research Unit: Magmatic and Hydrothermal Systems
- 02/2007 - 02/2008* Freelancer at Tethys Geoconsulting GmbH, Kiel
- 01/2006 - 03/2006* Internship in the Paleomagnetism Laboratory at SOEST-Hawaii Institute of Geophysics and Planetology (HIGP) at the University of Hawaii at Manoa
- 12/2002 - 01/2007* Student assistant at GEOMAR Helmholtz Centre for Ocean Research Kiel
- Research Division: Dynamics of the Ocean Floor, Research Unit: Magmatic and Hydrothermal Systems
 - Collaborative Research Center (SFB) 574 at GEOMAR Helmholtz Centre for Ocean Research Kiel "Fluids and Volatiles in Subduction Zones"

ACADEMIC EDUCATION

- since 10/2009* Doctoral Studies at the Christian-Albrechts University of Kiel
- 09/2009* Diploma in Geology/Paleontology
- Major subjects: Magmatic Petrology, Marine Environmental Geology and Historical Geology
 - Diploma thesis (at GEOMAR Helmholtz Centre for Ocean Research Kiel): "Geochemical variations along the Gough-Tristan seamount tracks"
- 08/2007* Field mapping in Kråkenes, Norway: „High-pressure and ultra high-pressure metamorphic rocks of the Western Gneiss Region, Norway“; University of Oslo
- 10/2002 - 09/2009* Studies of Geology/Paleontology, Christian-Albrechts University of Kiel
- 04/2002 - 09/2002* Studies of Mineralogy, Christian-Albrechts University of Kiel

10/2001 - 03/2002 Studies of Macroeconomics, University of Hamburg
2001 Abitur (German general qualification for university entrance)

EXPEDITIONS

05/2007 - 06/2007 Participation in the research cruise SO193, Mainihiki:
„Temporal, Spatial, and Tectonic Evolution of
Oceanic Plateaus“ with the R/V Sonne

11/2005 Participation in the SFB 574-field trip
„Volcanoes of the subduction zone in Nicaragua“

11/2005 Participation in the research cruise M66/3b:
„Subflux“ with the R/V Meteor

PUBLICATIONS and CONFERENCE CONTRIBUTIONS

PUBLICATIONS

Rohde, J., Hoernle, K., Hauff, F., Werner, R., O'Connor, J., Class, C., Garbe-Schönberg, D., and Jokat, W., 2013a, 70 Ma chemical zonation of the Tristan-Gough hotspot track: *Geology*, v. 41, p. 335-338, doi:10.1130/G33790.1.

Rohde, J.K., van den Bogaard, P., Hoernle, K., Hauff, F., and Werner, R., 2013b, Evidence for an age progression along the Tristan-Gough volcanic track from new $^{40}\text{Ar}/^{39}\text{Ar}$ ages on phenocryst phases: *Tectonophysics*, v. 604, p. 60-71, doi:10.1016/j.tecto.2012.08.026.

CONFERENCE CONTRIBUTIONS

Hoernle, K., **Deppe, J.**, Hauff, F., Werner, R., and Phipps Morgan, J., 2012, Geochemical Zonation of Mantle Plumes: Lower Mantle Chemical Heterogeneity and Plume Splitting. Invited Talk: Goldschmidt Conference, 24.-29.06.2012, Montreal, Canada

Deppe, J., van den Bogaard, P., Hoernle, K., Hauff, F., and Werner, R., 2012, Age progressive volcanism along the Tristan-Gough-Walvis track: evidence from new $^{40}\text{Ar}/^{39}\text{Ar}$ phenocryst ages.
Poster: SPP 1375 Colloquium, 12.06.-15.06.2012, Tutzing, Germany

Deppe, J., van den Bogaard, P., Hauff, F., Hoernle, K., Werner, R., O'Connor, J., Fietzke, J., and Jokat, W., 2011, New $^{40}\text{Ar}/^{39}\text{Ar}$ geochronological evidence for a hotspot chain origin of the Walvis Track.
Poster: SPP 1375 Colloquium, 07.06.-10.06.2011, Potsdam, Germany

Deppe, J., Hauff, F., Hoernle, K., Werner, R., Garbe-Schönberg, C. D., O'Connor, J., and Jokat, W., 2010, Evidence for a long-term geochemical zonation of the Tristan-Gough Hotspot.

Talk: SPP1375 Colloquium, 14.06.-17.06.2010, Kiel, Germany

Deppe, J., Hauff, F., Hoernle, K., Werner, R., Garbe-Schönberg, C. D., O'Connor, J., and Jokat, W., 2010, Evidence for a long-term geochemical zonation of the Tristan-Gough Hotspot.

Poster: EGU General Assembly, 02.05.-07.05.2010, Vienna, Austria

Hauff, F., **Deppe, J.**, Hoernle, K., Werner, R., Garbe-Schönberg, C. D., O'Connor, J., and Jokat, W., 2009, Geochronology and geochemistry of existing samples from the Walvis Ridge and Rio Grande Rise: aims, status and first results of the SPP1375 Project "WALVIS-I".

Talk: SPP1375 Colloquium, 04.05.-06.05.2009, Benediktbeuern, Germany

